

Beatrice Musig

Nanostructured catalysts for plasma-assisted CO₂ methanation

Director/es

Navarro López, M. Victoria
Gálvez Parruca, María Elena

<http://zaguan.unizar.es/collection/Tesis>



Universidad
Zaragoza

Tesis Doctoral

NANOSTRUCTURED CATALYSTS FOR PLASMA-ASSISTED CO₂ METHANATION

Autor

Beatrice Musig

Director/es

Navarro López, M. Victoria
Gálvez Parruca, María Elena

UNIVERSIDAD DE ZARAGOZA
Escuela de Doctorado

Programa de Doctorado en Ingeniería Química y del Medio Ambiente

2023



Universidad
Zaragoza



CSIC

CONSEJO SUPERIOR DE INVESTIGACIONES CIENTÍFICAS



INSTITUTO DE
CARBOQUÍMICA



d'Alembert

Institut Jean le Rond d'Alembert

Doctoral Thesis

Nanostructured catalysts for plasma-assisted CO₂ methanation

Beatrice Musig



Zaragoza, June 2023



This project has received funding from the European Union's Horizon H2020 research and innovation programme under the Marie Skłodowska-Curie grant agreement n 813393

Nanostructured catalysts for plasma-assisted CO₂ methanation

Catalizadores nanoestructurados para
metanización de CO₂ asistida por plasma

Catalyseurs nanostructurés pour la
méthanisation du CO₂ assistée par plasma

Beatrice Musig

Work presented for the double degree of:

Doctor por la Universidad de Zaragoza in the framework of the program of
Ingeniería Química y del Medio Ambiente

Diplôme national de Doctorat de Sorbonne Université, spécialité Energétique
génie des procédés.

Supervised by Dr. Maria Victoria Navarro (Instituto de Carboquímica ICB-CSIC)
and Dr. Maria Elena Galvez (Institut Jean le Rond d'Alembert CNRS-SU).

Zaragoza, June 2023

Table of Contents

Table of Contents	1
List of Figures	4
List of Tables	9
List of Symbols and Abbreviations	10
Abstract	11
Resumen	12
Résumé	14
Acknowledgements	16
Chapter 1: Introduction	17
1.1. Catalytic CO ₂ methanation	22
1.1.1. Catalysts used for CO ₂ methanation	24
1.1.2. Non-conventional catalysis: electro-, photo- and plasma catalysis	24
1.2. CeO ₂ -based catalysts for CO ₂ methanation	26
1.2.1. Effect of synthesis techniques of ceria	29
1.2.2. Effect of metal active phase supported on ceria	30
1.2.3. Comparison of ceria with different supports	32
1.3. Plasma	35
1.3.1. CO ₂ plasma for CCU applications	37
1.4. Plasma-assisted catalysis	38
1.4.1. Ceria-based catalysts for plasma-assisted CO ₂ methanation	42
1.4.2. Diagnostics for plasma catalysis	44
1.4.3. CO ₂ methanation reaction mechanisms in the presence of CeO ₂ -based catalysts	45
1.5. Motivation and objectives of the thesis	47
Chapter 2: Materials and Methods	49
2.1. Synthesis	50
2.1.1. Materials	50
2.1.2. Hydrothermal method	50
2.1.3. Design of experiments (DOE)	51
2.1.4. Wet impregnation	51
2.2. Physicochemical characterization	52
2.2.1. X-Ray Diffraction (XRD)	52
2.2.2. Scanning Electron Microscopy (SEM) and energy-dispersive X-ray (EDX)	54

Table of Contents

2.2.3.	Transmission Electron Microscopy (TEM).....	54
2.2.4.	N ₂ Physisorption	54
2.2.5.	Temperature-Programmed experiments.....	56
2.2.6.	Thermogravimetric Analysis (TGA).....	57
2.2.7.	X-Ray Photoelectron Spectroscopy (XPS).....	57
2.2.8.	Raman Spectroscopy	58
2.2.9.	Fourier Transform Infrared Spectroscopy (FTIR)	58
2.2.10.	Inductively Coupled Plasma Atomic Emission Spectroscopy (ICP-AES)	58
2.2.11.	Total Organic Carbon (TOC).....	59
2.3.	<i>DBD reactor for plasma-assisted CO₂ methanation</i>	59
2.3.1.	Plasma catalytic set-up.....	59
2.3.2.	Gas Chromatography (GC)	61
2.3.3.	Power supply	62
2.3.4.	Electrical characterization	62
2.3.5.	Energy efficiency calculations	64
2.4.	<i>Thermo-catalytic CO₂ methanation set-up</i>	65
Chapter 3: A factorial design study of the morphology of cerium oxide supports and the impact on Ni catalysts physicochemical properties.....		67
3.1.	<i>Introduction</i>	67
3.2.	<i>DOE methodology</i>	67
3.3.	<i>Results and discussion</i>	68
3.3.1.	<i>Physicochemical characterisation of the cerium oxide supports</i>	68
3.3.2.	Study of the effect of synthesis parameters on the physicochemical properties	72
3.3.3.	Oxygen storage capacity and surface planes	75
3.3.4.	Impact of the introduction of Ni on the CeO ₂ supports on the size, textural, morphology and surface properties	83
3.3.5.	Reducibility and basicity of the Ni/CeO ₂ catalysts obtained from the DOE supports	94
3.4.	<i>Conclusions</i>	98
Chapter 4: Plasma-assisted and thermal CO₂ methanation over Ni/CeO₂ catalysts: influence of physicochemical properties		99
4.1.	<i>Introduction</i>	99
4.2.	<i>Methodology</i>	99
4.3.	<i>Results and discussion</i>	101
4.3.1	Plasma-assisted CO ₂ methanation	101
4.3.2	Comparison with empty DBD reactor and packed with metal oxide supports	106
4.3.3	Thermal CO ₂ methanation	108
4.3.4	Comparison of thermal and plasma-assisted processes.....	109
4.3.5	Impact of DOE factors and physicochemical properties on the catalytic performance	111

4.3.6	Stability tests	116
4.3.7	Characterisation of the catalysts after plasma-assisted and thermal reaction	118
4.4.	<i>Conclusions</i>	127
Chapter 5: Electrical characterization of the packed bed DBD reactor		129
5.1.	<i>Introduction</i>	129
5.2.	<i>Methods</i>	130
5.2.1.	Q-V Lissajous cycle analysis.....	130
5.2.2.	Charge peaks analysis.....	132
5.2.3.	Current envelope	133
5.3.	<i>Results and discussion</i>	133
5.3.1.	Lissajous shape analysis and dielectric properties	133
5.3.2.	Statistical analysis of charge transfer events in the DBD reactor	139
5.3.3.	Current peaks analysis	142
5.3.4.	Effect of physicochemical features of the catalyst on the electrical behaviour of the packed bed DBD	147
5.4.	<i>Conclusions</i>	149
Chapter 6: Proposed reaction mechanism of plasma-assisted and thermal CO₂ methanation with Ni/CeO₂ nanoneedles catalyst via operando studies.....		151
6.1.	<i>Introduction</i>	151
6.2.	<i>Methods</i>	152
6.2.1.	DBD plasma operando set-up	152
6.2.2.	Thermal operando set-up	153
6.3.	<i>Results and discussion</i>	154
6.3.1.	DBD plasma operando study.....	154
6.3.2.	Thermal operando study.....	160
6.4.	<i>Conclusions</i>	164
Chapter 7: Conclusions and prospects.....		165
<i>Conclusiones</i>		168
<i>Conclusion</i>		171
References		174
List of contributions.....		188
Annex 1: Comparison of syntheses ceria with commercial metal oxides as supports for Ni catalysts.....		189
Annex 2: Effect of catalyst reduction and particle size on the plasma-assisted CO₂ methanation results in the DBD plasma reactor		192
Annex 3: Literature screening of FTIR bands of adsorbed C-species on ceria.....		194

List of Figures

Figure 1.1: a) Global annual CO ₂ emissions b) Equivalent CO ₂ of greenhouse gas emissions by sector as a function of year (source: ourworldindata.org dataset [2]).	18
Figure 1.2: Predicted effect of possible scenarios on global CO ₂ emissions and global warming (reproduced from Hausfather et al., Nature, 2020 [4]).	19
Figure 1.3: Technologies for climate change mitigation in the energy sector and their respective estimated cost and potential contribution to net-zero goal (reproduced from IPCC 2022 [9]).	19
Figure 1.4: Influence on CO ₂ methanation equilibrium of a) temperature (at atmospheric pressure conditions) and b) pressure (at temperature at 300 °C).	23
Figure 1.5: Comparison of non-conventional catalytic techniques applied to CO ₂ reduction (reproduced from Chen et al., Journal of CO ₂ Utilization, 2021 [43]).	25
Figure 1.6: Crystal structure of cerium oxide with presence of an oxygen vacancies.	26
Figure 1.7: Side view of the structure of selected facets of CeO ₂ crystal [46,47].	27
Figure 1.8: Number of publications about ceria utilized as catalyst per year (source: Web of Science search “ceria+catalysis” [58]).	28
Figure 1.9: Number of publications regarding plasma catalyst per year (source: Web of Science search “plasma+catalysis” [58]).	35
Figure 1.10: Literature results of specific energy input versus CO ₂ conversion in non-thermal plasma reactors grouped by plasma source type (symbol) and application (colour) (source: PIONEER Database [87]).	38
Figure 1.11: a) characteristic timescale of the various processes in NTP as well as on the catalyst surface (reproduced from Chen et al., Journal of CO ₂ Utilization, 2021 [43]); b) schematics of possible plasma-surface interactions [83,88].	39
Figure 1.12: Literature results of specific energy input versus CO ₂ conversion regarding plasma and catalyst material in-situ combination grouped by plasma source type (symbol) and application (colour) (source: PIONEER Database [87]).	40
Figure 1.13: Different factors that influence a plasma catalytic process (credits: PIONEER work package 3 M. Nguyen-Quang, M. Faedda, G. Hasrack, Y. Cai)	42
Figure 1.14: Graphical abstract of the PhD work.	48
Figure 2.1: Schematics of the a) hydrothermal synthesis and b) wet impregnation.	50
Figure 2.2: Overview of the main material characterization techniques and their purpose.	52
Figure 2.3: IUPAC classification of a) isotherm and b) hysteresis of N ₂ physisorption graphs reported from the 2015 IUPAC Technical Report [134].	55
Figure 2.4: Experimental set-up for the plasma-catalytic methanation of CO ₂ in the fixed bed reactor.	60
Figure 2.5: Gas chromatogram in a) column 1 (PBQ+MS5A) and b) column 2 (PPU) of mixture of CO ₂ , CH ₄ and H ₂ , used for the calibration of level 3.	61
Figure 2.6: Typical experimental Lissajous figure for an empty and packed bed DBD reactor, overlaid with a graphical example of linearization of the “plasma on” and “plasma off” for the empty case.	63
Figure 2.7: Equivalent electrical circuit of empty and packed bed DBD reactor.	64
Figure 2.8: Experimental set-up for thermal methanation of CO ₂ .	65

Figure 3.1: XRD diffractograms of the CeO ₂ supports of the DOE series. The (hkl) planes peaks are indexed on the top.	70
Figure 3.2: a) N ₂ Isotherm and b) pore size distribution plots of the DOE supports.	71
Figure 3.3: SEM images of nanoparticulate ceria a)-i) DOE0-8. The relative observed morphology is annotated above each image.	72
Figure 3.4: a) Pareto chart of the standardized effect and b) residual frequency histogram of the factorial DOE analysis with the crystallite size as response.	74
Figure 3.5: BF-TEM images of DOE0, 3, 5, 6 supports.	76
Figure 3.6: a) HRSTEM image of a single needle with FFT shown in the inset b) HRTEM image of a single needle showing formation of surface steps, the inset shows the FFT pattern taken from blue square region.	77
Figure 3.7: a) BF-TEM image of DOE3. b) SAED pattern taken from a). c) and d) IFFT of region 1 and 2 in a), respectively, that corresponds to spherical particles. d) HAADF-STEM image of DOE3. e) EDS spectrum of the region marked in d).	77
Figure 3.8: a) BF-TEM image and b) SAED pattern of DOE5 sample. c) HRTEM image of a single nanorod with the inset showing the FFT pattern and d) HRTEM image of the tip of the nanorod marked in c).	78
Figure 3.9: HRTEM images of the a) rod and b) cube structures in the DOE6 sample. The insets show the FFT patterns of the regions marked by the red squares.	79
Figure 3.10: Mass variation and temperature ramp during the TGA reduction-oxidation cycles with DOE0 CeO ₂ sample.	80
Figure 3.11: XPS spectra of DOE supports in the a) Ce3d b) O1s regions.	81
Figure 3.12: Raman spectra for DOE0, 3, 5, 6 supports.	82
Figure 3.13: XRD diffraction patterns of the Ni/DOE catalysts. The squares indicate the Ni phase peaks.	83
Figure 3.14: a) N ₂ isotherm and b) pore size distribution plots of the Ni/DOE catalysts.	85
Figure 3.15: Cube plot of Ni crystallite size as a function of the DOE factors [NaOH], temperature, and time.	86
Figure 3.16: a)- d) SEM and e)-h) TEM images of Ni/DOE selected catalysts.	88
Figure 3.17: a) SEM micrograph at x800 magnification and b) the relative EDX mapping of the area in a) of Ni/DOE5.	89
Figure 3.18: a) BF-TEM image of Ni/DOE0 and b) diffraction pattern.	90
Figure 3.19: (a), (e) and (i) shows HAADF-STEM image from different area of the Ni/DOE0. (b), (f) and (j) shows Ce L map, (c), (g) and (k) shows Ni K map, (d), (h) and (l) shows O K map.	90
Figure 3.20: a) HRTEM image of Ni/DOE3. b), c) FFT patterns of the regions marked by red and yellow squares in a).	90
Figure 3.21: a) HRTEM image of Ni/DOE5. b) FFT pattern of the region marked by red square in a). c) magnification of the region marked by red square in a). d) IFFT pattern of c).	91
Figure 3.22: a) HRTEM image of Ni/DOE6. b), c) and d) FFT pattern taken from three different regions in a).	91
Figure 3.23: XPS spectra of the a) Ni2p _{3/2} and b) O1s regions of the Ni/DOE0, 3, 5, 6 catalysts and relative deconvolutions.	92
Figure 3.24: Raman spectra of the Ni/DOE0, 3, 5, 6 catalysts.	93
Figure 3.25: H ₂ -TPR curves of samples a) Ni/DOE 0, 3, 5, 6 and CeO ₂ DOE0; and b) Ni/DOE1, 2, 4, 7, 8.	94
Figure 3.26: CO ₂ -TPD curves of samples a) Ni/DOE 0, 3, 5, 6 and CeO ₂ DOE0; and b) Ni/DOE1, 2, 4, 7, 8.	97
Figure 3.27: FTIR spectra of samples Ni/DOE0, 3, 5, 6.	97
Figure 4.1: measurement of furnace power a) over 30 minutes time and b) as a function of set temperature.	100

Figure 4.2: a) power as a function of the applied voltage b) CO ₂ conversion and c) CH ₄ selectivity results of plasma-assisted CO ₂ methanation tests with the Ni/DOE0-8 catalysts as a function of injected power. H ₂ /CO ₂ = 4, WHSV 30000 mL/hg _{cat}	102
Figure 4.3: Lissajous figures of a) Ni/DOE0, 3, 5, 6 and b) Ni/DOE1, 2, 4, 7, 8 samples at 24 kV _{p-p} applied voltage.....	103
Figure 4.4: a) Reactor temperature as a function of injected power. b) CO ₂ conversion as a function of reactor temperature during plasma-assisted CO ₂ methanation tests with the Ni/DOE0-8 catalysts as a function of injected power. H ₂ /CO ₂ = 4, WHSV 30000 mL/hg _{cat}	105
Figure 4.5: a) Power as a function of the applied voltage b) Lissajous figures at 23 kV _{p-p} applied voltage c) CO ₂ conversion and d) CH ₄ and CO selectivity results of plasma-assisted CO ₂ methanation tests performed with the empty reactor and with commercial CeO ₂ and Al ₂ O ₃ , and DOE0 supports as a function of injected power. H ₂ /CO ₂ = 4, WHSV 30000 mL/hg _{cat}	107
Figure 4.6: a) CO ₂ conversion and b) CH ₄ selectivity results of thermal CO ₂ methanation tests with the Ni/DOE0-8 catalysts as a function of temperature. H ₂ /CO ₂ = 4, WHSV 30000 mL/hg _{cat} . The equilibrium curve is added in dashed line.....	108
Figure 4.7: 3D plots of a) efficiency of plasma-assisted CO ₂ methanation 30.9 ± 3.8 W and b) thermal CO ₂ conversion at 300 °C as a function of physicochemical properties surface area and amount of medium strength basic sites. .	112
Figure 4.8: Contour plots of a) efficiency of plasma-assisted CO ₂ methanation at 30.9 ± 3.8 W and b) thermal CO ₂ conversion at 300 °C as a function of hydrothermal synthesis parameters NaOH concentration and temperature.	113
Figure 4.9: C _{reactor} plotted as a function of efficiency of the plasma-assisted CO ₂ methanation reaction carried out at 30.9 ± 3.8 W.....	114
Figure 4.10: 3D plots of efficiency of plasma-assisted CO ₂ methanation at 30.9 ± 3.8 W as a function of catalyst properties C _{reactor} and amount of medium strength basic sites.	116
Figure 4.11: Stability tests over 10 h for Ni/DOE0, 5, and 6 of a)-c) plasma-assisted at 50 W and d)-f) thermal CO ₂ methanation performed at 350 °C. H ₂ /CO ₂ = 4, WHSV 30000 mL/hg _{cat}	117
Figure 4.12: XRD diffraction patterns of the Ni/DOE catalysts after a) plasma exposure and b) thermal reaction. The cubes indicate the peaks of the Ni phase.....	118
Figure 4.13: SEM micrographs and TEM images of a),e) Ni/DOE0, b),f) Ni/DOE3, c),g) Ni/DOE5, d),h) Ni/DOE6 after plasma reaction.	120
Figure 4.14: SEM micrograph of Ni/DOE0 after thermal reaction.....	121
Figure 4.15: (a) HAADF-STEM image of Ni/DOE0 plasma. (b), (c) and (d) shows EDX mapping corresponding to Ce, Ni and O indicating Ni is distributed uniformly across whole sample.	121
Figure 4.16: (a) HRTEM image of Ni/DOE5 plasma and (b) its corresponding IFFT image considering only the FFT spots of Ni and NiO showing locations where Ni/NiO are present in (a). (c) HRTEM image of a Ni particle of Ni/DOE6 plasma, (b) and (c) FFT images of the regions marked by yellow and red square in (a) showing the presence of Ni and NiO diffraction patterns, respectively.	122
Figure 4.17: a) Ni2p XPS spectra of catalysts Ni/DOE0, 3, 5, 6 before and after plasma-assisted and thermal methanation reaction. b) C1s XPS spectra of Ni/DOE0 reduced, after plasma exposure, and after thermal methanation.	123
Figure 4.18: O1s XPS spectra of catalysts Ni/DOE0, 3, 5, 6 after plasma-assisted and thermal methanation reaction.	125
Figure 4.19: FTIR spectra of catalysts after plasma and thermal reaction.	125
Figure 4.20: TPD-MS of Ni/DOE0 before and after plasma and thermal reaction, and of Ni/DOE5 and 6 after plasma.	127

Figure 5.1: Experimental DBD set-up for the electrical diagnostics.	130
Figure 5.2: Ideal shape of a Lissajous Q-V plot for a DBD reactor.	131
Figure 5.3: Example of the analysis performed on the measured charge signal (in red) and its first derivative (in blue) for Ni/DOE0 packing at 25.3 kV _{p-p} over 1 period. The charge steps position t_{step} and width δt detected by the developed analysis are shown by the symbols.	132
Figure 5.4: Lissajous Q-V figure measured with empty DBD reactor and packed with Al ₂ O ₃ and CeO ₂ DOE0 supports at a) 25.4 ± 0.2 kV _{p-p} and b) 27.7 ± 0.3 kV _{p-p}	134
Figure 5.5: Lissajous Q-V figure measured with the DBD reactor packed with Ni/DOE0, 3, 5, 6 catalysts at a) 25.4 ± 0.2 kV _{p-p} and b) 27.7 ± 0.3 kV _{p-p}	135
Figure 5.6: Example of measured Lissajous Q-V cycle for Ni/DOE0 packing at 25.3 kV _{p-p} layered with the linearization obtained from the calculations performed with MATLAB.	136
Figure 5.7: Charge steps histograms obtained during the experiments with the DBD reactor packed with a),d) Al ₂ O ₃ and b),e) CeO ₂ DOE0 supports and with the c),f) empty DBD reactor at a-c) 25.4 ± 0.2 kV _{p-p} and d-f) 27.7 ± 0.3 kV _{p-p}	139
Figure 5.8: Charge steps histograms obtained during the experiments with the DBD reactor packed with the catalysts a),e) Ni/DOE0, b),f) Ni/DOE3, c),g) Ni/DOE5, d), h) Ni/DOE6 at a)-d) 25.4 ± 0.2 kV _{p-p} and e)-h) 27.7 ± 0.3 kV _{p-p}	140
Figure 5.9: Charge steps histograms obtained during the experiments with the DBD reactor packed with Ni/DOE0, 3, 5, and 6 at 27.7 ± 0.3 kV _{p-p} over charge interval 0-200 nC.	141
Figure 5.10: Example of measured V and Q signals and the current envelope over 2.5 periods during the experiment with Ni/DOE0 catalyst at 25.3 kV _{p-p} , power 15 W.	142
Figure 5.11: Current envelopes over 1 period obtained during the experiments with the empty DBD reactor and packed with Al ₂ O ₃ and CeO ₂ DOE0 supports at a) 25.4 ± 0.2 kV _{p-p} and b) 27.7 ± 0.3 kV _{p-p}	143
Figure 5.12: Current envelopes over 1 period obtained during the experiments with the DBD reactor packed with a),e) Ni/DOE0, b),f) Ni/DOE3, c),g) Ni/DOE5, d), h) Ni/DOE6 at a)-d) 25.4 ± 0.2 kV _{p-p} and e)-h) 27.7 ± 0.3 kV _{p-p}	144
Figure 5.13: Close-up in the 1-2.5 10 ⁻⁵ s range of the current envelopes obtained during the experiments with the DBD reactor packed with Ni/DOE0, 3, 5, 6 catalysts at 27.7 ± 0.3 kV _{p-p}	144
Figure 5.14: Example of measured Lissajous Q-V cycle for Ni/DOE0 at 25.3 kV _{p-p} layered with the linearization of the plasma “off” part obtained from the current envelope analysis.	145
Figure 5.15: Current envelope layered with the charge transfer events time histogram and the charge signal over 1 period. The experiments were performed with a), b) empty DBD reactor and packed with c), d) Ni/DOE0 catalyst at a), c) 25.4 ± 0.2 kV _{p-p} and b), d) 27.7 ± 0.3 kV _{p-p}	147
Figure 6.1: a) scheme of the operando DBD FTIR cell reproduced from [196]; b) a photograph of the operando DBD reactor while plasma is ignited.	152
Figure 6.2: FTIR subtracted spectra in the 3200-680 cm ⁻¹ range over 25 minutes time of plasma-assisted CO ₂ methanation reaction with a break between 2400-2300 cm ⁻¹ . An example of the full spectrum is shown in the inset.	154
Figure 6.3: Time evolution of FTIR spectra in the a) 2000-800 and b) 3200-2400 cm ⁻¹ regions during the plasma-assisted CO ₂ methanation reaction. Peak assignation is shown by symbols, the arrows indicate the suggested growth trends. The inset in b) shows the baseline subtracted last spectrum.	156
Figure 6.4: MS signals of H ₂ , CH ₄ , CO, and CO ₂ over time during the operando plasma-assisted CO ₂ methanation experiment.	158

Figure 6.5: a) Q-V Lissajous figures obtained at the two tested conditions of the operando plasma-assisted CO ₂ methanation experiment and V, Q, and I signals measured during the b) 22 kV _{p-p} and c) 25 kV _{p-p} conditions. ...	159
Figure 6.6: a) FTIR spectra of the surface of the catalyst in the 3500-900 cm ⁻¹ range with the full final spectrum is shown in the inset and b) FTIR spectra of the gas phase in the 4000-600 cm ⁻¹ range over 15 minutes time of thermal reaction.	160
Figure 6.7: Time evolution of FTIR spectra in the a) 2200-950 and b) 3000-2700 cm ⁻¹ regions during the thermal CO ₂ methanation reaction. Line assignation is shown by vertical lines and symbols. An example of peaks deconvolution is given in the insets.	162
Figure 6.8: a) MS signals of H ₂ , CH ₄ , CO, and CO ₂ and b) peak intensity of CH ₄ , CO, and CO ₂ in the gas phase FTIR spectra over 15 minutes thermal CO ₂ methanation reaction time.....	163

List of Tables

Table 1.1: Energy densities of energy storage solutions as hydrogen, fuels, and battery ^a [15] ^b [13]	21
Table 1.2: Power-to-X combined with CCU reactions [20,21]	21
Table 1.3: Comparison of ceria-supported catalysts used in thermal CO ₂ methanation.	34
Table 1.4: Comparison of ceria-containing catalysts used in plasma-assisted CO ₂ methanation.	44
Table 2.1: CeO ₂ nano-structured materials prepared through hydrothermal synthesis: Experimental factors and levels considered in the design of experiments analysis.	51
Table 3.1: Overview of the synthesis parameters and physicochemical properties of the CeO ₂ supports of the DOE series.	69
Table 3.2: p-values of the linear model coefficients of the factorial design.	73
Table 3.3: OSC study and surface characterisation of selected nanostructured support samples.	79
Table 3.4: Physical properties of nanostructured Ni/CeO ₂ catalyst.	84
Table 3.5: Results of particle size measured in TEM of Ni/DOE0, 3, 5, 6.	87
Table 3.6: Results of XPS and Raman spectroscopy of Ni/DOE0, 3, 5, 6.	92
Table 3.7: H ₂ -TPR and CO ₂ -TPD results of Ni/DOE0-8 catalysts.	96
Table 4.1: Results obtained from CO ₂ methanation test in DBD plasma with peak-to-peak applied voltage 22.3-24.3 kV _{p-p} at 12.3 kHz (21.2 ± 2.0 W) and in the thermal reactor at 300 °C (289 W).	109
Table 4.2: Results obtained from CO ₂ methanation test in DBD plasma with power 30.9 ± 3.8 W.	112
Table 4.3: Crystallite size of cerianite and nickel phases of samples Ni/DOE after the plasma-assisted and thermal catalytic reaction. The percentual variation compared to the crystallite size of the reduced catalysts is reported in brackets.	119
Table 4.4: Results of XPS of Ni/DOE0, 3, 5, 6 after plasma exposure.	123
Table 5.1: Overview of the CO ₂ conversion and the results obtained from the analysis of the Lissajous figure at the two voltage conditions (25.4 ± 0.2 and 27.7 ± 0.3 kV _{p-p}) and with different packing materials.	136
Table 5.2: Overview of the results obtained from the statistical analysis of the charge transfer events at the two voltage conditions (25.4 ± 0.2 and 27.7 ± 0.3 kV _{p-p}) and with different packing materials.	141
Table 5.3: Overview of the results obtained from the current envelope analysis at the two voltage conditions (25.4 ± 0.2 kV _{p-p} and 27.7 ± 0.3 kV _{p-p}) and with different packing materials.	146
Table 5.4: Overview of CO ₂ methanation catalytic results at 27.7 ± 0.3 kV _{p-p} applied voltage and with 29 ± 2 W injected power, electrical characterization, and selected physicochemical properties of the Ni/DOE0, 3, 5, and 6 catalysts.	148

List of Symbols and Abbreviations

AC: alternating current.	NP: nanopolyhedra.
BET: Brunauer–Emmett–Teller.	NPI: nanoplatelets.
C: Capacitance; capacitor.	NR: nanorod.
C _{balance} : Carbon balance.	NTP: Non-thermal plasma.
CCS: Carbon capture and storage.	OES: optical emission spectroscopy.
CCU: Carbon capture and utilization.	OSC: Oxygen storage capacity.
CCUS: Carbon capture, utilization and storage.	OV: Oxygen vacancy.
Ce _x Zr _(1-x) O ₂ : ceria-zirconia.	P: power. ; Power.
CH ₃ OH: methanol.	p/p ₀ : Partial pressure.
CH ₄ : methane.	Q: charge.
CO ₂ : Carbon dioxide.	R: resistor.
CO ₂ -TPD: CO ₂ temperature-programmed desorption.	RES: Renewable energy sources.
DBD: Dielectric barrier discharge.	RF: radiofrequency.
DC: direct current.	RWGS: Reverse water gas shift.
DOE: Design of experiments.	S _{CH₄} : Selectivity to methane.
EDX: Energy-Dispersive X-Ray.	SEI: specific energy input. ; Specific Energy Input.
EU: European Union.	SEM: Scanning Electron Microscopy.
f: frequency. ;	TEM: Transmission Electron Microscopy.
FTIR: Fourier Transform Infrared Spectroscopy.	TGA: Thermogravimetric analysis.
GC: Gas Chromatography.	TOC: Total Organic Carbon.
GDA: gliding arc.	TOF: turnover frequency.
GHSV: Gas hour space velocity.	TPD-MS: Temperature-programmed desorption coupled with mass spectrometer.
H ₂ -TPR: Hydrogen temperature-programmed reduction.	V: voltage.
I: Current.	V _p : Total pore volume.
ICP-AES: Inductively Coupled Plasma Atomic Emission Spectrometry.	WHSV: weight hour space velocity.
IPCC: Intergovernmental Panel on Climate Change.	W _p : Pore size.
IUPAC: International Union of Pure and Applied Chemistry.	X _{CO₂} : CO ₂ conversion.
kV _{p-p} : peak-to-peak voltage.	XPS: X-Ray Photoelectron Spectroscopy.
MSI: metal support interaction.	XRD: X-Ray Diffraction.
MW: microwave.	ε: dielectric permittivity.
N _A : Avogadro number.	η: Energy efficiency.
NC: nanocube.	V: Volumetric gas flow. ;
NO: nanooctahedron.	κ: thermal conductivity.
	λ _D : Debye length.

Abstract

Among the different processes for carbon capture and utilisation, CO₂ methanation is experiencing a renaissance as a promising technology for the development of Power-to-gas as an energy storage solution and carbon circular economy. The field of plasma catalysis, which considers the association of a catalyst with non-thermal plasma, has been recently developed for boosting CO₂ methanation. The challenges of plasma catalysis focus on taking advantage of the activated species and electrons created by the plasma to achieve more favourable reaction pathways and interaction with the active sites of the catalyst and on plasma-catalyst synergy, meaning the enhancement of the catalyst properties by contact with plasma and vice versa.

The goal of this work is to explore the effect of morphology and physicochemical properties of nanostructured Ni/CeO₂ catalysts on plasma-catalyst synergy and to highlight the key characteristics of the catalysis that control an efficient plasma-assisted CO₂ methanation in order to advance in the rational design of materials tailored for applications in plasma catalysis.

For the plasma-assisted CO₂ methanation tests, a suitable non-thermal plasma type is the dielectric barrier discharge due to mild temperature conditions, which allow the catalyst to be in direct contact with the plasma in a packed bed configuration, and operation at atmospheric pressure, promising for industrial applications. Nickel catalysts supported on Ce-based metal oxides have been proposed in recent publications for plasma-assisted CO₂ methanation. Ni is a reliable solution as it is active for CO₂ methanation as well as cost-effective. Cerium oxide (CeO₂) is an interesting material to be used as support thanks to its redox properties related to the tendency to form oxygen vacancies. Such property can be tuned by enhancing the non-stoichiometric nature of the CeO₂ surface, either by doping or, as in this case, by morphology modification, which has been reported for cerium oxide to be controllable via synthesis method. The parameters of the hydrothermal synthesis were varied and CeO₂ nanomaterials with different morphology (polyhedra, nanorods, nanocubes), crystallite size, and surface area were produced. The Ni catalysts synthesised with these supports were further characterised by state-of-the-art techniques to examine the most relevant physicochemical properties, e.g., surface area, reducibility and metal-support interaction, surface basicity, and formation of oxygen vacancies. In addition, the electrical behaviour of the catalysts was assessed with focus on how the materials affect the plasma discharge, charge transfer, and the dielectric property of the packed bed. FTIR operando technique was utilised to suggest a possible reaction pathway of the plasma-assisted CO₂ methanation on Ni/CeO₂.

In conclusion, it was found that the physicochemical properties which are relevant in conventional thermal methanation, such as surface area and basicity, are applicable to plasma catalysis but the importance of low dielectric permittivity of the catalyst and charge transfer mechanism was also highlighted for an energy efficient plasma-assisted methanation process. Furthermore, a rod or needle-like CeO₂ support allows enhancing the surface defects, the interaction with Ni, and macroporosity, which seem to facilitate the methanation reaction in plasma via formate route.

Resumen

Entre los diferentes procesos de captura y utilización del carbono, la metanización del CO₂ experimenta últimamente un renacimiento como tecnología prometedora para el desarrollo de la conversión de electricidad en gas, del almacenamiento de energía y de la economía circular del carbono. El campo de la catálisis asistida por plasma, que considera la asociación de un catalizador con plasma no térmico, se ha desarrollado recientemente para impulsar la metanización de CO₂. Los retos de esta tecnología se centran en aprovechar las especies activadas y los electrones para conseguir vías de reacción e interacción más favorables con los sitios activos del catalizador y en la sinergia plasma-catalizador, es decir, la mejora de las propiedades del catalizador por contacto con el plasma y viceversa.

El objetivo de este trabajo es explorar el efecto de la morfología y las propiedades físicoquímicas de los catalizadores de Ni/CeO₂ nanoestructurados en la sinergia plasma-catalizador y resaltar las características clave del catalizador que controlan una eficiente metanación de CO₂ asistida por plasma con el fin de avanzar en el diseño de materiales para aplicaciones en plasma catálisis.

Para los experimentos de metanación de CO₂ asistida por plasma, un tipo de plasma no térmico adecuado es la descarga de barrera dieléctrica debido a las condiciones de temperatura suaves, que permiten que el catalizador esté en contacto directo con el plasma en una configuración de lecho fijo, y el funcionamiento a presión atmosférica, prometedor para aplicaciones industriales. En publicaciones recientes se han propuesto catalizadores de níquel soportados sobre óxidos metálicos basados en Ce para la metanación de CO₂ asistida por plasma. El níquel es un metal adecuado ya que es activo para la metanación de CO₂, además relativamente de bajo costo. El óxido de cerio (CeO₂) es un material interesante para ser utilizado como soporte gracias a sus propiedades de redox relacionadas con la tendencia a formar vacantes de oxígeno. Dicha propiedad puede ajustarse potenciando la no estequiometría de la superficie del CeO₂, ya sea por dopaje o, como en este caso, por modificación de la morfología, que se ha descrito para el óxido de cerio como controlable a través del método de síntesis. Se variaron los parámetros de la síntesis hidrotermal y se produjeron nanomateriales de CeO₂ con diferente morfología (poliedros, nanorods, nanocubos), tamaño de cristalito y área superficial. Los catalizadores de Ni sintetizados con estos soportes se caracterizaron además mediante técnicas avanzadas para examinar las propiedades físicoquímicas más relevantes, por ejemplo, el área superficial, la reducibilidad y la interacción metal-soporte, la basicidad superficial y la formación de vacantes de oxígeno. Además, se evaluó el comportamiento eléctrico de los catalizadores centrándose en cómo afectan los materiales a la descarga de plasma, la transferencia de carga y la propiedad dieléctrica del lecho fijo. Se utilizó la técnica operando FTIR para sugerir una posible vía de reacción de la metanización de CO₂ con Ni/CeO₂ asistida por plasma. En conclusión, se encontró que las propiedades físicoquímicas que son relevantes en la metanación térmica convencional, como el área superficial y la basicidad, no son aplicables a la plasma catálisis, pero también se enfatiza la importancia de la baja permitividad dieléctrica del catalizador y el

mecanismo de transferencia de carga para un proceso energéticamente eficiente. Además, un soporte de CeO_2 en forma de barra o de aguja permite potenciar los defectos superficiales, la interacción con el Ni y la macroporosidad, que parecen facilitar la reacción de metanación en plasma por vía del formiato.

Résumé

Parmi les différents procédés de capture et d'utilisation du carbone, la méthanisation du CO_2 connaît une renaissance comme une technologie prometteuse pour le développement du Power-to-gas et en tant que solution de stockage de l'énergie et de l'économie circulaire du carbone. Le domaine de la catalyse plasma, qui considère l'association d'un catalyseur avec un plasma non thermique, a été récemment développé pour stimuler la méthanation du CO_2 . Les défis de la catalyse assistée par plasma consistent à tirer profit des espèces activées et des électrons créés par le plasma pour obtenir des voies de réaction et des interactions plus favorables avec les sites actifs du catalyseur, ainsi que de la synergie plasma-catalyseur, c'est-à-dire de la modification des propriétés du catalyseur par contact avec le plasma et vice-versa. L'objectif de cette thèse est d'explorer l'effet de la morphologie et des propriétés physicochimiques des catalyseurs Ni/CeO_2 nanostructurés sur la synergie plasma-catalyseur et de mettre en évidence les caractéristiques clés du catalyseur qui permettent une méthanisation efficace du CO_2 assistée par plasma, afin de progresser dans la conception rationnelle de matériaux adaptés aux applications de la plasma-catalyse. Pour les essais de méthanation du CO_2 assistée par plasma, les plasmas froids à décharge de barrière diélectrique (DBD) permettent des températures douces, ainsi qu'un contact direct entre le plasma et le catalyseur dans une configuration de lit fixe. Au même temps ils permettent l'opération sous pression atmosphérique, conditions idéales pour des applications industrielles. Des catalyseurs à base de nickel supportés par des oxydes métalliques à base de Ce ont été proposés dans des publications récentes pour la méthanisation du CO_2 assistée par plasma. Le nickel est une solution fiable, car il est actif dans la méthanisation du CO_2 et au même temps économiquement rentable. L'oxyde de cérium (CeO_2) est un matériau intéressant à utiliser comme support grâce à ses propriétés d'oxydoréduction liées à sa capacité d'échange d'oxygène. Ces propriétés peuvent être ajustées en améliorant la nature non stœchiométrique de la surface de CeO_2 , soit par dopage, soit, comme dans le cas présent, par modification de la morphologie, ce qui a été rapporté pour l'oxyde de cérium comme pouvant être contrôlé par la méthode de synthèse. Ainsi, les paramètres de la synthèse hydrothermale ont été modifiés, ce qui a permis d'obtenir des nanomatériaux de CeO_2 présentant différentes morphologies (polyèdres, nanorods, nanocubes), tailles de cristallites et surfaces actives. Les catalyseurs Ni synthétisés avec ces supports ont été caractérisés par des techniques de pointe afin d'examiner les propriétés physicochimiques les plus pertinentes, par exemple la surface, la réductibilité et l'interaction métal-support, la basicité de la surface et la formation de lacunes dans l'oxygène. En outre, le comportement électrique des catalyseurs a été évalué en mettant l'accent sur la manière dont les matériaux affectent la décharge du plasma, le transfert de charge et le comportement diélectrique du lit fixe. La technique FTIR operando a été utilisée pour suggérer une voie de réaction possible de la méthanisation du CO_2 assistée par plasma sur Ni/CeO_2 . En conclusion, il a été constaté que les propriétés physicochimiques qui sont pertinentes dans la méthanisation thermique conventionnelle ne sont pas entièrement applicables

à la catalyse par plasma, car l'importance d'une faible permittivité diélectrique du catalyseur et d'un mécanisme de transfert de charge est mise en évidence pour un processus de méthanisation efficace sur le plan énergétique. Finalement, un support CeO_2 contenant des nanostructures en forme de tige ou d'aiguille permet d'améliorer les défauts de surface, l'interaction avec le Ni et la macroporosité, ce qui semble faciliter la réaction de méthanisation dans le plasma par la voie du formiate.

Acknowledgements

This work was funded by the European Union's Horizon 2020 research and innovation programme under the Marie Skłodowska-Curie Action PIONEER project on plasma catalysts for CO₂ recycling. I also would like to acknowledge the Departamento de Ciencia, Universidad y Sociedad del Conocimiento of the Gobierno de Aragón for the project No LMP151_21.

The thesis was carried out as a joint PhD between Universidad Zaragoza and Sorbonne Université and it was possible thanks to the collaboration between Instituto de Carboquímica (ICB-CSIC) and Institut Jean le Rond d'Alembert. I would like to acknowledge the doctoral schools of Chemical and Environmental Engineering of Universidad Zaragoza and SMAER of Sorbonne Université and the respective directors and administrative staff for allowing me to carry out this thesis.

First, I need to send my most sincere gratitude to my supervisors Dr. Maria Victoria Navarro and Dr. Maria Elena Galvez. It was a privilege to work with two great models of women in STEM who welcomed me in an active but empathetic work environment. Thank you so much for your guidance and support! My acknowledgements are extended to all the colleagues in both institutions who contributed and assisted this work. In ICB, I would like to mention all the researchers and technicians in the Grupo de Investigaciones Medioambientales, and Dr. Tomas Garcia for his valuable insights. I would like to acknowledge the personnel of the Servicio de Analysis of ICB for their terrific work on the material's characterization and of the administration. Thank you to all the "precarios" of ICB who made the daily work lighter. A special thank you to Jairo, I hope I encouraged you throughout the last period of the thesis as much as you helped me! I would like to thank all the colleagues and fellow students on the St-Cyr-l'Ecole campus of Institut d'Alembert, including the Tech Team and secretaries for their great help. I need to send a special thought to Golshid who endured with me the tough times in the remote areas of St-Cyr with the DBD reactor, thank you! My gratitude goes also to Dr. Olivier Guaitella for allowing me to carry out my secondment in his lab in LPP (Ecole Polytechnique, Paris) and for his precious guidance. Thank you also to all the PhD students of LPP, it was short but the welcoming atmosphere you created was greatly appreciated. I would like to acknowledge Prof. Raul Arenal and Dr. Abhijit Roy of IMNA in Zaragoza for the TEM analysis for my catalysts and valuable discussion. I would like to also acknowledge Dr. Federico Azzolina-Jury and Dr. Minh Nguyen-Quang of CNRS-LCS lab in Caen for allowing me to carry out a short secondment, for the help and availability during and after my time in Caen and for their valuable expertise in the operando FTIR spectroscopy.

Last but certainly not least, I need to thank you my family in the most extended meaning. Grazie for your encouragement and unlimited love and patience to my mom and dad, my brother Lorenzo, my nonni, my aunt Anna, lovely Samuel, and Domenico. And to Mayank, with whom I made it through also the PhD thesis, as predicted years ago. Thank you to my near and far friends, including the PIONEERS I got to meet thanks to this project and hope to stay in touch with, I greatly appreciate you!

Chapter 1: Introduction

1.1.	<i>Catalytic CO₂ methanation</i>	22
1.1.1.	Catalysts used for CO ₂ methanation	24
1.1.2.	Non-conventional catalysis: electro-, photo- and plasma catalysis.....	24
1.2.	<i>CeO₂-based catalysts for CO₂ methanation</i>	26
1.2.1.	Effect of synthesis techniques of ceria	29
1.2.2.	Effect of metal active phase supported on ceria	30
1.2.3.	Comparison of ceria with different supports	32
1.3.	<i>Plasma</i>	35
1.3.1.	CO ₂ plasma for CCU applications	37
1.4.	<i>Plasma-assisted catalysis</i>	38
1.4.1.	Ceria-based catalysts for plasma-assisted CO ₂ methanation	42
1.4.2.	Diagnostics for plasma catalysis.....	44
1.4.3.	CO ₂ methanation reaction mechanisms in the presence of CeO ₂ -based catalysts	45
1.5.	<i>Motivation and objectives of the thesis</i>	47

The growth of production of energy and goods since the 19th century Industrial Revolution has led to an increment of emissions of greenhouse gasses, the most discussed being carbon dioxide (CO₂), and pollutants in the atmosphere, affecting irreversibly Earth's system. This effect of human activity on the global environment, though geologically recent, has been compared for its impact to a geological era, named by experts Anthropocene [1]. The presence of CO₂ in Earth's atmosphere is vital to the greenhouse effect for the heating of the planet's surface and to the development of life forms on the planet. CO₂ amounts had been balanced by the natural carbon cycle of release (fires, volcanic activity, organic decomposition) and capture (photosynthesis, water dissolution, rock sedimentation). The massive anthropogenic emissions over the last 100 years, with more than 37 billion tons of CO₂ released just in 2021 as shown in Figure 1.1a, have ruptured this cycle and caused an avalanche of risks to the planet's climate.

The rise of CO₂ concentration in the atmosphere caused the average global temperature to increase by 1 °C, therefore triggering climate change and ecosystems' degradation [2]. The scenarios predicting the consequences of unrestrained temperature increase (up to 5 °C) are devastating and include climate change with intense precipitations and droughts, the increase of sea levels and ocean acidity, the melting of ice caps and glaciers, and loss of biodiversity [3]. These scenarios hit the human population as well, with threats to health, water, and food security, and disproportionately affecting groups that are socio-economically marginalized [2].

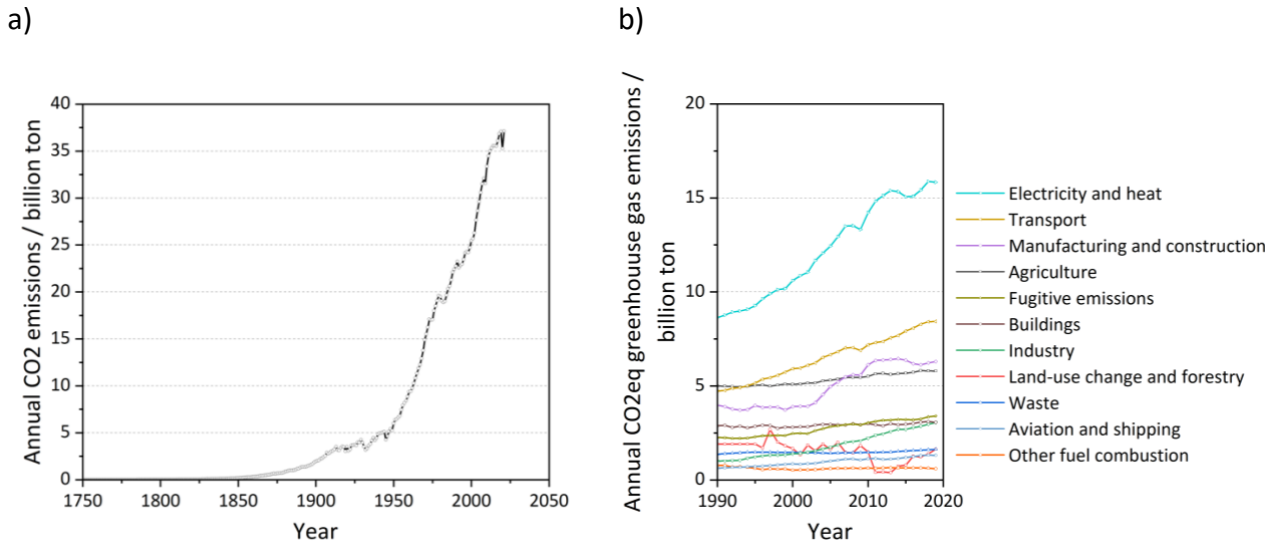


Figure 1.1: a) Global annual CO₂ emissions b) Equivalent CO₂ of greenhouse gas emissions by sector as a function of year (source: ourworldindata.org dataset [2]).

Scientists and policymakers have come together for three decades to spread awareness of global warming and the need of emissions to decrease, with the first legally binding climate treaty Kyoto Protocol signed in 1997 [4]. The graph in Figure 1.1a of world CO₂ emissions by year indicates that such political action has not seen a practical realization yet. As a reaction to this negative and irresponsible resources utilization, emissions, and pollution, the Paris Agreement on Climate Change was signed in 2015 [3]. This second agreement was expected to push countries to take responsibility and action to keep the global average temperature increase compared to the pre-industrial levels well below 2 °C or even pursue to limit global warming to 1.5 °C [3,5]. The European Union (EU) has also an ambitious target of climate neutrality by 2050 named European Green Deal [6]. In order to meet these expectations, a plethora of mitigation scenarios and projections on future emission decrease and energy supply have been analysed and considered, 400 just in the Intergovernmental Panel on Climate Change (IPCC) report of 2018 [2,3,7,8]. Hausfather and Peters [3] compiled in 2020 the graph in Figure 1.2 that collects possible trends of the needed reduction in emissions due to fossil fuels, including the requirement in order to meet the mentioned 1.5 °C goal, of course, such predictions depend on what policies will be put in place and when.

In order to achieve this goal, society and human activities will have to make an effort to decarbonize [9]. Figure 1.1b shows the equivalent CO₂ emissions by sector, electricity and heat being the first cause of greenhouse gases production, followed by transport. Indeed, examples of the sectors where it is important to work on the abandonment of fossil fuels are electricity generation, transportation, industry, and heating [9,10]. According to the IPCC Reports of 2018 and 2022, technological development and innovation are essential for bringing to the market cost-effective solutions for the transition to low- or zero-carbon energy options [2,8,10].

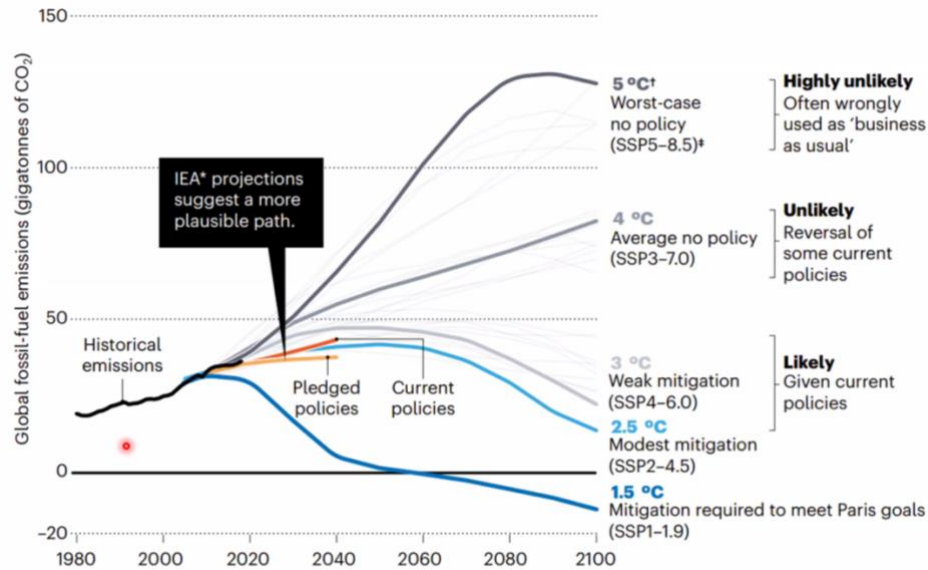


Figure 1.2: Predicted effect of possible scenarios on global CO₂ emissions and global warming (reproduced from Hausfather et al., Nature, 2020 [4]).

Figure 1.3 collects some technological mitigation options regarding energy and industry and their relative potential impact on the emission reduction and cost.

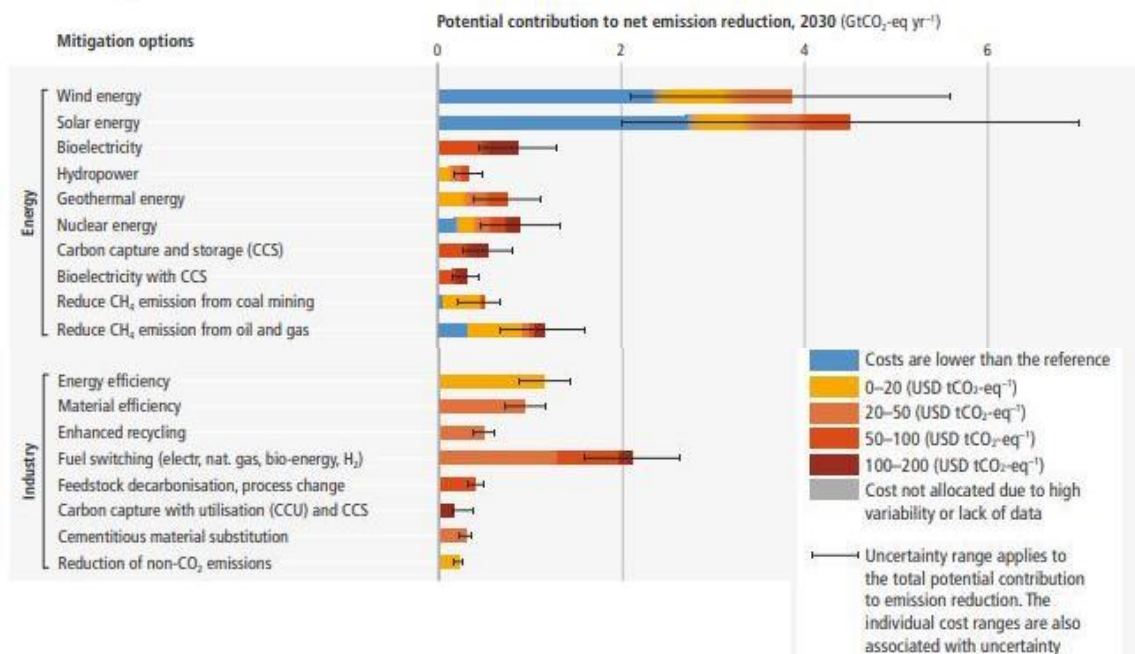


Figure 1.3: Technologies for climate change mitigation in the energy sector and their respective estimated cost and potential contribution to net-zero goal (reproduced from IPCC 2022 [9]).

There are different strategies that, if used together, could help to move in the direction of low-carbon budget. The first imperative point is the gradual abandonment of fossil fuels to the benefit of the development of electrical energy generation from renewable energy sources (RES), as shown

in Figure 1.3 using wind and solar energy will have a great impact on the global emissions. Moreover, development of RES will help the spreading of clean electric transportation and electrification of industrial production. In addition to this shift to RES, strategies for CO₂ removal from the atmosphere should be pursued for net-zero emissions. CO₂ sequestration can be accomplished through afforestation and agricultural land use policies as well as carbon capture, utilization and storage (CCUS) technologies [7].

CCUS refers to a large group of technologies and strategies for the removal of anthropogenic CO₂ and storage in geological or deep-sea reservoirs (CCS), or in products (CCU). The processes vary greatly but they all involve capture, separation, purification, and transportation of CO₂, the first one being the most technologically challenging and cost-intensive [11]. The CO₂ capture pathways differ and range among industrial separation, post-combustion, pre-combustion, oxy-fuel combustion, fuel cell conversion, chemical looping, and direct air capture [12,13]. The CCUS facilities in the European region had in 2021 a total capacity of 37.4 Mt/year of CO₂ capture and it is expected to grow with more projects being established [12]. The option of utilization and transformation of CO₂ through CCU is potentially viable and complements with storage [11]. The direct applications of recovered CO₂ are wide and space over many sectors including food and products (as in carbonated beverages, decaffeinating coffee, dry ice...), manufacturing and coating (in the liquid or supercritical state it can be used as a “green solvent”), in building materials (cement), or in the chemical industry for plastics or reactants synthesis [12,13]. CCU also considers the valorisation of CO₂ to added-value chemicals such as fuels [13]. There is a shift from the current perspective of CO₂ as an emission to a reservoir of carbon to be exploited as C1 building block for the production of more complex hydrocarbons [14]. CCU has the potential to revolutionize the petrochemical and chemical industries and allow the closure of the carbon loop [15]. This is an interesting perspective on CCU that introduces the concept of circular economy, where the “waste” molecule is recycled to synthetic fuel, that in turn will be burnt for electricity generation/heat/transportation and emit CO₂. Circular economy promotes strategies of reuse, refurbishment, recycling, and efficiency that might touch every field of human activity and will allow to distance itself from the current usage and disposal of linear economy [8]. Nonetheless, CCUS is indeed mentioned in the 2022 IPCC Report, but it is marked in Figure 1.3 as a costly and low-impact option. This is one of the motivations for further scientific and technological advancement on CCU and valorisation technologies, which are attracting interest from policymakers, industry, and investors, with global funding over 10 years close to 1 billion USD [16]. Furthermore, with the rise of fiscal and economic incentives to reduce emissions, for example with the so-called “Carbon Tax”, meaning implementing pricing on CO₂ emissions, the idea of CCUS might become financially relevant for industries to adopt and profit [13]. The matter of carbon pricing is still under debate and is very complex, especially if no consensus will be reached at the international level. At European level, the EU is promoting a Carbon Border Adjustment Mechanism to ensure fair pricing of carbon emissions [17].

Table 1.1: Energy densities of energy storage solutions as hydrogen, fuels, and battery ^a[15] ^b[13]

Energy storage solution	Gravimetric energy density, MJ/kg	Volumetric energy density, MJ/m ³
Hydrogen	141.7 ^a	12.7 ^a
Methane (liquefied)	55.5 (55.2) ^a	39.8 (23625) ^a
Methanol	23.0 ^a	18200 ^a
Kerosene	43.0 ^a	35300 ^a
Li-ion battery	0.5-0.8 ^b	1620 ^b

The concept of captured CO₂ transformation to hydrocarbons involves CO₂ reacting with a hydrogen-containing source, which might be H₂ gas or water, and it is energy intensive [13]. Such reactions enable the conversion of H₂ to a fuel with higher volumetric energy density, which is beneficial for storage and transportation, which are troublesome in the case of H₂. In fact, as reported in Table 1.1, H₂ has the highest gravimetric but lowest volumetric energy density [15]. Hydrocarbon molecules are found to be more efficient carriers, such as methane (CH₄) and methanol (CH₃OH), that can be supplied via the existing grid and using the current infrastructures for storage. Moreover, if “green hydrogen” from water electrolysis supplied by electricity from RES is used and the electrification of the whole process is achieved, synthetic fuels are considered green energy carriers [18]. In this view, CCU not only promotes a carbon circular economy, but it is also a method of chemically energy storage, which is greatly needed with further intensification of energy production from clean but intermittent RES to control and maintain the electricity that is fed to the network. Such strategies are named Power-to-X or in the case of H₂ and CH₄ Power-to-gas [19] with related reactions collected in Table 1.2. In fact, according to the environment and application, liquid fuels might be more convenient than batteries for energy storage, indeed liquefied CH₄ or CH₃OH are advantageous regarding volumetric energy density compared to commonly used Li-ion batteries [13].

Table 1.2: Power-to-X combined with CCU reactions [20,21]

Reaction name	Reaction equation	Eq.	Thermodynamics ΔH^0
Splitting	$\text{CO}_2 \rightleftharpoons \text{CO} + \frac{1}{2}\text{O}_2$	(1. 1)	+283 kJ/mol
RWGS	$\text{CO}_2 + \text{H}_2 \rightleftharpoons \text{CO} + \text{H}_2\text{O}$	(1. 2)	41 kJ/mol
Methanol production	$\text{CO}_2 + 3\text{H}_2 \rightleftharpoons \text{CH}_3\text{OH} + \text{H}_2\text{O}$	(1. 3)	-206 kJ/mol
Methanation	$\text{CO}_2 + 4\text{H}_2 \rightleftharpoons \text{CH}_4 + \text{H}_2\text{O}$	(1. 4)	-165 kJ/mol
Dry reforming of methane	$\text{CO}_2 + \text{CH}_4 \rightleftharpoons 2\text{CO} + 2\text{H}_2$	(1. 5)	+247 kJ/mol
Artificial photosynthesis	$\text{CO}_2 + 2\text{H}_2\text{O} \rightleftharpoons \text{CH}_3\text{OH} + 3/2\text{O}_2$	(1. 6)	+676 kJ/mol
Fischer-Tropsch	$(2n+1)\text{H}_2 + n\text{CO} \rightleftharpoons \text{C}_n\text{H}_{2n+2} + n\text{H}_2\text{O}$	(1. 7)	

Several reactions can be considered for Power-to-X and CCU applications, starting with simple CO₂ splitting, that forms pure O₂ and CO, the last one being used as feedstock for further transformation to hydrocarbons through Fischer-Tropsch process (eq. (1.7)). Other reactions involve H₂ or H-containing molecules, some candidates are CH₄ and H₂O. These reactions occur thanks to the energy transfer from the intrinsic chemical energy of hydrogen-bearing molecules and can be transformed into different energy carriers. The product of the reaction with pure H₂ depends on the ratio of CO₂/H₂ (eq. (1.2-1.4)), some most common options being reverse water gas shift (RWGS), methanation, and methanolation. CO₂ reaction with CH₄ is named dry reforming (eq. (1.5)), established by Fischer and Tropsch in 1928, but it has the drawback of being susceptible to soot formation. CO₂+H₂O reaction mimics photosynthesis, but among the options grouped in Table 1.2 is the most novel and endothermic, leading to the greatest technical challenge at the moment. CO₂ valorisation to both CH₄ or CH₃OH are valid options as they are thermodynamically favourable, and their products have direct applications as green synthetic fuels in current energy and heat production methods.

Despite the growing buzz and demand around H₂ and energy, the hydrogen economy era is yet to come [22], and a combination of CCUS and Power-to-methane can still play a role in the clean energy future [19]. Undeniably, the switch to a net zero-carbon budget economy requires several stepping stones and transition technologies and it will take decades to be achieved, among which CO₂ methanation can be included [10,23]. Nonetheless, if no action is taken now, the chances of staying under 2 °C global warming decrease dramatically, leading to drastic consequences [2].

1.1. Catalytic CO₂ methanation

The development of novel organic chemistry and catalysis is required in order to achieve the CO₂ valorisation revolution introduced in the previous section. The focus reaction of this thesis, namely CO₂ methanation in eq. (1. 4), also known as Sabatier's reaction, has been in turn essential to modern catalysis [14]. The concept of catalysis considers the increase in the rate of a reaction without modifying the overall standard Gibbs energy change according to the definition of the International Union of Pure and Applied Chemistry (IUPAC) [24]. Typically, catalysts facilitate reactions by providing an alternative pathway of lower activation energy, which leads to a faster rate or milder conditions of temperature. There is a main distinction to be done between homogeneous (where the catalysis is in the same phase of the reactants) and heterogeneous catalysis, which is the case of CO₂ methanation reaction. Therefore, the interaction between reactants and catalyst requires three steps of adsorption, reaction on the active sites and desorption of the products [25]. Traditional thermal catalysis requires together with the presence of solid catalyst heating to 500-1300 K and a possibly pressurized environment [26]. Most CO₂ valorisation alternatives gathered in Table 2 can be achieved via thermal catalytic processes, however not all efficiently. For instance, thermal CO₂ splitting eq. (1.1) has been reported to be not effective [20].

The reason for this unfavourable enthalpy ΔH^0 is the high thermodynamic stability of CO_2 molecule. The carbon-oxygen bonds are relatively strong with 783 kJ/mol, and the Gibbs free energy of formation is -394 kJ/mol [20]. Therefore, from a thermodynamic point of view, it would be more efficient to have CO_2 react with co-reactants, as H_2 in CO_2 methanation, which can input substantial energy.

Sabatier's reaction was first reported in 1902 by Sabatier and Sendersen [27] in the publication "Nouvelles synthèses du methane" regarding oxides of carbon reacting with hydrogen on nickel. It has been initially deployed only for CO_2 removal in ammonia and urea synthesis, since the 1980s it has come back to research and industrial relevance for the progress of Power-to-Methane plants [10,28]. Until now, several CO_2 methanation pilot plants have been established around the world (Japan, USA, and Germany) and two commercial operations: in 2013 in Werlte (Germany) and in 2016 in Denmark [10,28,29]. In a 2022 review, Barbaresi et al. [21] collected 87 Power-to-Methane projects worldwide, most of them started in the 2010s and are located in Germany. In their analysis, they highlighted the importance of the choice of electrolyser technology and heat management for efficient output [21]. Sabatier's reaction is experiencing a renaissance for the development of Power-to-gas, in the form of synthetic natural gas production (CH_4), as it meets several of the technical requirements to be exploited as an energy buffer and aid the transition to RES. However, it requires further advancements to make the process even more efficient and economically viable [15].

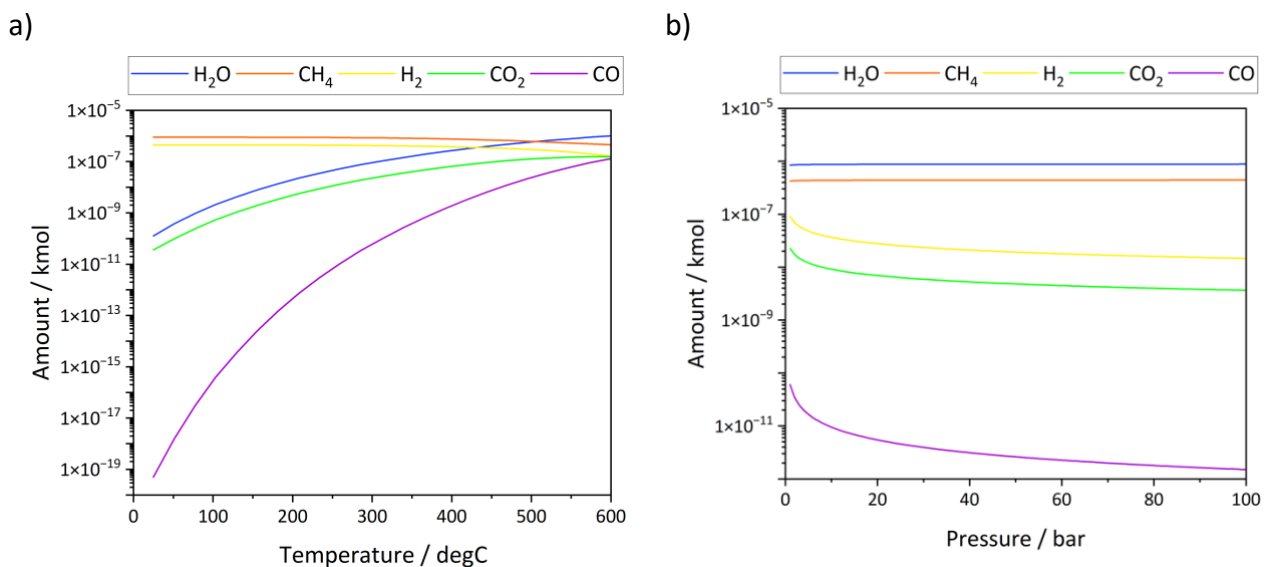


Figure 1.4: Influence on CO_2 methanation equilibrium of a) temperature (at atmospheric pressure conditions) and b) pressure (at temperature at 300 °C).

The reaction is exothermic, releasing 164 kJ per mole (eq. (1.4)). It typically operates between 200°C and 450°C, at pressures between atmospheric and 100 bar [29,30]. The selectivity toward CH_4 decreases at high temperature above 500-600 °C, shifting to the reaction of reverse water-gas shift

therefore the production of undesired CO (Figure 1.4a) [31]. In addition, the problem of catalyst deactivation by sintering arises with temperature $>500\text{ }^{\circ}\text{C}$ [29]. According to Le Chatelier's principle, Sabatier's reaction is favoured at high pressure, with an increase of CO_2 conversion (Figure 1.4b) [32]. Despite its thermodynamical favourability, due to the high oxidation of carbon in CO_2 , its reduction is an eight-electrons process, which highly limits the reaction kinetically and requires a metal-based catalyst for the electron transfer and improve the rate and selectivity [29,33].

Sabatier's reaction, despite the large amount of research and development, still consists of a challenging process due to the many factors that influence the reaction. Efforts have been made to determine the impact of different parameters on the reaction selectivity and mechanism, e.g. temperature, pressure, gas hourly space velocity, the kind of reactor, including the catalyst sensitivity [28,29,32,33]. In addition to thermal heterogeneous catalysis, novel methods for CO_2 hydrogenation have been recently investigated: electrocatalysis, photocatalysis, and plasma-assisted catalysis [29,34–36].

1.1.1. Catalysts used for CO_2 methanation

It is crucial to study and pick the right material to be used as a catalyst in Sabatier's reaction, and it is the focus of several studies from lab to industrial scale [21]. To be used in CO_2 methanation, the catalyst must be active and selective toward methane, but of course stable as well. In the standard thermochemical Sabatier's process, the goal is to limit the coke deposition and other kinds of activity degradation of the catalyst material. The metals used for CO_2 methanation are part of groups 8-11 with the addition of Mo [29,32,37]. The metal phases are characterized by different activity and selectivity, proving that the two are separate phenomena in the methanation process [29]. The most commonly used metals are ranked as $\text{Ru}>\text{Rh}>\text{Ni}>\text{Fe}>\text{Pt}>\text{Mo}>\text{Pd}>\text{Au}$ for activity, while the selectivity is $\text{Pd}>\text{Pt}>\text{Ni}>\text{Rh}>\text{Co}>\text{Fe}>\text{Ru}>\text{Mo}>\text{Au}$ [29]. Among these active phases, nickel stands out for its good selectivity and relatively low cost. In the case of CO_2 methanation, the supports are expected to have a high surface area and they are studied with the purpose of improving active metal reducibility, dispersion, interaction, and stability [32,33,36]. In addition, the support plays an important part in the molecules adsorption and reaction, tuning the mechanism and rate [21,28]. The most common supports include metal oxides, or mixtures of several oxides, hydrotalcite, and zeolites. Promoters can also enhance the performance: they have been investigated in addition to the Ni active phase and mixed within the support [28,32,36].

1.1.2. Non-conventional catalysis: electro-, photo- and plasma catalysis

Along with thermochemical catalysis, non-conventional catalytic methods with different activation mechanisms than temperature have been explored and reported in the literature for the valorisation of CO_2 , namely electrocatalysis, photocatalysis, and plasma-assisted catalysis [20]. Plasma catalysis stands as a promising technology to be developed alongside thermal conventional

catalysis for further advancements in the applications of CCU. The instance of CO₂ splitting eq. (1.1), which is an endothermic reaction and very hard to perform via a thermochemical process, shows the advantages of plasma catalysis. In this case, the conversion occurs with improved energy efficiency due to the excitation of the molecule in plasma and the high reactivity of plasma chemistry [20]. In addition to plasma-assisted catalysis, novel methods for CO₂ hydrogenation have been recently investigated: electrocatalysis and photocatalysis, which have several similarities with plasma catalysis. All processes rely on the transfer of charges caused by different mechanisms: photocatalysis relies on the absorption of photons by a semiconductor catalyst, creating electron-hole pairs [38], and electrochemistry relies on the transfer of electrons by a strong electric field established between two electrodes in an electrolyte while plasma and its strong electric fields have been reported to charge the surface of the catalyst and induce electron-hole pairs by electron impact [39–41]. Great advancements have been made in the electrochemistry field, including H₂ generation via water splitting. The reaction pathways and yield depend on the electrode/catalyst selection, medium, and temperature. The possible drawbacks of this process are the high potential required and the electrode stability. The photoreduction of CO₂ proceeds by the photoexcited electrons in the conduction band moving to CO₂. The efficiency for the photocatalysis case is influenced by the catalyst, temperature, pH conditions, and of course light intensity and spectrum. The electro- and photochemical processes are normally performed in aqueous media, being water (or aqueous species) oxidized either by the holes generated in photocatalysts or at the anode in electrocatalysis, which could be an issue for CO₂ reduction due to the low CO₂ solubility in water [42].

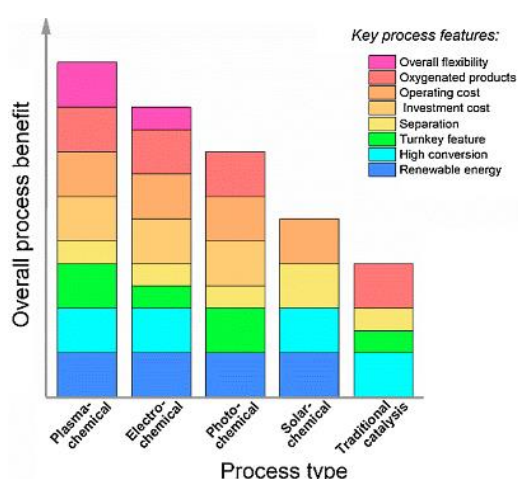


Figure 1.5: Comparison of non-conventional catalytic techniques applied to CO₂ reduction (reproduced from Chen et al., Journal of CO₂ Utilization, 2021 [43]).

Unlike thermal catalysis, plasma and electrocatalysis make direct use of RES electrical energy for CO₂ reduction. However, even more efficient is the direct use of sunlight in the case of photocatalysis, an optimization of solar irradiation adsorption (which lacks in ultraviolet) depends

usually on semiconductor properties. This advantage is in common with solar thermochemical processes, which exploits thermal energy from sunlight via concentration of solar irradiation [20]. Furthermore, NTP and electrocatalytic reactors are compact, modular, and have easy turn on/off which makes them flexible technologies, interesting for applications in both industrial and remote environments. A ranking of the advantages, which include RES use, easy and flexible operation, and high conversion, of the described non-conventional catalytic processes over traditional catalysis have been reported in a review by Chen et al. [43] and are depicted in Figure 1.5. According to the authors plasma catalysis accumulates the greatest overall benefits compared to the other technologies.

1.2. CeO₂-based catalysts for CO₂ methanation

Despite being a rare earth element, cerium is the most abundant of the rare earth family, with a higher concentration (66.5 ppm) in Earth's crust than copper (60 ppm) and tin (2.3 ppm), and it has a low supply risk and a decreasing price over the last years [44,45]. Cerium has two possible oxidation states +4 and +3 and spontaneously oxidizes to two possible extreme compositions: CeO₂ and Ce₂O₃, with fluorite and sesquioxide structure, respectively. The fluorite structure of CeO₂ has Fm3m space group and face-centered cubic (fcc) unit cell of cerium cations and O²⁻ anions occupying the octahedral interstitial sites with the lattice parameter a is 5.411 Å (schematics shown on the left side of Figure 1.6). The facile modification from the stoichiometric CeO₂ structure to a non-stoichiometric one CeO_{2-δ} (with 0 < δ < 0.5) makes it possible even to convert CeO₂ to Ce₂O₃ [44]. The formation of oxygen vacancies (OV) inside the CeO₂ crystalline structure can be expressed with Kröger-Vink notation as



where Ce_{Ce} represents a Ce(IV) ion on a Ce lattice site, O_O is ion on an O lattice site, Ce'_{Ce} represents a Ce(III) ion on a Ce lattice site and V''_O represents neutral OV site. Therefore, the change of valence of two cerium cations is the consequence of each OV that have their electrons in Ce 4f energy states. Furthermore, the presence of an OV in the crystalline structure of cerium oxide will cause the Ce cations to repel each other because of coulombic interactions [44].

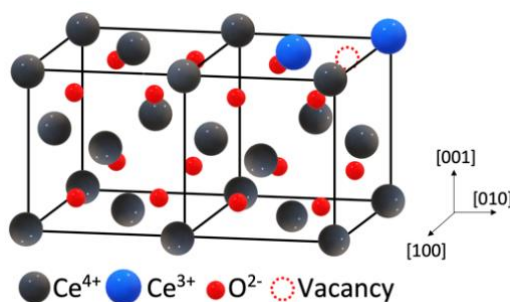


Figure 1.6: Crystal structure of cerium oxide with presence of an oxygen vacancies.

The structure of CeO_2 allows the exposure of different crystal facets according to the morphology and properties of the particles. A selection of the different possible facets, some of them are represented in Figure 1.7 have been investigated via density functional theory and the relative surface energies have been calculated, the general consensus ranks the facets as $(111) < (100) < (110) < (200) < (011)$, (111) being the most stable [46].

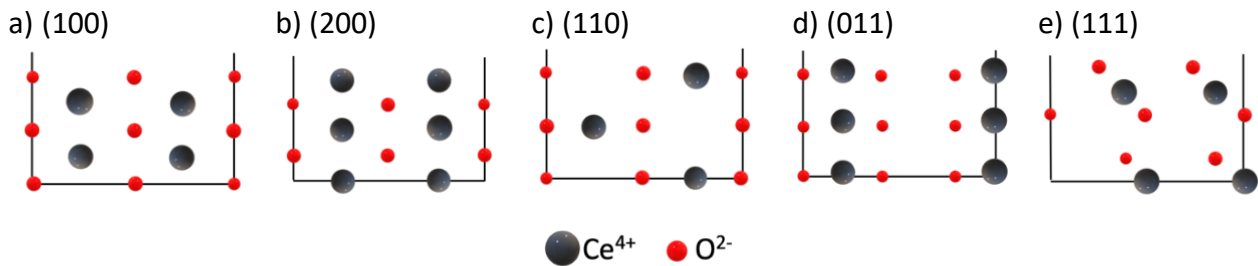


Figure 1.7: Side view of the structure of selected facets of CeO_2 crystal [46,47].

The OV formation energy on these surfaces has also been calculated theoretically for (100) , (110) , (111) , the order is opposite as the surface energy with $(110) < (100) < (111)$ [46]. Compared to the stable (111) facet, the other two are more reducible and active, and the high-energy surface (110) requires the lowest energy for OV [46]. Both (200) and (011) are energetic surfaces, therefore it is expected that defect and OV will be forming easily on them [48].

Oxygen storage capacity (OSC) is one of the most well-known properties of ceria, which makes it a good material for catalytic system development. The OSC has been linked to the fast change of oxidation state of the cerium ions (from IV to III) inside the fluorite $\text{Fm}3\text{m}$ crystalline structure and formation of oxygen vacancies, therefore the release of oxygen. Furthermore, in the fluorite structure, the oxygen atoms are all in the same plane, which allows for rapid diffusion as a function of the number of oxygen vacancies [49]. Oxygen vacancies are enhanced at the nanoscale, at defective surfaces and when dopant atoms are inserted in the crystalline structure of the oxide [44,50]. Several synthesis techniques have been tested for ceria to produce nanostructured materials possessing different morphologies and sizes [44,50]. The possibility to synthesize ceria-based nanomaterials allows to increase the surface area and the active phase dispersion.

Ceria is an ionic oxide with basic sites on its surface, the O^{2-} anion acts a base and Ce^{4+} as Lewis acid site. Surface basicity is important for interaction with CO_2 , as it is known to be a mildly acidic molecule, so it is attracted by the basic sites [34]. The adsorption and desorption kinetics of CO_2 on ceria surface has an important effect on methanation performance and it is influenced by the strength of the basicity [51]. The strength and the amount of basic sites have been reported to increase with decreasing particle size and therefore with larger area and more defects [51].

Another relevant property of ceria as catalyst support that has been reported is the unique metal-support interaction (MSI) [30]. MSI regards reducible oxide supports and it can have different origins, e.g., reduction or oxidation [52]. A strong MSI causes structural modifications, as encapsulation by a layer of support material, restructuring of metal nanoparticles, formation of specific metal-support interfaces, charge transfer from/to metal nanoparticles, consequently it could promote metal dispersion which is beneficial for catalytic applications [30,53]. However, strong MSI might also have a negative influence on the catalytic performance due to a decreased active metal surface area for the encapsulation of metal particles. MSI should be tuned and controlled with ceria support preparation methods and thermal pre-treatments. The interface of metal oxide support and metal particles can also influence the oxide reducibility and therefore the OSC [54]. The OSC increases with metal/support interface perimeter, and it has been proved by experiments and theoretical calculations that O spillover occurs at room temperature between ceria and metal nanoparticles on its surface [54].

Cerium oxide is technologically relevant for green energy as a catalyst and has other industrial applications that include magnetics, phosphors, and alloys [45,55]. Ceria's first known application in catalysis is as oxygen storage component in the three-way catalysis for the elimination of toxic gasses in automotive exhaust [44,45,50,56]. Cerium oxide has been investigated as a catalyst support for CO₂ methanation since the 1990s [57]. As introduced in section 1.1.1., several reports released in the past decades regard the use of such material as support, additive to other metal oxides, and promoter, as Figure 1.8 shows with increasing number of papers regarding ceria in catalysis in the last 30 years [45]. In addition, previous reports established the good activity of such catalysts for Sabatier's reaction [56].

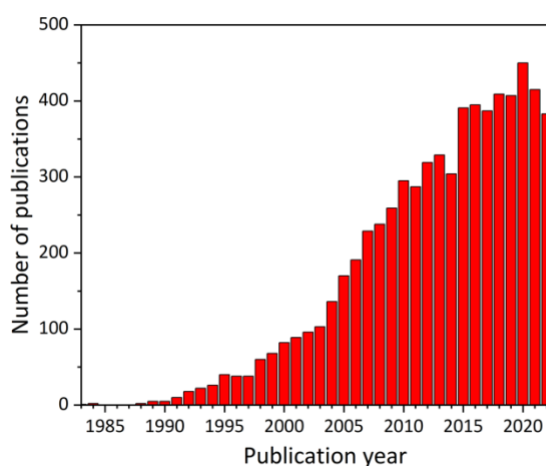


Figure 1.8: Number of publications about ceria utilized as catalyst per year (source: Web of Science search “ceria+catalysis” [58]).

1.2.1. Effect of synthesis techniques of ceria

There are several synthesis techniques that can be used for preparation of CeO_2 . The synthetic methods found in literature include soft and hard templating, pseudo sol-gel, precipitation, flame spray pyrolysis, hydro- and solvothermal, calcination of a cerium precursor, hydrolysis, and combustion [59-82]. In this section, different methods and parameters are considered to identify the most relevant features of synthesized ceria as catalysts support.

Zhou et al. [59] have compared two methods of templating ceria obtained from precipitation. Hard templating also known as nano-casting is the process of impregnating cerium oxide on a material used as mold, in this case mesoporous silica KIT-6, that is later removed [59,60]. Soft templating utilizes surfactants (CTAB and ammonium carbonate) for self-assembly of porous materials. 10 %wt. nickel is later impregnated on CeO_2 synthesized materials [59,60]. The porous structure of the samples obtained from templating is confirmed by N_2 physisorption and TEM. The hard-templating ceria has a more developed mesoporous structure, and the surface area of porous materials exceeds the one of the ceria synthesized by precipitation. The improved mesoporosity and higher surface area enable a better performance in CO_2 methanation with a higher conversion as for the ceria catalyst casted on KIT-6 (selectivity is 100% for all samples) [59].

Other synthesis techniques aim to change the morphology of the cerium oxide particles. One example is hydrothermal method with NaOH solution with variation of the synthesis parameters (temperature and NaOH concentration) to obtain nanocubes (NCs) [61–63], nanorods (NRs) [61–63], nanooctahedron (NOs) [63], nanopolyhedra (NPs) [61] and nanoplates (NPIs) [64]. NCs are synthesized at high temperature (180 °C) and adding a large NaOH amount (10-14 M). With a decrease of temperature to 100 °C NRs are formed, whereas at low NaOH concentration smaller particles (NPs) are obtained [42,43]. Wang et al. [61] show via TEM that the shape of the particle determines the exposed crystalline facets, therefore the coordination of atoms at the surface and the reducibility change for different morphologies. Indeed, the morphology of the cerium oxide particles, and therefore the exposed crystal planes on its surface, has been previously linked to enhanced OSC and improved performance in thermal CO_2 methanation [61–64]. The OSC is measured via oxygen pulse injection method and compared to the information regarding vacancies from Raman and positron annihilation spectroscopy. Pristine NPs and NRs should have an improved tendency to OV formation. However, after 3 %wt. Ru addition, NCs show the highest oxygen storage capacity and amount of oxygen in defect sites, therefore a promoting effect of Ru^0 for vacancies formation occurs. This property translates to an improved activity as catalyst for methanation, (X_{CO_2} 90% and S_{CH_4} 99% at 250 °C) [61]. Bian et al. [65] have also compared ceria NCs and NRs based catalysts using as metal phase 5 %wt. Ni. The Ni/ CeO_2 NRs synthesized in this group possess an improved reducibility shown by TPR analysis and higher Ce^{3+} concentration as calculated from XPS data. As highlighted before, oxygen vacancies can serve as a cooperative reaction site for CO_2 hydrogenation, therefore in this case NRs have a higher activity than NCs [65]. In agreement with this study, Hashimoto et al. reported improved activity for Ni supported on CeO_2 NRs, due to higher

concentration of surface OV, lower particle size, and enhanced surface area and reducibility [63]. They have also shown via density functional theory calculations that the CO₂ activation energy on a NiCeO₂ surface depends on the lattice facet (111), (110), or (100) that is exposed, (110) being the one that characterized the NRs and that facilitates the CO₂ to CO catalytic reaction. Du et al. [64] observed improved activity for Ni supported on CeO₂ NPLs, obtained via hydrothermal method with urea at 90 °C for 6 h, compared to commercial supports due to the OV-rich surface of synthesised ceria. Although some works point to some particular CeO₂ morphologies leading to improved activity towards CO₂ methanation, there is no general agreement concerning the optimal nanoshape and properties of these supports. All these studies agreed, however, on the importance of oxygen vacancy formation ability of these supports. Moreover, OV close to the metal-support interface are believed to strengthen the interaction between Ni and CeO₂ [66] and to play a role in the CO₂ hydrogenation reaction, providing sites for CO₂ adsorption and activation [63] or contributing to the formation of formate surface intermediates [62].

1.2.2. Effect of metal active phase supported on ceria

The results found in literature regarding catalysts obtained with dispersion of a metal phase (Ni, Ru, Rh) on pure CeO₂ show overall a good activity and remarkable yield for methane with a high selectivity >80%. Both commercial and synthesized ceria are evaluated.

The use of CeO₂ supports for catalytic CO₂ methanation was firstly reported in the 1990s by Trovarelli and co-workers [67–69]. The interaction of ceria with noble metals has been investigated by Trovarelli et al. [70] by varying the metal phase impregnated on ceria. 1 %wt. Rh, Ru, Pt, Pd, Ir on CeO₂ support differ in selectivity: the reaction on Ru and Rh produces exclusively CH₄, whereas on Pt, Pd, and Ir it results also in CO formed [70]. Different ceria-metal interaction and modification of the support surface must occur in the different samples. Sintering of metal particles or partial coverage by ceria is one possible surface alteration that takes place at high temperatures. Hydrogen spillover is particularly favored by Rh and Ru interacting with the support, hence the improved hydrogenation activity [70]. In this publication, the authors claim that the metal phase precursor used, in this case of Rh(NO₃)₃ and RhCl₃, does not play a relevant role on the catalyst activity [70], however the methanation rate of the catalyst obtained with Rh nitrate is slightly lower. In addition, this group published various papers reporting the use of 1%wt. Rh catalysts supported on ceria synthesized via ammonia precipitation [57,67,70]. Two different reaction conditions at atmospheric pressure were used in their experiments: transient and steady state. These require the use of pulse and flow microreactor, respectively [57,67,70]. The pulsed reaction (0.81 μmol 20 μL CO₂ pulses in 30 mL/min H₂ stream) shows a significant decrease in formation of methane after the first pulse, which might be linked to the restoring of the CeO₂ stoichiometric lattice by oxidation with H₂O formed by the reaction or with oxygen from CO or CO₂ [57,67,70]. In fact, they report the positive effect of Ce⁴⁺ reduction to Ce³⁺ as adsorption sites for CO₂ that favors the breaking of C-O bond [57].

After the second pulse, the conversion and selectivity remain constant. On the other hand, this partial deactivation is not observed in the steady state experiment at 500 K: the moles of CH_4 measured not vary significantly with time in the stream of H_2 and CO_2 [57]. Furthermore, for Rh/ CeO_2 materials Trovarelli et al. [67] prove the relevance of metal-support interaction to obtain a good rate for the hydrogenation of CO_2 . It is proposed that the Rh-Ce interaction does not comply with the behavior attributed to strong MSI of Rh with other reducible metal oxides, that leads to deactivation [67]. The formation of oxygen vacancies at the interface with the metal contributes to the enhanced interaction [57,67]. The reduction of CeO_2 is facilitated at lower temperatures by the presence of Rh thanks to the phenomenon of spillover [57,67]. Therefore, different geometric and electronic interfaces between metal and oxide at the Rh/ CeO_2 boundary may cause changes in catalytic activity [57].

The interaction between metal phase and cerium oxide has been assessed by changing the catalyst loading (0.7-20 %wt.) in one-step ligand-free adsorption-precipitation synthesis method of Ir/ CeO_2 [71]. Well dispersed Ir particles of small sizes on ceria nanorods are obtained (from 2.2 nm for 20 %wt. to 1.0 nm for 5 %wt.). The catalytic reaction of CO_2 methanation at 1 MPa and 300 °C occurs only with a sufficient amount of Ir, 20 and 15 %wt., with satisfactory selectivity, while the catalysts with lower loadings mostly produce CO. The synthesised materials have been compared to a commercial Ir/ CeO_2 catalyst (5 %wt.), that is not active at these conditions. Very small clusters of Ir atoms are proved to not have enough hydrogenation ability for methane production. XPS and EXAFS characterization are used to show the different chemical properties of the Ir particles: with lower size, hence loading, more oxygen atoms from the cerium oxide are incorporated in the metal sites due to strong MSI, leading to lower hydrogenation. Therefore, the authors claim that the decreased methane selectivity is not caused by the insufficient metal sites, instead it is due to the varying chemical nature of Ir and the interaction with ceria [71]. Finally, it has also been demonstrated that a mixture of Ni and CeO_2 powders does not result in an active catalyst [72]. Instead, the catalyst obtained by wet impregnation of 5 %wt. Ni on commercial ceria reaches at 523 K a turnover frequency of CO_2 (TOF_{CO_2}) of 271 h^{-1} and 100% selectivity [72]. This catalyst presents Ni hexagonal particles with size 3-14 nm dispersed on the support [72]. Therefore, the interface between ceria and metal plays a very important role: the two phases must be physically in contact and sharing a superficial boundary.

The use of nickel as active phase for CO_2 methanation is widely popular in synthesised and commercial catalysts thanks to the good activity of this metal and its relative low cost and good availability compared to the noble metals previously discussed. The choice of Ni precursor salts appears to be relevant for the performance of the catalyst comparing activity of catalysts synthesized with Ni nitrate and chloride [73]. The activity of the catalyst obtained with Ni chloride is considerably lower than the other case due to the chlorine blocking ceria sites [73]. The impregnated Ni and ceria is investigated via TPR and XPS in another study [74]. Ceria is synthesized by nano-casting on KIT-6. The creation of both Ni^0 and oxygen vacancies in CeO_2 during the

reduction step allows the formation of a redox circulation and of two possible active sites for CO₂ activation to CO to favour methanation [74]. The reaction performed with this catalyst at 340 °C with weight hour space velocity (WHSV) 22 L/g_{cat}h results in a remarkable conversion (>90%) and 100% selectivity toward methane [74].

1.2.3. Comparison of ceria with different supports

In several publications, ceria-based catalysts are proved to possess better activity than other metal oxides used as supports. CeO₂ is compared with α -Al₂O₃, γ -Al₂O₃, TiO₂, MgO, ZnO, ZrO₂, SiO₂, Ta₂O₅, Nb₂O₅ [57,72,75–80]. Cerium oxide, synthesized by calcination of Ce(NO₃)₃, was compared with TiO₂ and ZrO₂ [80]. All catalysts were wet impregnated with 5 %wt. nickel and thermally treated in H₂ or air [80]. The classification of the different supports is done based on their reducibility: TiO₂ is reducible, like CeO₂, and ZrO₂ is non-reducible [80]. As a matter of fact, TiO₂ shows a response to the thermal treatment in air or in reductive atmosphere similar to ceria, namely a better conversion is obtained with the reduced catalyst. Instead, the activity of Ni/ZrO₂ remains unchanged by the thermal pre-treatment. All three materials tested for CO₂ methanation have a high yield for CH₄ ($S_{CH_4} > 90\%$). However, Ni/CeO₂ achieves a better CO₂ conversion (X_{CO_2}) than the other two metal oxides and allows the reaction to start at a temperature 100 K lower; overall, the activity can be ranked as CeO₂>TiO₂>ZrO₂. The cations in the crystalline structure of the reducible supports can partially reduce ($Ti^{4+} \rightarrow Ti^{3+}$ and $Ce^{4+} \rightarrow Ce^{3+}$) and create oxygen vacancies at the surface, therefore allow a better interaction with the metal and an improved efficiency [80]. Dreyer et al. not only differentiate the metal oxides according to their reducibility but also according to their basicity [79]. They synthesise via single-step flame spray pyrolysis strongly basic ZnO, amphoteric MnO_x and CeO₂ (all reducible), and Lewis acid and irreducible Al₂O₃ with some weak basic sites [79]. Conversion of CO₂ on the pristine supports occurs according to the strength of their basic sites but it produces only CO. The catalysts become active for methanation with the addition of 5 %wt. Ru in the synthesis method. Ru/CeO₂ shows the best activity X_{CO_2} 83%, S_{CH_4} 99% at 300 °C followed by Ni/Al₂O₃ > Ru/MnO_x > Ru/ZnO. The improved activity with ceria support is related both to the basic and reducible properties of the material. The amount of basic sites on CeO₂ exceeds the other metal oxides. Moreover, the partial reducibility of CeO₂ helps the hydrogenation reaction thanks to the optimized strength of the C-O bond of adsorbed CO* and to the increased dissociation of hydrogen [79]. Ceria and alumina are further compared in two other publications, in both cases synthesized CeO₂ and commercial γ -Al₂O₃ or α -Al₂O₃ are considered. The Ni/CeO₂ catalyst produced by precipitation converts ten-folds more CO₂ in the range 300-350 °C with a higher selectivity for methane (100%), despite the superior surface area and porosity of γ -Al₂O₃ from Alfa Aesar [81]. This difference is explained by the mechanism study, that will be highlighted later. Ceria, unlike alumina, has the ability to contribute to the adsorption and reaction alongside Ni sites, that allows the optimal conversion to CH₄ [81]. A similar explanation is suggested by Wang et al. regarding the

different activity of Ru catalysts supported on CeO_2 obtained by hydrothermal method and $\alpha\text{-Al}_2\text{O}_3$ from Sigma-Aldrich [77]. Oxygen vacancies on ceria play an important role in the CO_2 dissociation whereas on irreducible and weakly basic $\alpha\text{-Al}_2\text{O}_3$ such interactions are not possible [77].

Commercial cerium oxides have also been evaluated. Tada et al. [75] report X_{CO_2} over 10 %wt. Ni/ CeO_2 around 90 % starting at 300 °C and 100 % CH_4 selectivity (S_{CH_4}) up to 450 °C with reaction conditions 20 vol% CO_2 , 80 vol% H_2 and gas hour space velocity (GHSV) 10,000 h^{-1} . At the same temperature range Ni/ TiO_2 , Ni/ $\alpha\text{-Al}_2\text{O}_3$ and Ni/MgO convert less CO_2 . The first catalyst has a similar selectivity compared to the ceria-based one, instead the other materials produce CO as well [75]. In agreement with the catalytic experiments, the CO_2 -TPD analysis shows a significant decrease in adsorption on alumina compared to ceria [75]. In another publication, 10 %wt. Ni dispersed on CeO_2 achieves X_{CO_2} of 60% and S_{CH_4} of 99% at 275 °C in $\text{H}_2/\text{CO}_2/\text{N}_2$ flow with GHSV 36000 h^{-1} , whereas on SiO_2 it converts CO_2 at a rate hundreds times lower and with a selectivity 9 times lower [76]. This proves that oxygen vacancies in ceria interact with nickel and improve the conversion rates toward methane with lower activation energies [76]. Finally, 5 %wt. Ni/ CeO_2 is full selective to CH_4 , converting CO_2 up to forty-fold higher than catalysts supported on TiO_2 and SiO_2 , the latter giving CO as by-product [72].

Table 1.3: Comparison of ceria-supported catalysts used in thermal CO₂ methanation.

Catalyst composition	Synthesis technique	Conditions				Results			Comparisons	Ref.
		Gas mix	GHSV	p	T range	T (°C)	X _{CO2} (%)	S _{CH4} (%)		
8.5%Ni/CeO ₂	Precipitation using cerium citrate	CO ₂ / H ₂ 1:4 + 20% He	12000 h ⁻¹	atm.	250-500 °C	325	75	100	Activity with support CeO ₂ >Al ₂ O ₃	[81]
10%Ni/CeO ₂	Hard templating for mesoporous CeO ₂	CO ₂ / H ₂ 1:4 + 44% Ar	22000 mL g ⁻¹ h ⁻¹	atm.	260-340 °C	340	91.1	100	CO ₂ activation on both Ni and CeO ₂	[74]
7.4-9.7% Ni/CeO ₂	Calcination of Ce(NO ₃) ₃ Ni impregnation with different precursors	1% CO ₂ / 65% H ₂ + He	29000 h ⁻¹	atm.	180-360 °C	250	100		Ni nitrate > Ni chloride	[73]
5%Ni/CeO ₂	Calcination of Ce(NO ₃) ₃	CO ₂ / H ₂ 1:4	36000 h ⁻¹	atm.	200-300 °C	300	70	100	Impact of different thermal treatments	[80]
10%Ni/CeO ₂	Commercial ceria	CO ₂ / H ₂ 1:4	10000 h ⁻¹	atm.	200-550 °C	300	90	100	Best activity with CeO ₂ support > TiO ₂ , Al ₂ O ₃ , MgO	[75]
10%Ni/CeO ₂ Nanoplates	Hydrothermal with urea	CO ₂ / H ₂ 1:4 + 5% N ₂	6000 mL g ⁻¹ h ⁻¹	atm.	200-440 °C	300	84.1	100	Nanoplates > commercial CeO ₂ , Al ₂ O ₃	[64]
5%Ni/CeO ₂ NC and NR	NaOH Hydrothermal	CO ₂ / H ₂ 1:4 + 50% He	24000 mL g ⁻¹ h ⁻¹	atm.	200-250 °C	250	23	100	NRs>NCs	[62]
Ni/CeO ₂ NC, NR, NO	NaOH Hydrothermal	CO ₂ / H ₂ 1:4 + 50% N ₂	80800 mL g ⁻¹ h ⁻¹	atm.	240-320 °C	320	74.1	>99	NRs>NCs>NOs CO ₂ activation energy on (110)<(100)<(111)	[63]
3%Ru/CeO ₂ NC, NR, NP	NaOH Hydrothermal	CO ₂ / H ₂ 1:4 + 25% Ar	360 mL g ⁻¹ h ⁻¹	atm.	100-300 °C	300	>90	100	NCs>NPs>NRs	[61]
5%Ru/CeO ₂	Single-step flame spray pyrolysis	CO ₂ / H ₂ 1:3 + 90% Ar	7640 h ⁻¹	atm.	250-700 °C	300	83	99	Best activity with support CeO ₂ > MnO _x , Al ₂ O ₃ , ZnO	[79]
3%Ru/CeO ₂	CeO ₂ nanocubes via hydrothermal	CO ₂ / H ₂ 1:4 + 25% Ar	360 mL g ⁻¹ h ⁻¹	atm.	100-325 °C	250	92.7		OV as reactive site	[77]
Ru _{0.05} Ce _{0.95} O _x	Combustion	CO ₂ / H ₂ 1:4 + 57% Ar	10 mL/min		350 °C	350	40	99	Relevance of degree of surface reduction	[82]

1.3. Plasma

As just discussed in section 1.1.2. there are several new technologies being developed to further advance and diversify the applications of CO₂ methanation. Plasma catalysis among them is gaining increasing interest from the research community as well as for industrial applications, especially in the field of CO₂ valorisation. The number of papers on the topic of “plasma catalysis” has been increasing in the last decade, with more than 500 publications per year in the last 4 years (Figure 1.9). The main applications that are studied are: CO₂ conversion, light hydrocarbons conversion, ammonia synthesis and pollutants removal from air [83].

The combination of plasma and catalysis merges several fields as plasma chemistry and physics, materials science, and catalysis, besides it opens new questions regarding thermodynamics and kinetics during the reaction, and interaction between plasma and materials, but it is promising thanks to its versatility and efficiency.

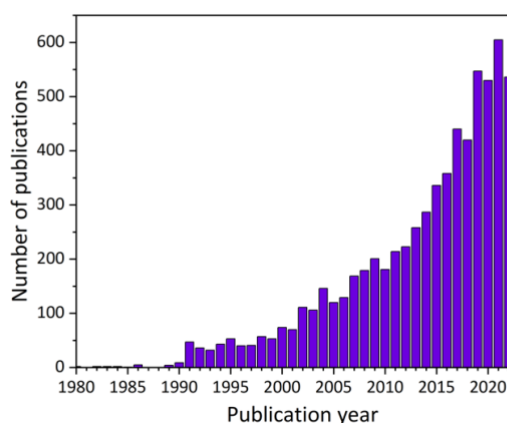


Figure 1.9: Number of publications regarding plasma catalyst per year (source: Web of Science search “plasma+catalysis” [58]).

The term plasma has been first adopted to indicate an ionized gas in 1928 by Irving Langmuir, who saw a similarity between the way blood plasma contains white and red corpuscles and the presence unbound electrons and positive ions in an ionized gas [84]. Plasma is also known as the 4th state of matter, and it makes up more than 99 % of visible matter as it is present in astronomical objects as stars and natural occurring phenomena as northern light and lightnings. Nonetheless, plasma consists of several other species both charged, as electrons and positively and negatively charged ions, and neutrals, as atoms, molecules, and radicals. The presence of these different species makes plasma very reactive and characterized by a complex chemistry. Moreover, the excitation of the atoms in a plasma may lead also to light emission. Nowadays, plasma’s main applications involve chip manufacturing, coating, light sources, and displays [20].

The ionization degree may vary from fully, known as fusion plasma (temperature $>10^7$ K), to partially ionized plasma, or gas discharges. A characteristic parameter of plasma is the Debye length defined as:

$$\lambda_D = \sqrt{\frac{\epsilon_0 k_B T_e}{n_e e^2}} \quad (1.9)$$

where ϵ_0 , k_B and e are constants (permittivity of free space, Boltzmann constant and electron charge, respectively) and T_e and n_e are the temperature and density of electrons, respectively, and it defines the scale over which the electrons screen out electric fields in plasma and charge separation occurs [85]. In order to have a plasma, considered as ionized gas that is macroscopically neutral, its dimension L must be $L \gg \lambda_D$. An additional division of gas discharges regards the thermal equilibrium, meaning whether the temperature of the various components (gas, electrons, ions with their respective degrees of freedom) of plasma are in thermal equilibrium or not. Thermal plasmas are considered to be in local thermodynamic equilibrium and their temperature goes up to $2 \cdot 10^4$ K. On the other hand, plasmas in non-local thermodynamic equilibrium are called non-thermal plasmas (NTP). In this case there is an imbalance between electron temperature and gas temperature, the first being much higher (1 eV) than the latter, which might remain at room temperature. The high electron temperature is due to the small mass compared to the larger atoms that form the gas, therefore electrons can be easily accelerated by the electric field and do not lose notable energy during elastic collisions. An in-between category of gas discharge has been identified as “warm” plasmas, which are characterized by non-equilibrium as well as high electron density and gas temperature (2000-3000 K).

There are several ignition mechanisms for NTP, but the easiest example is applying a potential difference between two electrodes in a gas tube establishing an electric field. Above a certain threshold, which depends on the gas composition, pressure, and distance between electrode according to Paschen’s law, the breakdown of the gas occurs and the acceleration of free electrons, which can collide with gas molecules to produce new ions and electrons via ionization, excitation, or dissociation. Due to this avalanche effect, or known as Townsend mechanism, the plasma can self-sustain. Different types of gas discharge set-ups and ignition mechanisms have been established:

- Glow discharge: normally made of a low-pressure gas tube and two electrodes between which a direct current (DC) voltage difference is applied. Usually operates at low pressure 10-5 mbar to atmospheric and at room temperature. It allows to have a uniform discharge which very well adapts to the needs of lab scale set-ups.
- Dielectric barrier discharge (DBD): consists of two parallel electrodes (planar or coaxial) among which at least one dielectric materials (quartz, alumina, polymers...) is placed. An alternating current (AC) Hz to MHz frequency (f) high voltage (V) power (P) 1-100 kV supply

is used for one of the electrodes while the opposite is grounded. It is usually a non-uniform plasma and operates in filamentary mode, meaning that the plasma zone is only partially filled by micro-discharges while the rest of the gas is not ionized.

- Corona: plasma is ignited with sufficiently high electric field at a sharp edge, by applying a negative or positive voltage. It is characterized by high ionization and electron density.
- Gliding arc (GDA): part of the warm plasma class. Normally operates at the atmospheric pressure, plasma is established at the closest gap point between two electrodes with a potential difference and using the effect of arc expansion.
- Microwave (MW): also a warm plasma. The discharge is ignited via electromagnetic microwave in the frequency range 300 MHz to 10 GHz.
- Radiofrequency (RF): warm plasma that is ignited by an electromagnetic radiofrequency 1-100 MHz wave.

1.3.1. CO₂ plasma for CCU applications

Several publications have studied NTP for CCU applications. In plasma, even a stable molecule as CO₂ can be excited in an energy efficient way as exploiting the vibrational levels. Indeed, as previously discussed, the CO₂ molecule is a thermodynamically stable, linear molecule in the ground state. It possesses three vibrational modes: symmetric stretch, bending, and asymmetric mode, defined by different energy gaps. Free electrons from NTP according to their energy can interact with CO₂ and vibrationally excite it. This is just one of the energy exchange mechanisms that can occur in NTP, including exchange to translational or rotational modes.

The high reactivity of plasma species and the beneficial vibrational excitation and interactions that can occur in NTP led to exploring the NTP discharge types described in the previous section for the known reactions of CCU (Table 1.2) without the addition of a catalytic material. The specific energy input (SEI), which is the ratio of the discharge power by the gas flow, is plotted against the CO₂ conversion obtained with plasma without any packing material in Figure 1.10. The six discharge types are reported with different symbols (with the addition of the “other” category) and the applications with different colours. The figure shows that most results regard CO₂ splitting applications, which was already commented in in section 1.1.2. to be beneficial with plasma rather than using thermochemical methods. These points mostly lie at conversion below 40 % and in the SEI range 10³ to 10⁵ J/L. For CO₂ splitting only a few results using RF and MW reactors stand out with higher conversion, due to the suitable electron temperature range and efficient vibrational excitation of these discharge types (they are indeed warm plasmas) [86]. CO₂ methanation is not a popular application for catalyst-free NTP, as only around 10 points with DBD reactors were found in the literature screening. In this case, the conversion increases linearly with SEI around 10⁴ J/L. Dry gas reforming has been investigated with several different plasma sources (DBD, GDA, RF, glow, MW) and typically requires lower SEI to achieve good conversion.

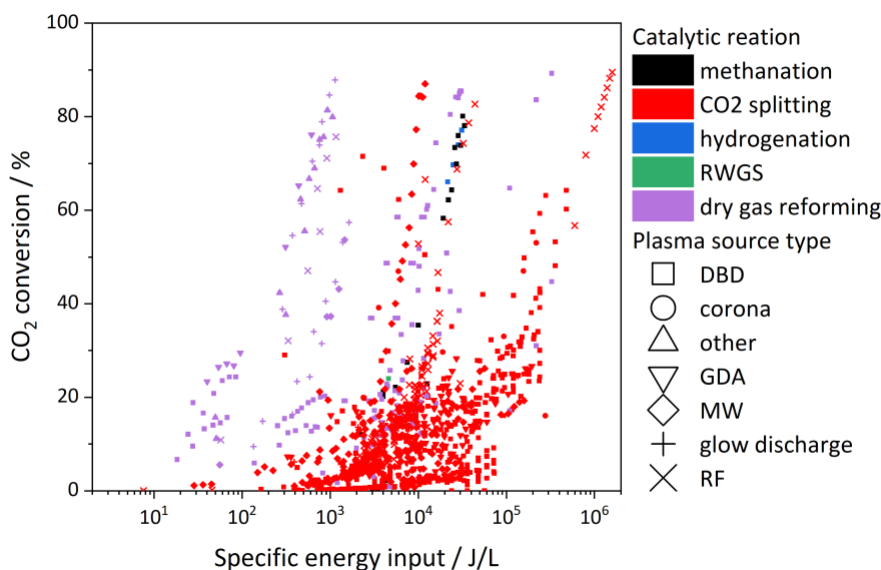


Figure 1.10: Literature results of specific energy input versus CO₂ conversion in non-thermal plasma reactors grouped by plasma source type (symbol) and application (colour) (source: PIONEER Database [87]).

1.4. Plasma-assisted catalysis

NTPs are usually applied in plasma catalysis as their non-equilibrium and highly energetic electrons make them very reactive but also of facile operation due to the favourable pressure and temperature conditions at which they are ignited. Plasma-assisted catalysis, or plasma catalysis, considers the combination of a NTP set-up, previously presented, with a catalytic material. While the plasma may activate the gas molecules, the catalyst controls and selects the yield of the reactions on its surface. Two configurations are found in literature: either by packing the reactor with the material (one-stage or in-plasma) or by locating the catalyst downstream of the plasma (two-stage or post-plasma) [88]. NTP affects both the gas feed, by collisions with electrons, which lead to ionization, excitation and dissociation, and the catalyst surface, but in different ways for in- and post-plasma configurations. An important factor to consider in the choice of configuration is the temperature of the gas discharge, which may be destructive for the catalyst, as well as the lifetime of the reactive species created in plasma. Figure 1.11a compares the order of magnitude of characteristic time of phenomena occurring in plasma (electron-vibrational e-V, vibrational-translational V-T, T-T, V-V, and rotational-translational R-T exchanges in Figure 1.11a) and on the catalyst surface. It can be observed that if the desired reaction requires the interaction of vibrationally excited, radical, or ion-related species, the vicinity of the material and a fast adsorption mechanism are necessary. The two-stage configuration allows the reaction of the catalyst to the long-lived intermediates, which are not electrons, and avoid any influence of the catalyst on the discharge properties. In an in-plasma configuration, in addition to excitation and dissociation occurring at the gas phase, other mechanisms of interactions should be considered to investigate plasma-catalyst synergy.

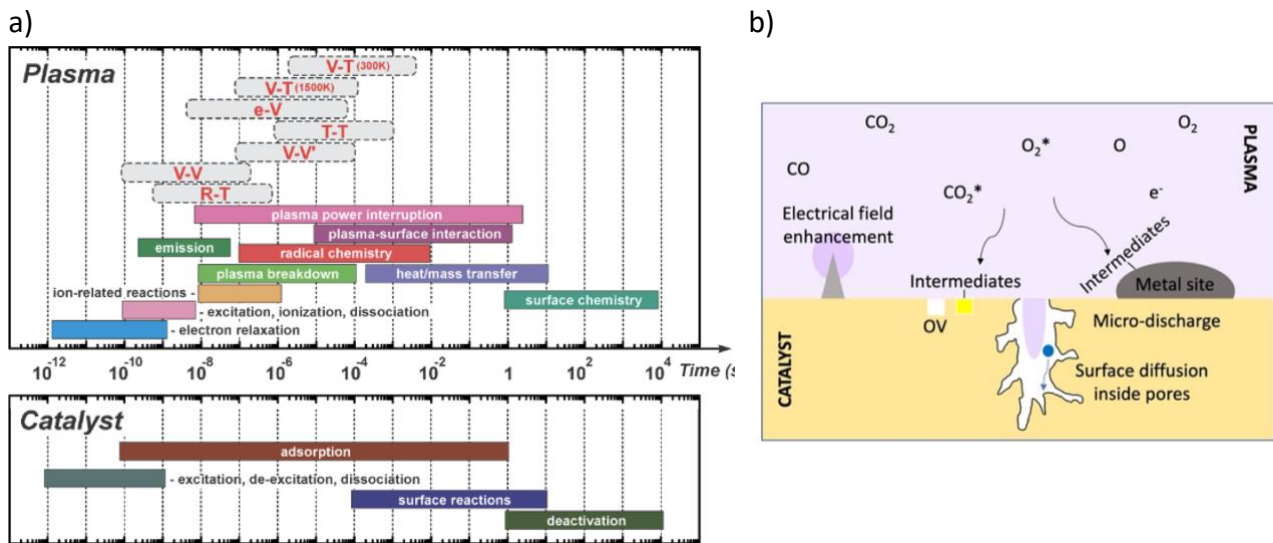


Figure 1.11: a) characteristic timescale of the various processes in NTP as well as on the catalyst surface (reproduced from Chen et al., Journal of CO₂ Utilization, 2021 [43]); b) schematics of possible plasma-surface interactions [83,88].

Plasma-assisted catalytic reactions for CO₂ valorisation are more commonly found in literature in an in-situ configuration with source types as DBD, corona, arc, and jets (the last two are marked as “other” as they were not discussed previously). The reactions explored via one-step plasma catalysis for CCU reported in Figure 1.12 are CO₂ splitting, hydrogenation to methane or other hydrocarbons, and RWGS. It is clear that the most common set-up found in literature for these applications is DBD reactor (squares). CO₂ splitting requires an increasing SEI in order to get high conversion, but a clear improvement with the addition of a catalyst is not observed (compared to Figure 1.10). The MW and RF source types, which reached good CO₂ splitting results without a catalyst, are not shown in this figure as the gas temperature in this kind of plasma reactors is too high for one-stage configurations and would destroy the catalytic material. Instead, CO₂ methanation reaction (less common in the catalyst-free tests) is a well explored application for plasma catalysts in DBD reactors, the specific energy input typically required is confined in the 10^3 to 10^4 J/L region and shows an improved conversion compared to splitting. Other reactions in DBD plasma of CO₂ with a co-reactant require a specific energy input above 10^4 J/L.

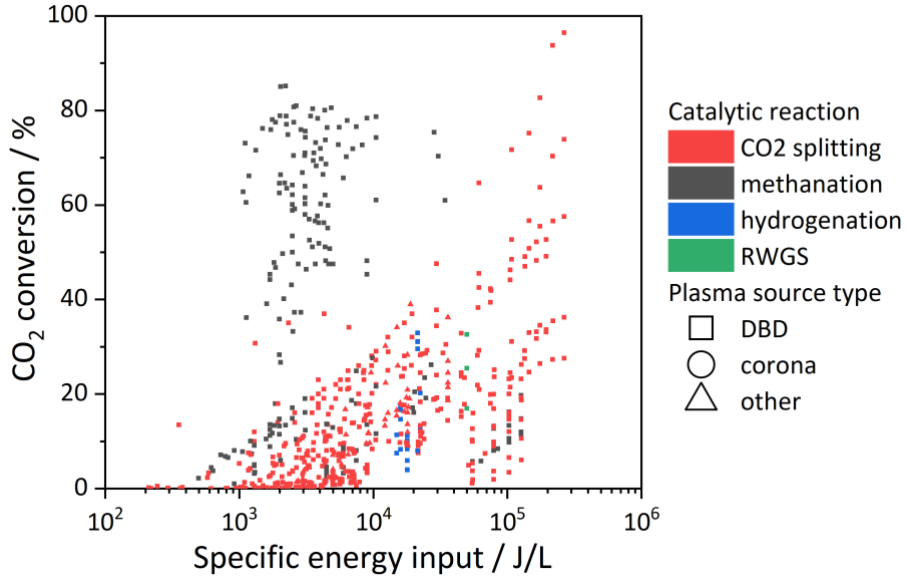


Figure 1.12: Literature results of specific energy input versus CO₂ conversion regarding plasma and catalyst material in-situ combination grouped by plasma source type (symbol) and application (colour)
(source: PIONEER Database [87])

Using a packed bed DBD reactor for plasma-assisted catalytic reactions, in which the catalyst is able to interact directly with the plasma and the reactive species created, allows to avoid that their short lifetime hinders the active species from reaching the catalyst bed [89]. Plasma affects the catalyst and vice versa the packing materials changes the discharge properties, a summary of these possible interactions is schematically reported in Figure 1.11b. Radicals are formed in NTP and can react with the functional groups on the surface and stick for deposition or enhance the catalytic activity [88,90]. These reactive species are normally characterized by short lifetime, therefore the probability of interaction of these species with the surface depends on the dimensionless parameter Λ defined in a review by Kim et al. [88] as:

$$\Lambda = \frac{l}{L_D + L_{ef}} \leq 1 \quad (1.10)$$

where l is the distance to the surface, L_D is the diffusion length, calculated with the lifetime and diffusion coefficient of the species, and L_{ef} is the migration length by electric field, which is determined by mobility, electric field and time period of the electric field. If the criterium is met, reactive species created in plasma will be able to interact with the catalyst and change its surface chemistry [88]. Plasma interacts with the catalyst and its surface in several other ways: by impact of electrons and charged species, which can lead to etching, ion implantation, charging or deposition, by reaction with radicals created in the gas phase, by overheating, and by photons irradiation [90]. Charged species bombardment due to plasma can induce as well morphological changes such as enhancing surface area, since it has been proved to lead to smaller and more uniform granularity [90]. Moreover, it can have an impact on the oxidation state, e.g., nickel reduction, and exposed facet [90–92]. All these features of the material define the catalyst work function that is a very

important property for its activity and selectivity [90]. Heating of the material can lead to hot spots formation and even melting of the nanofeatures of the support and catalyst due to the Gibbs-Thompson effect [90]. Hot spots are characterised by strong micro-discharges in sharp edges or small gaps in the catalyst, which were reported to promote catalytic reactions [93]. The heating of the catalyst due to plasma interactions is beneficial to the catalytic process especially if endothermic, decreasing the external heating required [90].

A final aspect to consider is the effect of the catalyst on plasma characteristics. The presence of a catalytic material having dielectric properties inside the plasma will have an impact on the discharge and electric field. Morphology and porosity of the catalyst, mostly the support plays a role since it has been reported that micro-discharges can occur at the surface and inside pores of catalysts. Having plasma inside micropores would vary its properties as well as increase the probability of reactive species interaction with the surface according to eq. (1.10). Empirical evidence reports a deviation from Paschen's law in air plasma at 1 atm for gaps smaller than 10 μm [88]. Furthermore, models and experiments suggest that discharge ignition is easier inside large catalyst pores or for materials with low dielectric constant and that the pore shape affects the electric field enhancement [83,94]. However, particle-in-cell/Monte Carlo collision model simulations suggest the limit of pore size to be the Debye length λ_D for plasma generation within the catalyst pores [95]. From this point of view, plasma cannot be created inside the catalyst pores lower than 50 nm size. Other authors support that in small pores plasma occurs at very short times at the beginning of the micro-discharge before the plasma sheath is formed at the surface [95]. Typically, a field augmentation is observed in in-plasma catalytic processes. These effects have been represented in the review by Kim et al. as extra components in the equivalent electrical circuit of the packed plasma reactor: a capacitor (C_{catalyst}) and resistor (R_{catalyst}) in series with C_{gas} and R_{gas} , respectively [88]. The C_{catalyst} depends on the dielectric constant of the material, while R_{catalyst} can be affected by humidity, conductivity and temperature [88]. Moreover, the onset voltage of the plasma usually decreases with catalyst packing. The enhancement of the electric field due to reactor packing and nanostructures of the catalyst leads to a variation of the electron energy distribution, which describes the behaviour of the generated gas discharge. In Figure 8, methods of reaction study as modelling and operando techniques are highlighted, in fact these tools are vital to gain insight on the plasma catalytic mechanism and on the impact of plasma-catalyst synergy [83,96]. All the phenomena previously presented add up to the plasma-catalyst synergy, that represents one of the key parameters to control for enhanced and efficient CO_2 catalytic methanation.

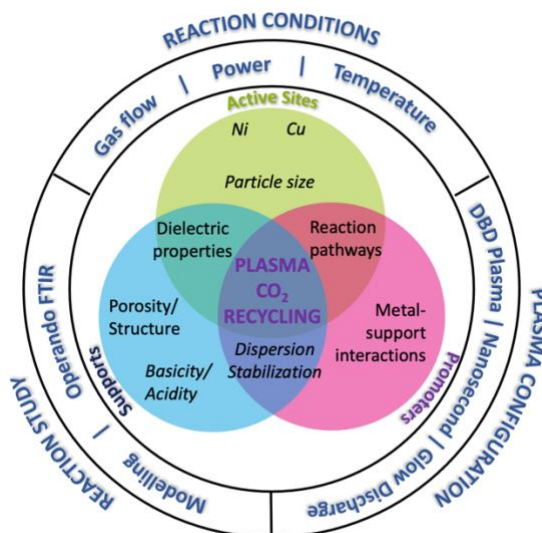


Figure 1.13: Different factors that influence a plasma catalytic process
(credits: PIONEER work package 3 M. Nguyen-Quang, M. Faedda, G. Hasrack, Y. Cai)

Other operational factors and catalyst properties affect the efficiency of a catalytic plasma set-up, they are summarized in Figure 1.13. Initially, the choice of NTP source type and power supply is a key element, together with the screening of operational range regarding frequency and voltage [97,98]. The reactor configuration, including the electrodes and dielectric materials and geometry, is the starting point of a rational NTP reactor design [99]. Controlling the injected power and ignition mechanism can improve the efficiency of the process, therefore different strategies of turn on/off are explored as an alternative to continuous operation [100]. The temperature and heating of the system is also a critical step, the reactor can operate at pseudo-adiabatic (heat is transferred to the surroundings) [101], adiabatic (with thermal insulation) [100,102], or isothermal conditions, as it can be maintained at a set temperature by imposing external heating or cooling [103,104]. Other parameters as gas flow, GHSV and pressure are also very relevant as they can affect the overall cost of operation of a plasma catalytic reactor [101,105]. As expected, it was found that higher GHSV, related to shorter contact time, leads to lower CO₂ conversion [101]. The packing of the plasma zone, meaning the macroscopic size of the catalyst (powder or macro-supports) and the packing mode (mid- or downstream packing) have also been investigated and are important for the plasma-catalyst interaction [105,106]. The characteristics of the catalyst, including active site, support, and promoter selection and beneficial properties, will be discussed in the next section 1.4.1.

1.4.1. Ceria-based catalysts for plasma-assisted CO₂ methanation

Several publications in the last decade have proved that the combination of cold plasma with an active and selective catalyst can lead to high yield for CO₂ methanation at ambient pressure and lower temperature than the thermochemical reaction [92,98,113,102,105,107–112]. On the other

hand, the effect of plasma or ceria supports alone are proved to be negligible for CO₂ methanation, resulting in low conversion of CO₂ without selectivity towards methane [112,114]. CeO₂ or ceria mixed oxides, predominantly Ce_xZr_(1-x)O₂ known as ceria-zirconia, supports were used mostly for nickel catalysts in these works (Table 4). Ni metal on commercial ceria for plasma-assisted CO₂ methanation were reported in two publications that also discuss the effect of Co and Y promoters on the activity in plasma [114,115]. The optimal amount of Co as promoter is fixed to 1%wt. and the positive effect on the activity is linked with improved surface basicity, which is also promoting the thermal reaction [115]. Guo et al. [114] obtained the Y-doped Ni/CeO₂ via mechanochemical synthesis and compared different amounts of Ni and Y. For the nickel content (0-10 %wt.), the best CO₂ conversion at 10 kV corresponding to 13 kJ/L is reached with 7.5%Ni/CeO₂. This result is improved only with the addition of 1%wt. Y, as lower or higher quantities were shown to be detrimental. Y improves the basicity and oxygen vacancy concentration on the surface of the catalyst, which are beneficial for CO₂ activation. Commercial ceria-zirconia mixed oxide was used as a support for Co [98,116] and for Ni catalysts [92,105,107–111,113] for plasma-catalytic CO₂ methanation. Mikhail and co-workers [108,109] also considered the influence of the presence of different promoters, observing improved performance for Gd-containing Ni/Ce_{0.58}Zr_{0.42}O₂ and the detrimental effect of K and Na used as dopants. Ceria-zirconia is widely recognized as an excellent catalyst support for this application due to enhanced formation of oxygen vacancies, which is a key step in the oxygen-electron exchange mechanism activated in the presence of the DBD plasma [113]. The dielectric properties of the catalyst were also related to the catalytic activity [109] since, together with its particle size and shape, they strongly influence the characteristics of the plasma discharge catalysts. CeO₂ was employed as well as a promoter, resulting in enhanced activity for Ni catalysts on Al₂O₃ and zeolites in DBD plasma [100,112,117]. The amount of CeO₂ was varied from 0 to 50 %wt. and it was found that for the plasma-assisted reaction the optimal amount is 10 %wt. while for thermal methanation a higher quantity (40 %wt.) is required for an enhanced methane yield as ceria promotes the CO₂ adsorption and activation on the catalyst surface [112]. On the other hand, the 15%Ni/10%Ce/Al₂O₃ catalyst in plasma assists the CO₂ splitting to CO and facilitates this reaction pathway.

Further studies on physicochemical and electrical properties of the ceria-based materials used as packing of a plasma DBD reactor are required in order to better understand the most favourable features and the effect of the material on plasma-catalyst synergy to improve the process performance [94,95,118].

Table 1.4: Comparison of ceria-containing catalysts used in plasma-assisted CO₂ methanation.

Catalyst composition	Plasma			Conditions			Results					Ref.
	Type	V (kV)	f (kHz)	Gas mix	Flow GHSV	p	X _{CO2} (%)	S _{CH4} (%)	P (W)	SEI (J/L)	T (°C)	
Ceria supports												
15%Ni/1%Co/CeO ₂	DBD	25-29	12.3	CO ₂ /H ₂ 1:4	52000 h ⁻¹	Atm.	75	98	47.6	4950	158	[115]
7.5%Ni/1%Y/CeO ₂	DBD	10	7.7	CO ₂ /H ₂ 1:4 + 25% Ar	50 mL/min	Atm.	84	83	15	18000	< 100	[114]
Ceria mixed oxides												
15%Ni/Ce _{0.58} Zr _{0.42} O ₂	DBD	14-18	40	CO ₂ /H ₂ 1:4	200 mL/min 42720 h ⁻¹	Atm.	71.2	100	10.4	3126	260	[101]
15%Ni/Ce _{0.58} Zr _{0.42} O ₂	DBD	13-16	70	CO ₂ /H ₂ 1:4	200 mL/min 44000 h ⁻¹	Atm.	73	100	13	3900	240	[113]
15%Ni/Ce _{0.85} Zr _{0.15} O ₂	DBD	10-15	40	CO ₂ /H ₂ 1:4	200 mL/min 50000 h ⁻¹	Atm.	82	100	1-3	300-900	270	[91]
15%Ni/Ce _{0.58} Zr _{0.42} O ₂	DBD	13-18	40	CO ₂ /H ₂ 1:4	200 mL/min 20000 h ⁻¹	Atm.	73	100	3.7	1110	120 - 170	[92]
15%Ni/Ce _{0.58} Zr _{0.42} O ₂	DBD	19	41	CO ₂ /H ₂ 1:4	200 mL/min 463001 h ⁻¹	Atm.	79	100	15.9	4560	220	[105]
Ni/CeO ₂ -ZrO ₂	Glow	2	50	CO ₂ /H ₂ 1:4 + 50% Ar	20 mL/min 360000 h ⁻¹	2.7 mbar	25	2.5% Yield CH ₄			RT	[97]
15%Ni/2%Na/Ce _{0.58} Zr _{0.42} O ₂	DBD	13-16	70	CO ₂ /H ₂ 1:4	200 mL/min 44000 h ⁻¹	Atm.	57.5	75.9	21.4	6420	272	[108]
15%Ni/4%Gd/Ce _{0.58} Zr _{0.42} O ₂	DBD	12-15	70	CO ₂ /H ₂ 1:4	200 mL/min 44000 h ⁻¹	Atm.	84.9	99.8	7.5	2250	249	[109]
5%Co/CeZrO ₄	DBD	20	1	CO ₂ /H ₂ 1:4	25 mL/min	Atm.	80	100		30600	200	[98]
10%Co/CeZrO ₄	DBD	18	1	CO ₂ /H ₂ 1:4	25 mL/min	Atm.	75	98			150	[116]
Cerium as promoter												
15%Ni/10%Ce/Al ₂ O ₃	DBD	4-15	54	CO ₂ /H ₂ 1:4	200 mL/min 40000 h ⁻¹	Atm.	75	98	27	8100	150	[112]
15%Ni/30%Ce/Al ₂ O ₃	DBD	4-9	52	CO ₂ /H ₂ 1:4	200 mL/min 13333 h ⁻¹	Atm.	84	100	10	3000	150	[100]
15%Ni/20%Ce/Cs-USY(38)	DBD	5-6	42	CO ₂ /H ₂ 1:4	200 mL/min 32000 h ⁻¹	Atm.	75	>95	35	10500	170	[117]

1.4.2. Diagnostics for plasma catalysis

The complexity of plasma chemistry, of vibrational, rotational and translational exchanges, and of plasma-catalyst mechanisms of interaction that occur in a one-stage plasma catalytic reactor require an exhaustive in-situ analysis, which ideally should be standardized to obtain comparable plasma parameters, e.g., gas temperature [83]. Reliable diagnostic techniques of plasma and plasma

catalytic systems also helps to correctly measure the plasma parameters used to input in numerical models that help understanding the behaviour, prospect, and limits of the plasma discharge [83]. Several spectroscopy techniques are commonly used in plasma diagnostics and may be applied for plasma catalytic systems. The most common ones are Fourier transfer infrared spectroscopy (FTIR) to identify the hetero-nuclear molecular species in plasma, gas and eventually adsorbed on the catalyst surface, and Optical emission spectroscopy (OES), to find the excited species by NTP. Other optical techniques are fast imaging with intensified charged coupled device cameras to follow the morphology of plasma filaments and laser diagnostics. Laser diagnostics include laser induced fluorescence spectroscopy for measurements with spatial and temporal resolution of species densities [119], Rayleigh/Raman/Thomson scattering for molecules and gas temperature detection [83], and electric field induced second harmonic generation for measuring the electric field inside filaments [83]. A similar measurement can be obtained via Mueller polarimetry, which can also gauge the electric field induced inside dielectric catalytic materials related to surface charge deposition and plasma electric field distortion [83]. OES can also be used to measure the gas temperature [120]. Other standard methods for temperature measurement are inserting an optical fiber temperature sensor in the discharge zone [121] or using an IR thermometric cameras on surfaces with known emissivity (meaning the outer surface of the reactor) [122]. The external temperature at the reactor surface is usually the most facile method of reactor temperature measurement via thermocouple or other temperature sensor, especially for the case of one-stage plasma catalysis reactors which do not have an optical access (even when using an optical fiber for OES) and/or do not allow a probe to be inserted directly inside the discharge. Furthermore, according to simulations for a packed bed DBD reactor, at steady-state conditions, the temperature at the external surface is close to the temperature in the catalyst bed with a difference of $<10\text{ }^{\circ}\text{C}$ [123]. The electrical characterization of plasma catalysis systems is also very important to fully understand the behaviour of plasma and the regime at which it is working. Langmuir probes are used to measure the ion/electron flux, they consist of metallic objects in contact with the plasma connected to an external electrical circuit that measures a current-voltage curve used for the calculations [124]. Further electrical diagnostics include using current probes (usually Rogowski coils) and monitoring the voltage drop across an external capacitor to measure the charge transferred in the discharge [125,126]. A thorough analysis of the current peaks will suggest the nature of the micro-discharges occurring in the NTP reactor and the impact of the packing material [125,126].

1.4.3. CO₂ methanation reaction mechanisms in the presence of CeO₂-based catalysts

There are two main CO₂ methanation reaction pathways proposed in literature: via CO or via formate. The first mechanism involves dissociation of CO₂ to CO which is absorbed as surface carbon species and subsequently hydrogenated to form CH₄. The second one involves direct hydrogenation

of adsorbed CO_2 to formate as reaction intermediate that is then transformed to HCOO and then to methane via reaction with hydrogen. Regarding Ni/CeO_2 catalysts, it is widely accepted that the adsorption site for H_2 is the metal Ni^0 particles and for CO_2 the ceria surface [78]. Further dissociation and reaction of CO_2 may occur at the metal-support interface. These mechanisms were proposed also for the plasma-assisted reaction, as the interaction and activation on the catalyst surface still plays a major role in the plasma-catalytic methanation. However, plasma might affect the mechanism as the discharge aids the CO_2 splitting and it may modify the catalyst surface, creating new active sites and therefore opening a new reaction path, or reactivating adsorption sites [96,97].

Already in the 1990s, Trovarelli and De Leitenburg [57] had considered a CO pathway for thermal CO_2 methanation, with a key role of OV of ceria for the adsorption of CO_2 and formation of CO. The vicinity of lattice defects of the support with the metal particles (Rh) facilitates the H_2 spillover and the reduction of the CO formed. The OVs have an important part in the selection of the mechanism according to Hao and co-workers [76]. On an OV-rich surface, CO_2 is attached on Ce^{3+} sites and the oxygen atoms are exchanged between the intermediates and OV, so it promotes the formate pathway with the reaction $\text{bi-HCOO} > \text{br-HCOO} > \text{H}_3\text{CO}$. On the other hand, if the ceria surface does not have lattice defects and the Ni is well dispersed on it, the reaction shifts to the carboxyl pathway and selectivity for CO: the oxygen from the adsorbed CO_2 is not retained by the surface and the adsorbed molecule is transformed to carboxyl species on nickel surface [76]. It was also reported by Cardenas-Arenas [78] that water desorption is the slowest mechanism step, however the Ni/CeO_2 surface does not accumulate carbonates or water species under reaction conditions, as the chemisorption sites are different. According to the authors, this is a perk of the ceria support that possesses high oxygen mobility, unlike $\text{Ni/Al}_2\text{O}_3$ catalyst, whose surface remains blocked by water and intermediates [78]. Unlike Ni, Ru sites are responsible for both CO_2 dissociation to CO^* and hydrogen chemisorption, these can react and hydrogenate to HCOH^* to then form methane [79]. The reaction rate depends on the CO/H adsorption ratio and strength. The type of support is helpful to determine the bond strength of the adsorbed CO, a partially reducible support as CeO_2 favours the H_2 dissociation on Ru over CO adsorption and allows a sufficiently weak CO bond for further reactions, which explains the better performance compared to other metal oxides [79].

Some studies were carried out regarding the mechanism of plasma-assisted CO_2 methanation, by means of operando FTIR [96,97], diffuse reflectance infrared Fourier transfer spectroscopy (DRIFTS) [116], OES [127], and temperature programmed plasma surface reaction (TPPSR) [98]. It was highlighted that the mechanism of the reaction in plasma conditions can be attributed to both Langmuir–Hinshelwood and Eley–Rideal mechanism due to the presence of gas-phase H species, while in thermal catalysis this latter proceeds only via Langmuir–Hinshelwood [128]. Benrabbah et al. [127] studied the formation of highly reactive species from CO_2 and H_2 in plasma, which are reaching the surface of the Ni/CeZrO_2 catalyst and consumed by the Ni sites. Parastaev and co-workers [98,116] investigated both DRIFTS and TPPSR using labelled $^{13}\text{CO}_2$ techniques to determine

the reaction mechanism in a DBD on Co/CeZrO₄ catalysts. It was found that CO₂ methanation occurs mainly through the conversion of gaseous CO₂ that is firstly converted to CO which is further adsorbed on the Co particle and hydrogenated to form CH₄, following the carboxyl pathway. There are formate peaks detected in the IR spectra, but they do not vary in intensity, therefore indicating that these species are not involved in the reaction. Furthermore, they showed that electron bombardment from plasma provokes the desorption of CO₂ and CO from CeZrO₄ surface, and even carbonate and formate species previously adsorbed are transformed to CO₂ and CO by electron impact [98]. Mikhail and collaborators [113] suggest an interesting reduction-oxidation cycle that maintains the CO₂ methanation, fed by the non-stoichiometric nature of ceria-based mixed oxides used for Ni catalysts in their publications. The metal/support interaction is compared to a P-N junction, which is the interface of two semiconductors, called N-type (electron rich) and P-type (electron deficient), in a single material. In this picture, with the superposition of an electric field from plasma, the ceria-containing support behaves as electron acceptor, i.e., N-type semiconductor, that releases oxygen to produce OV, and the metallic Ni behaves as a P-type semiconductor, releasing electrons and accepting the oxygen from the OV [113]. The flows of electrons and oxygen are maintained with the effect of the electric field established by the plasma and if the catalyst is characterized by good MSI, therefore a good interaction boundary at the P-N junction. Furthermore, the reduction-oxidation cycle is preserved thanks to the continuous interaction of the surface sites with CO₂ or H₂ species that provide oxygen to the oxygen-deficient Ce³⁺ sites and reduce the Ni sites via H₂ dissociative adsorption [113].

1.5. Motivation and objectives of the thesis

The previous bibliographical study was presented in order to encapsulate this thesis work within the multidisciplinary field of plasma catalysis, in the framework of the state-of-the-art of plasma-assisted CO₂ methanation and potential applications of ceria-based catalysts. It was shown that plasma-catalyst synergy and full exploitation of the physicochemical properties of cerium oxide, such as OSC and MSI, represent some of the key parameters to control for enhanced and efficient CO₂ catalytic methanation.

The goal of this work is to gather further insights into the optimal characteristics of a catalyst for plasma-assisted CO₂ methanation and the mechanism of plasma-catalyst synergy. This project positions itself within the framework of a Marie Skłodowska-Curie Action European training network named PIONEER regarding plasma catalysis for CO₂ recycling. The PIONEER network counts 14 PhD students and 17 senior researchers who collaborate to generate knowledge and expertise in the multidisciplinary field of plasma catalysis in order to propose new systems and materials for the efficient conversion of CO₂ to added-value chemicals via plasma catalysis.

In this thesis work, nickel catalysts on ceria supports are investigated and plasma catalytic tests are performed in a packed bed DBD reactor. The starting point of this study is the variation of support

morphology through modification of the synthesis parameters, which to our knowledge has not been explored in plasma catalysis. According to previous peer-reviewed results, CeO_2 morphology is expected to affect the cerianite crystal phases, the exposed facets on the surface, particle size, surface area, and interparticle porosity. The effect of ceria synthesis parameters on OSC and surface defects formation is explored. The contribution of support morphology to the physicochemical properties of the Ni catalysts, such as dispersion, MSI, and reducibility, is studied and reported in chapter 3. The behaviour in plasma of the different materials is assessed through catalytic tests in a cylindrical packed bed DBD reactor as well as thorough electrical characterization of the DBD set-up, which is usually neglected in plasma catalysis publications. The results of catalyst tests are shown in chapter 4. The effect of the physicochemical properties of the catalysts on the plasma-assisted CO_2 methanation is considered and the most relevant ones are highlighted. The electrical response regarding the dielectric permittivity of the packing material and how the plasma discharge and charge transfer are affected by the catalyst is studied and addressed in chapter 5. Finally, to gain further knowledge on the reaction mechanism of CO_2 methanation on Ni/ CeO_2 catalysts in plasma, an FTIR operando study is performed and reported in chapter 6.

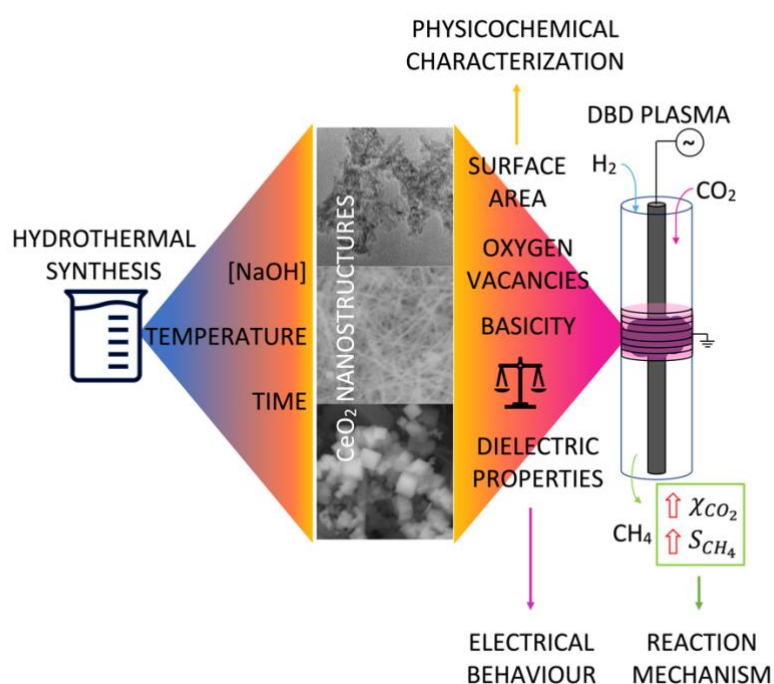


Figure 1.14: Graphical abstract of the PhD work.

Chapter 2: Materials and Methods

2.1.	<i>Synthesis</i>	50
2.1.1.	Materials	50
2.1.2.	Hydrothermal method	50
2.1.3.	Design of experiments (DOE)	51
2.1.4.	Wet impregnation	51
2.2.	<i>Physicochemical characterization</i>	52
2.2.1.	X-Ray Diffraction (XRD)	52
2.2.2.	Scanning Electron Microscopy (SEM) and energy-dispersive X-ray (EDX).....	54
2.2.3.	Transmission Electron Microscopy (TEM).....	54
2.2.4.	N ₂ Physisorption	54
2.2.5.	Temperature-Programmed experiments.....	56
2.2.6.	Thermogravimetric Analysis (TGA).....	57
2.2.7.	X-Ray Photoelectron Spectroscopy (XPS).....	57
2.2.8.	Raman Spectroscopy	58
2.2.9.	Fourier Transform Infrared Spectroscopy (FTIR)	58
2.2.10.	Inductively Coupled Plasma Atomic Emission Spectroscopy (ICP-AES)	58
2.2.11.	Total Organic Carbon (TOC).....	59
2.3.	<i>DBD reactor for plasma-assisted CO₂ methanation</i>	59
2.3.1.	Plasma catalytic set-up.....	59
2.3.2.	Gas Chromatography (GC)	61
2.3.3.	Power supply.....	62
2.3.4.	Electrical characterization	62
2.3.5.	Energy efficiency calculations	64
2.4.	<i>Thermo-catalytic CO₂ methanation set-up</i>	65

The goal of this chapter is to present the experimental techniques that were adopted to obtain the results that will be discussed all through the manuscript, more in detail in chapters 3 and 4. Furthermore, the synthesis methods of the catalysts used for the analysis presented in all next chapters is explained.

The materials preparation and most of the physicochemical characterization was performed in the Instituto de Carboquímica ICB-CSIC in Zaragoza, Spain. The thermal and plasma catalytic tests as well as the temperature programmed experiments were carried out at the Institut d'Alembert of Sorbonne Université located in St Cyr l'Ecole (France). The transmission electron microscopy was performed at the Instituto de Nanociencia y Materiales de Aragón (INMA), Universidad de Zaragoza-CSIC in Zaragoza by the group of Prof. Arenal.

2.1. Synthesis

2.1.1. Materials

For catalyst synthesis, metal nitrate salts $\text{Ce}(\text{NO}_3)_3 \cdot 6\text{H}_2\text{O}$ (Sigma Aldrich, 99.99% pure), and $(\text{NiNO}_3)_2 \cdot 6\text{H}_2\text{O}$ (Sigma Aldrich, extra pure), sodium hydroxide (NaOH) (PanReac AppliChem by ITW Reagents 98% pure) were utilized. Deionized water is denoted as dH_2O (Siemens Ultra Clear RO, conductivity $2 \mu\text{S}/\text{cm}$) and Ultrapore MilliQ water (Siemens Ultra Clear conductivity $0.055 \mu\text{S}/\text{cm}$) as MilliQ.

2.1.2. Hydrothermal method

Nano-structured CeO_2 materials were prepared following a standard hydrothermal synthesis method, which has been described in previous publications [129,130]. Basically, 0.6 g of $\text{Ce}(\text{NO}_3)_3 \cdot 6\text{H}_2\text{O}$ were added to a 40 mL NaOH solution in the range of 1–15 M and stirred magnetically for 10 min in a PTFE beaker (Stuart heat-stir C162). The solution was then placed in a 45 mL Teflon-lined autoclave inside an air-circulating oven (Mettmert vacuum oven), allowing gradient-less temperature to be achieved through its whole volume. Following hydrothermal synthesis, the autoclave was cooled down to room temperature. The powder obtained was filtered with a $0.45 \mu\text{m}$ pore size nylon filter, washed several times with dH_2O and finally with MilliQ water. The powder was dried at 120°C overnight, the resulting weight of CeO_2 product was around 250 mg. The same procedure was performed also with a larger autoclave of 530 mL volume, the amount of precursor and volume of NaOH solution was adjusted accordingly, in order to obtain a larger amount of CeO_2 sample.

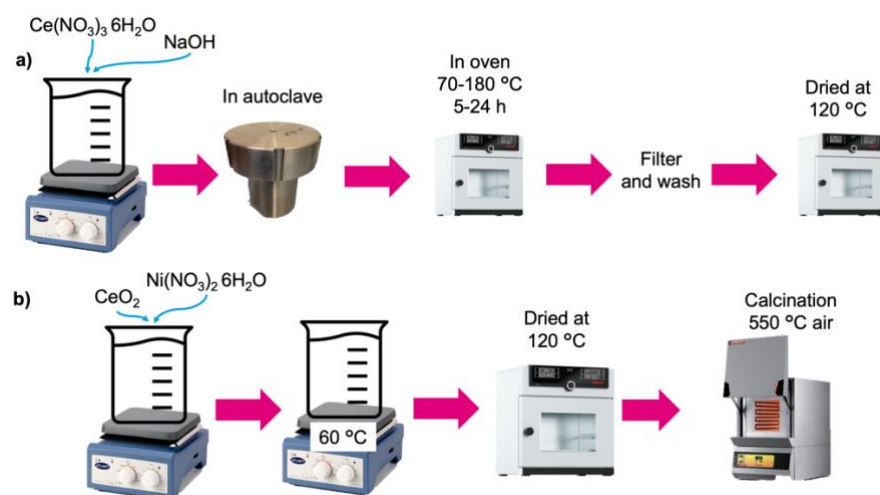


Figure 2.1: Schematics of the a) hydrothermal synthesis and b) wet impregnation.

2.1.3. Design of experiments (DOE)

A factorial design of experiments was designed following a centered two levels, three factors, full factorial model with one centered point concerning the hydrothermal synthesis conditions variation. The design and analysis of the experimental data were performed using a MINITAB 21 statistical software, allowing the determination of the influence of each factor on the final CeO₂ properties, named responses [131]. Three factors were selected following to a previous literature study regarding hydrothermal synthesis of CeO₂, i.e., NaOH concentration, synthesis temperature and time, which were studied at two levels, low and high, according to the values reported in the publications [129,132]. The minimum number of experiments needed for such factorial design is $2^3 + 1 = 9$. The experiments were randomized in order to minimize human error in the synthesis repetition. The samples are labelled DOE_n with n being the number 0 to 8 corresponding to the synthesis order. Each synthesis was repeated at three times (both with small and with large volume autoclaves), creating two blocks in the DOE. Table 1 summarizes these factors and levels, as well as the notation used for the different CeO₂ materials obtained.

Table 2.1: CeO₂ nano-structured materials prepared through hydrothermal synthesis: Experimental factors and levels considered in the design of experiments analysis.

Sample	NaOH concentration, M	Synthesis temperature, °C	Synthesis time, h
DOE0	8	125	14.5
DOE1	1	70	24
DOE2	15	180	5
DOE3	1	180	24
DOE4	15	70	24
DOE5	1	70	5
DOE6	15	180	24
DOE7	1	180	5
DOE8	15	70	5

2.1.4. Wet impregnation

The Ni catalysts were prepared following a conventional wet impregnation method. All DOE supports were used for catalyst preparation with the addition of commercial supports such as CeO₂ (nanopowder from Sigma-Aldrich), Al₂O₃ (Sasol) and Ce_{0.58}Zr_{0.42}O₂ (Solvay), used as benchmarks for the catalytic tests. Nickel was loaded in the previously synthesized CeO₂ supports from an aqueous solution of nickel nitrate hexahydrate (Ni(NO₃)₂·6H₂O) in MilliQ, containing 15 wt% Ni nominal load. The mixture was left on magnetic stirring for 30 minutes at room temperature and then placed in a

bath at 60 °C with continuous stirring until water was evaporated. The solid was dried overnight at 120 °C, and subsequently calcined in air at 550 °C for 4 h in a muffle oven (Carbolite CWF 1300). Upon calcination, all the catalysts were hand-milled and sieved to a grain size of 25-200 µm.

2.2. Physicochemical characterization

The catalytic materials whose synthesis was just described were thoroughly characterized by a number of techniques in order to determine their composition, surface composition, morphology, particle size, crystalline structure, textural characteristics, etc. The schematic of the techniques and relative purposes is shown in Figure 2.2, divided by structure, textural and surface characterization of the supports and catalysts.

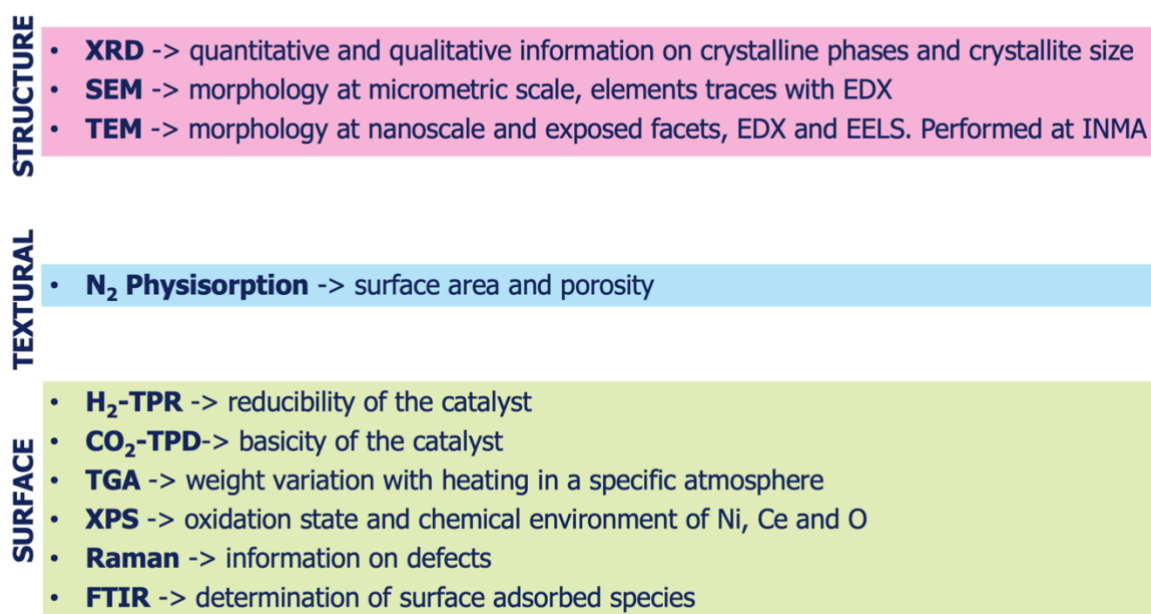


Figure 2.2: Overview of the main material characterization techniques and their purpose.

2.2.1. X-Ray Diffraction (XRD)

XRD is one of the first techniques to be used for characterization of materials. It allows to know if the sample is crystalline, identify the crystalline phases, and calculate the respective crystallite size. This technique relies on the reflection of X-ray wave with wavelength λ on the lattice planes of a crystalline material, which are at a specific distance d according to the material and crystalline lattice. The reflected waves diffract at the detector and result in diffraction peaks when constructive interference occurs, meaning at the angles at which Bragg's law is met:

$$n\lambda = 2d \sin(\theta) \quad (2.1)$$

where n is the order of reflection, λ the wavelength of the beam (Å), d the interplanar spacing (Å) and θ the Bragg angle (°). The scattering is spherical; therefore the measured angle will be 2θ . Each

lattice plane at interplanar distance d is characterized by the type of material and crystalline cell and described by the Miller indices (hkl). By the position of the peaks in the diffractograms it is possible to identify the (hkl) planes and therefore the crystalline material, as a fingerprint. In a perfectly crystalline material, the diffraction peaks are lines, however in real polycrystalline materials consisting of many small crystallites the peaks experience a broadening, due to the diffraction occurring among the reflected x-rays at deeper levels. If the crystallite analysed has very few crystalline planes (small crystallite size), the diffraction produced by deep planes will not be destroyed and will just experience a lower intensity and a broad peak produced by the sum of multiple reflections will be observed. It is possible to calculate the crystallite size L (nm) via Debye-Scherrer equation:

$$L = k \lambda / w \cos(\theta) \quad (2.2)$$

with w that is the peak width, λ the wavelength of the beam (nm), θ the Bragg angle ($^\circ$), and k is the dimensionless shape factor, which depends on how the peak width is measured, the morphology of the crystallites and the size distribution. The usual values used are ranging 0.87 for spheres to 1. The presence of an amorphous phase in the samples is generally shown by very broad peaks as background. A more in-depth analysis of the diffractograms can be achieved via analysis of the peak shape and Rietveld analysis. The diffraction profile is controlled by three contributions, which are spectral energy dispersion of the x-ray source, profile variation caused by the instrument, and finally sample characteristics, as size and microstrain. The first two contributions are adjusted experimentally with a standard sample and by defining the Instrumental Resolution Function. The profile controlled by the crystallite size and microstrain can be fitted with a Double-Voigt function [133]. The width w for the crystallite size calculation according to equation (2.2) is measured by the integral breadth method with $k=1$. The Rietveld method considers the fitting of the diffractograms with mathematical functions according to the peak position, area, and width. A shift in the peak position from the theoretical value defines the lattice parameters, which can be calculated according to the respective crystalline cell. The Rietveld peak integration and calculated intensity allows to achieve a quantitative determination of the crystalline phases in the sample.

The XRD diffractograms were acquired using a Bruker D8 Advance series II diffractometer using monochromatic Cu-K α radiation ($\lambda = 0,1541$ nm) operated at 40 kV and 40 mA. Data were collected in the 2θ range from 20° to 90° , using a step size of 0.03° and a step time of 1 s. All the patterns obtained were calibrated against a silicon standard. The sample preparation involved milling into a very fine powder and levelling into a thin and smooth layer on the rotating sample holder, which reduces noisy signal, improves the background, peak intensity and reliability. Brindley correction for spherical particles has been adopted to take into account the microadsorption from the grains of the powder and intensity reduction. The identification of crystalline phases was accomplished with EVA software using ICSD references while the Rietveld analysis was performed using the TOPAS software.

2.2.2. Scanning Electron Microscopy (SEM) and energy-dispersive X-ray (EDX)

Details on the morphology of the CeO₂ nano-structured supports and Ni catalysts prepared were gained through SEM analyses. SEM micrographs were acquired using a SEM-EDX Hitachi S-3400N microscope with variable pressure couple to a Röntec XFlash EDX analyzer operated at 10 kV, utilized to have an elemental analysis of the samples. To better determine the morphology of the samples, depending on the conductivity and the interaction of the atoms on the surface of the sample with the electron beam, different modes of the microscopy were used such as Back-scattered electrons (BSE), secondary electrons (SE), environmental SEM (ESEM) or Au covering. A small quantity of the powder sample was carried on a carbon holder for characterization in SEM.

2.2.3. Transmission Electron Microscopy (TEM)

TEM works by irradiation of the sample with an electron beam of uniform voltage, focused on the specimen by electromagnetic lenses. Part of the electrons are transmitted, the rest is dispersed or produce interactions that result in emission of light, x-ray, secondary and Auger electrons. From these signals information related to the sample (morphology, composition, crystalline structure and crystal defects, electronic structure, etc.) can be extracted. High-resolution TEM (HRTEM) was performed in a FEI Titan microscope at 300 kV containing spherical-aberration corrector at the objective lens. The high-resolution scanning TEM (HRSTEM), high-angular annular dark-field STEM (HAADF-STEM) images were acquired by a FEI TITAN low base TEM at 300 kV containing aberration corrector at the condenser lens and also equipped with EDX detector. A small quantity of the powder sample was carried on a copper grid for characterization in TEM.

2.2.4. N₂ Physisorption

The textural properties of both CeO₂ nano-structured supports and Ni-containing catalysts were assessed by means of N₂ physisorption at -196 °C, performed in an Autosorb 6 device (Quantachrome). Prior to the adsorption measurements, the samples were outgassed in situ under vacuum (4 mbar) at 250 °C for 4 h, in order to remove any adsorbed impurity. During the measurement, the gas amount (N₂) is recorded at isothermal conditions while the partial pressure p/p_0 of the gas is varied and a graph with adsorption and desorption lines is built as a function of p/p_0 , typically forming a hysteresis loop for mesoporous solids.

The amount of N₂ that is physically adsorbed depends on the surface and porosity of the sample. The Brunauer–Emmett–Teller (BET) method is the most common one for the calculation of the surface area S_{BET} (m²/g), assuming that a monolayer of adsorbed molecules is formed:

$$S_{BET} = \frac{V_m S_m N_A}{M} \quad (2.3)$$

where N_A is the Avogadro number (6.022 10²³ molecule/mol), S_m (m²/molecule) is the occupied area for an adsorbate molecule in the monolayer, M is the molar volume of the adsorbate (m³/mol), and V_m (m³/g) is the monolayer volume determined experimentally from N₂ isotherm data.

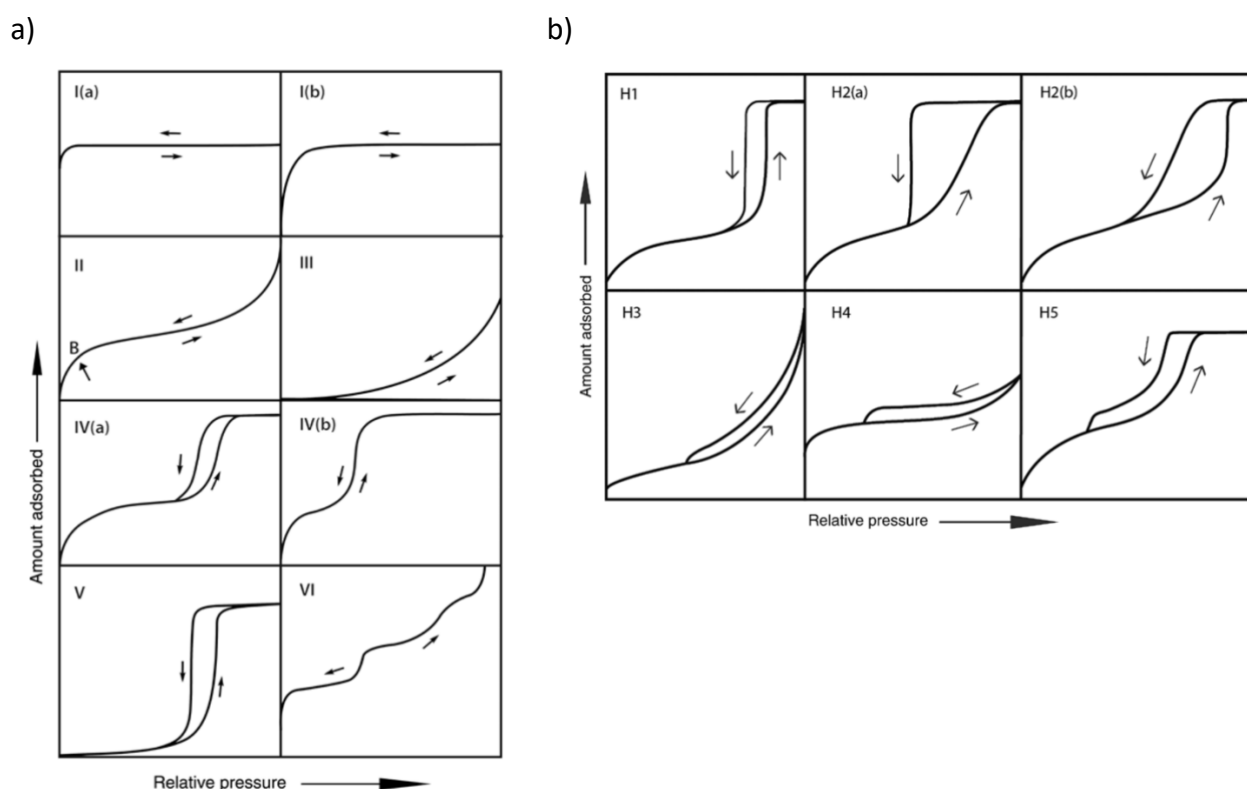


Figure 2.3: IUPAC classification of a) isotherm and b) hysteresis of N₂ physisorption graphs reported from the 2015 IUPAC Technical Report [134].

The porosity of the sample can be qualitatively assessed by observing the isotherm graph and hysteresis. The pores can be categorised according to their width as: macropores (> 50 nm), mesopores (50-2 nm), and micropores (< 2 nm). The International Union of Pure and Applied Chemistry (IUPAC) has defined some common characteristics on the porosity of the materials depending on the isotherm shapes collected in Figure 2.3a: type I is a microporous material, type II is macroporous or non-porous, type III is non-porous with low interaction of the surface with the adsorbate, type IV is typical of mesoporous samples, the hysteresis in this case occurs (type IVa) due to capillary condensation, type V is mesoporous with low interaction adsorbate-solid, and type VI is unusual and describes a non-porous and very uniform surface [134,135]. Mesoporous samples display a hysteresis in their isotherm graphs, that is also described by the IUPAC related to solid characteristics (Figure 2.3b): H1 almost vertical is linked with a narrow pore size distribution, in H2 the adsorption and desorption branches are quite different in slope and describes a material with a wide pore size distribution and undefined morphology in which pore blocking occurs, H3 is typical for slit-like pores, zeolites and carbons normally possess the hysteresis loop H4, H5 is associated with partially blocked mesopores [134]. For mesoporous samples, the S_{BET} calculations are restricted to the p/p_0 range 0.1-0.3.

The total pore volume (V_P) is obtained from the volume of nitrogen adsorbed at the highest point of relative pressure, meaning close to 1, considering the N₂ at standard conditions at -196 °C and

with a density of 0.808 g/cm³. This method is valid unless a steep increase in N₂ volume is observed at p/p_0 close to 1, which indicates condensation of the gas in the pores.

Density Functional Theory (DFT) method is applied to the adsorption isotherms to obtain the pore size distribution, therefore the modal pore size (W_p). The correct fluid, material surface and assumed pore shape (N₂, silica/oxide for CeO₂-based samples and cylindrical shape for the samples studied) must be selected to correctly apply this computational technique, calculate the fluid and solid interaction parameters and model the density profile of nitrogen adsorbed on the pore walls. The MicroActive and QuantaChrome softwares were used for the BET, total volume, and DFT analysis of the isotherms.

2.2.5. Temperature-Programmed experiments

2.2.5.1. H₂ Temperature-Programmed Reduction (H₂-TPR)

To assess the reducibility of the materials H₂-TPR measurements were conducted in a BELCAT-M apparatus (BEL Japan Inc.) equipped with a thermal conductivity detector (TCD). 60 mg of sample were pre-treated in 50 mL/min He at 100 °C for 1 h. Afterwards, the gas flow was switched to 50 mL/min 5% H₂/Ar mixture, maintaining 100 °C for 10 min, then ramping 10 °C/min from 100 °C to 600 °C. The TCD signal was recorded during this temperature ramp and H₂ consumption obtained through a calibration procedure.

2.2.5.2. CO₂ Temperature-Programmed Desorption (CO₂-TPD)

Immediately after the H₂-TPR experiment, the CO₂-TPD was carried out to study the basicity of the reduced catalysts. The 60 mg sample was let cool down in He atmosphere followed by treatment at 80 °C with 50 mL/min for 10 min. Then, the adsorption of CO₂ at 80 °C was performed in a 50 mL/min 10% CO₂/He flow for 1 h. After adsorption, pure He was used to flush the physically adsorbed CO₂ at 80 °C for 30 min. Finally, a heating ramp of 10 °C/min from 80 °C to 800 °C under 50 mL/min He was performed to measure CO₂-TPD profiles, the amount of CO₂ desorbed was obtained from a calibration of the TCD signal.

2.2.5.3. Temperature-Programmed Desorption coupled with Mass Spectrometer (TPD-MS)

A TPD experiment was designed to analyse the samples after the catalytic reactions. A pre-treatment of 30 minutes at room temperature, 10 °C/min ramp up to 100 °C and 30 minutes at 100 °C to clear the surface of physically adsorbed species. The TPD program consisted of 10 °C/min ramp 100-850 °C and 30 minutes at 850 °C. Both steps were carried out with 100 mL·min⁻¹ Argon flow. 60 mg of sample were placed in a U-type tubular quartz reactor, the temperature ramps were controlled by an electric furnace for heating (Eraly) and K-type thermocouple. To evaluate the species that are desorbed from the surface a MS equipment (Quadstar) was used to follow in time the species of mass/charge (m/z) 2, 12, 15, 16, 18, 32, 44. The focus was on 44 m/z that corresponds

to CO₂ in order to assess the desorption of CO₂ and reaction intermediates that decompose to CO₂ with temperature.

All TP curves were treated via baseline subtraction, normalization by the sample mass and fitting with Gaussian curves to determine the peaks position and contribution.

2.2.6. Thermogravimetric Analysis (TGA)

Oxygen Storage Capacity (OSC) measurements of the nanostructured CeO₂ supports were performed by TGA in a SETARAM Setsys Evolution device. Approximately 25 mg of CeO₂ were placed in a Pt crucible and submitted first to calcination in air at 500 °C, then cooled down to 300 °C. The sample was then heated up to 500 °C in N₂ to perform subsequent oxidation-reduction cycles, switching gas atmospheres from air to 20% H₂-N₂. The weight-change observed during oxidation and reduction cycles was used for the calculation of the OSC of the materials.

2.2.7. X-Ray Photoelectron Spectroscopy (XPS)

Via XPS it is possible to recognise the elements present at a depth up to 10 nm by identification of the photoelectric lines. The electronic states of the atoms also give information regarding the chemical environment around them by analysing peak shifts and variation in shape, width, and intensity of the peaks. XPS is also a quantitative technique: the detected intensity is directly correlated to the number of atoms at the surface contributing to the photoelectric line. However, there are several precautions to be taken while analysing a XPS spectrum. In the case of Ni/CeO₂ materials, mainly four regions are investigated: Ce3d, Ni2p, C1s, and O1s. Ce3d has two well separated (18.6 eV) spin-orbit components Ce3d_{5/2} and Ce3d_{3/2}, that are in turn split into multiplets. The peaks contribute to either the 3+ or the 4+ oxidation state: u_0 , u'_0 , u_1 , u'_1 are characteristic of Ce³⁺ and v_0 , v'_0 , v_1 , v'_1 , v_2 , v'_2 for Ce⁴⁺. Ni2p has spin-orbit components Ni2p_{3/2} and Ni2p_{1/2} split by 17.3 eV and can display the different oxidation states of Ni 0, +2, and +3, for simplicity only the first two are considered in the deconvolution in the Ni2p_{3/2} region. Ni⁰ has two satellites that lay in the same region at +3.7 and +6 eV [136]. Ni²⁺ is split into 3 multiplets and presents 3 satellites at +4.8, +6 and +8.5 eV [136]. The C1s peak is normally attributed to adventitious carbon adsorbed on the catalyst surface [137]. The O1s peak varies notably according to the environmental conditions. The oxygen atoms in the cerium oxide crystalline lattice emit photoelectrons at slightly different energy depending on the oxidation state of the neighbouring Ce atom, namely O-Ce⁴⁺ and O-Ce³⁺. Two peaks contribute to the O1s, O_α corresponds to lattice oxygen and O_β at higher binding energy represents the oxygen neighbouring a vacancy (so O-Ce³⁺) as well as surface adsorbed species such as oxygen, hydroxyl, and carbonate groups.

XPS measurements were performed using in ESCA+ (Omicron) photoelectron spectrometer using a non-monochromatic AlKα X-ray source ($h\nu = 1486.7$ eV). A pass energy of 50 eV was used for survey scans and 20 eV for detailed scans. Binding energies were referenced to the Ce3d v'_2 (917

eV). The choice of this reference to scale the spectra instead of the typical C1s is due to the fact that atoms belonging to the matrix of the analysed material (in this case Ce^{4+} inside the crystalline lattice of cerium oxide) should have approximately the same chemical environment, therefore do not experience a peak shift. On the other hand, C is present because of adsorbed species from the atmosphere on the ceria surface, so its C1s peak is not the most reliable reference [138]. The relative sensitivity factors are adjusted to the values reported in the library in order to obtain a correct atom concentration. Linear background is used. The obtained spectra were analyzed using the CasaXPS software. All the peaks of the corrected spectra were fitted with a Gaussian–Lorentzian shape functions (GL(30) and GL(70)), except for the Ni^0 peak which is asymmetric. Iterations were performed using the Marquardt method. Relative standard deviations were always lower than 1.5%.

2.2.8. Raman Spectroscopy

Raman spectroscopy provides information related to the chemical and structural properties of a given compound, including defects. The technique relies upon inelastic scattering of photons, known as Raman scattering, which occurs when a monochromatic laser light interacts with molecular vibrations. This interaction causes a shift in the photon energy, normally reported as a shift in the wavenumber, and provides information about the vibrational modes in the system. Raman spectra were acquired in a Horiba Jobin Yvon HR800 UV dispersive laser Raman microscope. The excitation source used was an Ar ion laser (532 nm) operated at a power of 26 mW and at room temperature. The laser was focused on powdered samples placed on a microscope slide to produce a spot size ca. 3 μm in diameter. A backscattering geometry with an angle of 180° between illuminating and collected radiation was used for recording the data. The acquisition time was 60 s for each spectrum, with a spectral resolution of 1 cm^{-1} .

2.2.9. Fourier Transform Infrared Spectroscopy (FTIR)

FTIR spectra were acquired in a Vertex 70 spectrometer by Bruker in transmission mode for solid samples. Very thin pellets were obtained by mixing the powder sample with KBr, which is transparent to IR. The IR beam passes through the pellet. The absorption spectrum peaks are obtained at the IR region wavelengths that are not transmitted by the sample. The absorbance, meaning the amount of light absorbed by the sample, depends on the molecules that are present on the surface of the material. This creates a molecular fingerprint according to the peaks in the spectrum, which is relevant only for molecules that possess interatomic bonds with stretching vibrations that interact with IR. FTIR allows identifying the functional groups on the surface of the catalysts before and after the reaction.

2.2.10. Inductively Coupled Plasma Atomic Emission Spectroscopy (ICP-AES)

ICP-AES is a multi-element analysis technique that uses an inductive coupled plasma source to produce excitation of electrons at higher energy levels. After this excitation, the electrons return to

their original state, emitting light with a characteristic wavelength for each element. The intensity of the emitted light is proportional to the atoms number of element present. ICP-AES was performed on the reduced catalysts and on the liquid samples using a Xpectroblue-EOP-TI FMT26 (Spectro) spectrophotometer and pre-treating the samples with lithium tetraborate. This technique is useful for elemental quantitative analysis from high percentage to ppm, therefore it was used to know if the expected Ni amount on the catalyst after impregnation is achieved.

2.2.11. Total Organic Carbon (TOC)

The TOC analysis facility allows the analysis of total carbon, inorganic carbon and total organic carbon present in liquid samples and with a wide measurement range from drinking water to samples with high organic matter load (up to 30.000 mg/L with dilution). Carbon measurement is carried out by means of a catalytic combustion-oxidation procedure followed by analysis of the CO₂ produced by means of an infrared cell. To carry out these analyses, the Instituto de Carboquímica has at its disposal a Shimadzu TOC-L CSH equipment.

2.3. DBD reactor for plasma-assisted CO₂ methanation

2.3.1. Plasma catalytic set-up

The activity and selectivity of the different materials prepared towards CO₂ methanation were assessed under both plasma and thermo-catalytic conditions. Prior to any experiments the catalysts were reduced in a 10% H₂/Ar gas mixture (100 mL/min) at 600 °C for 1 h. Plasma-catalytic experiments were performed using a non-thermal DBD plasma reactor, operating at atmospheric pressure and under pseudo-adiabatic conditions. The reactor geometry is coaxial cylindrical (schematics in Figure 2.4) with two dielectrics. It consists of a quartz tube (outer diameter 9.6 mm and wall thickness 1 mm) and an inner alumina tube (outer diameter 3 mm) that surrounds the high voltage electrode. The plasma was created between two electrodes in a gap of 2.3 mm: the inner one consists of a tungsten rod (2 mm diameter) while the outer one, which is a cylindrical stainless-steel ring, is placed around the quartz tube and acts as ground electrode. The height of the outer electrode is 1 cm and this zone is considered as the plasma zone of the reactor. The temperature of the reactor is monitored using a Pt100 temperature sensor (RS Electronics) attached to the outside ring electrode.

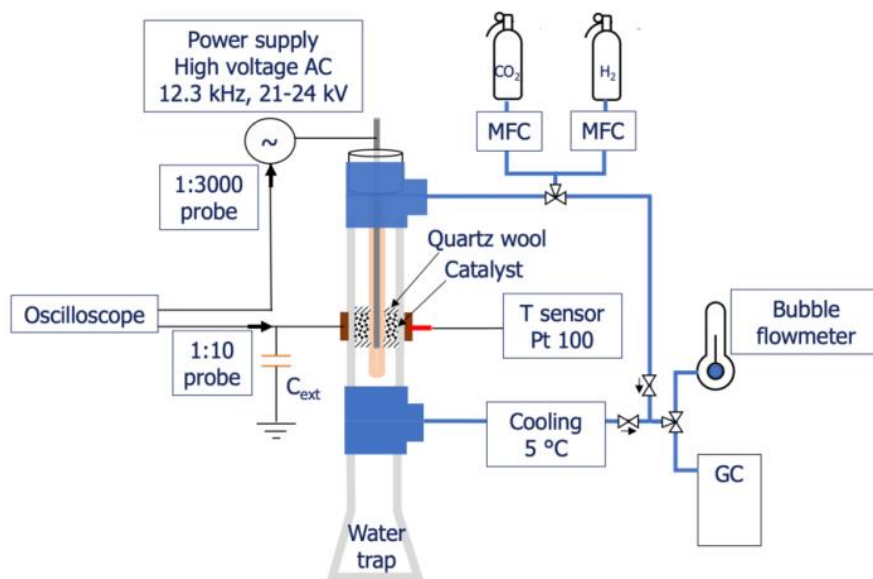


Figure 2.4: Experimental set-up for the plasma-catalytic methanation of CO₂ in the fixed bed reactor.

The reduced catalyst in powder form was packed in the plasma zone, meaning the annular space between the alumina and the quartz tubes, and glass wool was used to keep the catalyst fixed. The input CO₂/H₂ gas flow mixture (CO₂/H₂ = 1/4, 100 mL/min, WHSV 30 000 mL/hg_{cat}, 12 kg_{CO2}/k_{cath}) was controlled by mass flow controllers (BRONKHORST). A valve is placed in order to send the gas mixture to a bypass or through the reactor. The output flow was measured using a column bubble flow meter while the content was monitored using a double column microGC (Agilent 490 Micro GC) after passing through a water trap set at 5 °C. Different peak-to-peak voltages in the range 20-25 kV (kV_{p-p}) were tested, keeping each condition for 30 minutes.

For both catalytic tests the CO₂ conversion (X_{CO_2}) and CH₄ selectivity (S_{CH_4}) are calculated following the equations below:

$$X_{CO_2} = 100 \cdot \frac{[CO_2]_{in} \cdot \dot{V}_{in} - [CO_2]_{out} \cdot \dot{V}_{out}}{[CO_2]_{in} \cdot \dot{V}_{in}} \quad (2.4)$$

$$S_{CH_4} = 100 \cdot \frac{[CH_4]_{out} \cdot \dot{V}_{out}}{[CO]_{out} \cdot \dot{V}_{out} + [CH_4]_{out} \cdot \dot{V}_{out}} \quad (2.5)$$

where $[CO_2]_{in}$ (%) and $[CO_2]_{out}$ are respectively the concentration of CO₂ fed to the reactor and in the output, $[CH_4]_{out}$ and $[CO]_{out}$ are the concentration of methane and carbon monoxide produced (%), and \dot{V}_{in} , \dot{V}_{out} are respectively input and output volumetric gas flow (mL/min).

In order to assess the reproducibility of the catalytic tests, the experiment was repeated 3 times at the same conditions and standard deviation was measured.

The carbon balance ($C_{balance}$) is also assessed by:

$$C_{balance} = 100 \cdot \frac{[CH_4]_{out} \cdot \dot{V}_{out} + [CO]_{out} \cdot \dot{V}_{out} + [CO_2]_{out} \cdot \dot{V}_{out}}{[CO_2]_{in} \cdot \dot{V}_{in}} \quad (2.6)$$

with $[CO_2]_{in}$, $[CO_2]_{out}$, $[CH_4]_{out}$ and $[CO]_{out}$ are as described above, and \dot{V}_{in} , \dot{V}_{out} are respectively input and output volumetric gas flow (mL/min).

2.3.2. Gas Chromatography (GC)

The Agilent 490 Micro GC coupled with TCD detector used for the plasma set-up was equipped with two columns: 5m PoraBond Q (PBQ) + 10m Molesieve 5Å (MS5A), and 10m PoraPLOT U (PPU), using Ar and He as carrier gasses, respectively. They were set at 90 °C and 45 °C temperature, respectively, and pressure of 150 kPa. The injector temperature was kept at 110 °C with 50 ms injection time; backflush time 48 s and run time of 300 s per measurement. The first channel is designed to detect at different retention times: H₂ (66 s), CH₄ (166 s), and CO (213 s). Using its 5 Å pore size sieve the column separates components by molecular size but is notorious for absorbing water, therefore, periodic column conditioning is required. In column 2 CH₄ (30 s) and CO₂ (40 s) are observed. PPU columns are made of porous polymers which retain polar and apolar volatile compounds according to functionalization. At higher retention time C₂ species (ethane, ethylene, and acetylene) may also be detected. The first peak that is detected in this channel is referred as retention peak and it is not relevant for the gas composition analysis.

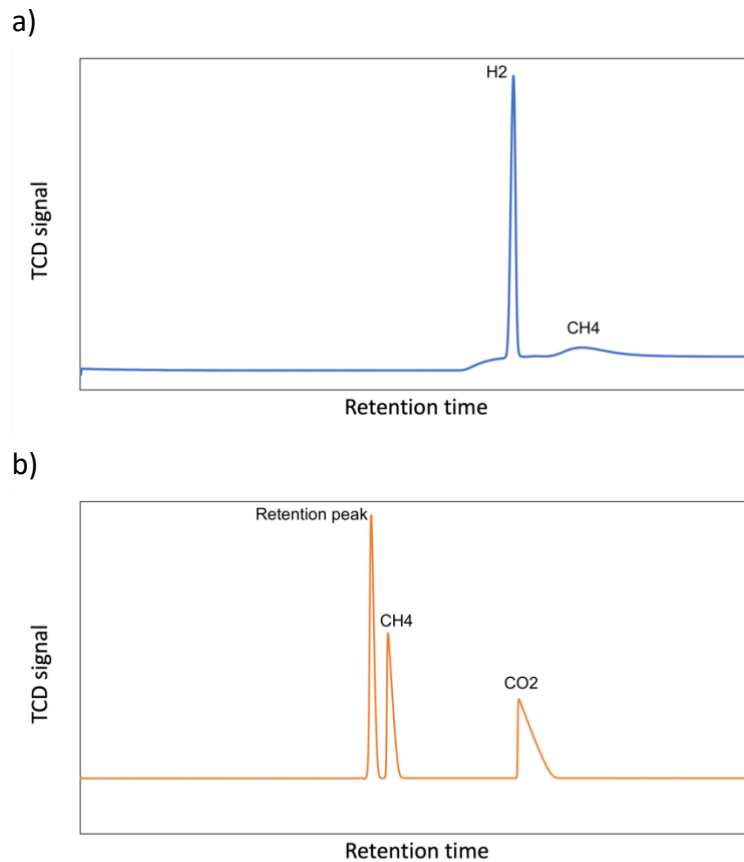


Figure 2.5: Gas chromatogram in a) column 1 (PBQ+MS5A) and b) column 2 (PPU) of mixture of CO₂, CH₄ and H₂, used for the calibration of level 3.

Automatic integration to obtain the area of the peaks was performed with the software provided by Agilent. The retention time and window together with width and threshold requirements were set for correct peak detection, the baseline is established automatically for each peak and integration is not performed in the regions where peaks are not expected.

A multi-level calibration was performed in order to obtain directly the gas concentration instead of the respective calculated area. Mixtures of H₂, CO₂, CH₄, CO and N₂ were used. The first 4 levels consisted of varying amounts of H₂, CO₂, and CH₄, which are the primary gasses involved in CO₂ methanation. Level 5 and 6 were added to calibrate small amounts of CO, at 3 % (using a 3%CO/N₂ calibration bottle from Air Liquide) and 2 % (mixture with N₂ and CH₄), respectively. The last level 6 was also used in order to well separate the CH₄ and CO peaks in column 1, which appear very broadened.

2.3.3. Power supply

The Minipuls 6 (GBS Elektronik) power supply was used for the plasma DBD reactor. The specifics of the power supply allow it to generate alternate current (AC) high voltage (HV) signal up to 30 kV peak and frequency range from 5 to 20 kHz. The device consists of a full bridge converter and a 5 stages transformer cascade, and it requires an external bench direct current (DC) power supply (40 V, 20 A, TTI CPX400SP from RS). The powerful low voltage signal is transformed in a square wave that is then enhanced by the transformers and filtered into a sine-like wave. The DC power supply is controlled by a remote, which selects the DC input voltage (0-30 V) and frequency of the square signal, therefore of the sinusoidal output. The pulse generator is controlled by the time-to-live signal input. The output of the Minipuls 6 is connected to the HV electrode of the reactor with a coaxial cable (60 kV, 1 A). The AC HV power supply is designed to be used at conditions close to the set-up resonance frequency, which was found to be 10.3 kHz, which depends on the capacitance, resistance and inductance of the system. For safekeeping of the Minipuls 6, 12.3 kHz frequency was selected for operation during the plasma catalytic tests, as it assures a good voltage gain and avoids current spikes which might occur if operating directly at the resonant frequency. For monitoring a 1:3000 voltage divider is already built in at the power supply output. The power supply boxes were cooled down by ventilation, exceeding current and temperature were continuously monitored for safety.

2.3.4. Electrical characterization

The inner electrode is connected to the Minipuls 6 power supply that delivers a sinusoidal signal having frequency (f) 12.3 kHz and tuneable high voltage ranging typically 20-25 kV_{pp}. The outer electrode is grounded and connected to an external capacitor C_{ext} of 3.2 nF, the voltage across the capacitor is measured (V_c in V) and is used to measure the charge (Q in C) transferred in the reactor, according to the relation:

$$Q = C_{\text{ext}} V_C \quad (2.7)$$

The high voltage (V_{in}) signal is monitored with a 1:3000 probe (Minipuls) and the voltage drop across the external capacitor V_C is measured with a 1:10 probe (Pico technology), both are measured using a PC oscilloscope (Picoscope 5000 series, Pico technology), as in Figure 2.4.

These V_{in} and Q signals are used to build the Q-V Lissajous plot, two examples shown in Figure 2.6. In the ideal case the Lissajous cycle is a parallelogram (approximated in Figure 2.6 with the dashed lines for the empty reactor), however, especially for packed bed DBD reactors (blue line in Figure 2.6), the discharge events do not all occur at the same time or across the whole reactor gap, therefore the Q-V graph is almond shaped [139].

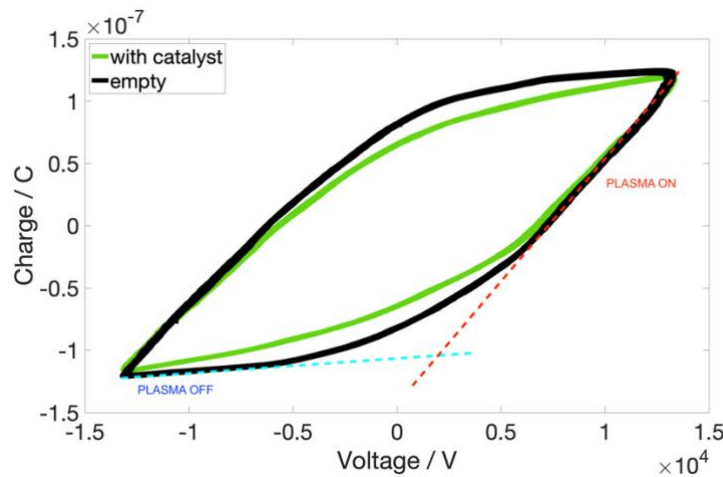


Figure 2.6: Typical experimental Lissajous figure for an empty and packed bed DBD reactor, overlaid with a graphical example of linearization of the “plasma on” and “plasma off” for the empty case.

The power (P) injected to sustain the plasma and the reaction is measured via the Lissajous plot, which equals the area of the curve over one cycle multiplied by the frequency of the high voltage signal [109,139,140]. The calculation is repeated and averaged over 6 periods.

$$P = f \oint V_{in}(t) dQ(t) \quad (2.8)$$

The shape of the Lissajous figure, which can be approximated to a parallelogram, is also analysed in order to assess the capacitance of the reactor. The slope of the sections of the parallelogram that relate to the “plasma off” (Figure 2.6), meaning input voltage increasing from the minimum and decreasing from the maximum, can be considered as the overall capacitance of the cell $C_{reactor}$. This capacitance corresponds to the contribution of the dielectric materials (quartz and alumina in this set-up, C_{quartz} and $C_{alumina}$), the catalyst in the packed bed ($C_{catalyst}$) and the gas fraction (C_{gas}), or only the gas capacitance in the of the empty reactor, as the gas is not in breakdown at this applied voltage range [139]. These capacitors are approximated as placed in series [141], as in the equivalent circuit in the Figure 2.7, and the overall packed bed DBD reactor capacitance $C_{reactor}$ can be calculated:

$$\frac{1}{C_{reactor}} = \frac{1}{C_{quartz}} + \frac{1}{C_{gas}} + \frac{1}{C_{catalyst}} + \frac{1}{C_{alumina}} \quad (2.9)$$

At a certain voltage, the discharge is ignited (“plasma on” region of the Lissajous in Figure 2.6), the gas fraction is converted into a “black box”, modelled as C_{gas} in parallel with a time-dependent resistor R_{on} (Figure 2.7).

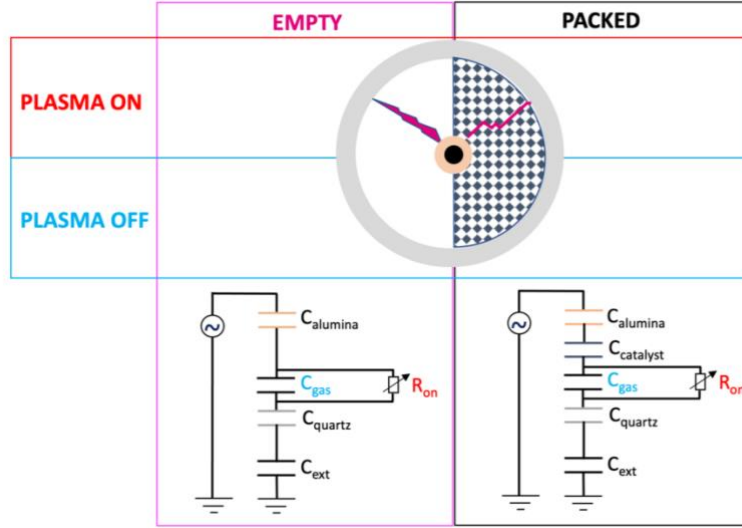


Figure 2.7: Equivalent electrical circuit of empty and packed bed DBD reactor.

For simplicity, any capacitor can be approximated to an equivalent capacitor, that has the same capacitance value C_{reactor} and is in plane-to-plane configuration, whose standard formula is:

$$C_{\text{reactor}} = \frac{\varepsilon_0 \varepsilon_{\text{reactor}} A}{d} \quad (2.10)$$

where ε_0 is the vacuum permittivity ($8.85 \cdot 10^{-12}$ F/m), A (m^2) and d (m) are respectively area of the planes of the equivalent capacitor and gap between the conductive plates (which do not necessarily match the physical dimensions of the reactor), $\varepsilon_{\text{reactor}}$ is the relative dielectric permittivity of the dielectric constituting the plane-to-plane equivalent capacitor, in this case it would be the permittivity of the DBD reactor. The eq. (2.10) is just to demonstrate that C_{reactor} is directly proportional to the resulting dielectric permittivity of the packed bed DBD cell $\varepsilon_{\text{reactor}}$, which considers the permittivity of the material that is used to pack the plasma reactor. This analysis was carried out in MATLAB.

2.3.5. Energy efficiency calculations

The specific energy input (SEI) is a common parameter in plasma-assisted CO_2 conversion and plasma catalysis publications [20]. It is calculated as:

$$SEI = \text{Power}_{\text{plasma}} / \dot{V}_{\text{total}} \quad (2.11)$$

and it defines the amount of energy per volume of reactants (J/L), with $\text{Power}_{\text{plasma}}$ calculated via the Lissajous figure in W and \dot{V}_{total} is the total reactants flow in L/s.

The efficiency (η) of the plasma-assisted CO₂ methanation reaction is evaluated with equation (2.11) in order to compare the catalysts' performance taking into consideration the power required for the CO₂ conversion to methane.

$$\eta (\%) = 100 \cdot \frac{Power_{out}}{Power_{in}} = 100 \cdot \frac{LHV_{CH_4} \cdot [CH_4]_{out}}{Power_{plasma} + LHV_{H_2} \cdot [H_2]_{converted}} \quad (2.12)$$

where LVH is the low heating value (801 kJ/mol for methane and 242 kJ/mol for hydrogen), $[CH_4]_{out}$ is the amount of methane produced in mol/s, $[H_2]_{converted}$ is the amount of hydrogen converted in the methanation reaction in mol/s, $Power_{plasma}$ refers to the injected power as measured via the area of the charge-voltage Lissajous figure in kW. It is relevant to evaluate the efficiency because it takes into account the conversion as amount of methane produced and the power injected to the plasma to sustain the reaction.

2.4. Thermo-catalytic CO₂ methanation set-up

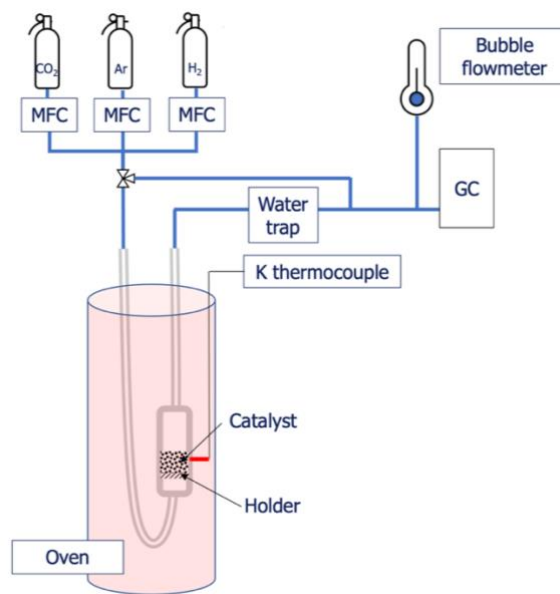


Figure 2.8: Experimental set-up for thermal methanation of CO₂.

The catalytic activity of the catalysts in thermal CO₂ methanation was conducted in a U-type tubular quartz reactor at ambient pressure with an electric furnace for heating (Eraly), using a K-type thermocouple positioned in the upper part of the catalyst bed to monitor the temperature (see Figure 2.8). The gas flow was controlled by mass flow controllers (BRONKHORST). A valve is placed in order to send the gas mixture to a bypass or through the reactor. Before the methanation test, the fresh catalyst was reduced in situ in a 10% H₂/Ar gas mixture (100 mL/min) at 600 °C for 1 h. After the reduction, the reactor was cooled down to 250 °C flushing inert gas (Ar) and then the reactant gas mixture (CO₂/H₂/Ar = 15/60/25, 100 mL/min) was fed into the sample, with a WHSV of 30 000 mL/hg_{cat} and 8.2 kgCO₂/kg_{cat}h. The water produced is condensed in a water trap set at 5 °C.

The testing temperature range was from 250 to 450 °C with an increasing step of 50 °C and the reaction was maintained at each temperature for 30 minutes in order to reach a steady state. The outlet gas mixture was analysed using a gas chromatograph (Agilent 490 Micro GC coupled with TCD detector) and the flow rate was also collected using a column bubble flow meter. The single column microGC used was equipped with a 1m Cox Heated injector column, set at 80 °C and 200 kPa, and the injector at 110 °C, with total run time of 300 s. The single column microGC was already calibrated for H₂, O₂, CO₂, CO, and CH₄.

Equations (2.4), (2.5), and (2.6) apply to the analysis of the thermal catalytic results.

All gas bottles (H₂, CO₂, Ar) used in the thermal and plasma-assisted catalytic tests were provided by Air Liquide.

Chapter 3: A factorial design study of the morphology of cerium oxide supports and the impact on Ni catalysts physicochemical properties

3.1.	<i>Introduction</i>	67
3.2.	<i>DOE methodology</i>	67
3.3.	<i>Results and discussion</i>	68
3.3.1.	<i>Physicochemical characterisation of the cerium oxide supports</i>	68
3.3.2.	Study of the effect of synthesis parameters on the physicochemical properties	72
3.3.3.	Oxygen storage capacity and surface planes	75
3.3.4.	Impact of the introduction of Ni on the CeO ₂ supports on the size, textural, morphology and surface properties	83
3.3.5.	Reducibility and basicity of the Ni/CeO ₂ catalysts obtained from the DOE supports	94
3.4.	<i>Conclusions</i>	98

3.1. Introduction

In this chapter, the results of the physicochemical characterization of all materials used for plasma-assisted catalysis tests is presented. The focus of the synthesis and of the experimental work is on CeO₂-supported catalysts with 15 %wt. of nickel as active phase having different morphologies at the nanoscale. The synthesis technique and characterization methods were described in the previous chapter. The influence of the synthesis parameters on the physicochemical properties of the supports is thoroughly studied via factorial analysis. Additionally, an in-depth analysis regarding surface structure, OV formation and OSC property is presented for four selected catalysts that differ mostly one from the other regarding particle shape and size (namely the materials called DOE0, 3, 5, and 6). The variation of the cerium oxide supports after Ni impregnation and further thermal treatments (calcination and reduction) is assessed and the physicochemical characterisation of the catalysts is carried out regarding particle size, basicity and reducibility properties to fully characterise the materials before putting them in contact with plasma.

3.2. DOE methodology

A full factorial design of experiments was designed with three factors, two levels for the systematic variation of the hydrothermal synthesis parameters. All the selected factors are numeric and continuous and for each one the low and high levels were specified as found from a literature study [129,132]. One centre point was added to have enough degrees of freedom. The $2^3 + 1$ runs were randomised and each one repeated three times, with two identical 48 mL autoclaves and once with

the large 0.5 L autoclave, which created three blocks in the design. The factors and levels are summarised in Table 3.1. The response of the model was chosen to be the result of the XRD characterisation of the samples, as it is a rapid analysis method that gives quantitative and discrete results (such as the full width half maximum of the peaks or the calculated crystallite size).

Regarding the analysis of the factorial design, all the terms up to 3rd order were included without the addition of weights nor covariates. A 95% confidence level was chosen in this study which means that the term is significant if the p-value is less than or equal to 0.05 [142]. The p-value is a quantification of the statistical significance that is calculated from the probability of observing a set of results if the null hypothesis were true (i.e., no statistical relationship and significance exists in a set of observed variables). The confidence interval, meaning the range of values that you expect your estimate to fall between, is selected as two-sided, which requires the bracketing from above and below of 0.05/2. The results of this analysis are p-values and standardized effects, the absolute values of the latter are depicted in a Pareto chart. The standardized effects of each factor are calculated from the t-statistics that test the null hypothesis, the magnitude gives a quantification of the statistical significance according to the model and the positive or negative sign signifies the increase or decrease of the response according to the increment of the relative factor. The residual plot was also included to examine the goodness of the fit and of the repetitions. The residuals are the difference between the observed and the predicted values and they are plotted in a histogram to determine anomalies in the data and eventual outliers. A linear model described by a regression equation averaged over the blocks was built to describe the relation between synthesis parameters and the preferred response.

The model with only one block was tested also with other physicochemical properties, which were measured only for one of the repetitions in the large autoclave.

3.3. Results and discussion

3.3.1. Physicochemical characterisation of the cerium oxide supports

The cerium oxide materials were synthesized via an alkaline hydrothermal method with a systematic variation of three factors namely NaOH concentration, time, and temperature of the thermal treatment. The results that will be shown here and in the next chapters concern the materials produce via the synthesis carried out with the larger 0.5 L autoclave. The nomenclature and relative synthesis parameters are recapped in Table 3.1.

The NaOH hydrothermal synthesis technique, despite being previously reported by several sources [129,130,143], was thoroughly examined regarding the repeatability and the removal of Na impurities from the CeO₂ materials obtained. Indeed, the solid recovered via filtration from the autoclave was washed several times also with MilliQ water. To make sure all the Na traces were removed, the washout water from each filtration from 1st to 5th were tested in ICP-OES. The amount of Na detected decreases from 286 mg/L to 0.9 mg/L, which is the same value measured for MilliQ

water. In all cases no Ce leaks during the filtration. The presence of Na in the ceria supports was also checked via SEM-EDX, in most cases no peaks attributable to Na were detected, at most a 0.6 %wt. of Na was calculated for the DOE6 sample that is synthesised with 15 M NaOH solution at the harshest conditions of the DOE series. It can be concluded that the performed protocol avoids any Na impurities to penetrate in the CeO₂ supports. To check the repeatability of the hydrothermal synthesis performed, the synthesis of the DOE0 sample was repeated 7 times: 6 times in the large autoclave and once in the small one. The samples were all characterized via XRD, and these results were used to calculate the standard deviation of the crystallite size and lattice parameters that are measured with this technique, which is 0.3 nm and 0.003 Å, respectively. The morphology observed in SEM for these seven repetitions was also the same needle-like shape (as in Figure 3.3a). This validates that the synthesis is repeatable and reliable.

Table 3.1: Overview of the synthesis parameters and physicochemical properties of the CeO₂ supports of the DOE series.

Sample	Synthesis parameters			XRD		N ₂ adsorption		
	[NaOH], M	T, °C	Time, h	Crystallite size, nm	Lattice parameter, Å	S _{BET} , m ² /g	W _P , nm	V _P , cm ³ /g
DOE0	8	125	14.5	4.6	5.431	78	12.1	0.34
DOE1	1	70	24	2.7	5.435	127	9.4	0.32
DOE2	15	180	5	11.3 (41.6)	5.437 (5.414)	39	6.1	0.12
DOE3	1	180	24	12.7	5.416	84	6.1	0.25
DOE4	15	70	24	3.8	5.437	112	11.7	0.38
DOE5	1	70	5	2.5	5.427	155	6.6	0.30
DOE6	15	180	24	15.1 (43.0)	5.437 (5.411)	7	6.1	0.03
DOE7	1	180	5	3.5 (10.1)	5.441 (5.418)	117	12.1	0.36
DOE8	15	70	5	3.2 (15.8)	5.434 (5.425)	104	11.7	0.27

The physicochemical properties of the CeO₂ supports analysed by XRD and N₂ physisorption vary with the synthesis parameters (Table 3.1). The diffractograms confirm that the materials are composed of Fm-3m cerianite phase with the presence of peaks relative to hkl planes (111), (200), (220), (311), (222), (400), (331), (420), and (422) (ICSD CeO₂ 88759) (Figure 3.1). The intensity and width of the listed peaks are different for each sample, the first increases with harsher synthesis conditions while the latter decreases. The diffractograms of samples DOE2, 6, 7, and 8 reveal a double distribution, a very narrow and intense one overlapped with wider peaks of lower intensity,

meaning that these materials contain two different cerium oxide phases. The Rietveld analysis of the diffractograms allows to have more information about the crystalline structure of the CeO_2 materials, giving the crystallite size and lattice parameter of the fluorite structure (Table 3.1). This analysis reveals that the main phase of all the DOE supports is characterized by a strained lattice parameter ranging from 5.416 to 5.441 Å, larger than the stoichiometric one (5.411 Å). This is usually linked with a lower nanoparticle size, increasing amounts of Ce^{3+} at the surface and therefore oxygen vacancies [144]. The two cerianite phases of the aforementioned samples DOE2, 6, 7, 8 have different lattice parameters and crystallite sizes: one is stoichiometric CeO_2 phase with large crystallite size (in brackets in Table 3.1), while the other one is in line with the other DOE samples with larger lattice parameter compared to the stoichiometric phase and smaller crystallite size.

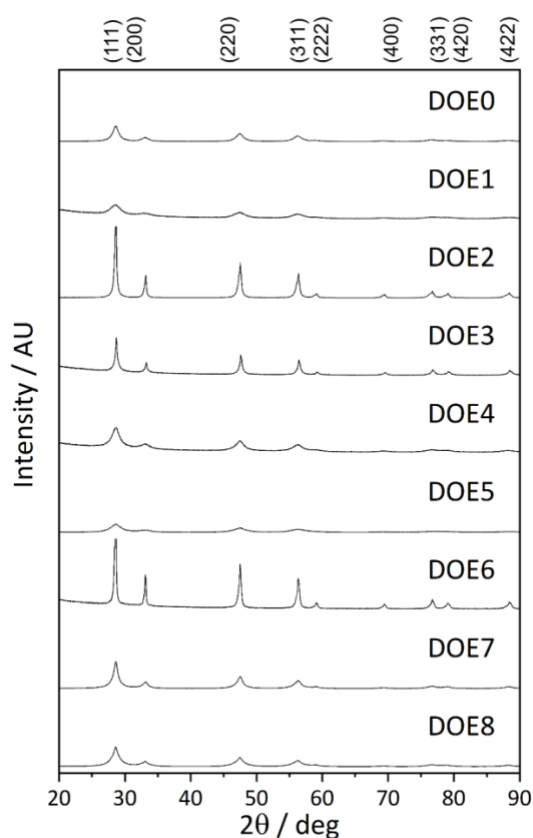


Figure 3.1: XRD diffractograms of the CeO_2 supports of the DOE series. The (hkl) planes peaks are indexed on the top.

The isotherms and pore size distribution of the supports obtained from N_2 physisorption are reported in Figure 3.2. All the samples exhibit type IVa isotherms with H3 hysteresis loops related to the samples having different meso- and microporosity linked with interstitial voids among particles. Only the sample DOE6 shows a type II with poorly developed mesoporosity. The pore size

distributions obtained from DFT analysis are related to the mesoporosity in the samples and for DOE2 and 6 reflect the low porosity shown by the isotherms. The other samples present either a wide pore size distribution such as for DOE0, 3, 4, and 7 or a narrow one as is the case of DOE1, 5, and 8. The modal pore width (W_p) of the of these last samples ranges from 6.6 to 11.7 nm. The surface area in Table 3.1 follows the expected trend and is inversely proportional to crystallite size. The sample that has the smallest crystallite size of 2.5 nm (DOE5) has the largest specific surface area calculated by BET S_{BET} (155 m²/g), and vice versa DOE6 with 15.1 and 43 nm crystallite sizes has a very low surface area of 7 m²/g with very poorly developed mesoporosity (type II isotherm). DOE6 has also very small total pore volume of 0.03 cc/g. The V_p , which takes into account micro-, meso-, and macroporosity, the latter linked with interstitial voids among particles depending on the morphology and clustering of the nanostructures, of the other samples ranges from 0.1 to 0.4 cc/g.

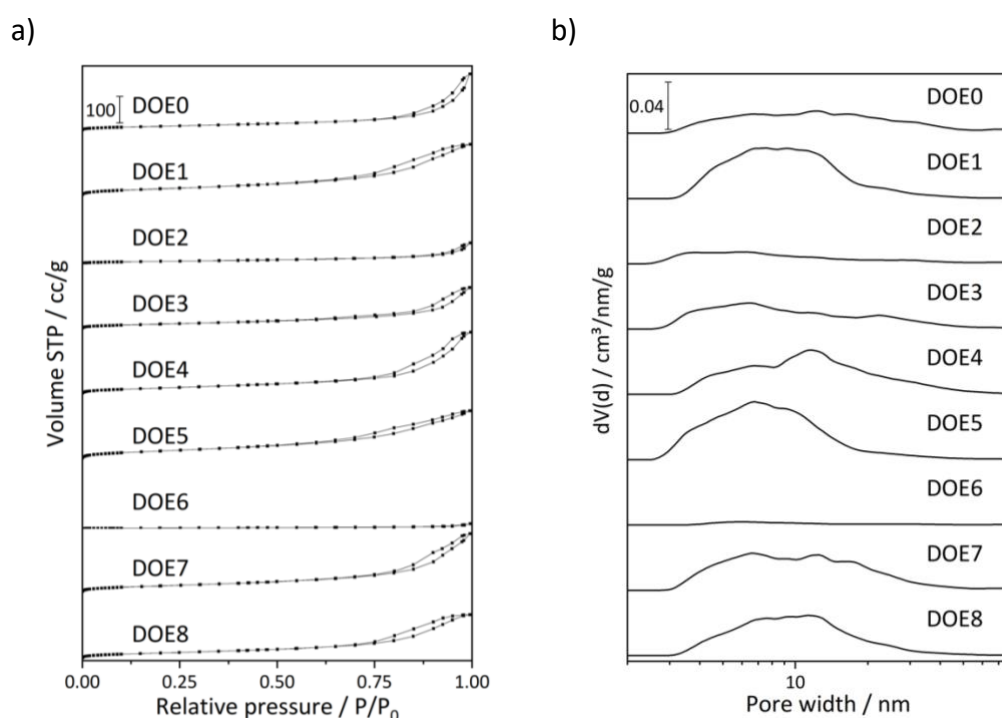


Figure 3.2: a) N₂ Isotherm and b) pore size distribution plots of the DOE supports.

The variation of physicochemical properties is reflected and linked with the morphology that is revealed by SEM images collected in Figure 3.3a-i. The micrographs are taken at the same magnification of x25000. The samples having the largest crystallite size (DOE2 and 6) show big rod-like particles with micrometric length and cubes of at least 100 nm size. DOE0 and DOE3 result in one specific morphology, needles and cubes, respectively. While it is not possible to identify the morphology from the SEM images of the ceria with small crystallite size (DOE1, 4, 5, 7, 8), as the particles are too fine and agglomerated to be distinguished with this instrumentation.

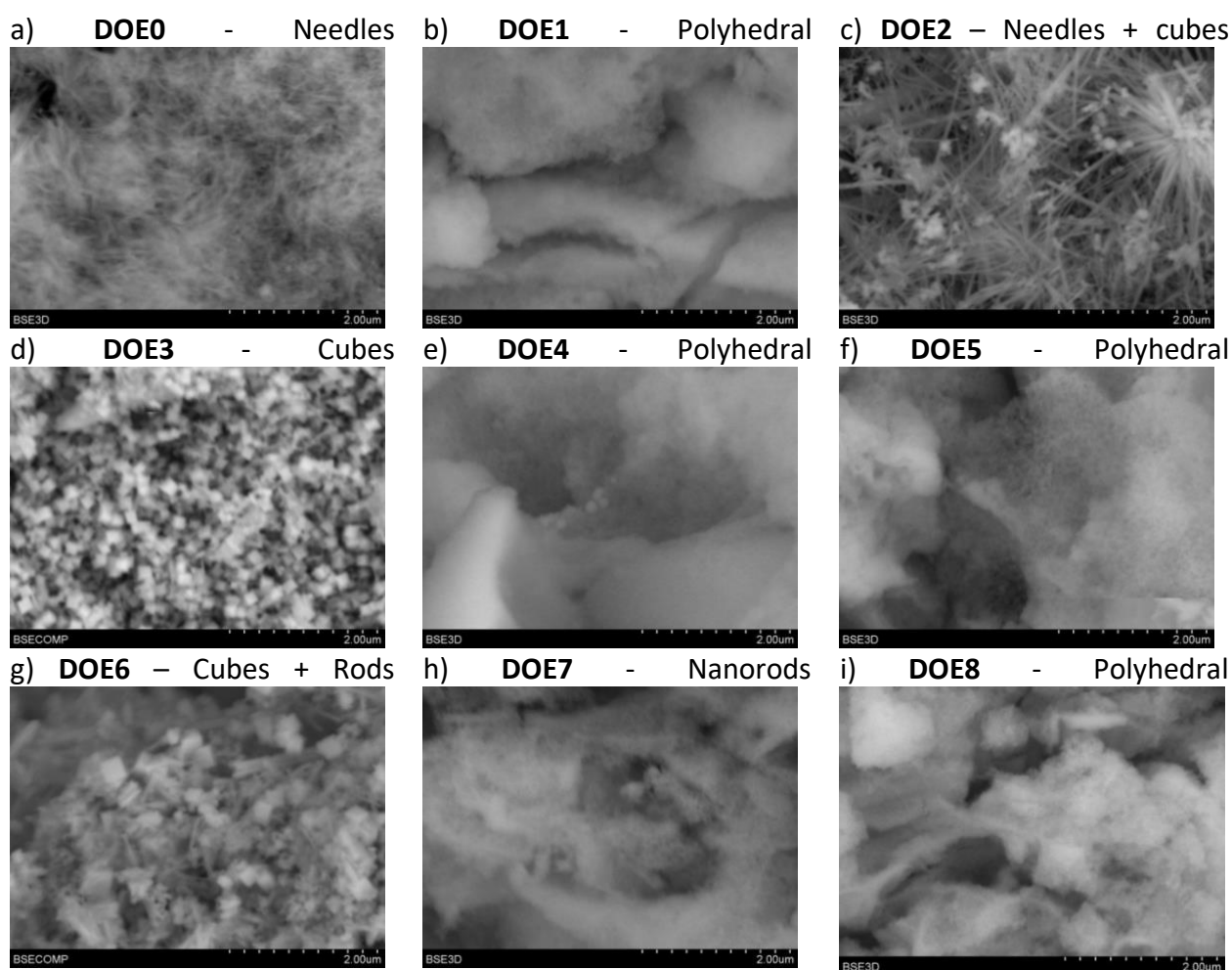


Figure 3.3: SEM images of nanoparticulate ceria a)-i) DOE0-8. The relative observed morphology is annotated above each image.

3.3.2. Study of the effect of synthesis parameters on the physicochemical properties

From the results previously described it can be already concluded that with larger NaOH concentration, temperature, and time we obtain larger structures. For instance, DOE6 synthesized with a NaOH concentration of 15 M is characterized by a large crystallite size linked to small surface area and big rod-like particles while DOE5 synthesized with a NaOH concentration of 1 M is

characterized by small crystallite and particle sizes linked to higher surface area. However, to systematically evaluate the effect of hydrothermal synthesis factors on the CeO₂ morphology obtained, 2³ full factorial DOE analysis was carried out. The synthesis was repeated for each sample three times, twice with a small 48 mL autoclave and once with a larger 0.5 L autoclave, creating three blocks in the DOE. The crystallite size of the non-stoichiometric phase of ceria was selected as the response of the model as this phase is common among all samples and its crystallite size sufficiently varies according to the synthesis parameters and generally agrees with the morphology observed in SEM, which as a non-numerical but categorical response is harder to use in such model. A linear model was built to determine how this property is affected by the three terms temperature, time and NaOH concentration ([NaOH]) as well as 2-Way interactions [NaOH]*Temperature, [NaOH]*Time, and Time*Temperature, and 3-Way interaction [NaOH]*Temperature*Time. The 2- and 3-way interaction terms describe the interaction between the independent variables (factors) on the response and identify a possible dependency on each other. The individual effect of each term was studied and reported in the Pareto chart in Figure 3.4a and the p-values that judge their statistical significance are shown in Table 3.2.

Table 3.2: p-values of the linear model coefficients of the factorial design.

Term	p-value
Model	<0.001
Curvature	0.107
Blocks	0.123
Time	0.001
[NaOH]	<0.001
Temperature	<0.001
[NaOH]*Temperature	<0.001
[NaOH]*Time	0.851
Time*Temperature	0.004
[NaOH]*Temperature*Time	0.905

The linear fitting has an R² value of 93.69 % and a p-value below 0.001. Moreover, the p-value of curvature is higher than 0.05 (0.107), which can be interpreted as all the factors (time, temperature, and [NaOH]) having a linear relationship with the response. This information validates the built linear model as a good description of the relationship between synthesis parameters and cerium oxide crystallite size. The blocks have a high p-value of 0.123, which makes the synthesis repetitions

and use of different autoclaves not statistically significant for the crystallite size of the material that is the outcome of each synthesis.

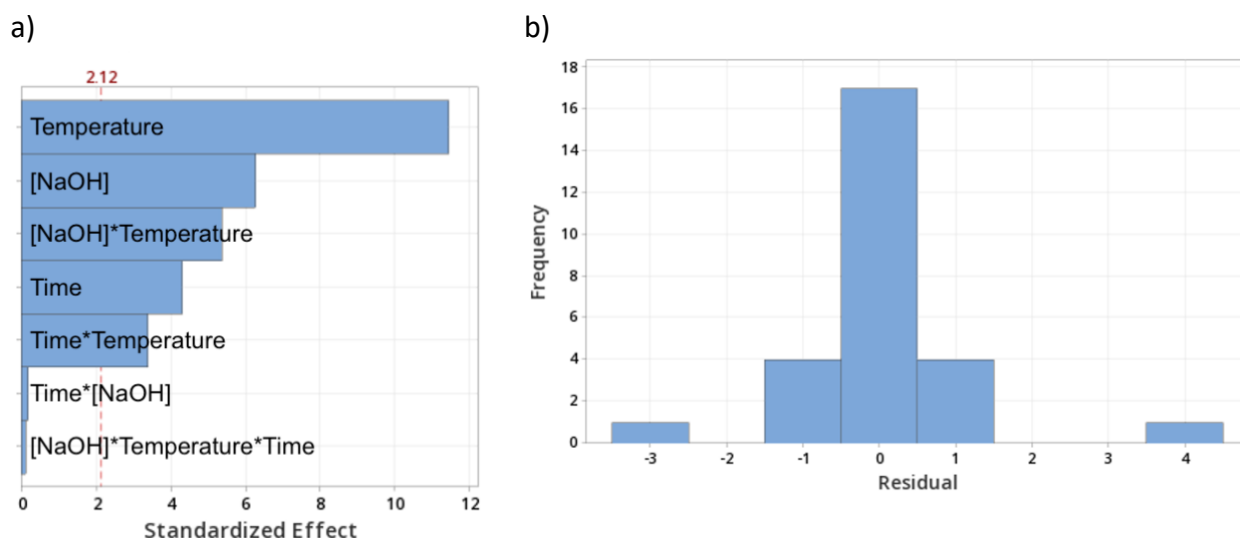


Figure 3.4: a) Pareto chart of the standardized effect and b) residual frequency histogram of the factorial DOE analysis with the crystallite size as response.

The Pareto chart in Figure 3.4a shows the absolute value of the standardized effects of each term. The standardized effects quantify the impact of each factor on the response, therefore the higher value it has, the more relevant that factor is. The standardized effects Pareto chart is also a clearer quantification of the importance of each term, as it is not possible with Minitab to evaluate the p-value below 0.001 (Table 3.2), so it does not give a clear ranking of the most statistically relevant factors. A reference line in this plot that marks the equivalent of p-value = 0.05, which is the boundary between statistical significance/insignificance. All the statistically significant terms have positive standardized effects, meaning that the increase of the factors lead to the growth of the crystallite size. The most relevant factor that determines the crystallite size is the temperature with largest standardized effect, followed by NaOH concentration. The term that combines these two, [NaOH]*Temperature, is the third most relevant factor on the synthesis, meaning that the crystallite size is affected by the variation of both simultaneously. According to this analysis, the time the autoclave stays in the oven is statistically relevant for the outcome of the ceria synthesis (p-value $0.001 < 0.05$) but has a lower impact compared to [NaOH] and temperature. In this sense, a visual comparison of the micrographs of DOE1 and 5 (1 M, 70°C, 24 and 5 h, in Figure 3.3b and f, respectively), or DOE2 and 6 (15 M, 180°C, 5 and 24 h, in Figure 3.3c and g, respectively), results in similar morphologies despite the different duration of the hydrothermal treatment. The Two-way term Time*[NaOH] and the Three-way term [NaOH]*Temperature*Time are not relevant and in fact have a p-values much greater than 0.05.

The residuals histogram (Figure 3.4b) shows a narrow distribution around 0 with two outliers, which means that generally the values adjust very well to the prediction made by the model. The larger residuals around -3 and +4 actually correspond to very specific runs which could link these unusual observations to an experimental error made during those syntheses.

It should be mentioned that the result of the DOE factorial analysis using the crystallite size of the cerianite non-stoichiometric phase calculated via Rietveld analysis as response is in agreement with the analysis carried out selecting as the full width half maximum of the (111) peak of the diffractograms of the samples produced by each synthesis run. In conclusion, the effect of the factors on the outcome of the hydrothermal synthesis can be ranked as Temperature>[NaOH]>Time.

The factorial analysis and quantification of the effect of each synthesis parameter on the materials suggests a possible synthesis mechanism. The cerium oxide particle formation and growth process seems to be thermodynamically controlled and not kinetically since the time that the synthesis reaction is allowed to run (5 to 24 h) is the least relevant factor in the time frame studied, while the temperature ranging from 70 °C to 180 °C is the most significant from the statistical study. It has been reported that the cerium oxide particles are formed during the hydrothermal treatment via nucleation-dissolution-recrystallization mechanism [129]. This method allows the synthesis directly of precipitated CeO₂ without a calcination step and morphology selection without the use of a template. The cerium III salt hydrolysed in the base solution forms Ce(OH)₃ nuclei, which have been reported to have anisotropic structure [129]. As shown by the factorial analysis, with higher treatment temperature and base concentration the crystallization is promoted, and larger structures are formed [143]. The intermediate temperature and NaOH molarity (125°C and 8 M) allows the formation of anisotropic structures as needles starting from anisotropic growth of Ce(OH)₃ nanocrystals. With low base concentration and temperature, the dissolution-recrystallization rate is slow and the CeO₂ nanocrystals do not grow much compared to the nuclei [129]. As shown by TEM analysis of the DOE5 that will be presented in the next section, this sample has actually nanorod morphology with very small particle size of a few tens of nanometres, which suggests the shape of the nuclei that are the precursor of the ceria structures.

3.3.3. Oxygen storage capacity and surface planes

The two samples synthesized at the extreme conditions, resulting the smallest and largest ceria structures, DOE5 and DOE6, respectively, were selected together with DOE0 and DOE3, which were synthesised at intermediate conditions, to carry out a more in-depth study of characterization of the morphology and surface structure. The goal is to understand the effect of the different synthesis conditions on the shape, surface crystallinity, and OSC properties of the samples that are interesting for the application of ceria nanomaterials in catalysis.

The bright-field TEM (BF-TEM) images of DOE0, DOE3, DOE5 and DOE6 samples are shown in Figure 3.5. The morphologies observed in SEM are mostly confirmed (annotated in Figure 3.3), except for DOE5 sample, for which TEM analysis allowed to identify the nanorod morphology with length 32 ± 17 nm and width 6 ± 2 nm and moreover confirms particles agglomeration. The inset shows a high-magnification image of a rod. DOE0 consists of CeO₂ nanoneedles with an average length of 188 ± 163 nm and width of 15 ± 4 nm. DOE3 mostly consists of nanocubes of average size 12 ± 5 nm shape but two different-sized spheres are also present (of size 21 ± 4 nm and 8 ± 2 nm) respectively. DOE6 morphology is confirmed to be a mixture of rod- and cube-like structures with much larger sizes compared to the previous samples, this sample is actually composed of micrometric structures. The average length and width of the rods is 1847 ± 1081 nm and 278 ± 199 nm, respectively, whereas the average side length of the cube is 154 ± 68 nm.

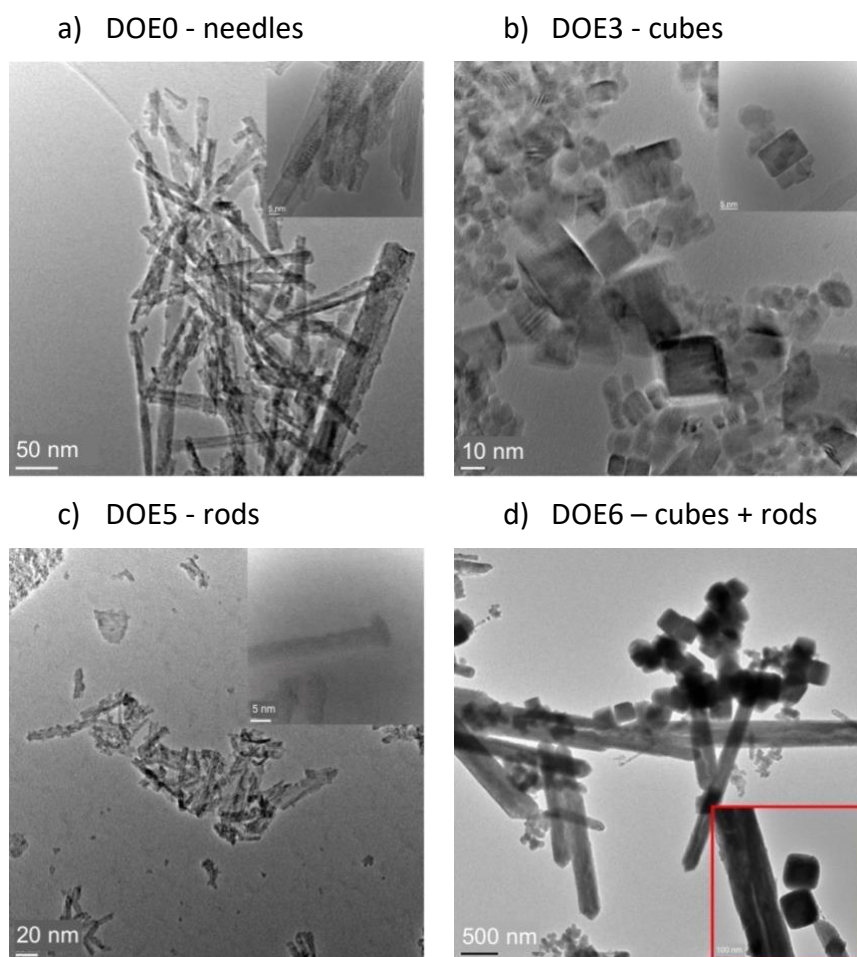


Figure 3.5: BF-TEM images of DOE0, 3, 5, 6 supports.

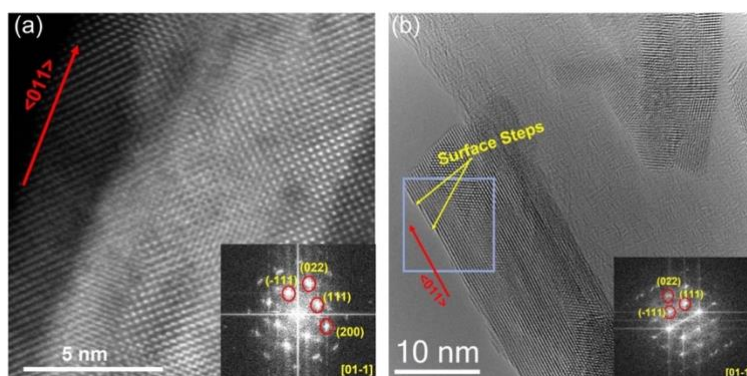


Figure 3.6: a) HRSTEM image of a single needle with FFT shown in the inset b) HRTEM image of a single needle showing formation of surface steps, the inset shows the FFT pattern taken from blue square region.

Figure 3.6 shows the HRSTEM and HRTEM images of a single nanoneedle of DOE0 sample. The corresponding fast Fourier transform (FFT) pattern indicates Fm-3m structure of CeO_2 consisting of (011), (200) and (022) planes. The nanoneedles are observed to grow along $\langle 011 \rangle$ direction (indicated by red arrow in Figure 3.6). The HRTEM image (Figure 3.6b) shows that the side facets of the nanorod contains atomic steps and kinks as indicated by the yellow arrow.

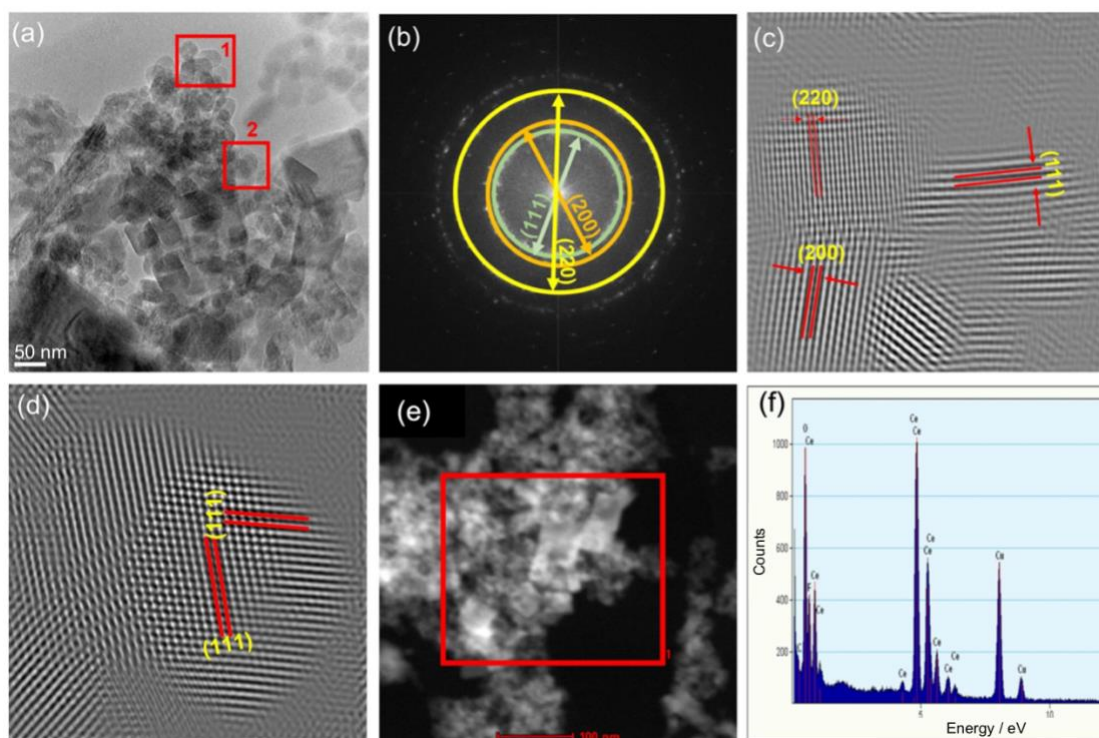


Figure 3.7: a) BF-TEM image of DOE3. b) SAED pattern taken from a). c) and d) IFFT of region 1 and 2 in a), respectively, that corresponds to spherical particles. d) HAADF-STEM image of DOE3. e) EDS spectrum of the region marked in d).

Figure 3.7a shows BF-TEM images and Figure 3.7b the relative SAED (selected area electron diffraction) pattern that shows presence of (111), (200) and (220) planes of CeO_2 . This is confirmed by the EDX spectrum in Figure 3.7f that clearly shows presence of Ce and O, and no contamination was observed, indicating the samples are pure CeO_2 . The inverse FFT (IFFT) patterns of regions 1 and 2 in Figure 3.7c and d, corresponding to spheres and cubes, respectively, show that the surface plane of the spheres consists of $\langle 110 \rangle$, $\langle 100 \rangle$ and $\langle 200 \rangle$ and that the side facets of the cubes grow along $\langle 100 \rangle$ plane, with two planes connected by a $\langle 111 \rangle$ plane along the corner.

Figure 3.8b shows diffraction pattern taken from the DOE5 nanorods captured in Figure 3.8a. The pattern shows diffraction spots corresponds to (111), (200), (220) and (311) planes of $\text{Fm}\bar{3}\text{m}$ CeO_2 . The diffraction spots correspond to polycrystalline nature of the sample and contains many defects indicated by the streaking to the diffraction spots. The HRTEM images (Figure 3.8c and d) of a single nanorod shows that the nanorod grows along $\langle 011 \rangle$ direction and the top surfaces are bounded by $\langle 311 \rangle$ and $\langle 3\bar{1}\bar{1} \rangle$ facets.

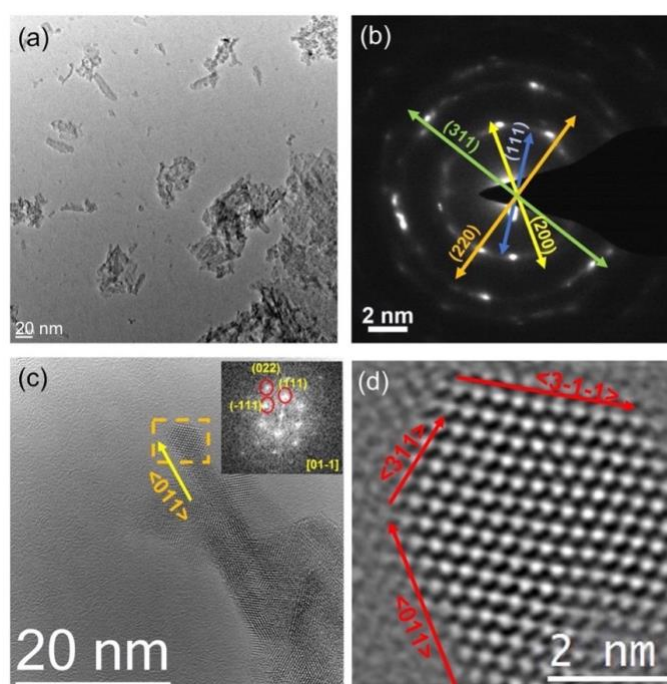


Figure 3.8: a) BF-TEM image and b) SAED pattern of DOE5 sample. c) HRTEM image of a single nanorod with the inset showing the FFT pattern and d) HRTEM image of the tip of the nanorod marked in c).

Figure 3.9a and b show the HRTEM images from the rod and cube, respectively. The rods and cubes are also observed to be much thicker compared to the previous samples, as expected by their larger size, which is observed from the dark contrast in the BF-TEM image (Figure 3.5d) showing the different planes of CeO_2 present in these two systems. In fact, the FFT pattern of the DOE6 rods had to be taken from thinner portion of the structure (marked by the red square in Figure 3.9a). The FFT patterns reveal the (111), (311), (200) and (111), (002), (220) planes for the rod and cube,

respectively. It was not possible to determine the exact plane exposed on the surface of these structures due to the large size of these ceria particles in DOE6 and to the roughness of their surface.

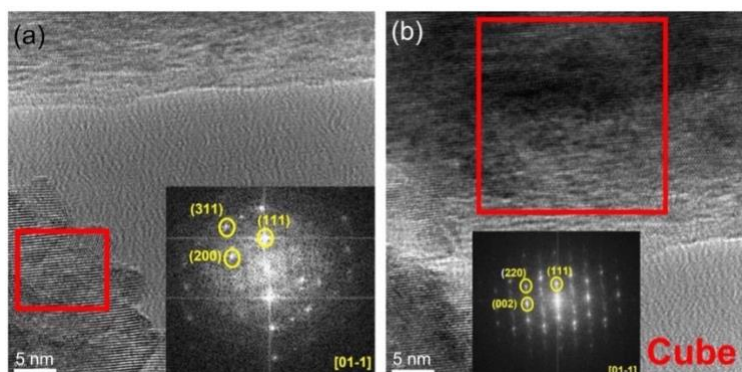


Figure 3.9: HRTEM images of the a) rod and b) cube structures in the DOE6 sample. The insets show the FFT patterns of the regions marked by the red squares.

The surface planes observed via TEM analysis for each sample are summarised in Table 3.3. Both anisotropic structures in DOE0 and DOE5 grow along $\langle 011 \rangle$ direction while the cubes in DOE3 grow along $\langle 100 \rangle$. $\langle 111 \rangle$ is known to be the most stable facet for CeO_2 [7], meaning the least active and reducible, but it is not common in the samples presented here. $\langle 100 \rangle$ has a medium surface energy, therefore the energy for its reduction and OV formation is also intermediate [46]. $\langle 011 \rangle$ is a high-energy surface that requires the low energy for VO formation [48].

Table 3.3: OSC study and surface characterisation of selected nanostructured support samples.

	TEM	TGA	XPS		Raman
	Surface facet	Oxygen storage, $\mu\text{mol/g}$ $\pm 26 \mu\text{mol/g}$	$\text{Ce}^{3+}/(\text{Ce}^{4+} + \text{Ce}^{3+})$, % $\pm 0.2 \%$	$\text{O}_{\text{surf}}/(\text{O}_{\text{lat}} + \text{O}_{\text{surf}})$, % $\pm 0.2 \%$	$I_{\text{D}}/I_{\text{F2g}}$ ± 0.006
DOE0	$\langle 011 \rangle$	201	21.3	36.5	0.041
DOE3	$\langle 100 \rangle$	114	20.0	24.8	0.032
DOE5	$\langle 011 \rangle$	247	23.6	39.6	0.052
DOE6		147	20.3	35.7	0.026

The OSC and presence of OV of the synthesized cerium oxide supports DOE0, 3, 5, and 6 was assessed via TGA, XPS, and Raman spectroscopy, and the results are summarised in Table 3.3. The facile and reversible modification from the stoichiometric CeO_2 structure to a non-stoichiometric one $\text{CeO}_{2-\delta}$ (with $0 < \delta < 0.5$) provides cerium oxide with high OSC [145]. This mechanism has been

linked to the fast change of oxidation state of the cerium ions (Ce^{4+} and Ce^{3+}) inside the crystalline structure and OV formation. This is an interesting feature of CeO_2 as a catalyst support for heterogeneous reactions involving oxygen [145]. The reducibility of ceria materials depends on their surface structure and on the exposed facet, as described earlier and examined via TEM.

The oxygen release and storage during reduction-oxidation cycles at 500 °C has been examined by TGA and as an example the results of DOE0 sample are reported in Figure 3.10 [145,146]. Once the surface of the ceria has been cleaned by the pre-treatment step, the weight loss and gain during these subsequent steps is linked with oxygen release in reductive atmosphere and accumulation in the lattice surface in oxygen rich atmosphere, respectively. The mass of the ceria sample decreases during the reduction (orange area in Figure 3.10) and returns to a value similar to the starting weight after the oxidation step (blue area in Figure 3.10). It is observed that the first reduction step at 500 °C results in the largest weight loss out of the three repetitions, probably due to surface modifications that are not entirely reversible. The average amount over 3 reduction/oxidation cycles is reported as oxygen storage in Table 3.3 ($\pm 26 \mu\text{mol/g}$). DOE5 is confirmed to have the highest OSC ($247 \mu\text{mol/g}$) among these samples, followed by DOE0, DOE6 and DOE3, the latest having the lowest oxygen release/storage amount with $114 \mu\text{mol/g}$.

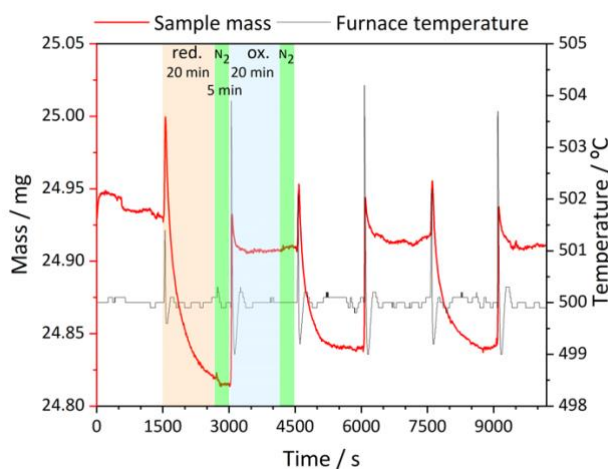


Figure 3.10: Mass variation and temperature ramp during the TGA reduction-oxidation cycles with DOE0 CeO_2 sample.

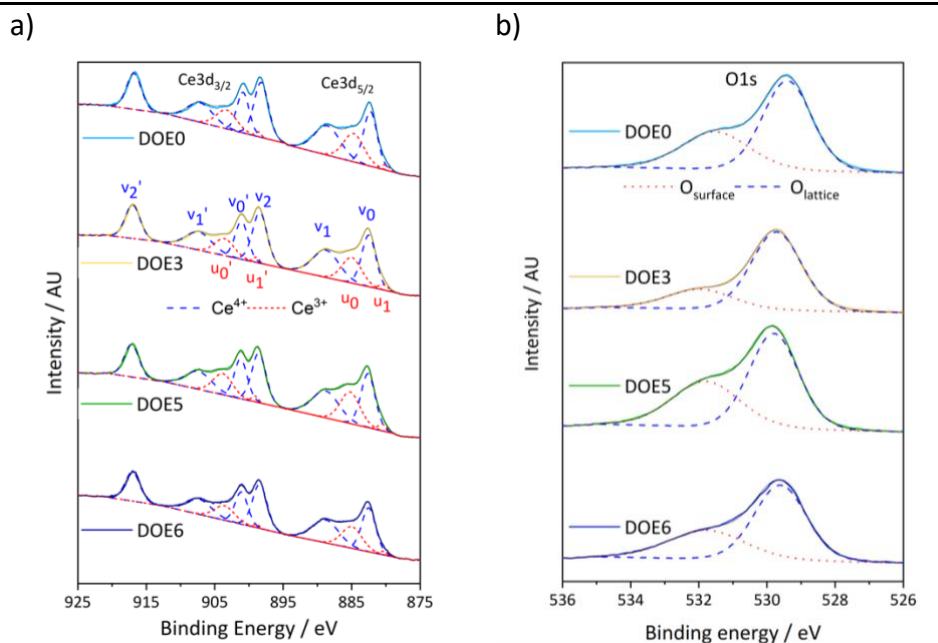


Figure 3.11: XPS spectra of DOE supports in the a) Ce3d b) O1s regions.

The XPS analysis was focused on the Ce3d and O1s regions. Ce3d has two well separated (18.6 eV) spin-orbit components $Ce3d_{5/2}$ and $Ce3d_{3/2}$, that are in turn split into multiplets. The peaks contribute to either the 3+ or the 4+ oxidation state as shown in Figure 3.11a where u_0 , u'_0 , u_1 , u'_1 are characteristic of Ce^{3+} and v_0 , v'_0 , v_1 , v'_1 , v_2 , v'_2 of Ce^{4+} . The surface analysis via XPS showed an increasing amount of Ce^{3+} (in Table 3.3) with lower crystallite size (in Table 3.1). Smaller particles (DOE5) accumulate defects on the surface and allow the spontaneous formation of oxygen vacancies, which leave Ce^{3+} instead of Ce^{4+} [144]. DOE0, which is composed of nano-needle structures displaying an important number of defects (atomic steps and kinks in Figure 3.6b), shows as well interesting values of OSC and Ce^{3+} amount.

The O1s region of the XPS spectra in Figure 3.11b reveals two peaks for all samples: one that is the dominant one around 529.3-528.7 eV for the lattice oxygen $O_{lattice}$ (known also as O_α) and a shoulder at higher binding energy (above 530.9 eV) for surface species $O_{surface}$ (or O_β), meaning adsorbed molecules and O linked with defective Ce^{3+} sites. The different ratios between $O_{surface}$ and $O_{lattice}$ should be linked with the lattice facet that is exposed on the surface of the ceria particle, each characterized by specific Ce/O ratios, therefore exposed oxygen atoms [46,47,147]. Furthermore, it has been reported that $O_{surface}$ is linked with OV on the cerium oxide surface, therefore a higher $O_{surface}/(O_{lattice}+O_{surface})$ ratio points to a larger amount of OV, as OV adsorbs and activates oxygen molecules to produce adsorbed oxygen species [148]. The $O_{surface}/(O_{lattice}+O_{surface})$ ratio reported is in agreement with the Ce^{3+} quantification (in Table 3.3). DOE3, which presents nanocubes structures surrounded by $\langle 100 \rangle$ planes characterised by alternate cation and anion layers ending with exposed Ce atoms [149], presents decreased $O_{surface}$ amounts and the lowest concentration of OV, which is linked with its poor OSC shown by the TGA experiment. On the other hand, DOE0 and 5 samples

expose <011> facets, that provide reactive and reducible surfaces resulting in enhanced formation of oxygen vacancies and improved OSC [46,47].

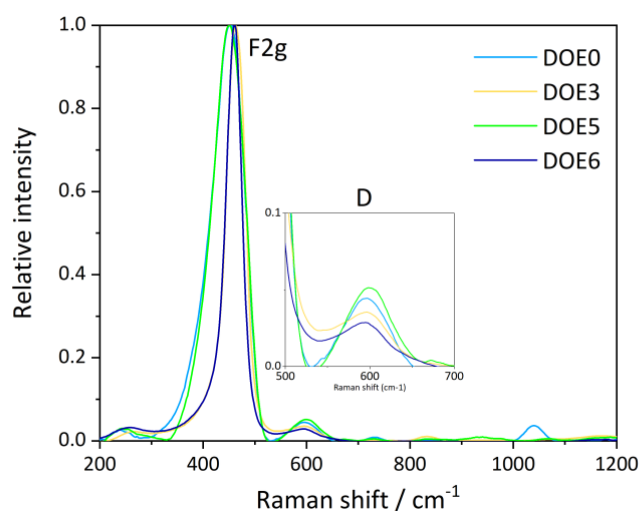


Figure 3.12: Raman spectra for DOE0, 3, 5, 6 supports.

The Raman spectra in Figure 3.12 reveal 4 different peaks. The most intense is F2g Raman active mode at 454.6 cm^{-1} , corresponding to the symmetric stretch mode of Ce-O of fluorite structure, at 597.5 cm^{-1} the D longitudinal optical mode assigned to defects, and then two less intense peaks that are the second order transverse optical mode and the second longitudinal optical mode [61,130,150,151]. The F2g peak broadens for DOE0, 3, and 5, which has been associated with smaller the crystallite size, inhomogeneous strain broadening, and higher concentration of oxygen vacancies [130,150]. The ratio between the intensities I_D and I_{F2g} gives a quantification of the defects for each sample [61], and it is related to the highest amount of oxygen vacancies present in the cerium oxide supports (Table 3.3). This result is in partially agreement with the XPS analysis, according to the quantification provided by the Raman results the OV amount follows the order $\text{DOE5} > \text{DOE0} > \text{DOE3} > \text{DOE6}$. Whereas the trend for the OSC calculated by TGA and of OV concentration by XPS changes the order of the last two: $\text{DOE5} > \text{DOE0} > \text{DOE6} > \text{DOE3}$. It should be noted that the values of I_D/I_{F2g} calculated for DOE 3 and 6 (0.032 and 0.026, respectively) fall within the experimental error range. Nonetheless, the large size of the structures of DOE6 do no facilitate the formation of defects on the surface, moreover the low surface area and low OV concentration hinder the OSC property.

The DOE0 and 5 samples having in general an improved OSC and higher concentration of OV on their surfaces compared to DOE3 structures agrees with the surface plane observed from the HRTEM images and IFFT patterns, as the surface energy of the facets is expected to be (100)<(011), therefore (011) being less stable and more prone to oxygen release [46]. These results point ceria

nanorods and nanoneedles structures as potential materials for supports of catalyst for CO₂ methanation in terms of OSC.

3.3.4. Impact of the introduction of Ni on the CeO₂ supports on the size, textural, morphology and surface properties

The catalyst obtained from the Ni wet impregnation of the ceria DOE series supports, that have been just discussed in the previous sections, were characterized by means of XRD and N₂ physisorption in order to assess the variation of physicochemical properties after Ni impregnation on the ceria supports having different morphologies. The morphology and state of the surface of selected samples (Ni/DOE0, 3, 5, and 6) were checked via SEM, TEM, XPS and Raman spectroscopy.

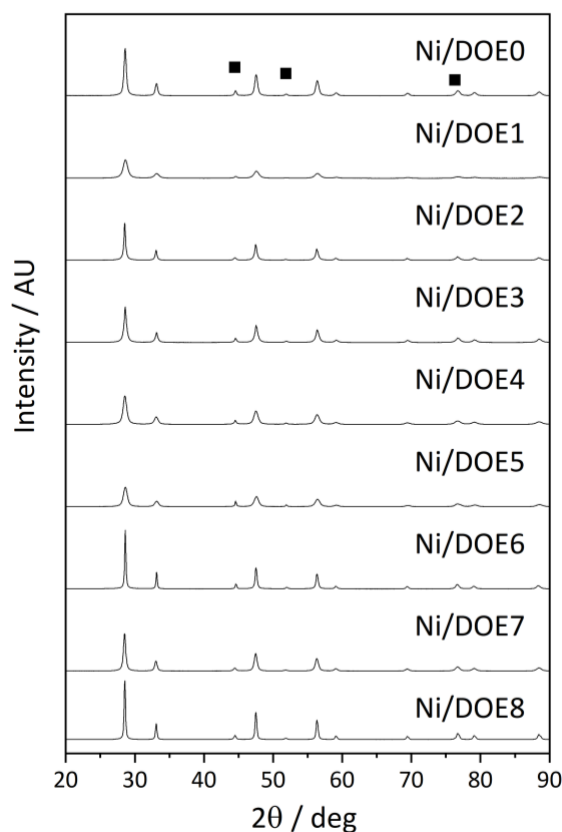


Figure 3.13: XRD diffraction patterns of the Ni/DOE catalysts. The squares indicate the Ni phase peaks.

The XRD diffractograms in Figure 3.13 clearly show peaks of the cerianite and metallic Ni Fm-3m phases (ICSD CeO₂ 88759 and Ni 260169). The respective crystallite sizes are reported in Table 3.4. The nickel phase has a Fm-3m spacegroup and lattice parameter 3.52 Å, the hkl planes (111), (200), (220) are observed. All samples, with the exception of Ni/DOE6, have underlying traces of amorphous Ni and NiO with size below 4 nm. The quantification via Rietveld analysis of the Ni phase ranges from 8 (Ni/DOE1) to 16 % (Ni/DOE5), which results in most cases lower than the expected

amount (15 %wt.). This is possible due to inaccuracies in the adjustments and estimations taken into account for the corrections of the Rietveld analysis. Furthermore, ICP-AES analysis confirmed the presence of Ni in the expected amount with 15 %wt. in Ni/DOE5 and Ni 14 %wt. in Ni/DOE0 and 6. The ceria phase crystallite size after Ni impregnation, calcination and reduction treatments increases compared to the support (Table 3.1) and its lattice parameter is comparable to the stoichiometric metal oxide 5.41 Å. The decrease of lattice parameter calculated for ceria after Ni incorporation could point to the formation of a $\text{CeO}_2\text{-Ni}^{2+}$ solid solution as the radius of Ni^{2+} is smaller than Ce ions and to a strong interaction between the Ni active phase and the CeO_2 support [152]. Moreover, the presence of two CeO_2 phases, one stoichiometric and one strained (which characterized the supports DOE2, 6, 7, 8), is not considered anymore with the exception of Ni/DOE2 and Ni/DOE6. These two samples reveal two cerianite phases with similar lattice parameters (5.42 Å), one of which can be considered amorphous ceria because of the small crystallite size of 4.1 and 1.7 nm, respectively, and that are not reported in Table 3.4. The larger lattice parameters calculated for both cerianite phases in Ni/DOE2 and 6 point to higher lattice strain and lower interaction between Ni and CeO_2 in this case.

The Ni crystallite size follows a general parabolic trend in function of the support size, leading to ceria crystallites of intermediate size to be linked with the lowest Ni crystallite size of 15-20 nm and improved dispersion.

Table 3.4: Physical properties of nanostructured Ni/ CeO_2 catalyst.

Sample	XRD		N ₂ adsorption		
	CeO ₂ Crystallite size, nm	Ni Crystallite size, nm	S _{BET} , m ² /g	W _P , nm	V _P , cm ³ /g
Ni/DOE0	17.5	17.8	44	7.0	0.21
Ni/DOE1	8.4	13.7	39	6.1	0.10
Ni/DOE2	22.7	16.0	23	23.6	0.12
Ni/DOE3	15.1	22.2	33	6.1	0.10
Ni/DOE4	11.0	21.2	51	11.7	0.19
Ni/DOE5	10.5	29.2	70	6.7	0.21
Ni/DOE6	35.6	30.0	8	7.0	0.05
Ni/DOE7	17.2	15.2	52	8.7	0.23
Ni/DOE8	35.8	22.4	16	29.0	0.12

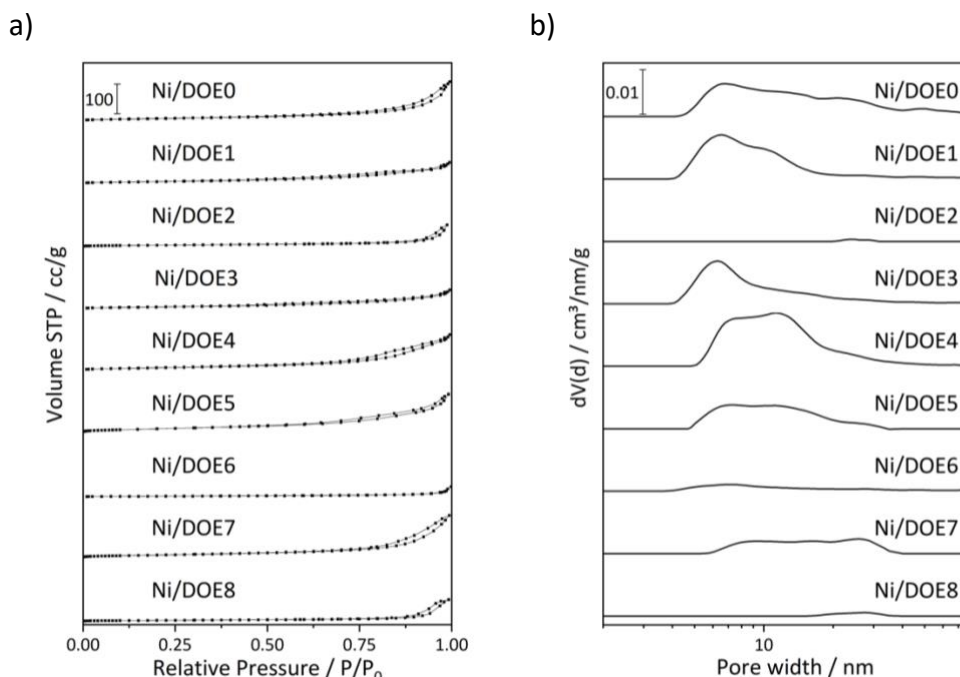


Figure 3.14: a) N_2 isotherm and b) pore size distribution plots of the Ni/DOE catalysts.

The analysis of the N_2 physisorption isotherms in Figure 3.14a results in measurements of the specific surface area and total pore volume, and from the pore size distribution in Figure 3.14b the modal pore size is extrapolated. These textural properties are reported in Table 3.4. Compared to supports, all samples, with the exception of Ni/DOE6, preserve a type IVa isotherm, whereas Ni/DOE6 does not show any hysteresis (type II), hence is almost non-porous. The values of S_{BET} and of N_2 adsorption capacity, meaning the pore volume V_p , decrease for all Ni/DOE catalysts compared to the previously obtained for the counterpart supports. The values of BET surface areas calculated from these isotherms point to considerable pore blockage occurring upon Ni incorporation and the calcination and reduction thermal treatments. The surface area changes linearly, generally decreasing by half, except for Ni/DOE6 and 8 which result in materials with the lowest S_{BET} (8 and 16 m^2/g , respectively). The expected relationship between CeO_2 crystallite size and S_{BET} is inversely proportional [153], in fact this is the general trend for the Ni/DOE catalysts except for Ni/DOE1, which has the lowest size but an intermediate surface area (39 m^2/g) as well as low pore volume and width, which could suggest that the Ni particles block the pores created between ceria structures. The largest surface area (70 m^2/g) is achieved by the catalyst named Ni/DOE5, whose support was characterised by the smallest structure with nanorod morphology. The largest total pore volume V_p , which considers the micro-, meso-, and interparticle macroporosity, is obtained with catalysts Ni/DOE0, 5, and 7.

A correlation between the synthesis parameters of the DOE and the properties of the catalysts has been investigated by factorial analysis, similarly to what was done for the supports. The DOE factorial analysis was carried out for one block using Ni crystallite size measured from XRD data of the Ni/CeO₂ materials as response. The results of this analysis, however, do not point to any statistically relevant effect of one single synthesis parameter ([NaOH], Temperature, and Time). The cube plot in Figure 3.15 depicts the Ni phase crystallite size as a function of the levels of the three factors, including the central point. The cube plot shows that the effect of one factor depends on the value of at least another one. The effect on metal crystallite size of the increase of temperature (from 70 to 180 °C) and of NaOH concentration (from 1 to 15 M) changes if the synthesis of the CeO₂ support was performed over 5 or 24 hours. For example (red arrows showing the Ni crystallite increase were included in Figure 3.15 for clarification), for the samples synthesised with 5 h hydrothermal treatment the increase of temperature causes a decrease of crystallite size (from 29.2 to 15.2 nm with 1 M NaOH solution and from 22.4 to 16.0 nm at 15 M), while for the 24 h case the crystallite size increases with treatment temperature (from 13.7 to 22.2 nm at 1 M [NaOH] and from 21.2 to 30.0 nm with 15 M solution). It was already shown in section 3.3.2 that the crystallite size of the support increases with higher temperature and NaOH concentration used during the hydrothermal synthesis, and generally it would be expected that Ni is more dispersed on a support having smaller structures and larger surface area [59], therefore the Ni crystallite size should also increase with temperature, which the case only for the samples synthesised at 24 hours (Figure 3.15). The opposite trend seen for the 5 hours synthesis samples could point to the fact that the ceria supports are less stable if they undergo a shorter and low temperature hydrothermal treatment, therefore the ceria particles are more affected by the thermal treatments performed after Ni wet impregnation and are more prone to enlargement and hinder the dispersion of the catalyst. Enhanced metal dispersion has also been reported to be linked with strong SMI and with optimal and intermediate support particle size [53].

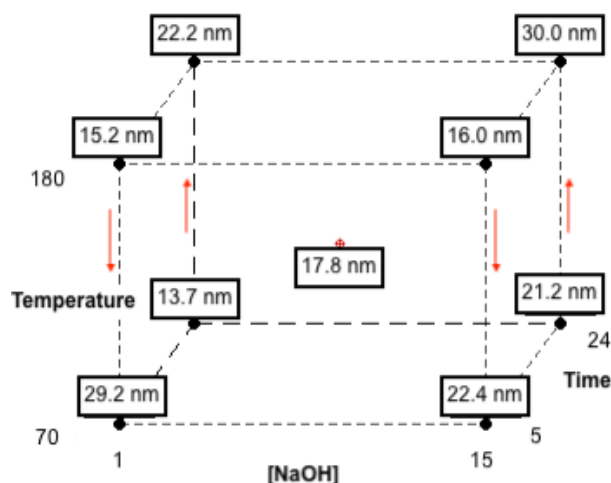


Figure 3.15: Cube plot of Ni crystallite size as a function of the DOE factors [NaOH], temperature, and time.

Regarding the crystallite size of the CeO₂ phase, which was selected as the response for the supports DOE analysis in section 3.3.2., in the case of the corresponding catalysts there is still a strong impact of [NaOH] and Temperature factors, while Time not statistically relevant according to this model. The morphology of Ni/DOE catalysts remains mostly unvaried after the introduction of the Ni phase and subsequent thermal treatments, as shown in Figure 3.16 for the Ni/DOE 0, 3, 5, 6 samples. The SEM micrographs of Ni/DOE0 and 6 (Figure 3.16a and c) resemble the corresponding support in Figure 3.3a and g. The same can be said observing at a smaller scale in the BF-TEM images of Ni/DOE0 and Ni/DOE6 Figure 3.16e and h. As was already discussed for DOE6 support, Ni/DOE6 shows very large size structures with rods of micrometric length, which do not vary notably in size (Table 3.5). However, in this case, the Ni nanoparticles were not identified separately due to excessive agglomeration. Some cubic particles that were clearly visible in Figure 3.3d for DOE3 can be observed also for the respective catalyst in Figure 3.16b, however in this case the morphology is not as defined. Indeed, only the spherical morphology for the CeO₂ particles, which was not predominant in this sample before the introduction of the Ni phase, is observed in TEM (Figure 3.16f). The sample that changes the most due to the impregnation, calcination, and reduction steps is Ni/DOE5 in Figure 3.16b, which shows larger structures compared to Figure 3.3f, which is confirmed by the average particle size reported in Table 3.5. This agrees with the XRD analysis as the measured crystallite size of the cerianite phase quadruplicates. The particles appear to have grown and to be more agglomerated compared to the CeO₂ support, which is also observed in TEM in Figure 3.16g. The size distribution of ceria particles in Ni/DOE5 is very wide and the measurement was burdensome due to the high level of agglomeration. The morphology of Ni particles is found to be quasi-spherical in all catalysts. The particle sizes of Ni and CeO₂ measured via TEM are reported in Table 3.5. According to this measurement, Ni/DOE3 has both the smallest support and metal particle size (15 and 11 nm, respectively), followed by Ni/DOE0, Ni/DOE5 and of course Ni/DOE6 has the largest structures.

Table 3.5: Results of particle size measured in TEM of Ni/DOE0, 3, 5, 6.

Sample	TEM	
	CeO ₂ particle size, nm	Ni particle size, nm
Ni/DOE0	106 ± 33	34 ± 12
Ni/DOE3	15 ± 8	11 ± 3
Ni/DOE5	121 ± 116	36 ± 17
Ni/DOE6	1883 ± 1264	NA

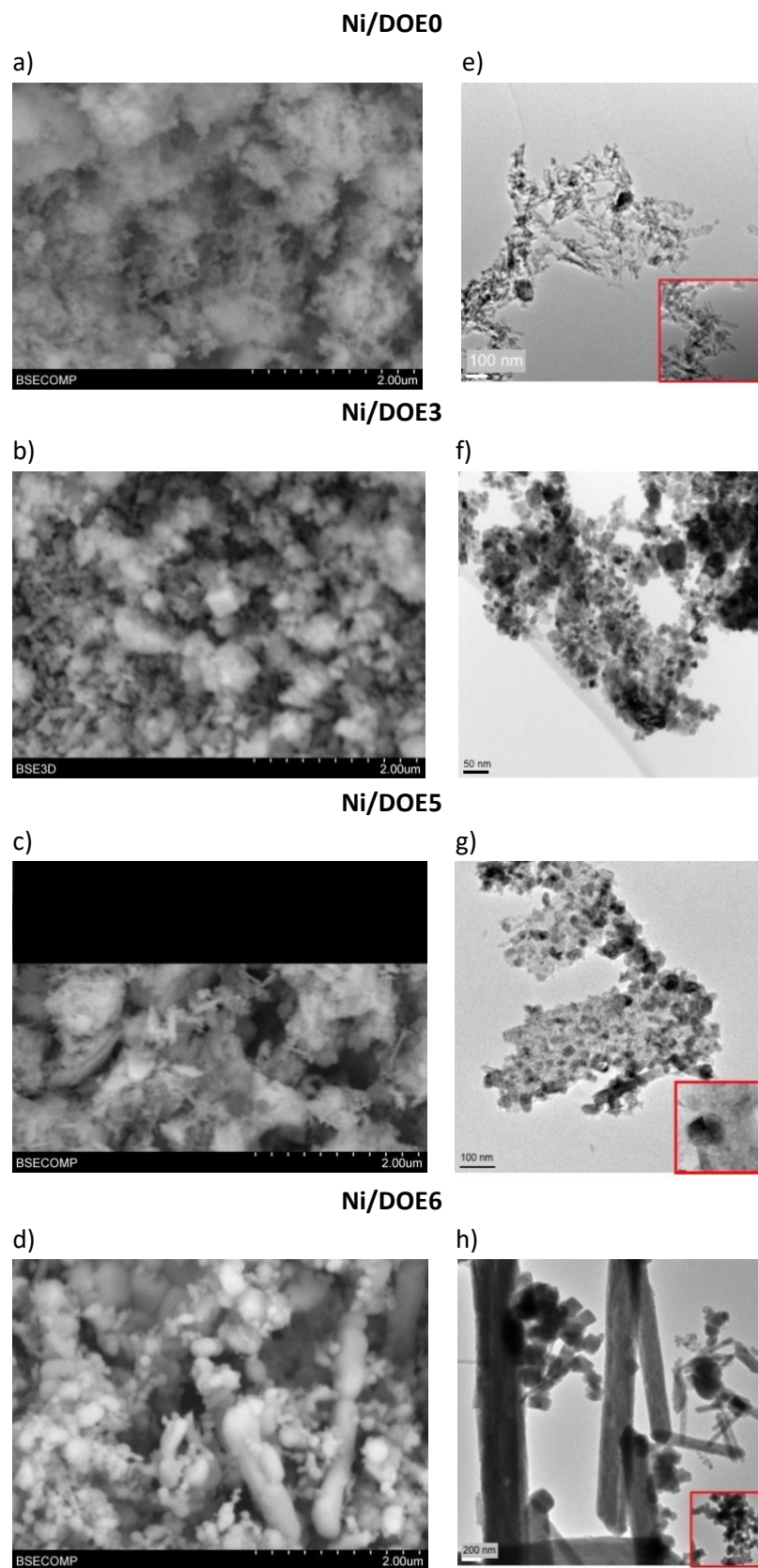


Figure 3.16: a)- d) SEM and e)-h) TEM images of Ni/DOE selected catalysts.

At the micrometric scale that can be appreciated with SEM, nickel appears to be homogeneously distributed on the catalyst surface, and it is not possible to identify the metal particles in SEM. The EDX mapping reported for Ni/DOE5 in Figure 3.17b shows a homogeneous dispersion of Ni and Ce on the surface of the region that is analysed.

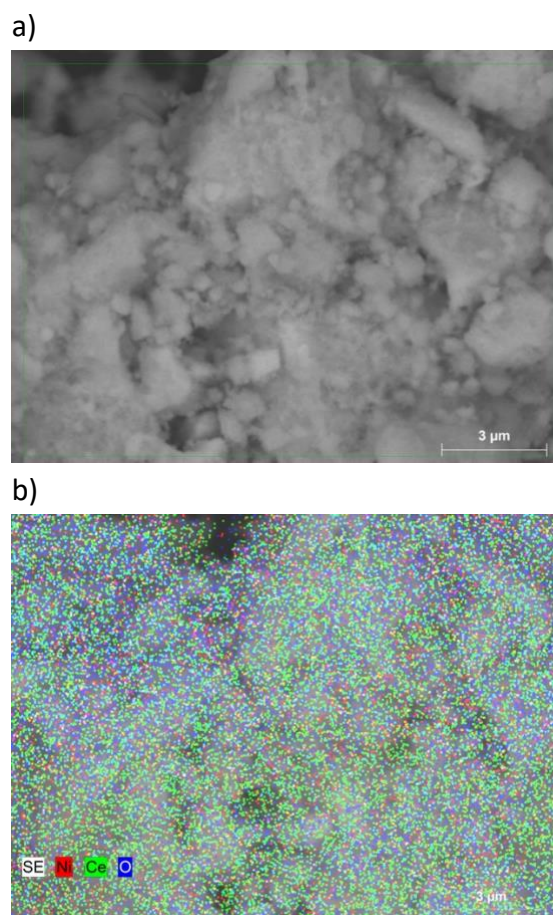


Figure 3.17: a) SEM micrograph at x800 magnification and b) the relative EDX mapping of the area in a) of Ni/DOE5.

A closer look at the nanoscale is achieved by TEM analysis of the Ni/DOE0, 3, 5, 6 catalysts. Figure 3.18 shows the BF-TEM image of Ni/DOE0 and the diffraction pattern taken from this region. It shows the polycrystalline nature of the sample with diffraction spots corresponding to (111), (200), (220), and (311) planes of Fm-3m CeO₂ and (200), (220) planes of fcc Ni. The splitting and streaking of the diffraction spots indicate that the sample has a lot of defects present. Figure 3.19 shows the HAADF-STEM image of a single Ni/DOE0 nanoneedle (Figure 3.19a) and the relative EDX elemental mapping of Ce, Ni, and O in Figure 3.19b, c, and d, respectively. It is clear that Ce and O are spread over the whole structure of supporting CeO₂ nanoneedle, while Ni is not uniformly distributed along the nanoneedle but is present explicitly in two main spots corresponding to metal nanoparticles on the surface of ceria of about 20 nm size.

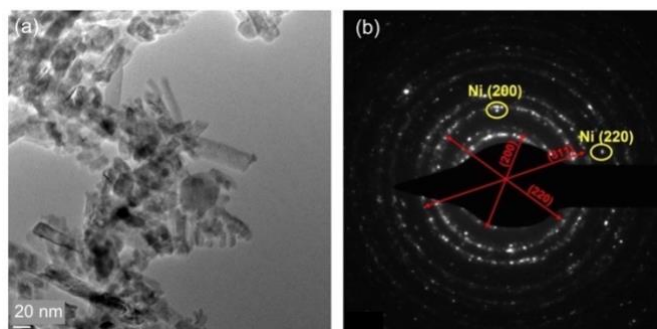


Figure 3.18: a) BF-TEM image of Ni/DOE0 and b) diffraction pattern.

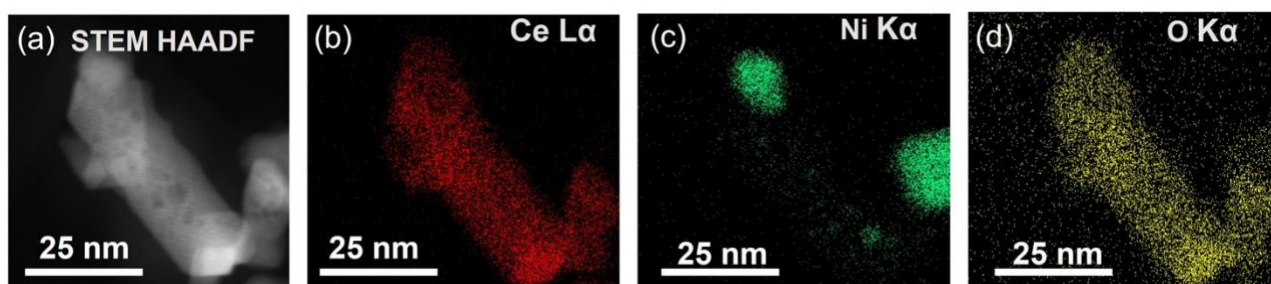


Figure 3.19: (a), (e) and (i) shows HAADF-STEM image from different area of the Ni/DOE0. (b), (f) and (j) shows Ce L map, (c), (g) and (k) shows Ni K map, (d), (h) and (l) shows O K map.

Figure 3.20a is the HRTEM image of Ni/DOE3. The FFT patterns in Figure 3.20b and c taken from two different regions marked in Figure 3.20a show spots corresponding to (111), (200) planes of fcc Ni, which indicates that metallic Ni is present in this area of the nanostructure.

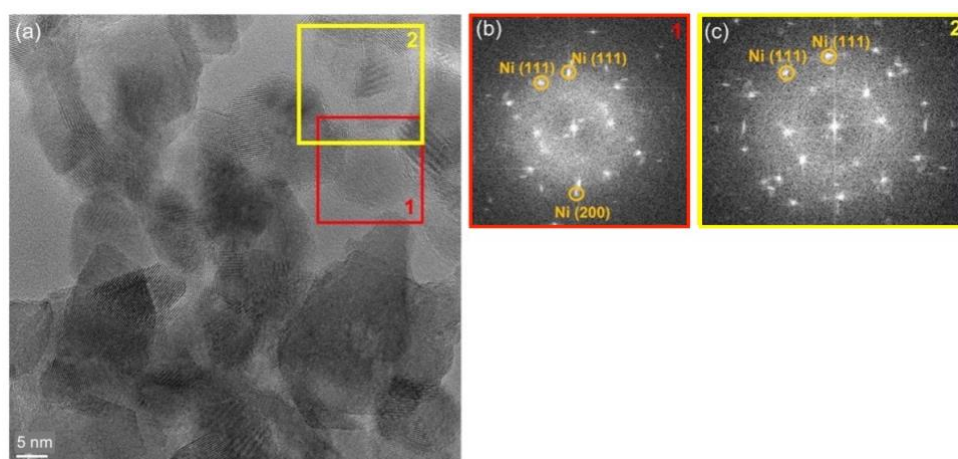


Figure 3.20: a) HRTEM image of Ni/DOE3. b), c) FFT patterns of the regions marked by red and yellow squares in a).

The HRTEM image in Figure 3.21a and the magnification of the area highlighted by the red square (Figure 3.21c) illustrate the interface between a CeO₂ nanorod and a Ni particle in sample Ni/DOE5. Indeed, both the FFT and IFFT patterns in Figure 3.21b and d reveal the distinct crystal pattern that

corresponds to both CeO_2 and Ni, with (111) crystal plane of Ni being dominant in the metal nanoparticle.

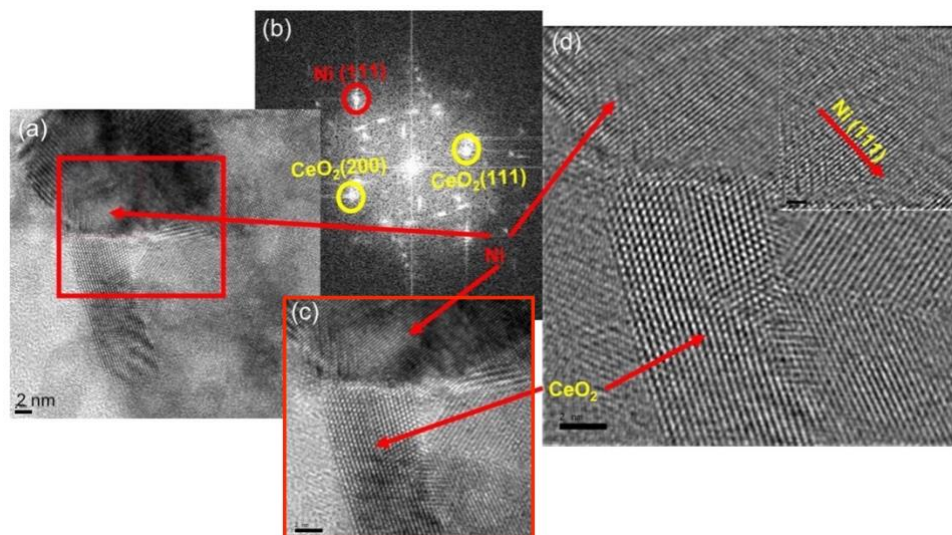


Figure 3.21: a) HRTEM image of Ni/DOE5. b) FFT pattern of the region marked by red square in a). c) magnification of the region marked by red square in a). d) IFFT pattern of c).

For Ni/DOE6 three different regions marked by blue, yellow and red squares of the HRTEM image in Figure 3.22a are examined by FFT pattern Figure 3.22b-d. Each region corresponds to CeO_2 , Ni/ CeO_2 interface and Ni particle. Only in this sample the diffraction pattern of NiO with (200) crystal plane is observed (Figure 3.22d), probably due to the passivation of the outer layer of the Ni particle.

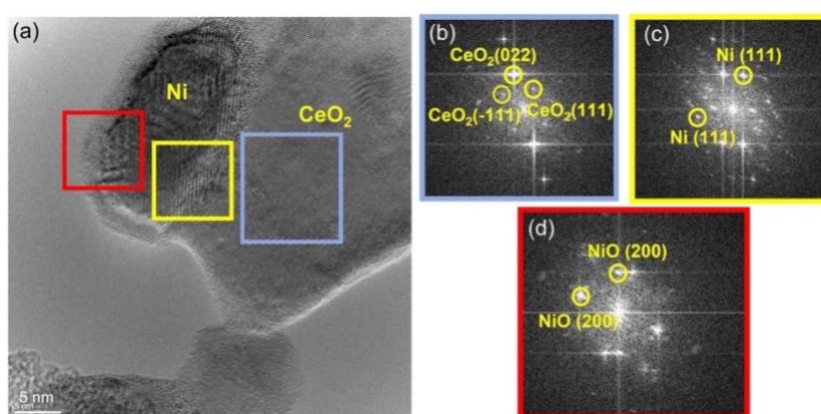


Figure 3.22: a) HRTEM image of Ni/DOE6. b), c) and d) FFT pattern taken from three different regions in a).

This TEM study allows to better examine the Ni nanoparticles and their interaction with the cerium oxide support. It was, indeed, possible to discern specific metal nanoparticles and study their crystalline nature, the lattice distortion that occurs at the Ni- CeO_2 interface, and the Ni surface.

In order to study further the state of the Ni/DOE surface, XPS was utilised. The quantification of the Ce^{3+} , $\text{O}_{\text{surface}}$, and metallic Ni contributions to the XPS spectra in the Ce3d, O1s and Ni2p regions, respectively, are reported in Table 3.6 for Ni/DOE0, 3, 5, and 6.

Table 3.6: Results of XPS and Raman spectroscopy of Ni/DOE0, 3, 5, 6.

Sample	XPS			Raman
	$\text{Ce}^{3+}/(\text{Ce}^{4+}+\text{Ce}^{3+})$, %	$\text{O}_{\text{surf}}/(\text{O}_{\text{lat}}+\text{O}_{\text{surf}})$, %	Ni^0 , %	$I_{\text{D}}/I_{\text{F2g}}$
Ni/DOE0	19.3	35.3	14.9	0.16
Ni/DOE3	18.7	37.7	17.6	0.15
Ni/DOE5	16.6	41.4	23.4	0.39
Ni/DOE6	19.4	38.2	15.8	0.10

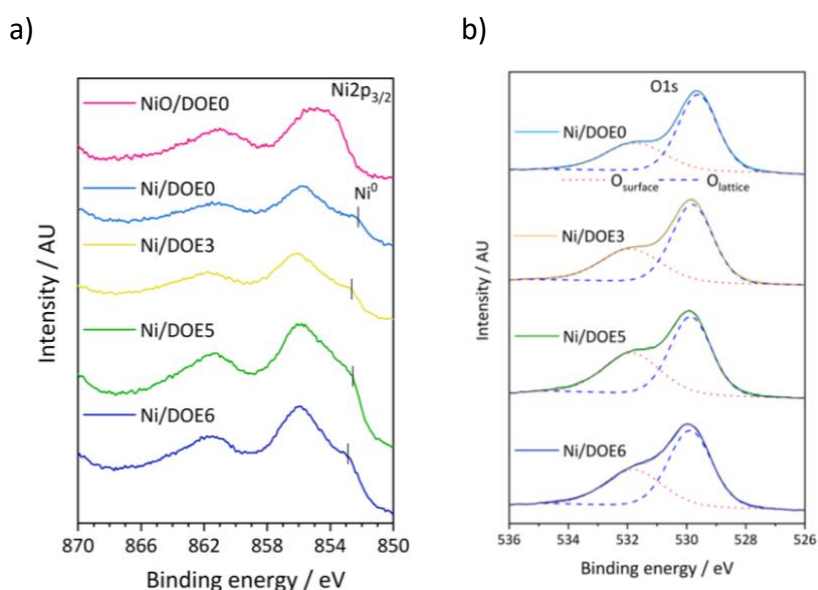


Figure 3.23: XPS spectra of the a) Ni2p_{3/2} and b) O1s regions of the Ni/DOE0, 3, 5, 6 catalysts and relative deconvolutions.

The $\text{Ce}^{3+}/(\text{Ce}^{4+}+\text{Ce}^{3+})$ ratio in the catalysts (Ce3d spectra not shown) does not vary greatly compared with the respective support (Table 3.3). The Ce^{3+} amount decreases, mostly for Ni/DOE5, probably due to strong MSI and oxygen migration between metal and defective CeO_2 at the interface which might oxidise part of the Ce^{3+} ions. Consequently, Ni/DOE5 has also the largest Ni^0 amount among these four samples. Similarly to the case of DOE5 support, Ni/DOE5 has the largest $\text{O}_{\text{surface}}$ amount, which is linked with defects and adsorbed molecules (Figure 3.23b) [148]. $\text{O}_{\text{surface}}$ increases for Ni/DOE3 compared to the bare ceria DOE3, which has the lowest OV concentration among the tested supports (Table 3.3), probably due to the chemisorption of O on the metal surface [154].

The main peak of metallic Ni^0 is identified in the $\text{Ni}2\text{p}_{3/2}$ spectral region around 852.6-853 eV in Figure 3.23a for the reduced samples, the appearance of this peak is particularly clear if the spectra are compared to calcined $\text{NiO}/\text{DOE0}$. The area of this Ni^0 peak compared to the overall region is quantified in Table 3.6. The $\text{Ni}/\text{DOE0}$, 3, 5, 6 catalysts have been reduced at 600 °C before the characterization and the calcined $\text{NiO}/\text{DOE0}$ sample is shown as comparison with the reduced counterpart. This sample lacks the contribution below 853 eV attributable to metallic Ni and shows the peaks of NiO [136]. The wide peak around 856-855 eV is present for all catalyst and it probably results from the contributions of Ni^{2+} (854-5 eV) and Ni^{3+} (856-856.7 eV) species linked with vacancies and defects at the metal/ CeO_2 interface where mixed oxides are formed, and with surface passivation [155]. Such oxidation state of Ni agrees with the XRD analysis discussed earlier which reveals traces of amorphous NiO in the reduced catalysts, probably due to a partial reoxidation at the surface of the nickel particles or at the interface with the support. The presence of NiO on the surface of the metal nanoparticle was also revealed by TEM in Figure 3.22 for the case of $\text{Ni}/\text{DOE6}$, which indeed shows a large contribution of the Ni^{2+} peak in the XPS spectrum in Figure 3.23a. It is also possible that the metal partially oxidises due to adsorbed species on the surface as water $\text{Ni}(\text{OOH})$ and carbonates [155]. Nonetheless, there is yet no agreement in literature regarding the binding energy of such Ni compounds and the attribution of this peak can be proposed according to the position of highest intensity [156]. However, once the Ni/DOE catalysts are reduced, the contributions of metallic Ni^0 clearly appears in the $\text{Ni}2\text{p}$ components and the amount of Ni^0 on the surface of the catalyst changes for the four samples ranging from 23.4 % for $\text{Ni}/\text{DOE5}$ to 14.9% for $\text{Ni}/\text{DOE0}$ (Table 3.6).

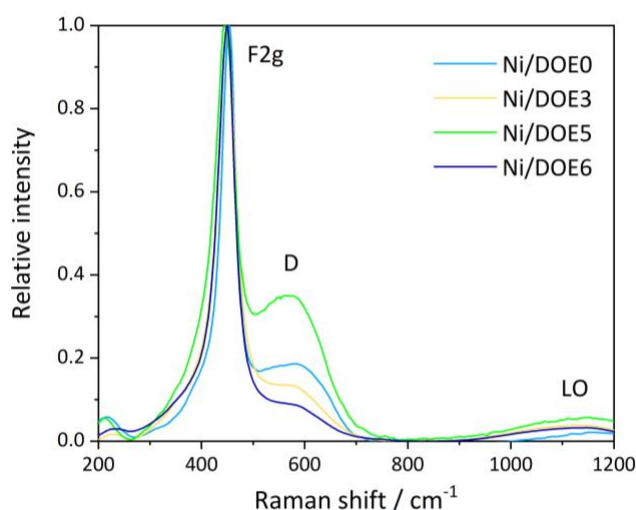


Figure 3.24: Raman spectra of the $\text{Ni}/\text{DOE0}$, 3, 5, 6 catalysts.

The analysis of OV via XPS showed a decrease in Ce^{3+} surface species for $\text{Ni}/\text{DOE0}$, 3, 5, and 6. However, the metal-support interface creates other defects as shown by Raman spectra in Figure

3.24. The F2g mode red-shift is linked with a variation of the Ce-O bond, furthermore, the band centred around 575 cm^{-1} enclosed the contributions of oxygen vacancies (D) as well as cation substitution, leading to an increase in the intensity of such peak [157] and of I_D/I_{F2g} ratio (Table 3.6) for the Ni/CeO₂ samples compared to CeO₂. 3 repetitions were performed with a standard deviation ± 0.04 . Despite the different order of magnitude of I_D/I_{F2g} , the ranking of defects concentration for the four samples according to this ratio remains unvaried compared to the support with Ni/DOE5>Ni/DOE0>Ni/DOE3>Ni/DOE6. The band around 1100 cm^{-1} of the second longitudinal optical mode (LO) for CeO₂ appears very widened due to the introduction of the components linked with Ni [157].

In conclusion, the introduction of Ni disrupts the surface of CeO₂, changing its lattice parameter, crystallite size, and in some cases morphology and OV concentration. Nonetheless, the Ni-CeO₂ interface introduces new defects due to the mixing of Ni and ceria crystalline solids, and potentially medium or strong MSI depending on the catalyst.

3.3.5. Reducibility and basicity of the Ni/CeO₂ catalysts obtained from the DOE supports

The curves resulting from H₂-TPR and CO₂-TPD experiments, and the relative quantitative properties are reported in this section.

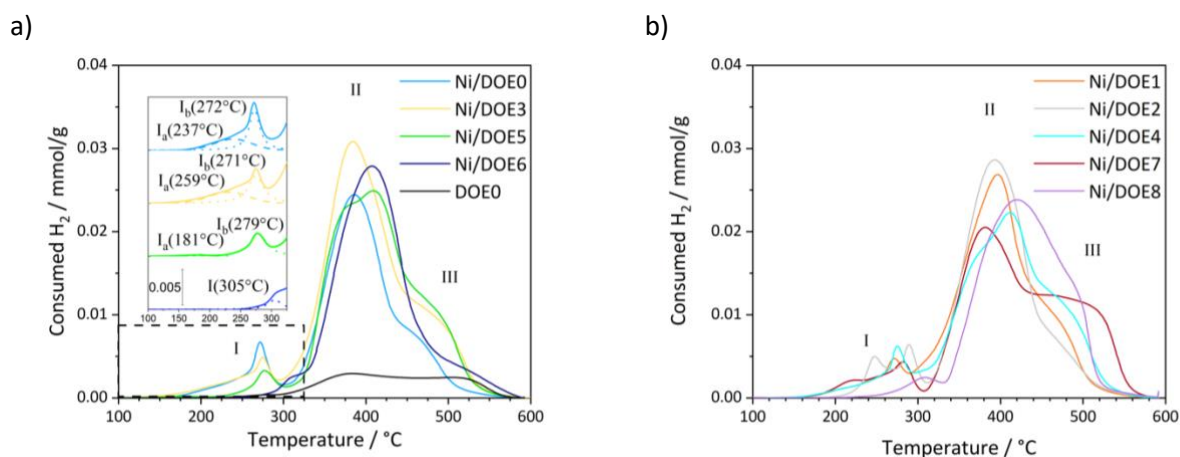


Figure 3.25: H₂-TPR curves of samples a) Ni/DOE 0, 3, 5, 6 and CeO₂ DOE0; and b) Ni/DOE1, 2, 4, 7, 8.

The H₂-TPR experiments show good reducibility of all Ni/CeO₂ catalysts (see Figure 3.25), with values of consumed H₂ ranging from 3.28 to 2.46 mmol/g (Table 3.7). This H₂ consumption during reduction can be mostly attributed to NiO reduction since the amount for the CeO₂ support alone is one order of magnitude lower (0.59 mmol/g of hydrogen consumed in the TPR experiment of DOE0 as an example of CeO₂ support, shown in Figure 3.25a). Furthermore, the consumed H₂ measured in TPR experiments corresponds to a theoretical nickel amount of 14-19%, which is in good agreement with the expected Ni amount dispersed on the ceria supports (15 %wt.), confirmed by ICP-AES as

explained in the previous section. The NiO particles are fully reduced to metallic Ni at 600 °C, this is a good choice of reduction temperature as used for catalyst preparation.

The fitting of the TPR curves (reported for the case of Ni/DOE0, 3, 5, and 6 in Figure 3.25a) highlights three main regions centred around 260 (I), 400 (II) and above 450 °C (III). One or two peaks might contribute to the same region (e.g., I_a and I_b of Ni/DOE0, 3, 5 in Figure 3.25a), the exact position and area of each peak varies depending on the sample. The first peak is linked with readily reducible NiO species exposed on the catalyst surface. A shift to lower temperature and larger area of this region (Table 3.7) is related with a lower Ni crystallite size measured by XRD, therefore probably to an enhanced metal distribution on the CeO₂ support, as is the case of Ni/DOE0, 1, and 2, whose Ni crystallite size is below 20 nm. On the contrary, the TPR curves of Ni/DOE6 and 8 samples show a complete shift of the first reduction peak to higher temperatures (305 and 297 °C, respectively), indicating a lack of easily reducible species on the surface. In addition, only a few samples have a small peak appearing below 250 °C. In literature this is assigned to the reduction of weakly adsorbed surface oxygen such as – OH or O₂ species [113]. In the range 300-450 °C (II) the most significant hydrogen consumption is observed for all samples. Generally, this is considered the reduction of NiO moderately interacting with CeO₂ and Ni-O-Ce solid solution at higher temperatures [113]. The last peak above 450 °C (III) can be interpreted as the reduction of CeO₂ in strong interaction with Ni at the interface [113]. Indeed, it can be observed in Figure 3.25a that the last peak of the TPR curve of DOE0 (above 500 °C) shifts to lower temperatures with the addition of nickel in the Ni/DOE0 sample. The area below the H₂-TPR curve in the regions II and III of Ni/DOE0 is lower compared to other samples, leading to the lowest H₂ consumption (2.46 mmol/g). However, this sample shows an improved low temperature reducibility (region I). This different behaviour of Ni/DOE0 could be linked to different strength of interaction between Ni and CeO₂ probably due to the morphology of the support (nanoneedle) and formation of surface defects. Regions II and III in Ni/DOE6, 7, and 8 appear shifted to higher reduction temperatures, pointing, in the case of Ni/DOE6 and 8, to overall lower reducibility. The support of Ni/DOE6 possesses the lowest OSC and poorer non-stoichiometric behaviour among the studied materials, which probably decreases the reducibility of the catalyst. Ni/DOE5, which has the largest surface area and whose support is characterized by enhanced OV concentration, is the most reducible catalyst of this series with 3.28 mmol/g overall consumption.

Table 3.7: H₂-TPR and CO₂-TPD results of Ni/DOE0-8 catalysts.

Sample	TPR		TPD	
	Consumed H ₂ , mmol/g	Low temperature H ₂ consumption, mmol/g	Desorbed CO ₂ , mmol/g	Medium strength basic sites, μmol/g
DOE0	0.59	0.03 (5 %)	0.322	39 (12 %)
Ni/DOE0	2.46	0.30 (11 %)	0.133	71 (53 %)
Ni/DOE1	3.11	0.34 (11 %)	0.158	115 (73 %)
Ni/DOE2	3.14	0.38 (12 %)	0.068	21 (32 %)
Ni/DOE3	3.00	0.25 (9 %)	0.149	112 (75 %)
Ni/DOE4	3.12	0.35 (11 %)	0.174	110 (64 %)
Ni/DOE5	3.28	0.18 (5 %)	0.168	115 (69 %)
Ni/DOE6	2.95	0.06 (2 %)	0.042	6 (14 %)
Ni/DOE7	3.23	0.28 (9 %)	0.191	78 (41 %)
Ni/DOE8	3.05	0.08 (3 %)	0.030	11 (38 %)

The CO₂-TPD experiments were performed on the reduced catalysts to assess their basicity and the strength of CO₂ adsorption on their surface (see Figure 3.26). The first relevant difference among the DOE catalysts regards Ni/DOE6 and 8 that show a remarkably low amount of CO₂ desorbed, probably due to the low surface area of the ceria-based catalyst and the lack of basic sites (Table 3.7). The CO₂ adsorption is proved to be happening on the cerium oxide sites as the amount desorbed from the DOE0 support alone is higher compared to the respective catalyst (Figure 3.26a). This could be due to a higher surface area of the support compared to the material impregnated with Ni, but also for the blocking of the CeO₂ surface by the metal particles in the catalysts. The TPD curves show three main regions linked with basic sites of increasing strength (Figure 3.26). According to literature, the desorption peaks at low temperature of 80–200 °C can be ascribed to weak basic sites formed by surface Bronsted hydroxyl (OH) groups [109]. The peaks at temperatures higher than 400 °C are attributed to high strength basic sites, which are typically Lewis basic sites of O₂[−] anions [109]. Finally, the medium strength basic sites, which are the most interesting for CO₂ methanation reaction, are considered to range between 200 and 400 °C (highlighted in Figure 3.25). This moderate basicity is generally provided by acid-base Ce⁴⁺ or Ce³⁺-O^{2−} pairs and allows optimal adsorption of the CO₂ available for the reaction [109]. The percentage of the area integrated below the curve in 200–400 °C range is reported in Table 3.7. The percentage of medium strength sites increases with the addition of nickel for the catalyst preparation. However, this amount varies according to the samples: Ni/DOE2, 6, 7, 8 have less than 50 % of intermediate basic sites. The CO₂-TPD curves of these catalysts in fact show lower intensity in this region as reported in Figure 3.26. Once again, the lowest presence of medium strength basic sites can be linked to the poor OSC and

low defects CeO₂ surface of the support as it the case of Ni/DOE6. The highest intermediate basicity is achieved by Ni/DOE1, 3, and 5 with 75-69 %, which point to an enhanced activity of these catalysts for CO₂ methanation.

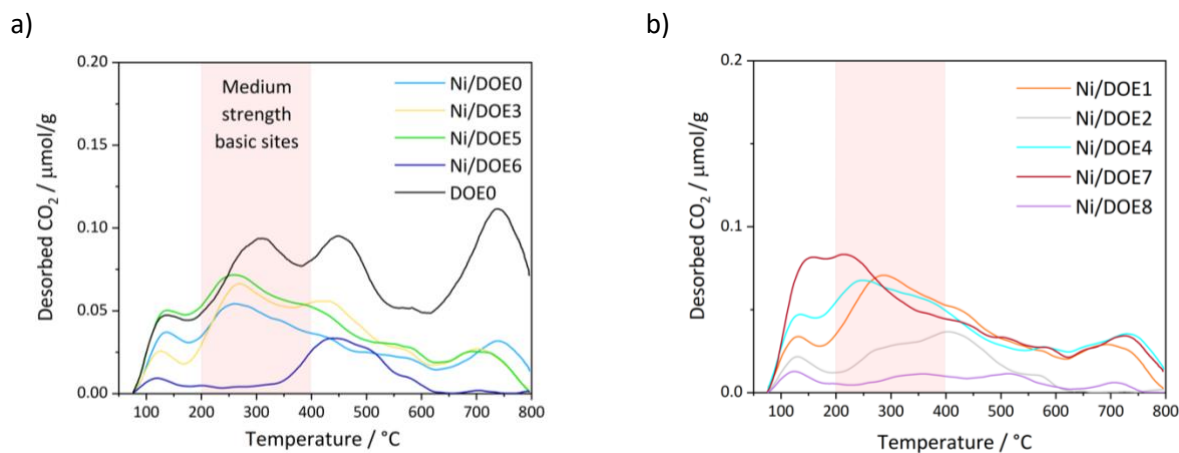


Figure 3.26: CO₂-TPD curves of samples a) Ni/DOE 0, 3, 5, 6 and CeO₂ DOE0; and b) Ni/DOE1, 2, 4, 7, 8.

The surface interactions with air at room temperature and relative adsorbed molecules on the Ni/CeO₂ surface were investigated by FTIR and should depend on the catalyst surface configuration and properties. Figure 3.27 compares the spectra of the reduced catalysts in the range of 800 to 2000 cm⁻¹.

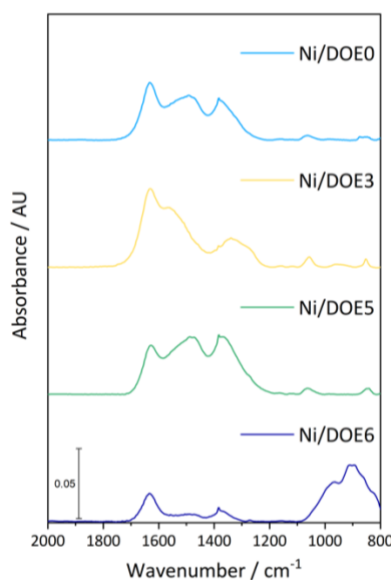


Figure 3.27: FTIR spectra of samples Ni/DOE0, 3, 5, 6.

The peaks in this region can be attributed to water and carbonate species. In all the spectra, the peak at 1633 cm⁻¹ is the H-O-H bending attributed to molecular H₂O adsorbed on the surface of the

material [158]. In all spectra it is also possible to distinguish two regions centred at 1500 and 1380 cm^{-1} , these are composed of the contributions of peaks of mono-, bi- and polydentate carbonates [78,159]. The most intense peaks at 1486 and 1373 cm^{-1} are attributed to monodentate [78,160]. Bidentate carbonates peaks (1265 and 1551 cm^{-1}) [78] can be distinguished as shoulders in the spectra of Ni/DOE0 and DOE5, while they are more intense for Ni/DOE3. This larger amount of bidentate carbonates points to a stronger interaction of CO_2 to the surface of the Ni/DOE3 catalyst, as can be observed in the CO_2 -TPD curve in Figure 3.26a, which is less intense below 200 °C compared to Ni/DOE0 and 5. With the exception of Ni/DOE6, the region below 1200 cm^{-1} consists of smaller peaks: two at 1061 and 850 cm^{-1} attributed to monodentate and one at 990 cm^{-1} for bidentate [78,160]. This region is linked with polydentate carbonates species on the surface [113] and it increases in absorbance in the Ni/DOE6 spectrum compared to the other catalysts. In fact, the main contributions to the spectrum of this sample come from bidentate and tridentate carbonates [78,160], which further evidences the strong basic sites possessed by this catalyst (Figure 3.26a), which are unfavourable for CO_2 methanation [113]. As expected, the catalysts before the reaction already present adsorbed CO_2 and H_2O from the atmosphere, depending on their surface basicity.

3.4. Conclusions

The physicochemical properties of cerium oxide nanomaterials having different morphologies were assessed and their connexion with the synthesis parameters of the hydrothermal method was studied by means of DOE factorial analysis. This study disclosed the strong effect of base concentration in the solution of Ce salt precursor and temperature of the hydrothermal treatment on the increase of the size of the ceria structures. Moreover, a variation of morphology as nanorod>nanoneedle>nanocube>microrods+cubes was observed with increasingly harsher synthesis conditions regarding temperature, NaOH concentration, and time. The surface defects, linked with OSC, were characterized, showing an increase of OV with lower particle size and preferential formation on the more active <011> surface facets of the nanoneedle and nanorod structures. The properties of the cerium oxide supports vary after the introduction of the Ni phase and calcination and reduction steps. The crystallite size of ceria increases while S_{BET} decreases, but there are still relevant morphology and surface structure differences among the 9 catalysts. Furthermore, the Ni- CeO_2 interface introduces new defects and, in some cases, evidences of strong MSI.

The Ni/ CeO_2 DOE samples result in a set with different metal particle size, surface area, reducibility, and basicity properties, which make this series of catalysts interesting to explore in plasma-assisted CO_2 methanation tests in order to study how the physicochemical properties influence the activity and reaction mechanism despite the samples having the same elemental composition.

Chapter 4: Plasma-assisted and thermal CO₂ methanation over Ni/CeO₂

catalysts: influence of physicochemical properties

4.1.	<i>Introduction</i>	99
4.2.	<i>Methodology</i>	99
4.3.	<i>Results and discussion</i>	101
4.3.1	Plasma-assisted CO ₂ methanation	101
4.3.2	Comparison with empty DBD reactor and packed with metal oxide supports	106
4.3.3	Thermal CO ₂ methanation	108
4.3.4	Comparison of thermal and plasma-assisted processes.....	109
4.3.5	Impact of DOE factors and physicochemical properties on the catalytic performance	111
4.3.6	Stability tests	116
4.3.7	Characterisation of the catalysts after plasma-assisted and thermal reaction	118
4.4.	<i>Conclusions</i>	127

4.1. Introduction

The results of plasma-assisted CO₂ methanation with the catalysts described in the previous chapter are presented in this chapter. The CO₂ conversion obtained with Ni catalysts supported on CeO₂ synthesised via hydrothermal method is compared with the performance of the empty DBD reactor or using metal oxide supports as packing materials. The activity in the DBD reactor is compared with the thermal methanation results at temperatures from 250 °C to 450 °C, performed at similar input conditions and varying the activation method (plasma or heat). The differences in the catalytic activity of the DOE series catalysts with different morphology and physicochemical properties are examined and correlated with the most relevant features of the materials. The catalysts after the CO₂ methanation reaction have been characterized again and eventual variations in their physicochemical properties are evaluated.

4.2. Methodology

The set-ups for plasma and thermal catalysis used to obtain the results that will be presented in this chapter have been described in chapter 2, together with the characterization techniques that are used to examine the materials after exposure to the methanation reaction. The physicochemical characterization of the catalysts after plasma and thermal reactions were performed via XRD, SEM, and TEM, to evaluate the bulk structure of the material, the crystallite and particle size and eventual variation of the morphology, and XPS, FTIR, and TPD-MS to investigate the surface composition and the adsorbed species during the methanation reaction.

4.2.1 Energy efficiency calculation in the thermochemical process

The efficiency of the plasma catalytic process (eq. (2.12)) is assessed based on the injected power determined by Lissajous method, which is already a studied and published procedure [109]. For comparison purposes, it would be interesting to have a similar parameter for the thermochemical CO₂ methanation process based on the power injected to the furnace to reach the target temperature of the process. The optimal way would be to use a wattmeter at the plug of the furnace (and as a comparison at the electric input of the plasma power supply as well). However, this instrument was not available, therefore an estimation was conducted. The Eraly furnace specifications are a voltage of 230 V, a maximum current of 5.4 A (1242 W maximum power) and a maximum working temperature of 1050 °C. This tubular oven displays in real-time the temperature together with the percentage of the total power consumption, which was recorded over 30 minutes (reaction time at each condition) at three temperatures 250, 300, 350 °C. The trend of power consumption over time for the three conditions is shown in Figure 4.1a with the same steps: 100 % power requirement in the first 5 minutes to reach the set temperature, and a decrease (more or less abrupt depending on the oven temperature) to a stable lower power stage that is maintained over time. The average values of the power over 30 minutes is reported in Figure 4.1b in comparison with the linearization obtained from two points: 1050 °C considered as 100 % power requirement (therefore 1242 W), and room temperature 20 °C with 0% power consumption (0 W). The averaged power necessary to heat the furnace at 300 and 350 °C (289 and 312 W, respectively) is much lower than the expected one and was used for the efficiency calculation according to eq. (2.12).

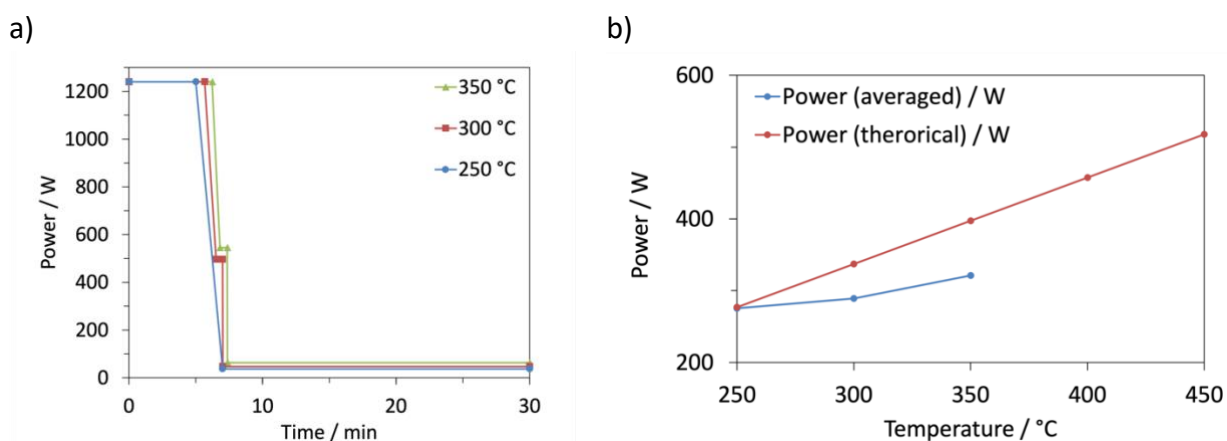


Figure 4.1: measurement of furnace power a) over 30 minutes time and b) as a function of set temperature.

4.3. Results and discussion

4.3.1 Plasma-assisted CO₂ methanation

All the catalysts obtained from the Ni wet impregnation of the ceria DOE series supports, reduced at 600 °C and with particle size 200-25 µm, were tested for plasma-assisted CO₂ methanation reaction. The results of the plasma catalytic tests regarding plasma injected power, CO₂ conversion and selectivity toward CH₄ are reported in Figure 4.2 for these DOE catalysts. DBD plasma experiments were performed at reactants ratio H₂/CO₂ 4/1, total flow of 100 mL/min, 12 kg_{CO2}/kg_{cat} h, WHSV of 30000 mL/h g_{cat}, frequency of 12.3 kHz and different voltage conditions of 21-24 kV_{p-p}. These conditions correspond to the injected power range of 13.3 W to 50.3 W depending on the catalyst response in the plasma discharge (see Figure 4.2). The power is calculated using the Lissajous method and corresponds to the area of the charge-voltage plot (Figure 4.3) calculated through eq. (2.7). As mentioned in chapter 2, during the experiments in the DBD reactor it was attempted to maintain the input voltage supplied by the Minipuls power generator constant at each condition tested (corresponding to the averaged values 22.3, 23.5, 24, 24.5 kV_{p-p}). The behaviour of the power supply and the actual power injected to the packed bed DBD reactor depend on the resulting impedance of the system, therefore on the catalyst. In Figure 2a the power calculated is plotted as a function of the input voltage. It is reported here to show the direct P-V relationship that is common to all catalysts despite the different responses. Furthermore, it should be clarified that the power reported in Figure 4.2, which greatly differs for the different catalysts, does not depend on the input conditions to the set-up during the experiments but on the behaviour of each sample in plasma.

In plasma, most catalysts start with negligible conversion at low power, followed by a fast ramping to above 50 % conversion, which ends up in a plateau around 70-80 % CO₂ conversion (Figure 4.2b). The best behaving catalysts in plasma-assisted CO₂ methanation are Ni/DOE0, 1 and 5, reaching conversion above 70 % at around 20 W. For the other catalysts, the conversion versus power curve shifts to larger power range above 35 W in order to reach a mild conversion around 50 %. Ni/DOE2, 6 and 8 do not reach conversion above 60 % even at the highest voltage studied that injects power to the system from 35 W to 45 W and it can be establish that these catalysts are not optimal for CO₂ methanation in DBD reactor. The selectivity obtained with these series of Ni/CeO₂ catalysts is good (above 98 %) when a high conversion is achieved, which confirms that Ni/CeO₂ materials are a good choice for CO₂ methanation. At these conditions, the carbon balance adjusts to values close to 100 % (97.6 ± 4.5 %), proving that CO and CH₄, which are detected and quantified by the GC, are the only relevant C-containing products of the reaction in plasma. Moreover, the carbon deposition on the catalyst and deactivation are negligible according to the measured C_{balance}. The only case with lower C_{balance} is the Ni/DOE8 catalyst, which presents the lowest conversion of the series and 85 % C_{balance}. This could be linked with the strong basic sites on the surface of the material, which traps CO₂ and does not allow the reaction to occur. It should also be mentioned that this catalyst is the only one

displaying low selectivity for CH₄ and favouring, despite the low CO₂ conversion, the production of CO.

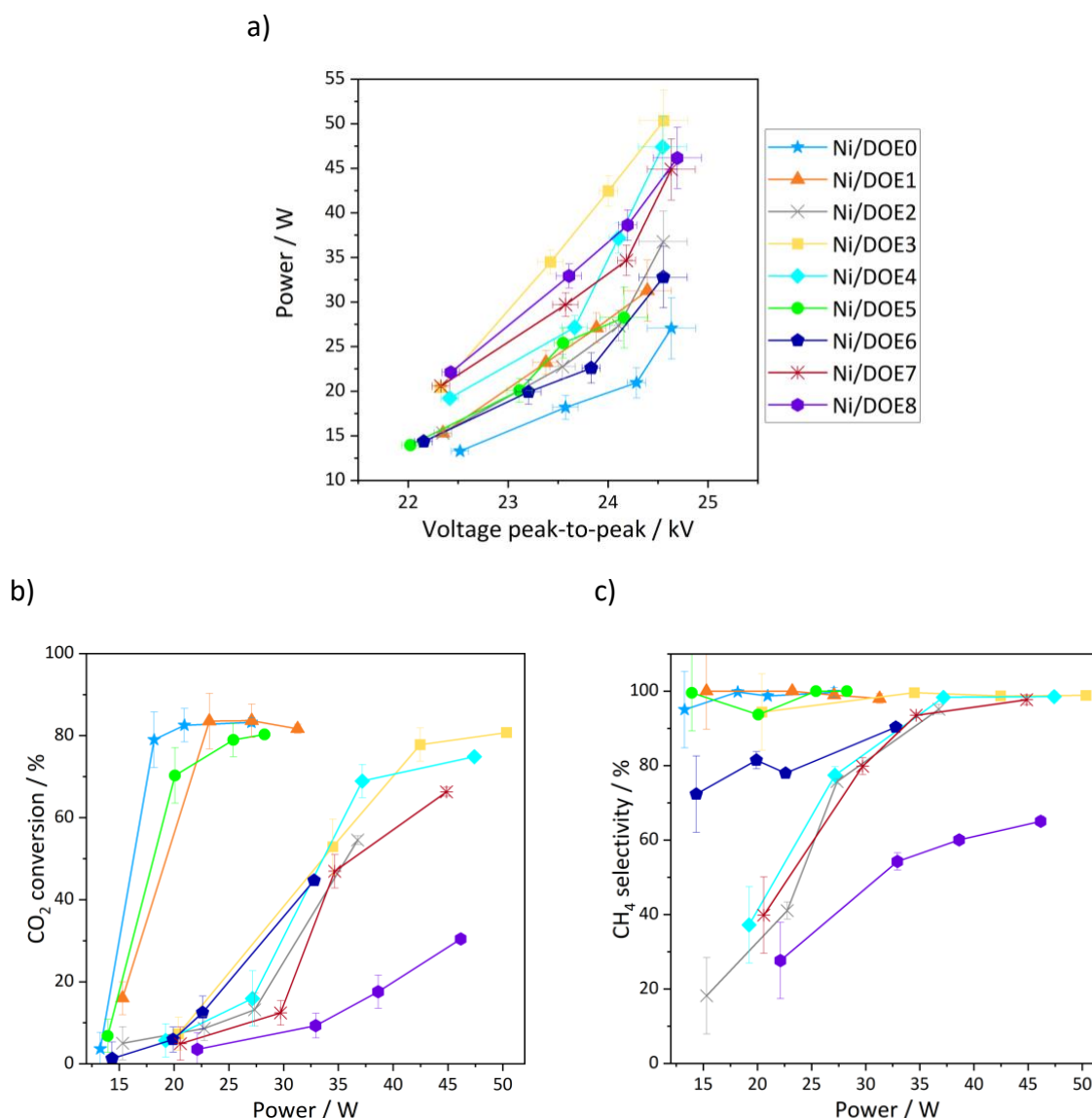


Figure 4.2: a) power as a function of the applied voltage b) CO₂ conversion and c) CH₄ selectivity results of plasma-assisted CO₂ methanation tests with the Ni/DOE0-8 catalysts as a function of injected power.

H₂/CO₂ = 4, WHSV 30000 mL/hg_{cat}.

The water produced by methanation reaction and gathered in the reservoir has been analysed by TOC to determine the organic carbon content. The total carbon consists mostly of organic carbon with the following concentration for three catalysts: Ni/DOE0 76.5 mg/L, Ni/DOE3 83.5 mg/L, Ni/DOE6 79.87 mg/L (with almost neutral pH ranging from 7.4 to 7.6). As comparison TOC of dH₂O has been measured as 8 mg/L, the water samples gathered after methanation have a TOC 10 times higher than deionized water but still at low concentration, that could be caused by dissolution of the CO₂ in water and not from larger liquid hydrocarbons formation.

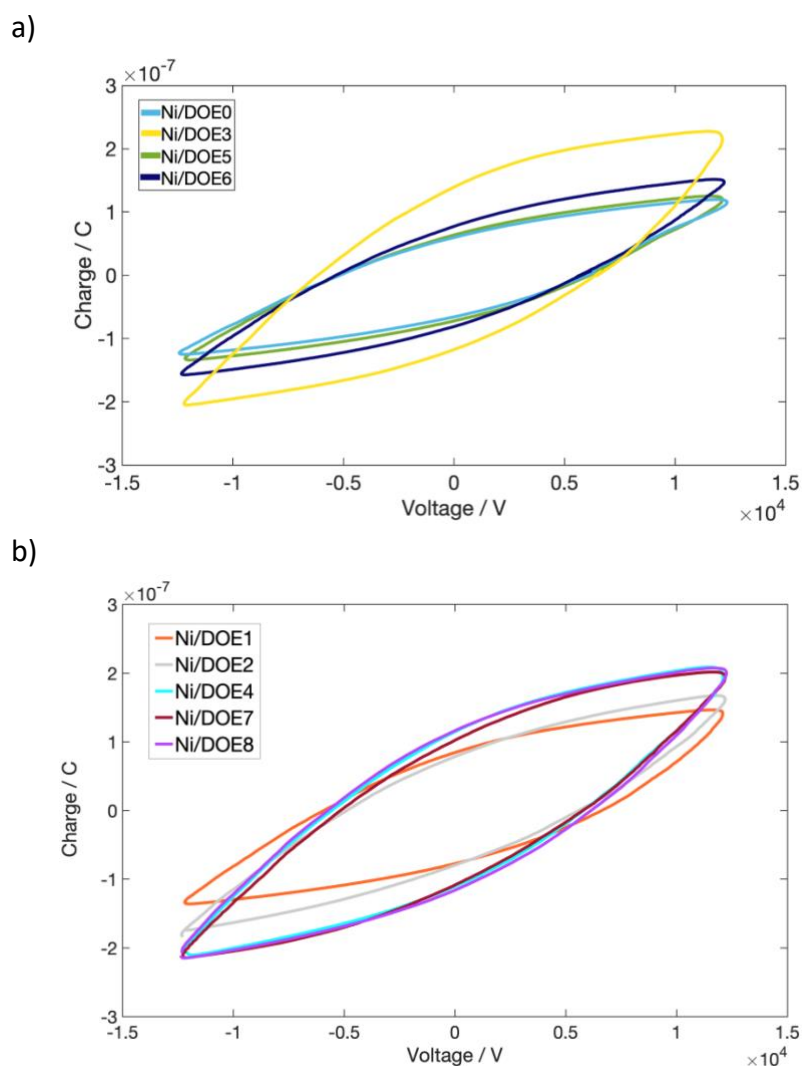


Figure 4.3: Lissajous figures of a) Ni/DOE0, 3, 5, 6 and b) Ni/DOE1, 2, 4, 7, 8 samples at 24 kV_{p-p} applied voltage.

As briefly commented in the beginning of this section, several differences can be observed concerning the behaviour of the DBD set-up according to the packing material (Figure 4.2a), and the shape of the Q-V Lissajous plots acquired for the catalysts Ni/DOE0-8 evidences these differences (Figure 4.3). Once the catalysts are directly placed in the discharge area, the dielectric properties of catalysts should be measured and considered that the catalytic material is subjected to interactions with electrons and electric field. The response of the material to the applied high voltage for plasma discharge can be assessed by the Lissajous charge-voltage cycle in Figure 4.3, where the curves for Ni/DOE catalysts are compared for the same applied peak-to-peak voltage of 24 kV. The curve corresponds to the measured charge across the capacitor connected to the counter electrode of the DBD reactor as a function of the applied voltage over one period. At low peak-to-peak voltages, before plasma ignition (i.e., below breakdown voltage), the Q-V plot is linear, developing a hysteresis cycle once the plasma is ignited. The area of these cycles is used for the calculation of the

injected power. The Lissajous plot has an almond shape, which differs from the expected parallelogram due to the different discharge events happening in the non-uniform discharge area, which is heightened by the packing with powdered catalysts [139]. The first thing that can be noticed is the different area of the cycle, which is much larger for Ni/DOE3, corresponding to the larger power injected (Figure 4.2 and 4.3) to the plasma in the DBD reactor packed with this material compared to Ni/DOE0 and 5. The dielectric behaviour of the catalytic material that is packed in the plasma discharge area can be described with the equivalent capacitance of the reactor (C_{reactor}), which is also obtained via the analysis of the Q-V curve. The almond shaped cycle has sharp apexes at maximum and minimum voltages. Starting from the minimum voltage and charge point, the charge increases linearly until the breakdown voltage is reached (plasma “off” part), at this voltage the filaments start igniting in the packed reactor (plasma “on”). The voltage further increases until the maximum peak value is attained, followed by a voltage decrease, which corresponds to the beginning of the positive part of the period. The same behaviour is observed in the positive part of the voltage period. The slope of the linear “off” sections of the Lissajous figure corresponds to the C_{reactor} , therefore, according to ideal equivalent circuit (Figure 2.7), it is the resulting contribution of the capacitances of the gas, the quartz and alumina (dielectric materials of the DBD), and of the catalyst (eq. (2.9)) [139]. The different slopes of the linear parts of the “off” sections can be observed qualitatively in Figure 4.3, for example, Ni/DOE4 has the steepest lines among the shown catalysts, which translates to the largest C_{reactor} (5.11 pF). The quantitative values of C_{reactor} are reported in Table 4.1 later in section 4.3.4. A more in-depth and quantitative approach to the Lissajous figures analysis is addressed in the next chapter.

The reaction occurs at pseudo-adiabatic conditions without external heating. The temperature in the catalytic reactor increases during the experiments due to heat dissipation during plasma ignition and as a consequence of the intrinsic exothermicity of the CO₂ methanation reaction. The temperature at the external ring electrode is measured for each power setting. The reactor temperature increases with applied voltage and power, as shown in Figure 4.4. The temperature measured during the experiments with Ni/DOE0, 1, and 5 at low power is higher than for the other catalysts at the corresponding conditions due to the high conversion achieved with these samples below 30 W. The catalysts that result in the lowest conversion, Ni/DOE6 and 8, also have the lowest recorded temperature (150 °C), which is 10 to 20 °C lower than the condition with on-going methanation reaction at similar power conditions (Ni/DOE1 at 30 W and Ni/DOE4 at 45 W), this difference can be attributed to the exothermicity of the catalytic conversion of CO₂ to methane. The temperature of the reactor when high conversion is observed in plasma catalysis is 140-180 °C. In addition, in order to compare the plasma catalysis results to the known thermal CO₂ methanation the conversion, the CO₂ conversion is plotted also as a function of reactor temperature in Figure 4.4b. The trends of CO₂ conversion versus reactor temperature for Ni/DOE0, 1, 3, 4, and 5 are very

similar with a small shift to lower temperatures for Ni/DOE0. Therefore, the most efficient catalyst, regarding the reactor heating and power consumption, is proved to be Ni/DOE0.

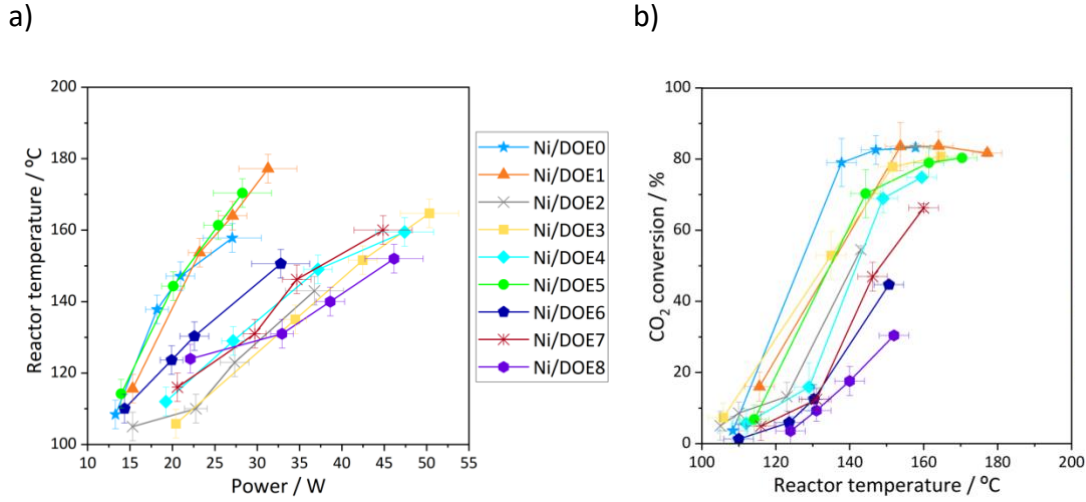


Figure 4.4: a) Reactor temperature as a function of injected power. b) CO₂ conversion as a function of reactor temperature during plasma-assisted CO₂ methanation tests with the Ni/DOE0-8 catalysts as a function of injected power. H₂/CO₂ = 4, WHSV 30000 mL/hg_{cat}.

Due to the configuration of the DBD reactor, an optical window was not designed for optical plasma diagnostics, and it was not possible to measure the gas temperature inside the reactor. Instead, the reactor's external temperature could be measured during the experiments and is reported. Furthermore, due to the large potential drop and electric field across the gap, it is not advisable to insert a metallic thermocouple inside the discharge zone. The temperature at the external electrode (where it is measured with a Pt100 temperature probe) is considered equal to the temperature at the quartz wall (outer dielectric) due to the high thermal conductivity of metals [123].

Eliasson et al. provided a formula for the temperature shift within the gap compared to the temperature of the reactor wall (T_{reactor}) due to dissipation of electric power in the case of DBD used for ozonisers [161,162]. The expected radial temperature profile is a half-parabola with its peak value at the quartz tube [161]. The average increase temperature inside the gap (T_{gap}) is determined by a balance of the dissipated discharge power and heat removal by conduction radially [161], therefore depends on the thermal conductivity of the gas or the material filling the gap:

$$T_{\text{gap}} = T_{\text{reactor}} + \frac{1}{3} \frac{dP}{\kappa S} \quad (4.1)$$

where T is temperature (in °C or K), d is the gap size (in m), κ (W/Km) is the thermal conductivity, P/S (W/m²) is the power density referred as power over the electrode area. The shift between the T_{gap} and T_{reactor} is large if only the gas, which has a low conductivity, (for simplicity H₂ κ_{H_2} 200 mW/Km) is considered, however, the heat flux is expected to improve by the presence of solid materials in the discharge gap [161], as it the case of the packed bed DBD reactor. If the κ of cerium

oxide (κ_{CeO_2} 14.2 W/Km [163]) is taken into account in this calculation, the T_{gap} is 86 °C higher than T_{reactor} , without considering the 15 %wt. portion of Ni, which has κ 7 times larger than ceria and should improve the heat removal. Such temperature shift was even lower according to the heat transfer simulation proposed by Wang et al. for a DBD reactor with a similar design as the one reported in this work [123]. According to their calculations, the temperature drop due to the dielectrics (quartz and alumina) and the catalyst is only 6 °C (at 21 W, 20 mL/min) and it reported to be almost negligible between the reactor surface and the catalyst bed [123].

4.3.2 Comparison with empty DBD reactor and packed with metal oxide supports

The impact of catalysts having different physicochemical properties has been assessed in the previous section, however it should be considered the eventual reactions occurring in plasma in the empty DBD reactor or using powdered materials as packing that are not considered as catalysts. For this purpose, two different commercial supports were used (CeO₂ from Sigma-Aldrich, and Al₂O₃ from Samsol) and compared to one of the synthesised supports without nickel phase (DOE0). The powders were sieved to keep the fraction with particle size 200-25 μm . The results of CO₂ conversion and selectivity to CH₄ and CO are reported in Figure 4.5c, d. The conversion over the power range 20-40 W is almost negligible (below 11%) compared to the results obtained with the catalysts, indicating the great influence of the presence of catalytic material on the CO₂ activation and reduction. Furthermore, the selectivity is completely switched to almost 100 % selectivity toward CO, which is the opposite of the Ni/DOE catalysts (>99% to CH₄). The C_{balance} is adequate in all cases (empty, commercial CeO₂ and Al₂O₃) except for DOE0 support, which results in 78 % C_{balance} for the point at highest conversion. This is maybe due to the interaction of CO₂ with non-stoichiometric ceria and the adsorption on the defects and basic sites on the surface of ceria nanoneedles, which is expected to be more reducible and have more OV compared to the commercial CeO₂ and to non-reducible materials such as Al₂O₃.

With growing power, the T_{reactor} increases from 112 to 164 °C for the empty reactor and from 105 to 150 °C according to the material. In general, the temperatures that were measured are similar to the reactor heating that occurs during the methanation reaction with the Ni/DOE catalysts, and slightly lower with supports as packing material compared to the empty DBD.

It can be concluded that without a catalyst (with any material lacking an active phase or without any packing) in the plasma discharge only the CO₂ splitting reaction takes place, with very low yield as shown previously for DBD reactors [114,117]. The presence of Ni or an equivalent active phase is probably required for the adsorption and activation of H₂ on the active phase particles, which then participates to the methanation reaction pathway. This hypothesis is proved by the comparison of ceria and alumina supports alone (Figure 4.5) and impregnated with 15 %wt. Ni (Ni/DOE0, Ni/CeO₂ and Ni/Al₂O₃), whose results can be found in Figure 4.2 and Annex 1.

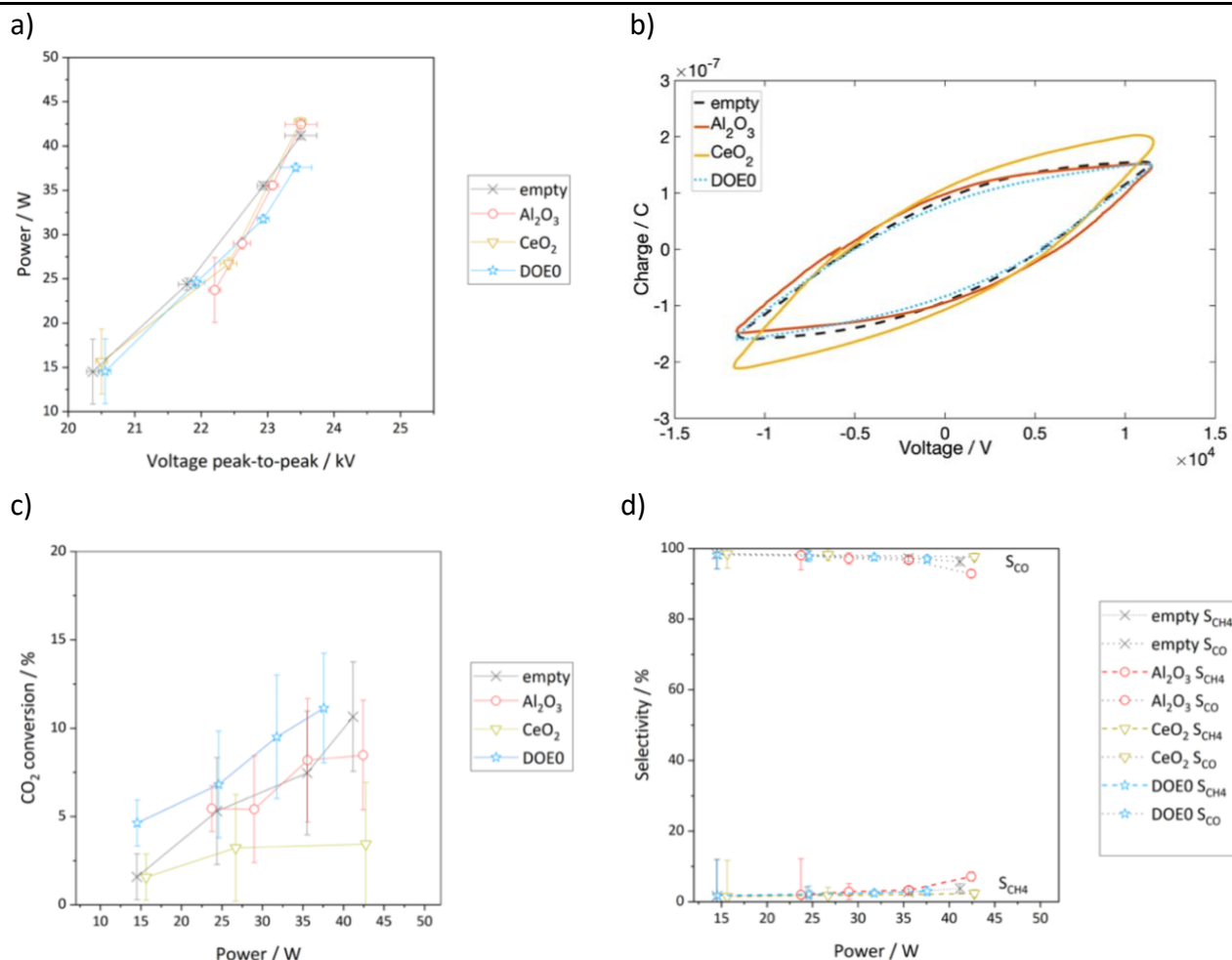


Figure 4.5: a) Power as a function of the applied voltage b) Lissajous figures at 23 kV_{p-p} applied voltage c) CO₂ conversion and d) CH₄ and CO selectivity results of plasma-assisted CO₂ methanation tests performed with the empty reactor and with commercial CeO₂ and Al₂O₃, and DOE0 supports as a function of injected power. H₂/CO₂ = 4, WHSV 30000 mL/hg_{cat}.

The comparison of the shape of the Lissajous figures of the empty DBD reactor and the different packing materials is analysed in Figure 4.5b. The graph of the empty reactor has the narrowest cycle, together with DOE0 and Al₂O₃, and the smallest slope of the “off” part among these examples (2.17 pF). Al₂O₃ packing has, as expected by its low ϵ_r (9-10 compared to ϵ_r of ceria that is 23 [164,165]), the lowest C_{reactor} (2.66 pF), which is very similar to the slope of the Lissajous figure of the empty DBD reactor. In addition, the C_{reactor} values of the ceria samples (DOE0 and commercial) are very different as well as the charge transferred at 23 kV_{p-p}, proving how the physicochemical properties and not just the chemical composition has an impact on the dielectric properties of material. The same ranking of C_{reactor} Al₂O₃ < CeO₂ is confirmed after the Ni addition (see Annex 1) although no relevant differences of Lissajous cycles of these Ni catalysts can be reported.

The results with the catalyst supported on commercial materials are similar to the Ni/DOE3 and 4 catalysts, with high conversion achieved only above 35 W. The optimal behaviour of some ceria nanostructures (Ni/DOE0, 1, 5) is not observed for the case of these benchmark catalysts.

4.3.3 Thermal CO₂ methanation

The thermal catalysis experiments are carried out in a packed bed reactor heated with an external furnace with the catalysts reduced in-situ at 600°C. The results of CO₂ conversion and CH₄ selectivity as a function of temperature are reported in Figure 4.6a and b, respectively.

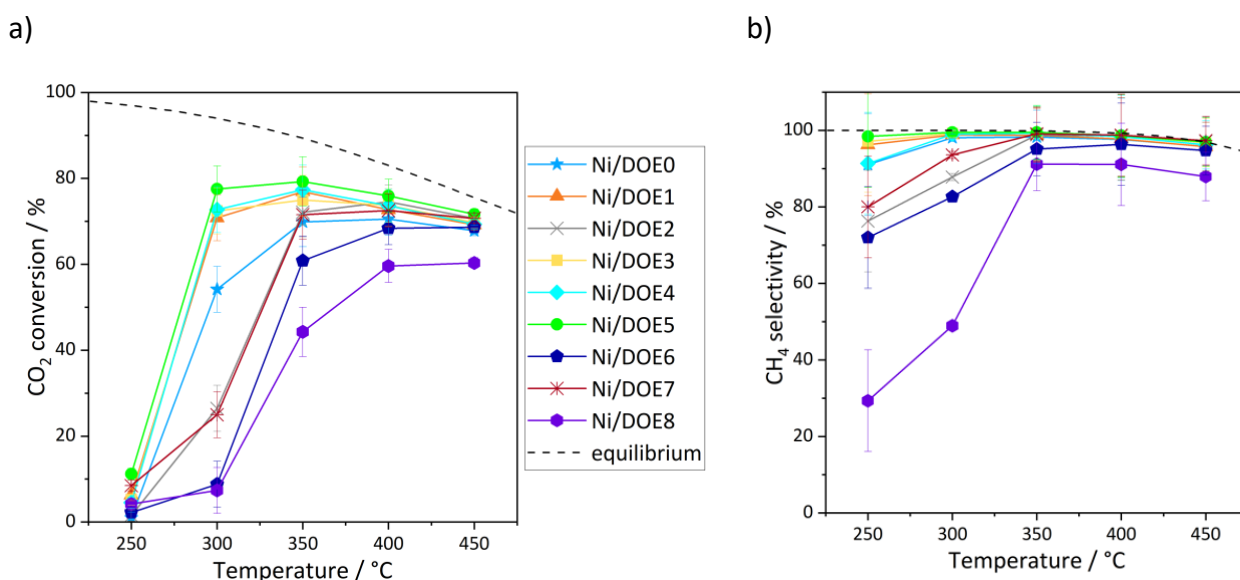


Figure 4.6: a) CO₂ conversion and b) CH₄ selectivity results of thermal CO₂ methanation tests with the Ni/DOE0-8 catalysts as a function of temperature. H₂/CO₂ = 4, WHSV 30000 mL/hg_{cat}. The equilibrium curve is added in dashed line.

The conversion in the thermal reaction is negligible at 250 °C for all samples. The catalytic reaction starts at 300 °C for some catalysts (Ni/DOE1, 3, 4, and 5) with CO₂ conversion maxima at 350 °C above 70 % and 100% selectivity to CH₄ to slowly decrease both conversion and selectivity to CH₄ at a higher temperature, as predicted by the thermal equilibrium calculations. The results of CO₂ conversion and CH₄ selectivity acquired with synthesised nanostructured Ni/CeO₂ catalysts of the DOE series are similar to published results of CO₂ methanation obtained at similar conditions and with catalysts with the same composition [80,166]. Similarly to previous reports, at temperatures lower than 350 °C the conversion is far from the value expected by the thermodynamic equilibrium calculations [80,166,167]. The good activity of Ni/CeO₂ catalysts above 300 °C has been ascribed to the presence of both metallic Ni and CeO₂ active sites for H₂ dissociation and CO₂ adsorption, respectively [166]. All Ni/DOE samples are good catalysts for CH₄ selectivity even at lower temperatures and conversion (above 70 % for low conversion, and above 98 % for high conversion), with the exception of Ni/DOE8. This catalyst results in poor methane selectivity in both plasma-assisted and thermal methanation experiments, probably due to the deficient basicity of the surface. Comparing the results obtained with the plasma-assisted tests, the optimal temperature

observed in thermal catalysis of 350 °C is much higher (200 °C difference) than the one recorded previously for similar conversion (Figure 4.4).

Finally, the thermo-catalytic results obtained with catalysts Ni/CZ and Ni/CeO₂ supported on commercial materials (Annex 1) resemble the activity of best-performing cases of the Ni/DOE series, meaning Ni/DOE1, 3, 4, and 5, which is in line with previous thermal CO₂ methanation reports (73 % at 300 °C over Ni/CZ) [167,168]. This similarity in activity with benchmark materials points to the good selection of appropriate physicochemical features by tuning of the hydrothermal synthesis parameters.

4.3.4 Comparison of thermal and plasma-assisted processes

Table 4.1 compiles the results obtained from Ni/DOE series catalysts in plasma at isopower condition (21.2 ± 2.0 W) and for the thermal catalytic results at a temperature of 300 °C. It contains the values of CO₂ conversion, CH₄ selectivity and energy efficiency for plasma-assisted and thermal methanation for Ni/DOE0-8. These two points were selected for a critical comparison of the two catalytic techniques as at these conditions the reaction occurs most efficiently for the best performing catalysts. It is relevant to evaluate the efficiency, especially for plasma-assisted catalysis, in order to compare the catalysts as it takes into account both the conversion as amount of methane produced and the power injected to sustain the plasma (or to heat the reactor in the thermochemical case). For the plasma case, also the power and C_{reactor} are reported for Ni/DOE0-8.

Table 4.1: Results obtained from CO₂ methanation test in DBD plasma with peak-to-peak applied voltage 22.3-24.3 kV_{p-p} at 12.3 kHz (21.2 ± 2.0 W) and in the thermal reactor at 300 °C (289 W).

Sample	Plasma-assisted methanation						Thermal methanation		
	X _{CO₂} , %	S _{CH₄} , %	Power, W	T _{reactor} , °C	C _{reactor} , pF	Efficiency, %	X _{CO₂} , %	S _{CH₄} , %	Efficiency, %
Ni/DOE0	82.5	98.7	20.9	147	2.99	32.2	54.2	98.1	1.8
Ni/DOE1	83.5	100	23.2	154	3.17	29.6	70.8	98.8	2.1
Ni/DOE2	8.6	/	22.8	110	4.65	1.5	26.5	87.8	0.5
Ni/DOE3	7.3	/	20.4	106	4.06	1.2	72.4	99.2	2.1
Ni/DOE4	5.7	/	19.2	112	5.11	1.4	72.7	99.0	2.1
Ni/DOE5	70.3	93.7	20.1	144	3.50	30.7	77.5	99.5	2.2
Ni/DOE6	5.9	/	19.9	124	3.40	2.5	8.8	/	0.1
Ni/DOE7	4.9	/	20.6	116	4.09	1.1	25.0	93.6	0.9
Ni/DOE8	3.5	/	22.1	124	4.40	0.3	7.3	/	0.1

For comparison with the thermal reaction the reactor temperature measured during the plasma-assisted test is also reported. The reaction assisted by plasma occurs at a lower reactor temperature compared to the thermal catalysis test, the minimum temperature at which methanation occurs in plasma is at least half the temperature used in the thermal test, e.g., Ni/DOE1 has 83.5 % conversion at 154 °C (23.2 W) in plasma against 70.8 % at 300 °C for the thermal test. This comparison still stands if the temperature correction of equation (4.1) is taken into account, leading to T_{gap} of 240 °C for the plasma-assisted methanation, at a similar temperature (250 °C) the conversion in the thermal catalysis reactor is indeed negligible.

The energy efficiency of both techniques is calculated using the methods in eq. (2.12) and described in section 4.2.1. As reported in Figure 4.1 the power required to heat up the furnace is much higher than the one injected to the plasma discharge, therefore the energy efficiency of thermochemical methanation is one order of magnitude lower than the plasma reaction. The energy efficiency is used in this study as a parameter for comparison between the Ni/CeO₂ catalysts in the thermal and plasma-assisted catalysis methods and it is not meant to be considered as an optimised result. In fact, also the DBD set-up and its power generator have not been purposely designed for optimal energy efficiency and further reactor design studies should be carried out for an improved performance. Enhanced efficiency results have been previously reported in plasma catalysis studies for CO₂ methanation with Ni catalysts, reaching 72 % energy efficiency with Gd doped Ni/CZ catalyst at higher frequency (70 kHz) and lower injected power (7.5 W) [109]. In plasma catalysis, another important parameter is the specific energy input (SEI), which is the ratio of power over the input gas flow, as described in equation (2.11) [83]. The tests in the DBD reactor were all performed at constant gas flow (100 mL/min), therefore the only factor that affects the SEI is the power calculated from the Lissajous Q-V cycle. For the condition reported in Table 4.1, the SEI ranges from $1.1 \cdot 10^4$ J/L (Ni/DOE0) to $1.3 \cdot 10^4$ J/L (Ni/DOE1). However, for the power range 10-50 W which is considered for the catalytic tests the SEI spans $7.8 \cdot 10^3$ - $4.4 \cdot 10^4$ J/L, which lies in the range reported in literature for DBD plasma used for similar reactions and described in Figure 1.12. In the plasma DBD reactor, the most efficient methanation reaction is achieved by Ni/DOE0, 1, and 5, with the best results obtained by Ni/DOE0. This catalyst with needles morphology reached 82.5 % conversion and 98.7 % CH₄ selectivity at 20.9 W and 147 °C reactor temperature. Ni/DOE0 is linked with the smallest C_{reactor} of the Ni/DOE series but is not the most active catalyst for thermal CO₂ methanation at 300 °C, in fact, it results in 54.2 % conversion. The most efficient catalysts (2.2-2.1 %) in thermal methanation are Ni/DOE1, 3, 4, and 5. Ni/DOE5 achieves the highest conversion in the thermochemical process with 77.5 % conversion and 99.5 % CH₄ selectivity at 300 °C. Ni/DOE2, 6, 7, and 8 achieve poor reaction yield in both methods, this is probably linked with their unfavourable physicochemical properties for a catalyst applied to CO₂ methanation.

4.3.5 Impact of DOE factors and physicochemical properties on the catalytic performance

In the previous section in Table 4.1 it was possible to appreciate the different activity of the Ni/DOE catalysts in plasma-assisted and thermal methanation. These variations in the catalyst behaviour can be linked with their physicochemical characteristics shown in 3.3.4 and 3.3.5, meaning crystallite size, textural properties, reducibility, and basicity. For both processes (plasma and thermal) it can be concluded that the catalysts possessing large Ni and CeO₂ crystallite size, low surface area and lacking intermediate strength basic sites achieve a poor methanation yield. These features can be grouped as poor physicochemical properties for catalyst designed for the methanation reaction [169,170]. This is the case of samples Ni/DOE6 and 8, that have large Ni and CeO₂ crystallite size (above 30 nm), the lowest S_{BET} of the batch as well as low medium strength basicity. Ni/DOE2 and 7 also present low conversion in plasma due to the lesser amount of intermediate basic sites (32 and 41 %, respectively) and small surface area of Ni/DOE2 (23 m²/g).

The surface area and medium strength basic sites amount are considered in this study as the most relevant physicochemical properties determining the quality of a material as CO₂ methanation catalyst. The relationship of the activity in thermal and plasma-assisted methanation with these two features is shown in the plots in Figure 4.7. In this section, the activity of the catalysts is quantified with two different parameters for the plasma-assisted and thermal reactions, meaning energy efficiency and CO₂ conversion, respectively. For the thermochemical process, the power considered for each temperature setting of the furnace is the same for every catalyst, as explained in section 4.2.1, and the selectivity is generally high. Therefore, in this case, the efficiency, which depends on CH₄ production and power requirement as in eq. (2.12), and the CO₂ conversion at the same temperature point are equivalent descriptors of activity of the catalyst that is examined. For the plasma-assisted process, the efficiency at 30.9 ± 3.8 W calculated with equation (2.12) is used (results reported in

Table 4.2). Energy efficiency is a more accurate description of the behaviour of the catalyst in plasma for comparisons as it takes into consideration not only the CO₂ and H₂ conversion and production of methane but also the power required for this reaction, which, as observed in Figure 4.2, significantly varies with different materials. The selected results reported in

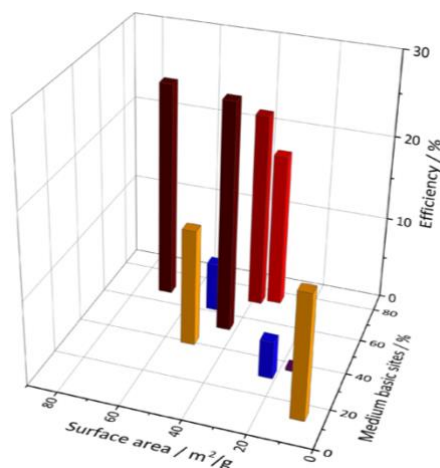
Table 4.2 correspond to a different power condition compared to what was discussed in Table 4.1. In the previous section, the aim was to show the best performance in terms of efficiency for the most active catalyst (e.g., Ni/DOE0). In this section, instead, the focus is on choosing a power condition at which most catalysts of DOE series achieve conversion of at least 50 % and the most diverse behaviour regarding plasma-assisted CO₂ methanation among the Ni/DOE samples is observed. Therefore, the aim is to highlight the differences in activity in plasma of the catalysts depending on their properties. The thermal catalysis results at 300 °C that were reported in Table 4.1 are considered again in this section. In fact, the 300 °C temperature point is the most efficient

one for catalysts such as Ni/DOE5, but also, as can be observed in Figure 4.6a, shows the largest variation in terms of CO₂ conversion among Ni/DOE catalysts, which allows to appreciate differences in activity depending on physicochemical properties.

Table 4.2: Results obtained from CO₂ methanation test in DBD plasma with power 30.9 ± 3.8 W.

Sample	Plasma-assisted methanation				
	X _{CO₂} , %	S _{CH₄} , %	Power, W	T _{reactor} , °C	Efficiency, %
Ni/DOE0	83.3	99.7	27.1	158	27.0
Ni/DOE1	81.7	98.0	31.3	177	23.0
Ni/DOE2	13.2	75.7	27.3	123	4.4
Ni/DOE3	52.9	99.6	23.4	135	18.3
Ni/DOE4	15.9	77.4	27.2	129	5.8
Ni/DOE5	80.3	100	28.3	170	25.6
Ni/DOE6	44.7	90.3	32.8	151	14.7
Ni/DOE7	46.9	93.5	34.7	146	13.8
Ni/DOE8	9.3	/	32.9	131	1.5

a)



b)

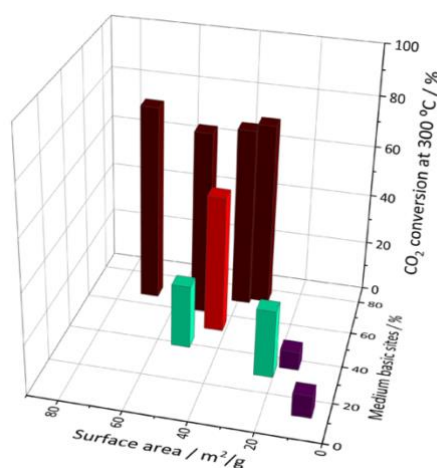


Figure 4.7: 3D plots of a) efficiency of plasma-assisted CO₂ methanation 30.9 ± 3.8 W and b) thermal CO₂ conversion at 300 °C as a function of physicochemical properties surface area and amount of medium strength basic sites.

By studying the conversion at 300 °C, it is possible to find a relationship between physicochemical properties and catalyst activity. There is a direct relationship of conversion with both percentage of intermediate strength basic sites and surface area in Figure 4.7b. Ni/DOE1, 3, 4, and 5 that achieve conversion above 70 % at 300 °C all possess the best basicity properties (large CO₂ desorption amount and fraction of intermediate strength basic sites of 64-75 %), and large surface area (especially Ni/DOE4 and 5 with 51 and 70 m²/g). For samples with similar S_{BET} around 50 m²/g it can be observed a progressive increase of the CO₂ conversion at 300 °C with improving medium strength basicity from 41 to 64 %. Ni/DOE0 is characterized by intermediate properties of S_{BET} (44 m²/g) and amount of medium basic sites (53 %), which lead to the mild conversion at 300 °C. On the contrary, the materials that have the lowest surface area and lack the preferred basic sites, as Ni/DOE2, 6, 7, and 8, do not perform well as catalysts in thermal CO₂ methanation, as discussed above. Ni/DOE6 and 8 achieve the lowest conversion among the catalysts of this series in thermal CO₂ methanation with 8.8 and 7.3 % conversion at 300 °C, respectively.

The same straightforward relationship of energy efficiency of the plasma-assisted methanation reaction with these physicochemical properties is not observed in Figure 4.7a. The intermediate basicity and large area of the catalyst surface seem to promote the reaction also in plasma, but there are a couple of cases that stand out and reveal that there are other factors to be taken into consideration in plasma catalysis. These instances are the intermediate efficiency of 14.7 % of the Ni/DOE6 sample that possesses both the lowest S_{BET} and medium strength basic sites and the low activity (5.8 %, one of the blue columns) of Ni/DOE4, compared to what expected from the thermal results, with high surface area (51 m²/g) and good basicity (64%). Furthermore, the Ni/DOE0 catalyst, which is the nanoneedles supported catalyst and does not have the most favourable physicochemical features for methanation, is the catalyst reaching the most efficient reaction in plasma within this series.

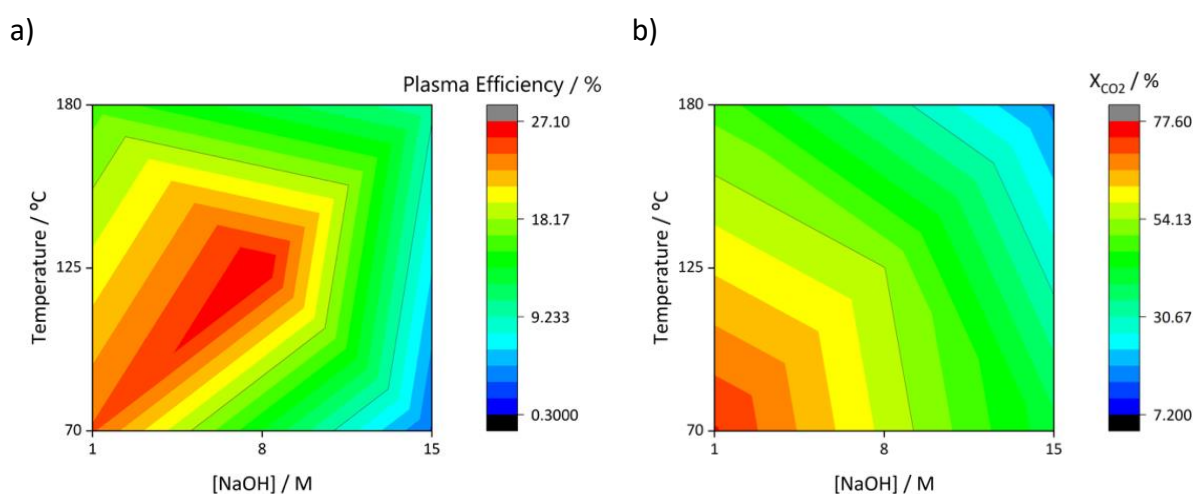


Figure 4.8: Contour plots of a) efficiency of plasma-assisted CO₂ methanation at 30.9 ± 3.8 W and b) thermal CO₂ conversion at 300 °C as a function of hydrothermal synthesis parameters NaOH concentration and temperature.

To further show these differences of impact of catalyst properties on the plasma-assisted and thermal reactions, the contour plots in Figure 4.8 are reported to show the activity as a function of the synthesis parameters NaOH concentration and temperature, that in Section 3.3.2 were established as the most relevant ones for the outcome of the hydrothermal synthesis of the ceria supports and of the derived catalysts. Different values of the factors determine a maximum of efficiency in plasma and X_{CO_2} at 300 °C, 8 M - 125 °C and 1 M – 70 °C, respectively. The activity for both processes decreases for the catalysts synthesised with 15 M NaOH solutions, reaching the minimum at 15 M – 70 °C in plasma and at 15 M – 180 °C in thermal methanation. In general, small ceria crystallite size, intermediate basic sites, and good surface area, which are obtained with catalysts supported on ceria synthesised at low temperature and with low [NaOH], promote a good activity of the catalyst, but these features are not univocally linked to conversion in plasma. Therefore, there are more properties of the samples that could come into play when an electrical discharge is applied to create the plasma around them.

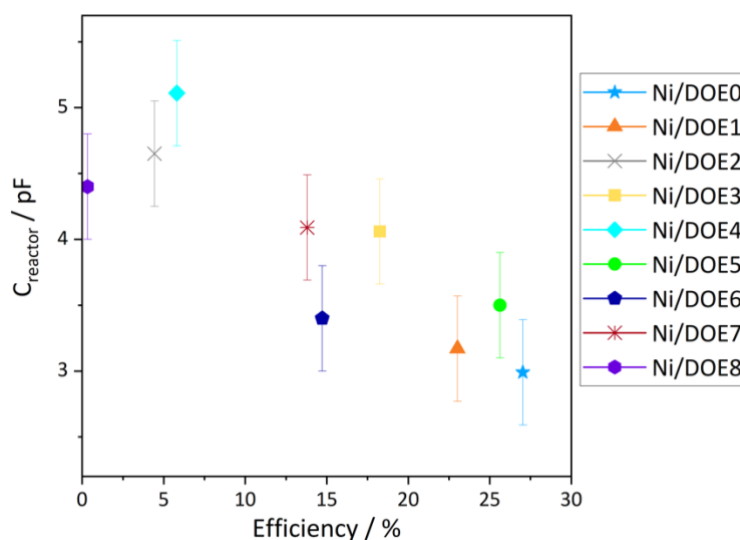


Figure 4.9: C_{reactor} plotted as a function of efficiency of the plasma-assisted CO₂ methanation reaction carried out at 30.9 ± 3.8 W.

The dielectric properties of the packing materials help describing the activity of the Ni/DOE catalysts in the plasma-assisted CO₂ methanation reaction. This feature was touched upon in the section 4.3.1 and is quantified by the C_{reactor} value already reported in Table 4.1. The efficiency of the plasma-assisted reaction at 30.9 ± 3.8 W is reported in Figure 4.9 plotted against the values of C_{reactor} . From the three repetitions of the plasma-assisted methanation tests the error for the energy efficiency is measured (± 0.3 %). At this condition, a relationship between the plasma catalytic activity and the dielectric properties of the packed DBD reactor can be extrapolated, leading to higher efficiency with smaller C_{reactor} . The C_{reactor} is directly proportional to the resulting dielectric permittivity of the

packed bed DBD cell, which considers the permittivity of the material that is used to pack the plasma reactor as well as of the dielectric materials of the DBD and of the gas in the gap. Smaller C_{reactor} , therefore smaller dielectric permittivity of the Ni/CeO₂ materials such as Ni/DOE0, 1, and 5, leads to more efficient CO₂ conversion to methane in DBD plasma. Such dependency has already been illustrated by Mikhail et al. [109], the authors suggest that catalysts with low dielectric constant should be used in plasma-assisted CO₂ methanation as a high polarisation of the surface of the catalyst is not favourable for the conversion of CO₂ to methane, instead it would promote the splitting to CO. As one would expect, the C_{reactor} factor is not related to the conversion in thermal catalysis.

The dielectric permittivity should be taken into account together with the physicochemical properties to assess the catalyst activity in plasma. It is revealed that a high C_{reactor} above 4 pF, and therefore large dielectric permittivity of the material, which is the case of Ni/DOE2, 3, 4, 7, 8, is unfavourable for a good performance for this reaction in DBD plasma. For Ni/DOE6 poor physicochemical features intersect with a low C_{reactor} (3.4 pF), however, the good dielectric response is not sufficient to outbalance the large CeO₂ crystallite size, small surface area and absence of appropriate sites for CO₂ adsorption. In the case of Ni/DOE3 and 4, this adverse dielectric property overlaps with advantageous physicochemical features, which leads to a satisfactory conversion but at higher power consumption, hence low efficiency of the catalysts in plasma. The intersection of low C_{reactor} with small CeO₂ crystallite size (Table 3.4), good OSC of the ceria support (as for DOE0 and 5, reported in Table 3.3), high amount of medium strength basic sites (Table 3.7), large surface area, and small pore width (Table 3.4) leads to the most efficient catalysts in plasma-assisted CO₂ methanation, meaning Ni/DOE0>5>1. It should also be mentioned that the catalysts that reach the best plasma-assisted CO₂ methanation yield, i.e., Ni/DOE0 and 5, have similar anisotropic morphology, just with different particle size (length of the support particles 188 to 32 nm, respectively). In fact, it was shown by TEM imaging (Figure 3.5) that the supports DOE0 and DOE5, with nanoneedles and nanorods morphology, grow long $\langle 011 \rangle$ axis, which facilitates OV formation, and have an elongated shape (see Table 3.3). Moreover, good OSC of the ceria support has been previously linked with electrochemical properties and ionic conductivity [171] and low permittivity. The link between physicochemical, dielectric properties, and catalytic activity in DBD plasma is depicted in the 3D plot in Figure 4.10, where efficiency in plasma-assisted methanation is reported versus C_{reactor} and medium strength basicity. The inversely proportional relation between efficiency and C_{reactor} is confirmed, but it can also be appreciated that for two samples having similar C_{reactor} around 3.5 pF (Ni/DOE5 and 6) the increase of intermediate strength basic sites has a positive effect on the activity: efficiency improves from 15 to 26 % and the CO₂ conversion at 31 W from 80 to 45 % for Ni/DOE5 and 6, respectively. Therefore, an efficient Ni/CeO₂ catalyst for plasma-assisted methanation must possess the intersection of properties of low dielectric permittivity and good surface basicity for interaction with CO₂.

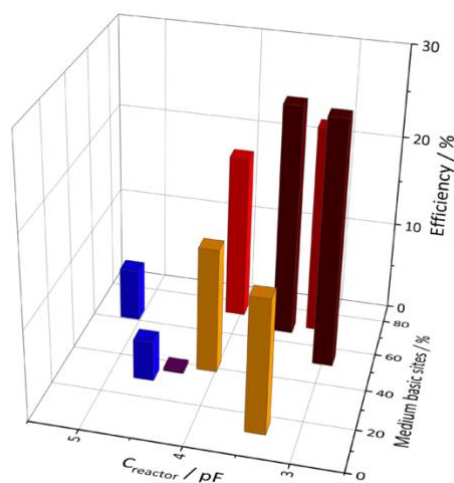


Figure 4.10: 3D plots of efficiency of plasma-assisted CO₂ methanation at 30.9 ± 3.8 W as a function of catalyst properties C_{reactor} and amount of medium strength basic sites.

To conclude, it can be established that the physicochemical properties required by a catalyst in thermal methanation are not directly translated in the plasma-assisted case. In fact, the dielectric behaviour of the material influences its efficiency in plasma catalysis. The different yield of the Ni/DOE catalysts in plasma and thermal methanation suggests an effect of plasma-catalyst interaction and a dissimilar reaction mechanism in both cases. These will be analysed in the following chapters with an in-depth analysis of the electrical behaviour of the DBD reactor with different packing materials and operando study of both thermal and plasma-assisted catalytic reactions.

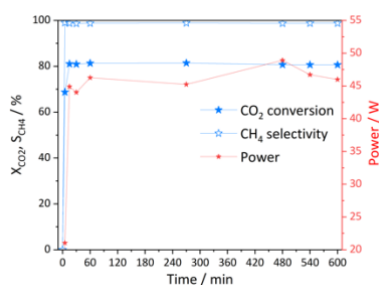
4.3.6 Stability tests

Stability tests both in the DBD and thermal set-ups with selected catalysts were performed over 10 hours at comparable conditions of 50 W power and 350 °C, respectively. The samples that were picked are the best catalysts in plasma and thermal reaction, Ni/DOE0 and 5, respectively, and the catalyst which reached low conversion in both cases (Ni/DOE6). These samples also represent the two extremes and centre point of the factors used in the DOE study performed for the ceria supports synthesis. The results of X_{CO_2} and S_{CH_4} over 600 minutes are reported in Figure 4.11. For the plasma-assisted CO₂ methanation also the power over the 10 hours experiments was monitored in Figure 4.11a-c.

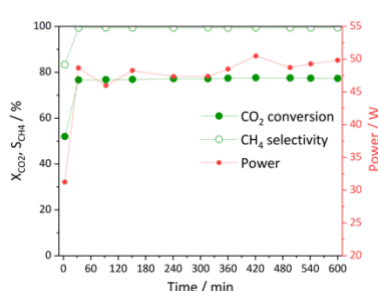
The CO₂ conversion and CH₄ selectivity for the plasma-assisted CO₂ methanation follow the same ranking reported in the section 4.3.1. Both Ni/DOE0 and 5 have good and stable conversion and >99 % selectivity to methane results, with Ni/DOE0 reaching a bit higher conversion with smaller power

injected (81 % at 45 W average). The power increases in the first 30 minutes for all catalysts and then stabilizes with ± 1.6 W fluctuations at 46, 48 and 50 W for Ni/DOE0, 5, and 6, respectively. As expected, with Ni/DOE6 catalyst the lowest conversion is achieved both in thermal and plasma reactions. In plasma the conversion decreases between 30 minutes and 10 hours from 29.4 to 25.8 % (Figure 4.11c). In the thermochemical reaction at 350 °C the conversion with Ni/DOE6 increases from 25 to more than 60 % from 0.5 to 1 h, which is then maintained from 1 to 10 hours with adequate selectivity above 90 % (Figure 4.11f). In the plasma-assisted 10 hours reaction Ni/DOE6 also shows lower selectivity at around 70 % compared to the thermal experiment with the same catalyst and results obtained with Ni/DOE0 and 5. Ni/DOE0 has similar activity in plasma-assisted and thermal CO₂ methanation with conversion close to 80 %, which is comparable within the error to the previous results reported in Figure 4.2 and Figure 4.6. Ni/DOE0 catalyst seems to be more stable in the thermal reaction than Ni/DOE5, which decreases 5 % in conversion. Generally, the Ni/CeO₂ catalyst keep a stable activity at these conditions both in plasma and thermal CO₂ methanation over 10 hours.

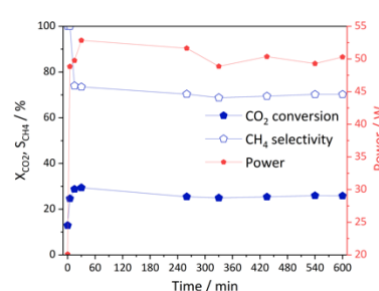
a) Ni/DOE0



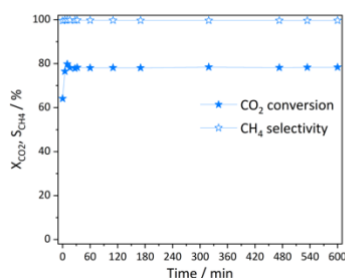
b) Ni/DOE5



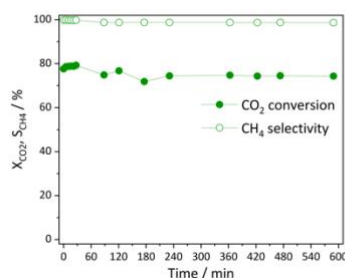
c) Ni/DOE6



d) Ni/DOE0



e) Ni/DOE5



f) Ni/DOE6

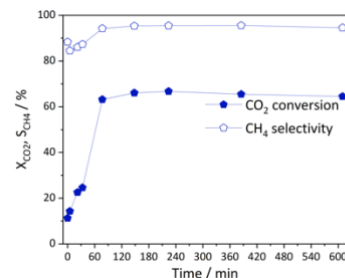


Figure 4.11: Stability tests over 10 h for Ni/DOE0, 5, and 6 of a)-c) plasma-assisted at 50 W and d)-f) thermal CO₂ methanation performed at 350 °C. H₂/CO₂ = 4, WHSV 30000 mL/hg_{cat}.

4.3.7 Characterisation of the catalysts after plasma-assisted and thermal reaction

The plasma exposure and methanation reaction can influence the physicochemical properties and surface of the Ni/CeO₂ catalysts. To study the effect of both plasma and thermal methanation on the catalysts, they were analysed by several techniques such as XRD, XPS, FTIR, TPD-MS, and electron microscopy (TEM and SEM).

In Figure 4.12 the XRD diffractograms of catalysts after plasma and thermal reactions are reported. The analysis of the catalysts after thermal methanation was carried out only on selected samples due to the limited amount of the recovered material. It is observed that only the metallic Ni phase is present in the sample and no NiO phase, meaning that there has not been bulk reoxidation of the active sites. The results of the Rietveld analysis of Ni/DOE samples after plasma-assisted and thermal methanation are reported in Table 4.3.

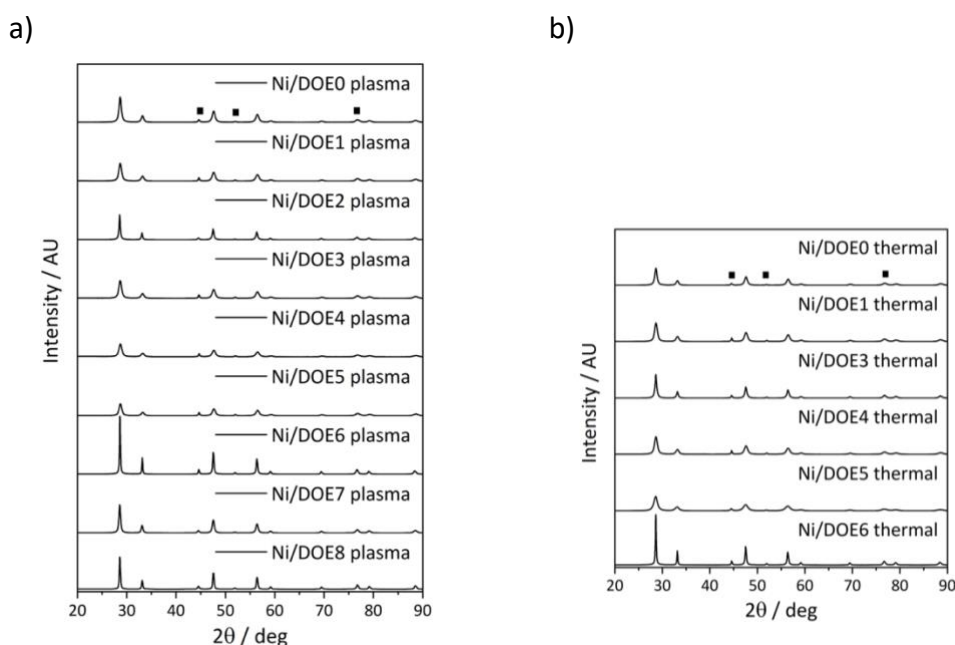


Figure 4.12: XRD diffraction patterns of the Ni/DOE catalysts after a) plasma exposure and b) thermal reaction. The cubes indicate the peaks of the Ni phase.

Table 4.3: Crystallite size of cerianite and nickel phases of samples Ni/DOE after the plasma-assisted and thermal catalytic reaction. The percentual variation compared to the crystallite size of the reduced catalysts is reported in brackets.

Sample	After plasma		After thermal	
	CeO ₂ Crystallite size, nm	Ni Crystallite size, nm	CeO ₂ Crystallite size, nm	Ni Crystallite size, nm
Ni/DOE0	11.2 (-36 %)	14.7 (-17 %)	10.7 (-39 %)	14.4 (-19 %)
Ni/DOE1	10.7 (28 %)	23.4 (71 %)	9.6 (14 %)	21.8 (59 %)
Ni/DOE2	15.9 (-30 %)	14.0 (-13 %)	NA	NA
Ni/DOE3	15.4 (2 %)	17.6 (-21 %)	14.9 (2 %)	17.7 (-20 %)
Ni/DOE4	9.5 (-14 %)	21.9 (3 %)	9.0 (-18 %)	25.8 (22 %)
Ni/DOE5	11.0 (5 %)	25.5 (-13 %)	7.4 (-29 %)	17.3 (-41 %)
Ni/DOE6	33.6 (-6 %)	30.2 (1 %)	35.6 (-11 %)	31.6 (5 %)
Ni/DOE7	17.2 (0 %)	13.7 (-10 %)	NA	NA
Ni/DOE8	32.2 (-10 %)	18.6 (-17 %)	NA	NA

The comparison with the crystallite sizes of the reduced samples in Table 3.4 reveals a variation of Ni and CeO₂ crystallite sizes, which is reported as percentage of the initial value in Table 4.3 in brackets. It should be mentioned, however, that this XRD analysis showed no variation of the lattice parameter of the cerianite phase, maintaining a 5.41 Å. The change in crystallite size is observed both in the plasma-assisted and thermal case, so it cannot be considered as a plasma effect but rather a consequence of the exposure to the reaction gas mixture of CO₂/H₂. For the needles supported catalyst (Ni/DOE0) a redistribution of the ceria and nickel phases occurs during the reaction with a decrease above 35 % of the CeO₂ crystallite size and a diminution of 3 nm for the Ni phase. It was shown in previous publications that plasma pre-treatment can improve Ni dispersion and catalyst activity in thermal methanation [172]. Also, for Ni/DOE2 after plasma exposure a shrinking of Ni and CeO₂ are observed of 30 % and 13 %, respectively. Instead, CeO₂ and Ni crystallite sizes of Ni/DOE1 increase. Ceria crystallites grow of 28 % and 14 % and Ni crystallite size increases from 13.7 nm to 23.4 and 21.8 nm after plasma and thermal reactions, respectively. The cerianite and Ni phases of the other catalysts are not greatly affected by the plasma exposure. Sample Ni/DOE5 undergoes an important size variation after the thermal reaction, with Ni crystallite shrinking from 29.2 to 17.3 nm, which does not occur under plasma exposure. The Ni and CeO₂ crystallite sizes of Ni/DOE6 are not affected in both cases. This reorganization of the crystallites of nickel and ceria could be linked to the more intense activity of these samples or to a variation in morphology. It was also already mentioned that the <011> facet that characterizes DOE0 and 5

supports is a reactive surface, which makes these nanostructures not completely stable and therefore more prone to size variation, compared to the catalysts supported on DOE3, which has <100> facet exposed, which is very stable.

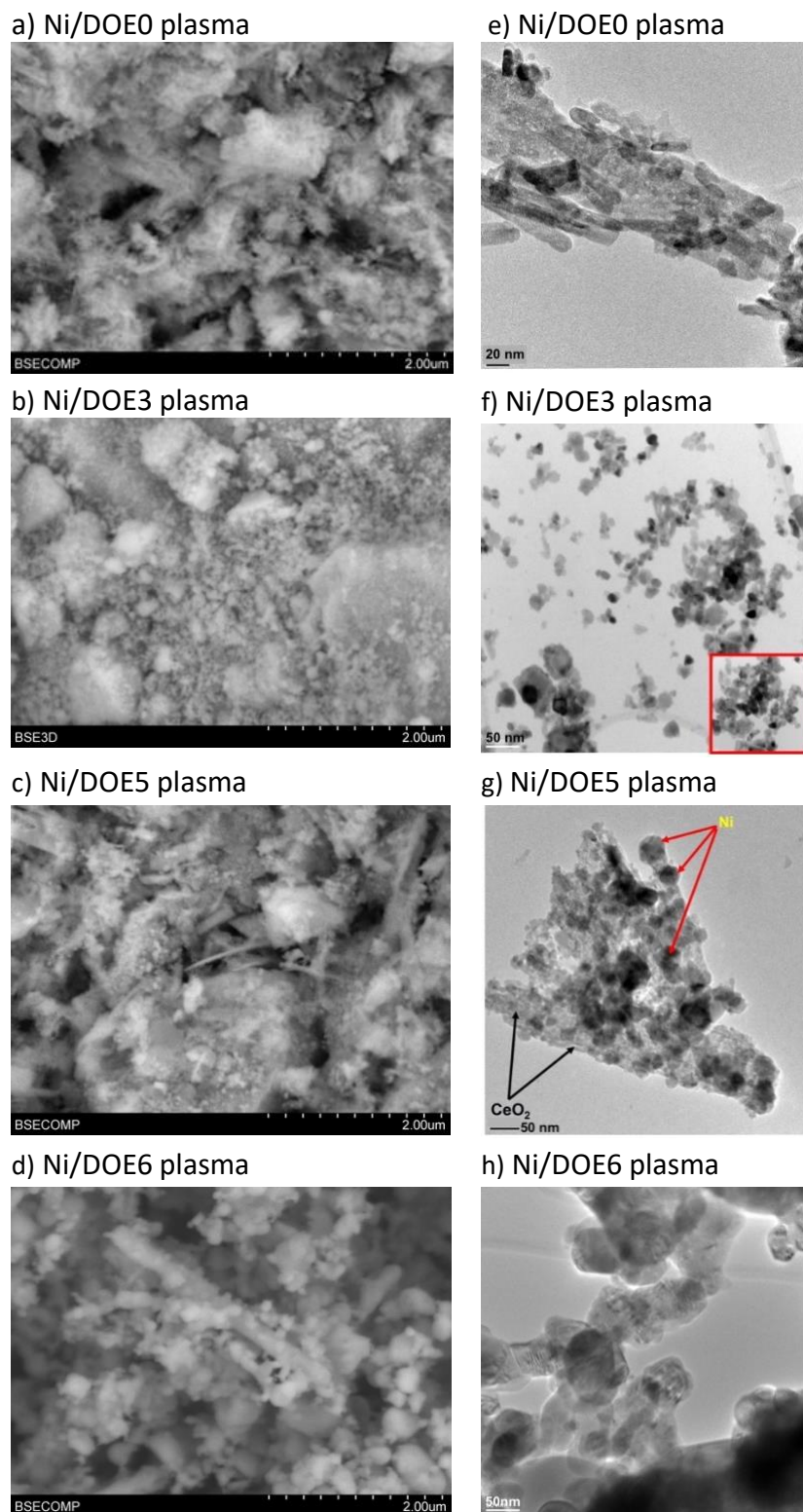


Figure 4.13: SEM micrographs and TEM images of a),e) Ni/DOE0, b),f) Ni/DOE3, c),g) Ni/DOE5, d),h) Ni/DOE6 after plasma reaction.

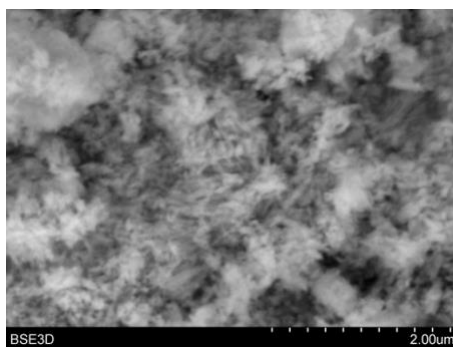


Figure 4.14: SEM micrograph of Ni/DOE0 after thermal reaction.

The appearance of the morphology of Ni/DOE selected samples (0, 3, 5, 6) after plasma exposure as observed in SEM (Figure 4.13a-d) does not vary compared to the reduced samples (Figure 3.16). And it is confirmed with a closer look by TEM in Figure 4.13e-h. The same can be stated for Ni/DOE0 after thermal methanation (Figure 4.14), which is the only sample analysed with electron microscopy after the thermal process. No carbon depositions are observed on the surface the spent catalysts, which agrees with the good stability observed after 10 hours experiment and with the maintained $C_{balance}$ as reported in previous sections.

The average length and width of the CeO₂ nanoneedle of Ni/DOE0 is 134.9 ± 97.3 nm and 15.7 ± 6.8 nm, which is virtually unvaried. The average size of the Ni nanoparticles in this sample is 9.1 ± 3.7 nm. So, there is a decrease of 24 nm in the average size of the Ni nanoparticle after plasma reaction, which agrees with crystallite size measured via XRD. Ni/DOE3 particle sizes are 11.5 ± 3.8 for CeO₂ spheres and 7.8 ± 3.4 nm for Ni, they both appear unchanged. The other samples are too agglomerated to have a size distribution measurement.

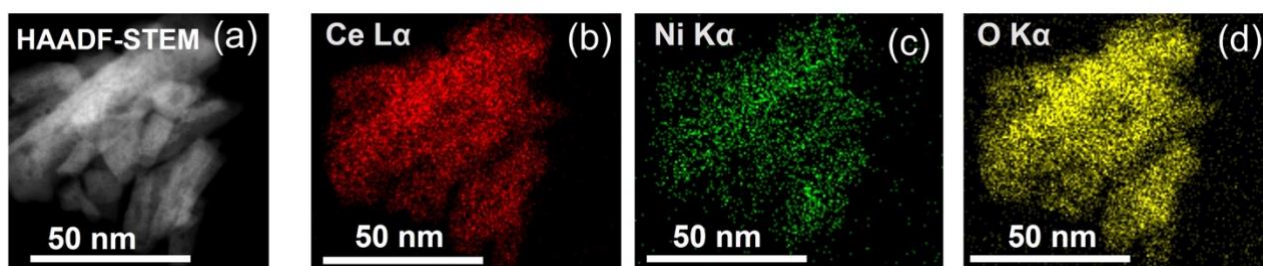


Figure 4.15: (a) HAADF-STEM image of Ni/DOE0 plasma. (b), (c) and (d) shows EDX mapping corresponding to Ce, Ni and O indicating Ni is distributed uniformly across whole sample.

The EDX analysis of Ni/DOE0 (Figure 4.15) also shows the distribution of Ni indicating very good homogeneity, which is distributed uniformly throughout CeO₂ nanorod. Nickel appears more distributed after plasma exposure compared to the reduced sample shown in Figure 3.19 in section 3.3.4, as indicated by the particle size decrease. Ni particle size decrease and enhanced dispersion

is thought to promote a stronger MSI and activity in methanation [170]. Such effect on Ni dispersion was previously reported for plasma-assisted methanation with a Ni/zeolite catalyst [103].

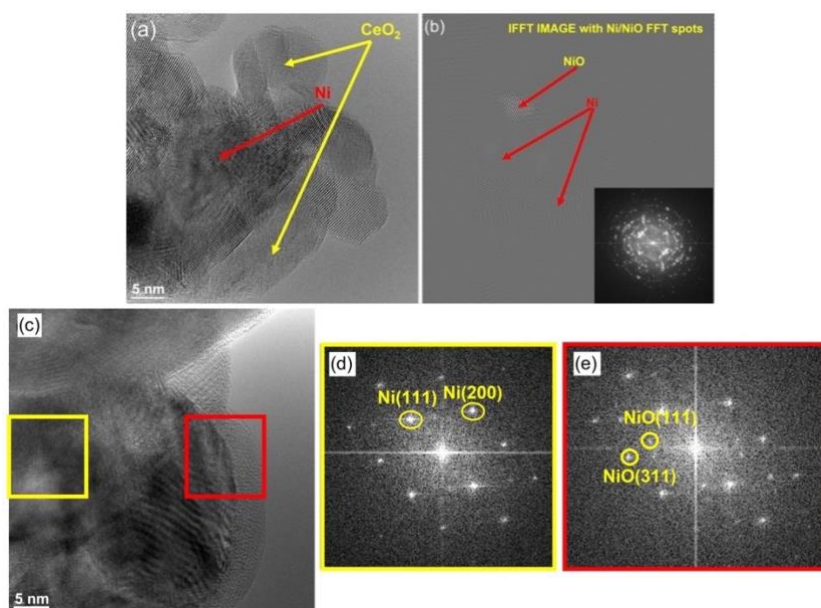


Figure 4.16: (a) HRTEM image of Ni/DOE5 plasma and (b) its corresponding IFFT image considering only the FFT spots of Ni and NiO showing locations where Ni/NiO are present in (a). (c) HRTEM image of a Ni particle of Ni/DOE6 plasma, (b) and (c) FFT images of the regions marked by yellow and red square in (a) showing the presence of Ni and NiO diffraction patterns, respectively.

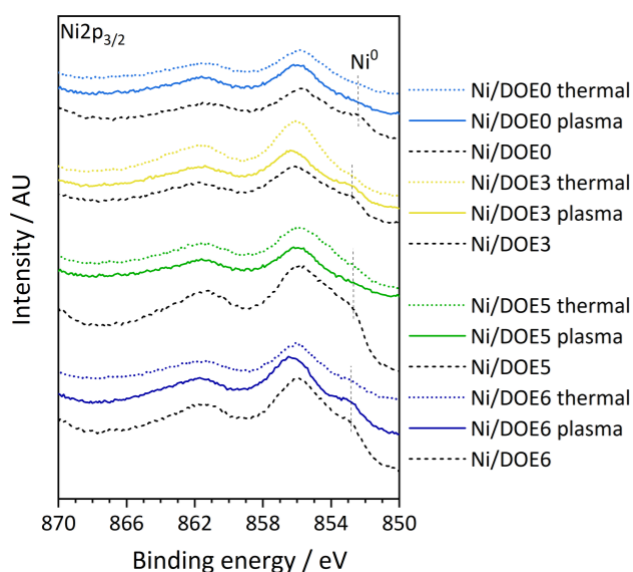
Both Ni and NiO are found on the surface of the metal nanoparticles of all samples after reaction with cases of Ni/DOE5 and 6 after plasma taken as examples in Figure 4.16. The IFFT image shown in Figure 4.16b shows the portions where Ni and NiO are present on Ni/DOE5, NiO being at the interface between Ni and CeO₂. Figure 4.16c focuses on a single Ni nanoparticle of Ni/DOE6 after plasma sample. The FFT patterns in Figure 4.16d and e show that the outer portion of the nanoparticle has dominant presence of NiO whereas the inner portion shows presence of Ni in this region.

The results of XPS analysis in Table 4.4 of the spent catalysts give some insight on the variation of oxidation state of the surface. The Ni2p, C1s (Figure 4.17) and O1s (Figure 4.18) regions of the Ni/DOE0, 3, 5, 6 catalysts analysed before reaction are studied also after plasma-assisted and thermal methanation.

Table 4.4: Results of XPS of Ni/DOE0, 3, 5, 6 after plasma exposure.

Sample	After plasma			After thermal		
	$\text{Ce}^{3+}/(\text{Ce}^{4+}+\text{Ce}^{3+})$, %	$\text{O}_{\text{surf}}+\text{O}_{\text{H}_2\text{O}}/\text{O}_{\text{tot}}$, %	Ni^0 , %	$\text{Ce}^{3+}/(\text{Ce}^{4+}+\text{Ce}^{3+})$, %	$\text{O}_{\text{surf}}+\text{O}_{\text{H}_2\text{O}}/\text{O}_{\text{tot}}$, %	Ni^0 , %
Ni/DOE0	17.3	29.8 + 9.8	9.2	17.3	39.8 + 1.7	9.9
Ni/DOE3	19.6	47.2 + 11.4	12.2	20.4	39.9 + 2.1	11.1
Ni/DOE5	18.4	50.1 + 13.9	8.9	21.4	42.0 + 1.9	16.4
Ni/DOE6	15.7	41.7 + 10.4	13.8	17.6	36.8 + 8.8	11.5

a) Ni2p



b) C1s

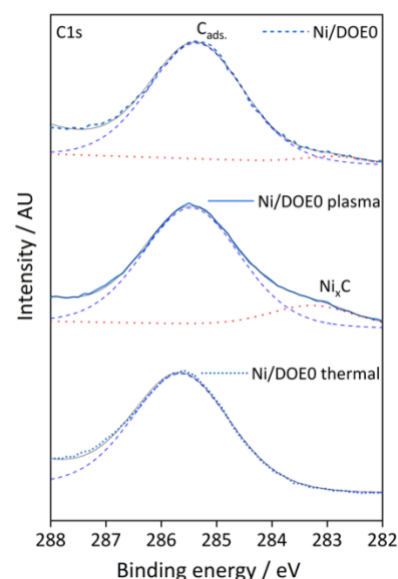


Figure 4.17: a) Ni2p XPS spectra of catalysts Ni/DOE0, 3, 5, 6 before and after plasma-assisted and thermal methanation reaction. b) C1s XPS spectra of Ni/DOE0 reduced, after plasma exposure, and after thermal methanation.

The nature of the surface of the nickel particles is checked in the XPS Ni2p_{3/2} region, reported for Ni/DOE0, 3, 5, and 6 catalysts after plasma-assisted and thermal reactions in Figure 4.17a. The spectra (already shown in Figure 3.23a) of the corresponding reduced catalysts are reported in black dashed lines as comparison with the used catalysts. The wide peak around 856 eV is present for all catalysts, both before and after catalytic reaction. As discussed in chapter 3, it is probably linked with Ni oxidation states +2 and +3, therefore to species related to defects in the Ni framework or at

the metal/CeO₂ interface or to Ni compounds formed with water and CO₂ such as Ni(OOH) and carbonates, which might increase after methanation [156]. The comparison of Ni/DOE0, 3, 5, 6 before and after CO₂ methanation shows that the metallic Ni phase is maintained, in agreement with XRD. The Ni2p spectra of the reduced catalysts have a clear contribution of the main Ni⁰ peak, which decreases after plasma-assisted and thermal methanation, proving that there is partial reoxidation of the Ni surface due to its involvement in the reaction or as intermediate adsorption site. This is quantified by the comparison of Ni⁰ % in Table 3.6 and Table 4.4, especially for the Ni/DOE5 sample. This might be linked with the Ni particles shrinking and redistributing, as is the case of Ni/DOE0 plasma and Ni/DOE5 thermal, leading to an increase of Ni²⁺ (NiO) contributions in the Ni2p spectrum and the decrease of Ni⁰ as the increased surface of the Ni particles passivates. The presence of Ni²⁺ agrees with the NiO on the surface of the metal particles seen in TEM (in Figure 4.16), probably due to a partial reoxidation at the surface of the dispersed nickel, however the contribution of this oxidation state of nickel decreases after plasma exposure for all catalysts. The environment and oxidation state of Ni changes after assisting the methanation reaction (both in thermal and plasma) and it is likely that reaction intermediates are linked with the Ni²⁺ species. An upward shift of the Ni⁰ peak is observed mainly for Ni/DOE0 after use (centred at 852.6 and 853.1 eV) could be due to an enhancement of Ni-CeO₂ interaction [154,173] and to the change in the chemical environment of the metallic Ni after contributing to the methanation catalytic reaction [174]. In fact, the C1s region in Figure 4.17b compares the spectra of Ni/DOE0 before and after methanation and shows the increase, especially after plasma, of the shoulder at lower binding energy of the main peak attributed to adventitious C [137], which has been linked in literature to Ni_xC species [175] that might take part to the reaction or grow due to the exposure of the catalyst to CO₂/H₂ plasma. However, it should be noted that such noticeable difference has not been observed for the other Ni/DOE samples.

The O1s spectra of the catalysts after plasma exposure in Figure 4.18a change compared to the spectra of the reduced catalysts in Figure 3.23b, especially Ni/DOE3, 5, and 6, due to an increase of surface oxygen, adsorbed species, and adsorbed water [81,176]. The lattice O peak is located around 530 eV, while the two peaks at higher binding energy (around 532 and 533.5 eV) increase in intensity and area compared to the reduced counterpart, probably due to the molecules remaining from the methanation reaction on the catalyst surface. The first one could be related with defects or adsorbed species such as -CO_x, while the second one at 533.5 eV is characteristic of hydroxyl groups, which could be directly on the surface or linked with chemisorbed H₂O [81,176,177]. Such large increase of the surface species contribution is not seen in Figure 4.18b for the post thermal catalysts, whose O1s spectra are similar to the ones reported in Figure 3.23b. Ni/DOE6 is the catalyst that after thermal methanation presents the most intense shoulder below 533.5 eV for OH adsorbed on the surface.

The $\text{Ce}^{3+}/(\text{Ce}^{4+}+\text{Ce}^{3+})$ ratio in Table 4.4 calculated from the deconvolution of the Ce3d region of the XPS spectrum (not shown) slightly changes after CO₂ methanation compared to the reduced catalysts (Table 3.6), maintaining values between 15.7 and 19.6 %. For Ni/DOE0, the Ce^{3+} amount decreases accordingly to Ni^0 , showing the reoxidation involving the whole surface of the catalyst.

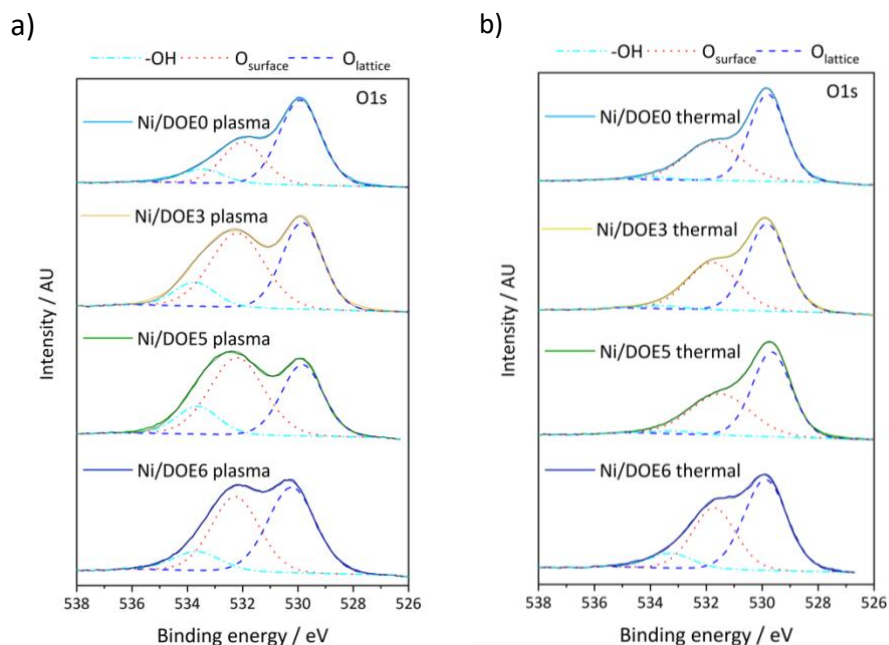


Figure 4.18: O1s XPS spectra of catalysts Ni/DOE0, 3, 5, 6 after plasma-assisted and thermal methanation reaction.

This variation of the adsorbed molecules on the Ni/CeO₂ surface was also investigated by FTIR in Figure 4.19 in the range 1800-800 cm⁻¹ and 3000-2800 cm⁻¹ for the post plasma and thermal Ni/DOE0, 3, 5, and 6 samples.

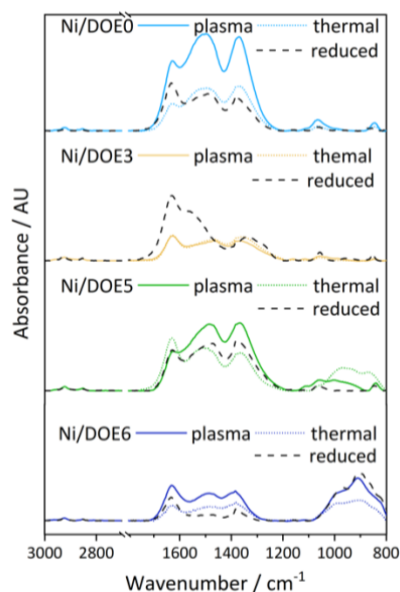


Figure 4.19: FTIR spectra of catalysts after plasma and thermal reaction.

This region is attributed to water and carbonate species, which are present also on the surface of the reduced catalysts due to adsorption of CO₂ and humidity from air (Figure 3.27). The peak at 1633 cm⁻¹ is the H-O-H bending attributed to molecular H₂O [178]. This peak is the most prominent for Ni/DOE3 after plasma and thermal methanation, which can be linked with the adsorbed species contribution in the XPS O1s spectrum (Figure 4.18a). The absorbance of the spectra of Ni/DOE3 samples after thermal and plasma reaction decreases compared to the reduced catalyst. The main contributions to the 1600-1200 cm⁻¹ region are monodentate (1486 and 1373 cm⁻¹) and bidentate carbonates peaks (1265 and 1551 cm⁻¹) [81]. Ni/DOE3 before reaction is characterised by a larger contribution of bidentate carbonate peaks compared to monodentate, such ratio is inverted after CO₂ methanation. This region 1600-1200 cm⁻¹ increases in absorbance for Ni/DOE0 after plasma and thermal reaction and the peaks become wider with a more pronounced shoulder around 1580 cm⁻¹, which suggests that additional adsorbed species are present on the surface of Ni/DOE0. The peaks at 2924 and 2855 cm⁻¹ in the 3000-2700 cm⁻¹ region of Ni/DOE0 FTIR spectra increase after plasma reaction, such peaks reveal the presence of C-H containing molecules on the surface of the used catalyst, probably formates (1585 and 2924 cm⁻¹) [81,97,159]. According to this peak assignation, there is a clear increase in the intensity of the carbonates and formates peaks after the reaction, probably due to the intermediate species that play a role in the plasma-assisted methanation. Such variation is less prominent for the Ni/DOE0 catalyst after thermal methanation. Ni/DOE5 spectra in the 1600-1200 cm⁻¹ region are similar to Ni/DOE0 after plasma reaction, however the spectra indicate an increase in intensity in the region 1000-800 cm⁻¹. Such region was linked in section 3.3.5 to polydentate carbonates [113], which characterises the strongly basic Ni/DOE6 sample also post methanation (which does not vary significantly compared to the reduced one). It points to an increase of tightly bound carbonates on the surface of Ni/DOE5 after the catalytic reactions.

The presence of different species deriving from the adsorption of CO₂ on the catalyst surface and the reaction happening at these sites is shown also by TPD-MS experiments, following mass 44 in relation to CO₂ species released, carried out on the Ni/DOE0, 3, 5, 6 catalysts after the plasma-assisted methanation and as comparison on the reduced (Figure 4.20). All samples present a first peak at around 200 °C probably linked to the weak physisorbed CO₂. The CO₂ desorption curve of the reduced Ni/DOE0 also has a second peak at 325 °C that is related to the medium strength basicity properties of this catalyst (see the CO₂-TPD in Figure 3.26), carbonates and hydrogen carbonates are adsorbed from air and bound with intermediate strength on the surface, therefore being decomposed and leaving the surface at higher temperatures. The Ni/DOE0 samples after plasma and thermal reaction have different profiles of CO₂ desorption. Ni/DOE0 thermal shows a more intense signal compared to the reduced Ni/DOE0 sample, but the peaks are positioned at similar temperatures, suggesting that similar adsorbed species are present in both cases. However, the second peak at a higher temperature is wider, probably linked to different species attached with

increasing strength to the surface (hydrogen carbonates < bidentate carbonates and formates) [179]. The Ni/DOE0 plasma curve maintains the first peak at 200 °C but the second peak is shifted to higher temperature above 350 °C, possibly due to the degradation of formates on the surface that are more thermally stable compounds and whose presence is shown by FTIR (Figure 4.19) [179]. The species that decompose at lower temperature (325 °C) are less present after plasma exposure, in fact this curve shows a valley at the temperature at which the curve of Ni/DOE0 has a peak.

Ni/DOE5 TPD-MS curve after plasma shows a second peak above 400 °C, therefore linked to more strongly bound C-containing molecules, which could point to the polydentate species seen in the FTIR spectrum (Figure 4.19) [179]. Ni/DOE6 has the smallest CO₂ desorption after plasma-assisted methanation among these samples, as expected by the low amount of basic sites and small surface area (see Table 3.4, Table 3.7), and, as suggested by the FTIR peaks, the desorption mostly occurs at temperature higher than 250 °C therefore molecules adsorbed with medium/high strength.

The adsorbed intermediate species vary according to the catalyst and its physicochemical properties, as shown for the example of Ni/DOE6 compared to Ni/DOE0. Plasma plays a role in the surface modification of the catalysts but at the present moment it is unclear how to identify the contributions of the methanation reaction, heating and plasma.

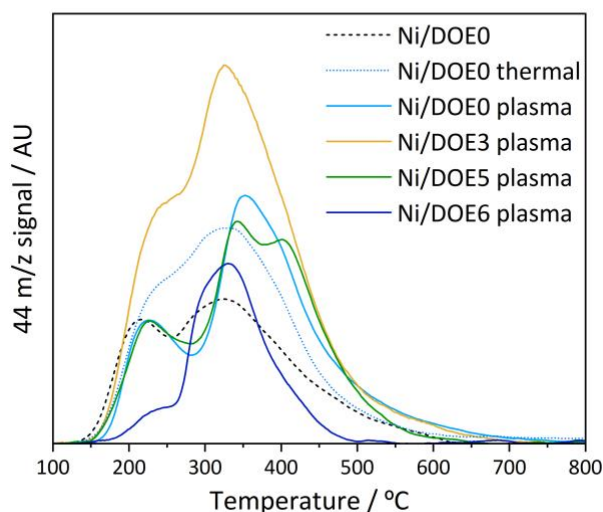


Figure 4.20: TPD-MS of Ni/DOE0 before and after plasma and thermal reaction, and of Ni/DOE5 and 6 after plasma.

4.4. Conclusions

In this chapter, the results of plasma-assisted CO₂ methanation with the Ni/DOE catalysts having different morphologies were analysed, compared to the performance in thermal catalysis, and related to the physicochemical properties of the materials. It was proved that the methanation

reaction occurring in the DBD reactor is the result of the cooperation between an appropriate catalyst and the plasma discharge. Furthermore, it was shown that the catalytic activity of the synthesised catalysts is comparable to previously reported results and that they are stable over 10 hours of reaction time. The physicochemical properties such as surface area and basicity have a strong impact on the thermal methanation activity but have less influence on the results in plasma. The synthesis parameters of the materials play a role since they affect the ceria crystallite size, surface area, surface basicity, Ni dispersion and interaction with the support, and oxygen vacancy formation, which are very important for the catalytic performance of the Ni/CeO₂ material. The energy efficiency of the plasma-assisted process also depends on the response of the packed bed DBD reactor with the different catalysts, therefore on their dielectric behaviour. In fact, once the material is exposed to the electrons and excited species from plasma, and the electric field, further features of the catalyst should be explored. It was shown that the most effective catalysts for plasma-assisted CO₂ methanation are those that combine low dielectric permittivity (quantified by C_{reactor}) with small CeO₂ crystallite size, good OSC of the ceria, a high amount of medium strength basic sites, and large surface area. Additionally, these results point to a common anisotropic morphology between the catalysts that combine such beneficial features, meaning nanorods and nanoneedles along the <011> axis of DOE0 and DOE5 supported samples.

Finally, variations in the Ni and CeO₂ structures and surface configuration are revealed by examining the catalysts after the methanation reaction via several characterization techniques. In some cases, particle redistribution and surface reoxidation are observed and the adsorbed species change after the catalyst participates in the reaction. Such variations suggest that the material is very active and taking part into the reaction.

Chapter 5: Electrical characterization of the packed bed DBD reactor

5.1.	<i>Introduction</i>	129
5.2.	<i>Methods</i>	130
5.2.1.	Q-V Lissajous cycle analysis.....	130
5.2.2.	Charge peaks analysis.....	132
5.2.3.	Current envelope	133
5.3.	<i>Results and discussion</i>	133
5.3.1.	Lissajous shape analysis and dielectric properties.....	133
5.3.2.	Statistical analysis of charge transfer events in the DBD reactor	139
5.3.3.	Current peaks analysis	142
5.3.4.	Effect of physicochemical features of the catalyst on the electrical behaviour of the packed bed DBD	147
5.4.	<i>Conclusions</i>	149

5.1. Introduction

As briefly touched in the previous chapter, the electrical characterization of the packed bed catalytic DBD reactor is significant to determine the efficiency of the catalysts and their behaviour in plasma. In general, the plasma diagnostic is important in order to know at what regime it is operating and to gather information on the discharge, the gas temperature and the excited species present. As the DBD plasma reactor available was designed for plasma catalysts tests and is packed with a dark powdered material, it would be very laborious to apply the optical plasma diagnostic techniques frequently used in reactors provided with an optical access and without packing materials in the discharge zone. A more in-depth study of the electrical behaviour of the DBD reactor varying packing materials and using different catalysts of the Ni/DOE series was carried out, with the purpose of collecting information on the discharge characteristics and how is it affected by the choice of catalyst. Three complementary techniques were used for the electrical characterisation: analysis of the shape of the Q-V Lissajous figure, statistical analysis of the charge transfer events and acquisition of the envelope of the current peaks. The current envelope was previously used by Guaitella et al. [126] to understand the interaction between the photocatalytic material (silica fibres coated with TiO₂ nanoparticles) and plasma in a packed bed DBD reactor. In this publication the authors were able to identify difference regarding injected energy and current peak population with and without the packing material.

The results of these electrical diagnostics techniques are reported and discussed in this chapter. These will be shown for different configurations of the DBD reactor (empty or packed) and using different materials including the Al₂O₃ and CeO₂ supports and selected Ni/DOE catalysts (0, 3, 5, and 6).

5.2. Methods

This study was performed thanks to the guidance and supervision of Dr. Guaitella (LPP, École Polytechnique, Paris). The set-up described in section 2.3 and depicted in Figure 2.4 has been modified in order to improve the sensitivity of the measurement and a current probe (Pearson 4100) was added for the current peaks measurement. The CO_2/H_2 stoichiometric gas mixture was flowed in the reactor during the tests as described in section 2.3.

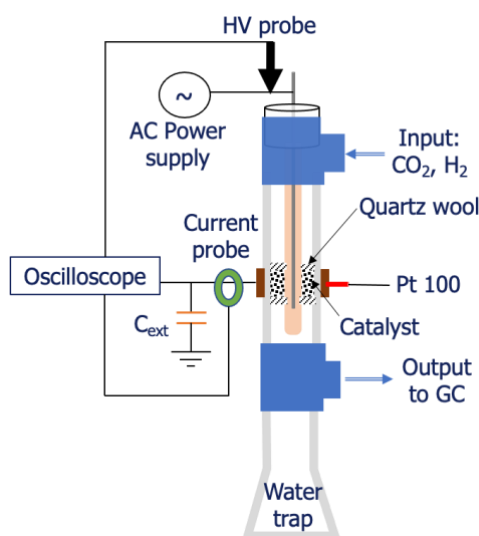


Figure 5.1: Experimental DBD set-up for the electrical diagnostics.

An oscilloscope Le Croy WaveSurfer 104MXs-BA with 1 GHz bandwidth and 10-5 GS/s sampling rate was used for the measurements. Furthermore, the C_{ext} and the voltage probe (for V_{in} monitoring) were replaced with a 600 pF solid state capacitor and GE 3830 30 kV Elditest HV probe. The 600 pF C_{ext} is used, as in the previous set-up, to measure the charge Q transferred in the reactor: the voltage across the capacitor V_C is measured and Q is derived using eq. (2.7). The schematic drawing of the set-up is in Figure 5.1. Two power conditions were tested for the electrical behaviour study: a low power point (around 15 W, corresponding to 25.4 ± 0.2 kV_{p-p}) at which no conversion of CO_2 is expected, and a high power condition that should allow the methanation reaction to occur with the active catalysts (around 30 W, 27.7 ± 0.3 kV_{p-p}). The measurement was repeated three times with Ni/DOE0 sample to assess the reproducibility and standard deviation was calculated for the reported values. The data analysis described in the following sections was carried out in MATLAB.

5.2.1. Q-V Lissajous cycle analysis

The V_{in} and Q signals were averaged over 100 sweeps and acquired over a time scale corresponding to ~ 5 periods with 5 GS/s rate. This data was used to build the Q-V Lissajous plots, previously introduced in section 2.3.4. The ideal parallelogram shape of the Lissajous plot is depicted in Figure

5.2. For a packed bed DBD reactor, the measured Q-V plot is almond shaped with sharp apexes at maximum and minimum voltage, and it can be approximated to a parallelogram to better designate the observed parameters of the figure (as drawn in Figure 2.6) [139]. Starting from the minimum voltage and charge point, the charge increases linearly until the breakdown voltage is reached (“plasma off” part), at this voltage the filaments start igniting in the packed reactor (“plasma on”). As not all the events occur at the same time neither they go all the way across the reactor and the plasma expansion through the gap is gradual, the Q-V graph does not resemble a parallelogram, especially in the case of the packed bed reactor [141]. The voltage further increases until the maximum peak is reached, the voltage then decreases, and the same behaviour is observed in the positive part of the voltage period.

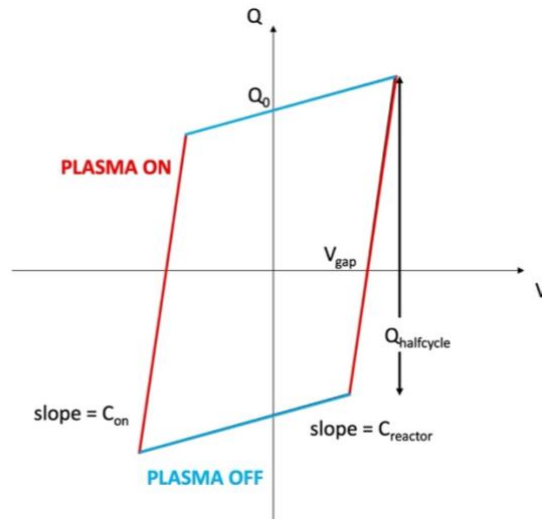


Figure 5.2: Ideal shape of a Lissajous Q-V plot for a DBD reactor.

The four lines obtained from the linearization of the apexes of the Lissajous plot are used to build the equivalent ideal parallelogram and calculate the electrical parameters. The lines correspond in pairs to the “plasma off” (blue in Figure 5.2) and “plasma on” (red in Figure 5.2) regimes. C_{reactor} and C_{on} correspond to the slopes of the lines of “plasma off” and “plasma on” sections, respectively, and this analysis has been previously discussed in section 2.3.4. Further information can be obtained from the linearization. The charge Q_0 at $V = 0$ can be calculated in the “plasma off” region as the line equation is $Q = C_{\text{reactor}} \cdot V - Q_0$. Q_0 is the residual charge deposited in the system before the plasma is ignited. In the ideal situation, the “plasma on” region of the Lissajous is described by the linear equation $Q = C_{\text{on}} \cdot (V - V_{\text{gap}})$. This requires V_{gap} to remain constant once the discharge is ignited and equal to the ideal ignition voltage for the case of a uniform discharge. At this voltage, the gas fraction is converted into a “black box”, modelled as C_{gas} in parallel with a time-dependent resistor R_{on} (the ideal circuit scheme is in Figure 2.7). The behaviour of the discharge is difficult to predict and model, as the plasma in the DBD reactor is not homogeneous and the discharge events are not simultaneous

and cover the whole ground electrode surface considered as active area. Therefore, the slope of this region is referred as C_{on} and varies with the applied voltage. The final parameter that is calculated from the Lissajous plot is the $Q_{half-cycle}$ (Figure 5.2), which is the charge transferred considered just during the discharge, meaning the difference between Q_0 and the maximum Q at the apex of the Lissajous.

5.2.2. Charge peaks analysis

The Q signal was also recorded over 120 periods (not averaged, 20 repetitions of the measurement with timescale equivalent of ~ 6 periods) using the highest possible sampling rate (10 GS/s corresponding to 5 MS per datafile) and keeping the x and y scales constant for the different experiments. The purpose of this measurement is the statistical analysis of the charge steps that are visible in the Q signal plotted versus time, Q is recorded using the voltage across C_{ext} (as shown in equation (2.6)). This is why this element of the set-up was modified in order to use a device that could provide a faster response. Each charge step corresponds to a charge transfer event, meaning one or more filament ignited across the gap or surface discharges. The objective of the analysis of the Q signal is to isolate the charge steps over the noise signal, calculate their height and time at which the event occurs. In order to do so, the first derivative of the Q signal is calculated to have a quantification of the slope variation of the signal at each time point. A sudden and intense variation in the signal, corresponding to a charge step, translates to a peak in the first derivative. The most prominent peaks of the derivative of Q are found using threshold parameters that depend on the experiment conditions. The position (t_{step}) and width (δt) of each peak is calculated with this function and then used to quantify the charge transferred in each step ΔQ_{step} as the difference in the Q signal in the interval $[t_{step}-\delta t, t_{step}+\delta t]$. An example of peaks detection and Q_{step} is shown in Figure 5.3.

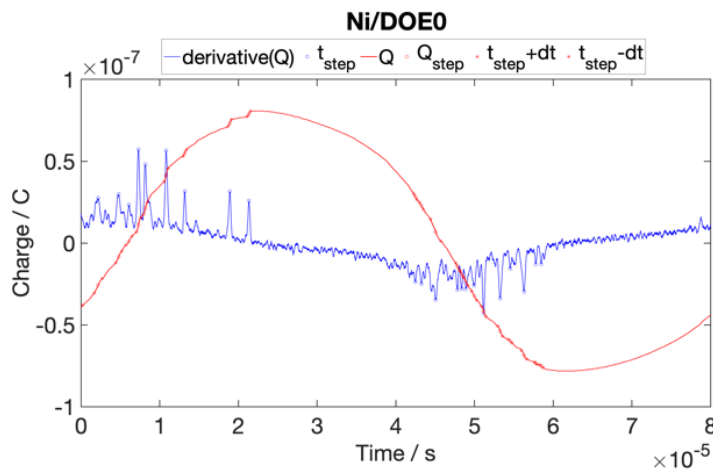


Figure 5.3: Example of the analysis performed on the measured charge signal (in red) and its first derivative (in blue) for Ni/DOE0 packing at 25.3 kV_{p-p} over 1 period. The charge steps position t_{step} and width δt detected by the developed analysis are shown by the symbols.

The cumulative ΔQ_{step} for all the observed events normalized by the number of periods quantifies the total charge transferred Q_{total} . In the end, the results gathered are the number of events, the time at which they occur over 6 periods, the values of ΔQ_{step} and Q_{total} which is a parameter analogous to $Q_{\text{half-cycle}}$.

5.2.3. Current envelope

The current probe was added to the DBD set-up and measures the current signal at the ground electrode before C_{ext} . It was connected to the Le Croy WaveSurfer oscilloscope using the low impedance 50 MW load. The acquisition of the current peaks (I) was performed using the built-in envelope function of the oscilloscope over 1000 sweeps. The function records only the extremes in maximum and minimum of the signal, making the current peaks measurement more significant and avoid the comparison of a single shot of the current peaks configuration over one acquisition. The current envelope was measured over ~ 2.5 periods with 5 GS/s sampling rate, maintaining the same y-axis scale in order to avoid saturation and different values of the envelope. One period of the current envelope was then plotted and used for comparison between the different configuration of the DBD reactor in the study.

5.3. Results and discussion

5.3.1. Lissajous shape analysis and dielectric properties

The shape of Lissajous figures was briefly discussed in the previous chapter in relation with the behaviour of the Ni/DOE catalysts in plasma. It can be observed in Figure 5.4 and Figure 5.5 that the differences among the area and shape of Lissajous figures with different packing materials is less evident than what was observed in the graphs reported in Figure 4.3 and Figure 4.5b. It should be noted that the mode of acquisition and the set-up were modified between these experiments, as presented in section 5.2. In fact, the Q and V signals were averaged over 100 acquisitions and a different C_{ext} (with smaller capacitance of 600 pF compared to the previous set-up) as well as different current and voltage probes were utilized, changing the overall impedance of the equivalent circuit of the set-up, therefore partially the response of the DBD set-up. However, it is still valid to discuss variations among the catalysts and packing materials, which will be studied in this section. Furthermore, it is worth to point out that the features that will be discussed in this section are reactor-averaged and include the contributions of several discharge events.

Figure 5.4a and b report the Lissajous figure at 25.4 and 27.7 kV_{p-p}, respectively. Qualitatively, the shape of the Q-V cycles of the empty reactor and with alumina packing are similar, while the Lissajous graph of the case with CeO₂ DOE0 packing is narrower with an accentuated almond shape, especially in the case at higher voltage and power in Figure 5.4b. Such comparison agrees with the analysis and discussion in section 4.3.2, which links this behaviour to the low dielectric permittivity of alumina compared to ceria.

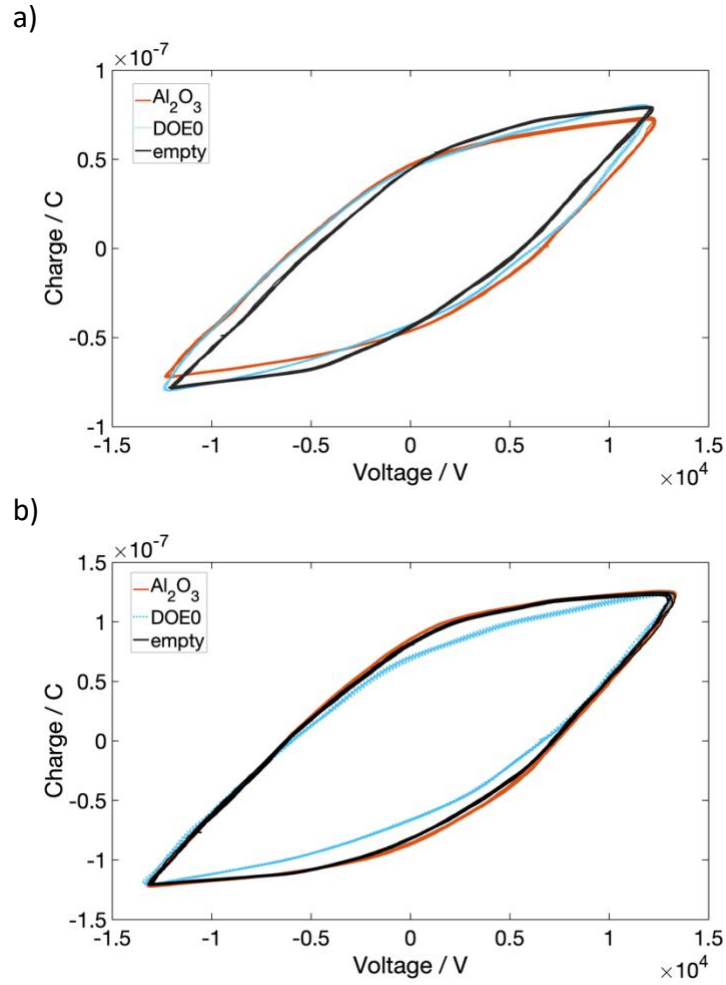


Figure 5.4: Lissajous Q-V figure measured with empty DBD reactor and packed with Al₂O₃ and CeO₂ DOE0 supports at a) 25.4 ± 0.2 kV_{p-p} and b) 27.7 ± 0.3 kV_{p-p}.

The qualitative comparison of the graphs reported in Figure 5.5a and b of the Lissajous cycles for Ni/DOE0, 3, 5, and 6 do not lead to considering a different behaviour in plasma of these catalysts, especially in the case of low voltage $25.4 \text{ kV}_{\text{p-p}}$ (15 W power and negligible conversion, see Table 5.1.) condition. When the power is increased and the methanation reaction occurs (CO_2 conversion reported in Table 5.1.), small variations in the charge peaks and slopes of the linear regions can be observed in Figure 5.5b.

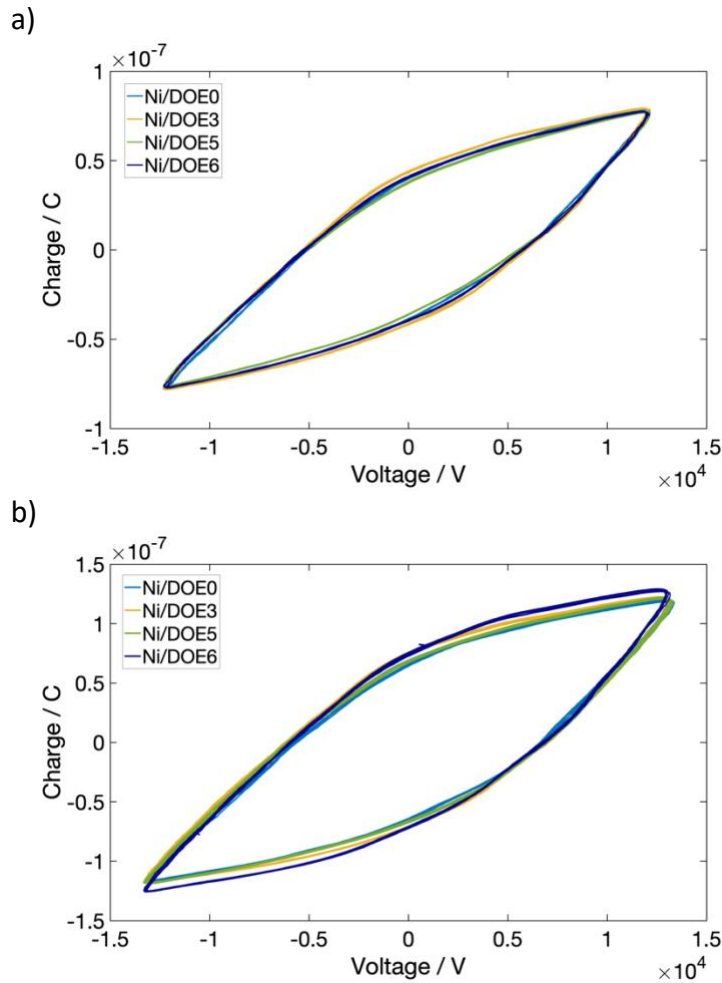


Figure 5.5: Lissajous Q-V figure measured with the DBD reactor packed with Ni/DOE0, 3, 5, 6 catalysts at a) $25.4 \pm 0.2 \text{ kV}_{\text{p-p}}$ and b) $27.7 \pm 0.3 \text{ kV}_{\text{p-p}}$.

As the qualitative analysis of the shapes of the Lissajous figures could not point to interesting differences in the electrical behaviour of the DBD reactor packed with these samples, a quantitative analysis was performed in order to extract several parameters of the Q-V cycles, which are reported in Table 5.1. Namely, the quantities calculated are (as described in section 5.2.1) the slopes of the plasma “off” and “on” regions of the Lissajous, which correspond to the capacitances of the reactor and the dielectric materials once the plasma is ignited (C_{reactor} and C_{on} , respectively), the residual charge in the reactor Q_0 and the total charge transfer during one half-cycle of plasma discharge $Q_{\text{half-cycle}}$, and finally the V_{gap} which corresponds to the breakdown voltage in the ideal parallelogram. An

example of the linearization of the plasma “off” and “on” regions, and the equivalent ideal Lissajous that is built from these lines is reported in Figure 5.6 for Ni/DOE0 sample.

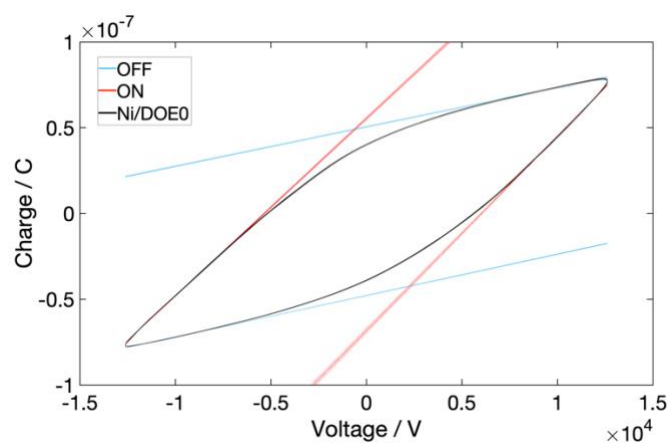


Figure 5.6: Example of measured Lissajous Q-V cycle for Ni/DOE0 packing at 25.3 kV_{p-p} layered with the linearization obtained from the calculations performed with MATLAB.

Table 5.1: Overview of the CO₂ conversion and the results obtained from the analysis of the Lissajous figure at the two voltage conditions (25.4 ± 0.2 and 27.7 ± 0.3 kV_{p-p}) and with different packing materials.

Sample	X _{CO₂} , %	Power, W	C _{reactor} , pF ±0.2	C _{on} , pF ±0.04	V _{gap} , kV ±0.4	Q _{half-cycle} , nC ±10	Q ₀ , nC ±2
Empty	7.9	16	1.3	10.12	5.1	140	63
	11.7	34	1.3	15.60	6.5	230	105
Al ₂ O ₃	7.1	18	1.4	10.94	6.5	130	55
	10.5	35	1.4	15.82	6.5	210	105
DOE0	0.4	18	1.8	14.48	6.7	180	80
CeO ₂	3.5	29	2.7	17.21	7.0	230	86
Ni/DOE0	9.4	15	2.4	10.85	5.7	130	49
	80.9	27	2.5	12.88	6.1	160	66
Ni/DOE3	12.8	17	2.1	11.12	5.8	130	52
	78.1	31	2.3	15.05	6.5	200	84
Ni/DOE5	12.8	15	2.4	10.54	5.5	120	47
	79.8	29	2.7	14.49	6.2	180	76
Ni/DOE6	5.2	16	2.2	10.63	5.7	130	50
	59.3	31	2.8	16.25	7.2	170	70

The error range reported in Table 5.1 has been calculated from the 3 repetitions of these measurements carried out with Ni/DOE0 catalyst. Furthermore, it should be noted that these values obtained from this analysis are the result of the averaging over at least 500 periods.

The C_{reactor} might differ from what was previously reported in Table 4.1, which is due to the different configuration of the set-up and improved sensitivity of these measurements, as disclosed earlier. As expected by the Lissajous figures in Figure 5.4, the C_{reactor} of the empty and packed with Al_2O_3 DBD reactor are similar and have the smallest value among all samples. For the other ceria-based materials (either support or Ni catalyst) an increase on C_{reactor} is observed with the power step up. Furthermore, it should be noted that C_{reactor} as calculated here does not differ significantly (within the error ± 0.2 pF) comparing the different catalysts Ni/DOE at the same power condition. According to these calculations, other parameters appear more relevant to describe the behaviour of Ni/ CeO_2 catalysts in CO_2/H_2 DBD plasma and to be linked with the efficiency of the methanation reaction.

The effective capacitance C_{on} should be considered, as it is more intimately linked with the contribution of the dielectric materials (packed bed and the alumina and quartz of the dielectric barriers). It is in principle it is the resulting capacitance of the series of capacitors of the dielectric materials illustrated in Figure 2.7 excluding the C_{gas} during ignition, as in the equation below:

$$\frac{1}{C_{\text{on}}} = \frac{1}{C_{\text{quartz}}} + \frac{1}{C_{\text{catalyst}}} + \frac{1}{C_{\text{alumina}}} \quad (5.1)$$

The equivalent circuit in Figure 2.7 considers a time-dependent resistor R_{on} in parallel with C_{gas} . This component should shunt the capacitor C_{gas} and allow all the current to pass through once the breakdown voltage is reached, simulating the gap bridging carried out by the plasma filaments [139,141,180]. According to this model, it is expected that $C_{\text{on}} > C_{\text{reactor}}$, as is the case of the results obtained with this packed DBD reactor [141]. Furthermore, the effective capacitance when plasma is ignited varies with the voltage increasing over time. Such behaviour is displayed by the almond shape of the Lissajous figures, which are characterized by varying slope, that reaches the maximum at C_{on} value. Such gradual variation of Q as a function of applied V has been linked with the plasma and surface discharge expanding over the packing and across the reactor over time [139,141]. In fact, the exact behaviour of plasma is hard to predict and describe by equivalent circuit models. In actuality, a partial contribution of C_{gas} to C_{on} , not considered in the ideal case described by equation (5.1), cannot be ruled out but it is difficult to determine as it varies over time and with different packed beds [139,141]. Furthermore, the discharge is not uniformly spread on the dielectric barrier materials of the DBD reactor [141], therefore the C_{quartz} and C_{alumina} , which in principle can be calculated from the known ϵ_r and geometrical dimensions, might be overestimated. According to eq. (2.10) and (5.1), it can be concluded that $C_{\text{on}} \propto \epsilon_{\text{catalyst}}$, therefore, with larger capacitance value a larger dielectric permittivity constant of the packing material is expected. Nonetheless, considering all the approximations just shown, it would be inexact to calculate from C_{on} the $\epsilon_{\text{catalyst}}$, so only C_{on} values will be taken into account as quantification of the dielectric behaviour of the

packed bed for further comparisons. The empty DBD reactor, as expected, has both the lowest C_{reactor} and C_{on} . CeO_2 is the material with the largest C_{on} . Interestingly, with ceria support only the lowest conversion of CO_2 is obtained (in agreement with previous results, see Figure 4.5). The addition of 15 %wt. Ni, which is conductive despite being well dispersed on the surface, seems to decrease the dielectric permittivity of ceria at both power conditions. At around 30 W C_{on} is ranking as $\text{Ni}/\text{DOE0} < 5 < 3 < 6$, same as X_{CO_2} . Furthermore, the direct relation between C_{on} and activity in plasma assisted methanation, which was suggested in the previous chapter, is maintained.

The results in Table 5.1 suggest that lower dielectric permittivity of the material is linked with lower V_{gap} , therefore easier ignition of plasma across the reactor gap. The breakdown occurs more easily without any packing, especially at the low voltage condition, as the discharge is established in the empty reactor at lower V_{gap} and it can be hypothesised that the discharge filament can bridge the whole length of the gap without being modified by the packing material. It has been suggested that a packing material with low or intermediate $\epsilon_{\text{catalyst}}$ enhances surface polarisation which aids the micro-discharges being established across the reactor [95,181]. Furthermore, it was suggested that packing a DBD reactor with a material with large ϵ_r would enhance the electric field locally, especially at contact point between packing and electrode, increase the electron temperature but not aid the electron density and the uniform spreading of plasma in the gap, which would not be beneficial for catalyst-plasma interaction and for the catalytic reaction to occur [94,182]. Most of the studies on dielectric behaviour of packing materials have been carried out by fluid modelling and considering macro-sized beads, as in the experimental conditions it is difficult to separate the dielectric behaviour from the chemistry at the interface of the catalyst and its physicochemical properties [118,181–184]. Nonetheless, such findings are useful to interpret these electrical characterization data regarding the dielectric behaviour of the catalysts used for plasma-assisted CO_2 methanation.

The other two parameters in Table 5.1 regard the charge transferred and deposited during the discharge, $Q_{\text{half-cycle}}$ and Q_0 . As expected, with larger applied voltage, more charge is transferred by the events in the plasma discharge. The values at the low voltage condition show negligible differences, except for DOE0 support which has the largest $Q_{\text{half-cycle}}$ and Q_0 at 25.4 kV_{p-p}. At higher applied voltage $Q_{\text{half-cycle}}$ does not vary significantly with the different catalysts. In the empty DBD the largest charge transfer occurs, the same goes with the alumina packing, which was showing to have very small impact on the dielectric properties of the reactor.

Q_0 follows the same trend as $Q_{\text{half-cycle}}$, but the measured values vary more appreciably. The proportionality of Q_0 and conversion or efficiency could not be established, however the lowest charge is linked with the most efficient catalyst (Ni/DOE0). Such differences in Q_0 could be linked with the tendency of the material surface to polarize.

5.3.2. Statistical analysis of charge transfer events in the DBD reactor

More details on the charge transfer events are obtained from the statistical analysis over 120 periods of the charge steps, as described in section 5.2.2. An example of the charge steps of the unfiltered and not averaged Q signal over 1 period is reported in Figure 5.3, together with the first derivative, which is used for the steps detection. The parameters used for finding peaks are adequate for the signal/noise discrimination to detect each event and calculate ΔQ_{step} .

Such analysis carried out over more than 100 periods gives a picture of what is the distribution of charge transferred by the several discharge events occurring and at what time over one period the events mostly occur. Such steps can be appreciated typically due to the small HV electrode area that allows to separate the contribution of individual filamentary events per discharge cycle [139]. It should be noted that it is not possible to link each charge step to one filament, as different discharge mechanisms can coexist in a DBD reactor and several charge transfer events might be ignited simultaneously adding up to the same step being recorded on the Q signal [126]. The average ΔQ_{step} (in Table 5.2) is measured to lay in the range of 4-10 nC, which corresponds to the charge transferred in several filaments, expected to be per micro-discharge filament 0.1-1 nC [185,186]. Such mechanism has been named “collective effect” and relies on the triggering of several filaments from one filament breakdown [126]. Furthermore, the steep part of each Q step would correspond to a current peak [139]. The sum of the charge steps ΔQ_{step} normalized by the number of periods Q_{total} is expected to be equivalent to $Q_{\text{half-cycle}}$.

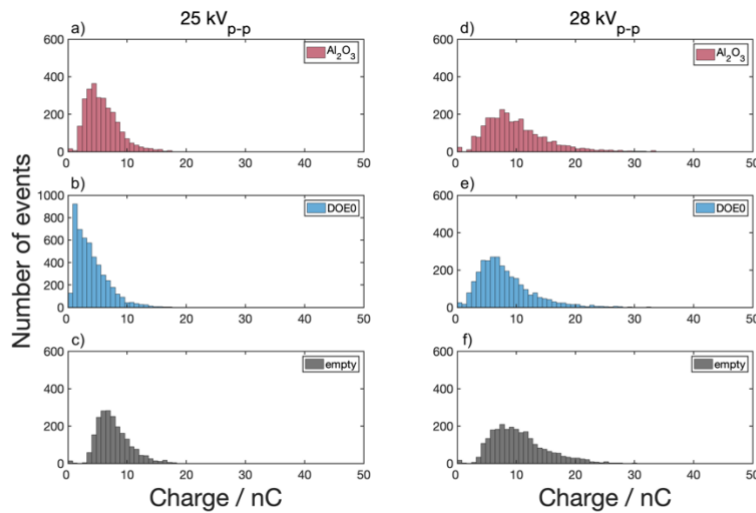


Figure 5.7: Charge steps histograms obtained during the experiments with the DBD reactor packed with a),d) Al_2O_3 and b),e) CeO_2 DOE0 supports and with the c),f) empty DBD reactor at a-c) 25.4 ± 0.2 kV_{p-p} and d-f) 27.7 ± 0.3 kV_{p-p}.

The comparison of the charge transfer in the empty DBD reactor with the packed bed (with alumina and ceria supports) is shown in Figure 5.7, that compare the low and high voltage conditions. At low applied V more micro-discharge events occur, but on average each one transfers less charge (ΔQ_{step} below 10 nC) compared to the high V case. With increased V the distribution widens, the ΔQ_{step}

increase but less events are registered, which overall reflects the larger Q in the Lissajous figure (Figure 5.4a compared to b). Such difference is heightened with ceria packing the DBD. The largest number of events is recorded for DOE0, especially at 25.4 kV_{p-p}, which is in agreement with the results of the analysis of Lissajous figure $Q_{\text{half-cycle}}$, and the average ΔQ_{step} increases $\text{CeO}_2 < \text{Al}_2\text{O}_3 < \text{empty}$.

Regarding the comparison of Ni/DOE catalysts in Figure 5.8, a similar average ΔQ_{step} at low V is observed, however the charge distributions in Figure 5.8a-d vary slightly in width. The width and mode of the charge distribution increase with larger power (Figure 5.8e-h), and at this condition the differences between the materials become more apparent. The lowest average and maximum ΔQ_{step} are recorded for Ni/DOE0 and 5, leading to results in agreement with the $Q_{\text{half-cycle}}$ calculation. Largest average and maximum ΔQ_{step} is measured for the Ni/DOE3 catalyst.

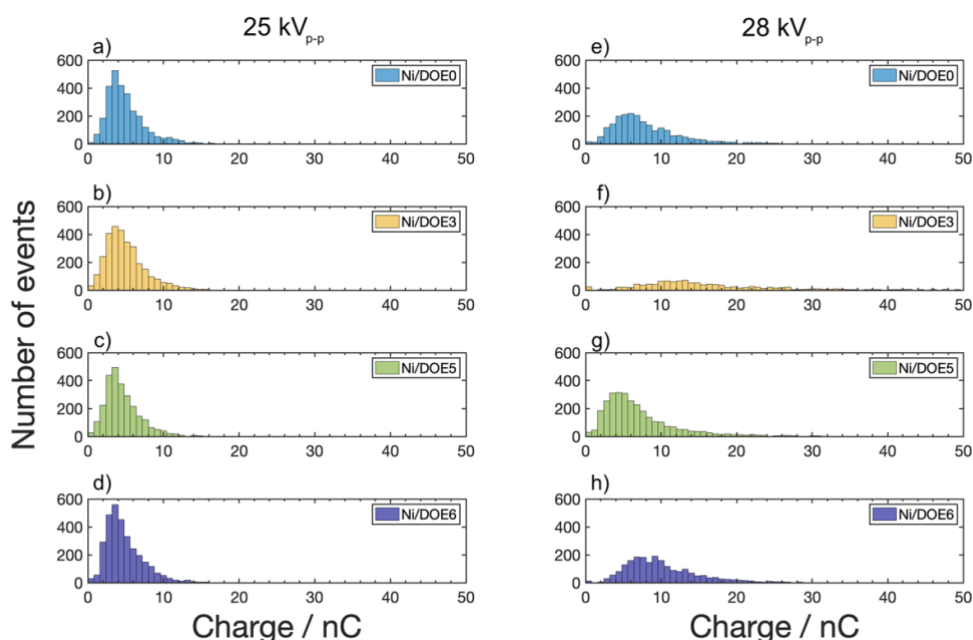


Figure 5.8: Charge steps histograms obtained during the experiments with the DBD reactor packed with the catalysts a),e) Ni/DOE0, b),f) Ni/DOE3, c),g) Ni/DOE5, d), h) Ni/DOE6 at a)-d) 25.4 ± 0.2 kV_{p-p} and e)-h) 27.7 ± 0.3 kV_{p-p}.

At this condition (27.7 kV_{p-p}), Ni/DOE3 in Figure 5.8f shows the broadest charge distribution together with the lowest number of recorded charge transfer events (1325). Such difference can be better noticed when the histograms are plotted with a wider Q scale in Figure 5.9, in this case it is shown that a few events are recorded above 50 nC for Ni/DOE3 sample. In fact, the average ΔQ_{step} is 20.1 nC and the maximum ΔQ_{step} of the distribution is 174 nC. Such different charge transfer behaviour with the ceria nanocubes supported catalyst Ni/DOE3 was previously recorded also by the Lissajous figure analysis and with the calculation of $Q_{\text{half-cycle}}$ and Q_0 (200 nC and 84 nC, respectively), confirmed to be the largest values among the four catalysts used for packing the DBD reactor. Such behaviour might be ascribed to the different tendency to surface polarisation or response to

electron impact of this material compared to the others, probably affecting the plasma expansion and discharge mechanism.

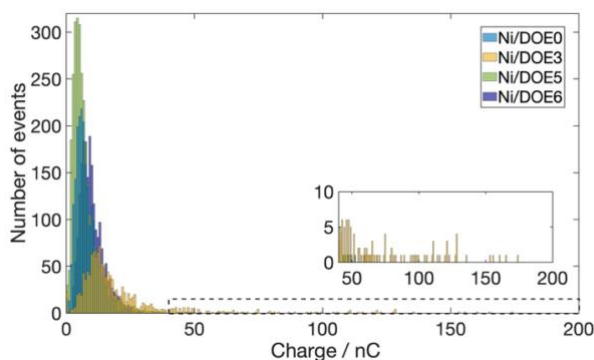


Figure 5.9: Charge steps histograms obtained during the experiments with the DBD reactor packed with Ni/DOE0, 3, 5, and 6 at 27.7 ± 0.3 kV_{p-p} over charge interval 0-200 nC.

In most cases, both the number of events and average ΔQ_{step} increase with applied voltage. Furthermore, Q_{total} is comparable to the $Q_{\text{half-cycle}}$ from the Lissajous analysis within the 10 nC error.

Table 5.2: Overview of the results obtained from the statistical analysis of the charge transfer events at the two voltage conditions (25.4 ± 0.2 and 27.7 ± 0.3 kV_{p-p}) and with different packing materials.

Sample	Condition: Power, W	Number of events ± 157	Average ΔQ_{step} , nC ± 0.1 nC	Maximum ΔQ_{step} , nC ± 1 nC	Q_{total} , nC ± 10 nC
Empty	16	2217	7.7	23	140
	34	2685	10.6	45	230
Al ₂ O ₃	18	2798	5.8	30	130
	35	2786	10.0	45	220
DOE0	18	5126	4.0	23	170
CeO ₂	29	3073	8.2	47	200
Ni/DOE0	15	2980	5.0	17	120
	27	2300	8.0	53	160
Ni/DOE3	17	3214	5.0	21	140
	31	1325	20.1	174	210
Ni/DOE5	15	2785	4.6	25	110
	29	3154	7.2	48	180
Ni/DOE6	16	3288	4.8	21	130
	31	2231	10.1	60	180

5.3.3. Current peaks analysis

The last tool used for the analysis of the electrical behaviour of the packed bed DBD is the current envelope. The envelope records the most relevant events in terms of current peak intensity in the positive and negative half periods. An example of the current envelope together with V and Q signals over 2.5 periods is reported in Figure 5.10 for sample Ni/DOE0. The current peaks have positive intensity when the applied voltage rises from minimum to maximum, and negative in the other half of the period of the sinusoidal V signal. The recorded negative envelope in the first half of the period and the respective positive peaks in the second half are to be considered as noise and not related to events occurring due to the DBD discharge, as they rise from ringing of the Rogowski coil used as current probe. Figure 5.10 also shows that the steep section of the Q signal where the charge transfer steps are observed correspond with the area in which current peaks are recorded.

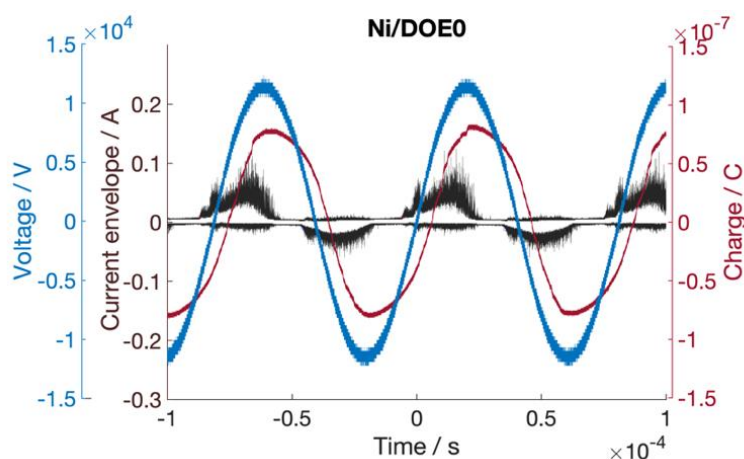


Figure 5.10: Example of measured V and Q signals and the current envelope over 2.5 periods during the experiment with Ni/DOE0 catalyst at 25.3 kV_{p-p}, power 15 W.

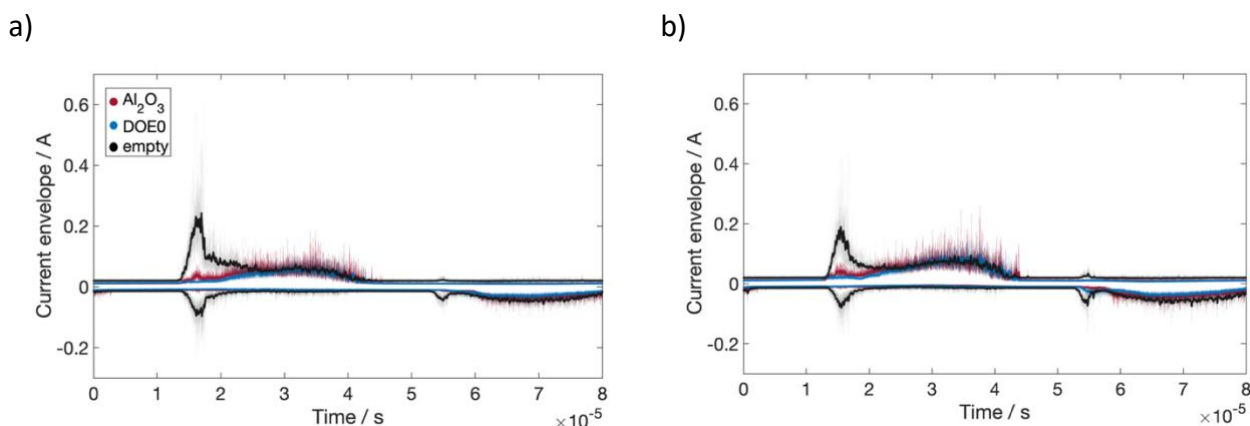


Figure 5.11: Current envelopes over 1 period obtained during the experiments with the empty DBD reactor and packed with Al_2O_3 and CeO_2 DOE0 supports at a) $25.4 \pm 0.2 \text{ kV}_{\text{p-p}}$ and b) $27.7 \pm 0.3 \text{ kV}_{\text{p-p}}$.

The current envelopes of the empty DBD reactor and packed with Al_2O_3 and CeO_2 are reported in Figure 5.11 and with Ni/DOE catalysts is Figure 5.12. First of all, an asymmetry between the positive and negative half periods of current peaks is observed, as reported in [126]. This is due to the cylindrical geometry of the DBD reactor used, meaning a disparity regarding surface area of the internal and external electrodes on which electrons are deposited according to the polarity of the applied voltage. Both the positive and negative sections of the envelope display a first smaller peak and a second broad one, the latter in common among all tests. It can be suggested that this wide distribution in the second region of each half period is linked with the current peaks due to the discharge occurring in the quartz wool layers due to the plasma expansion above the packing zone, which is also present in the empty reactor experiments (the volume where the catalyst powder would have been loaded was left empty but the quartz wool layers were inserted for this experiment). The first section of current envelope half period seems to be the most relevant for comparisons, to help this evaluation a zoomed portion of the current envelopes of Ni/DOE0, 3, 5, and 6 is depicted in Figure 5.13. The most evident difference in intensity of the first peak is observed for the empty DBD reactor case in Figure 5.11. The current peaks are intense reaching 0.6 A and greatly differ for the packed bed DBD, which despite the varying materials all display a lower intensity in the first zone. The intensity of this first region decreases with larger power (Figure 5.11b) This could be linked with the filaments that in the case of the empty reactor can freely cross the reactor gap and allow an easier flow of electrons at the beginning of the breakdown. The current envelope of the Al_2O_3 packing shows a more marked and intense first peak between 1 and $2 \times 10^{-5} \text{ s}$ compared to the CeO_2 material.

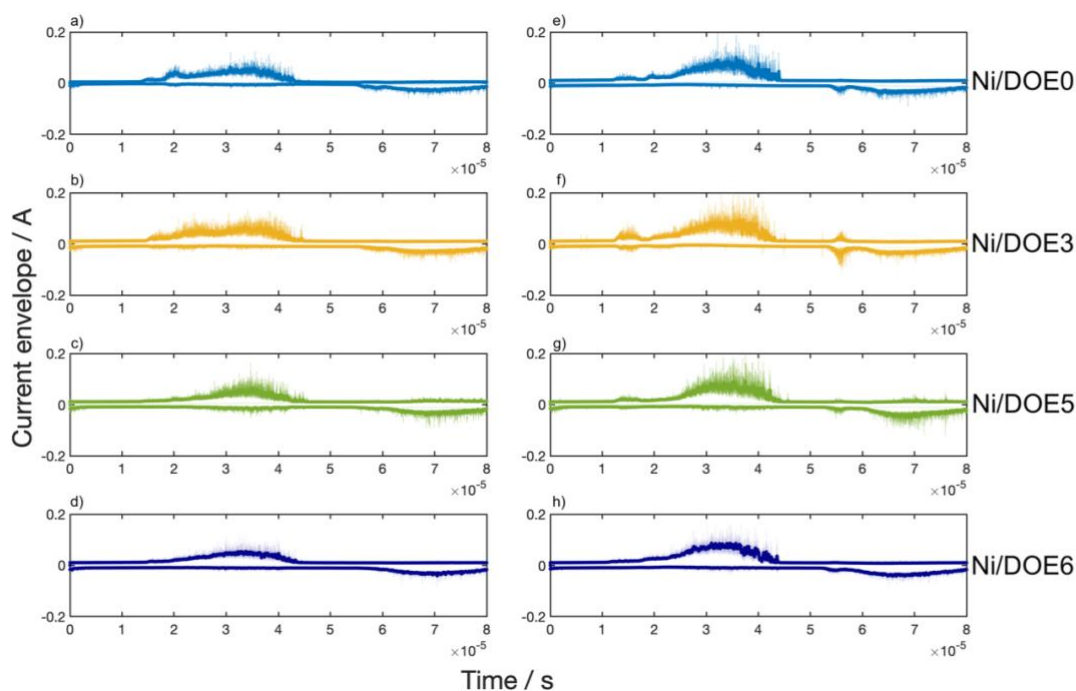


Figure 5.12: Current envelopes over 1 period obtained during the experiments with the DBD reactor packed with a),e) Ni/DOE0, b),f) Ni/DOE3, c),g) Ni/DOE5, d), h) Ni/DOE6 at a)-d) 25.4 ± 0.2 kV_{p-p} and e)-h) 27.7 ± 0.3 kV_{p-p}.

The qualitative comparison of the current envelopes related with the different catalysts (Figure 5.12a-d and e-h) reveals differences in the modality of the current peak distribution and a variation also due to the increase of power. A close-up of the first section of the envelopes of Figure 5.12e-h in the $1\text{--}2.5 \times 10^{-5}$ s range is reported in Figure 5.13, which helps to appreciate the change in current peak distribution. Ni/DOE0 shows double peaks (which also characterize the envelope for this sample at 25.4 ± 0.2 kV_{p-p}, see Figure 5.12a), Ni/DOE3 a wider first peak, similar to Ni/DOE5, while Ni/DOE6 is flat in the first region and shows a low intensity but wide distribution later.

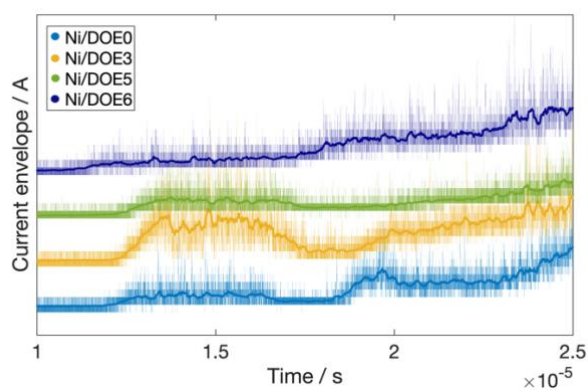


Figure 5.13: Close-up in the $1\text{--}2.5 \times 10^{-5}$ s range of the current envelopes obtained during the experiments with the DBD reactor packed with Ni/DOE0, 3, 5, 6 catalysts at 27.7 ± 0.3 kV_{p-p}.

The first current peak registered by the envelope is considered the beginning of plasma ignition in the DBD. The time at which the first current peak is observed is linked with a relative applied voltage value which corresponds with breakdown voltage. The Q and V signals reported in Figure 5.10 can also be plotted one versus the other to build a Lissajous cycle, as shown in Figure 5.14. The ignition voltage for the positive and negative half periods are pointed on this graph with small circles, it is shown graphically that such measurement is in agreement with what can be assessed from the Lissajous figure regarding plasma breakdown. In fact, the V_{ignition} corresponds with the end of the linear portion of the plasma “off” region of the Q-V cycle, the subsequent increase of slope and appearance of the Q steps, which are tied to discharge occurring in the gap.

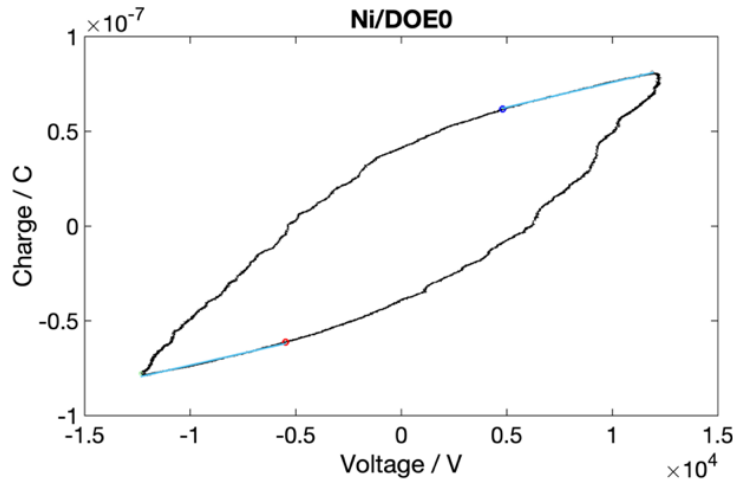


Figure 5.14: Example of measured Lissajous Q-V cycle for Ni/DOE0 at 25.3 kV_{p-p} layered with the linearization of the plasma “off” part obtained from the current envelope analysis.

The V_{ignition} values are reported in Table 5.3, they differ from the V_{gap} calculations discussed in section 5.3.1, however they maintain roughly the same ranking among the experiments with different packing materials. A lower V_{ignition} could be linked with more facile breakdown, which has been related with the dielectric properties of the packing, surface charging and local electric field enhancement [181,187].

Table 5.3: Overview of the results obtained from the current envelope analysis at the two voltage conditions (25.4 ± 0.2 kV_{p-p} and 27.7 ± 0.3 kV_{p-p}) and with different packing materials.

Sample	Condition: Power, W	V _{ignition -envelope,} kV	V _{ignition +envelope,} kV
Empty	16	6.5	-5.6
	34	7.5	-6.0
Al ₂ O ₃	18	5.6	-6.0
	35	9.1	-7.1
DOE0	18	4.5	-5.0
CeO ₂	29	7.8	-7.5
Ni/DOE0	15	7.0	-5.6
	27	7.8	-7.6
Ni/DOE3	17	5.6	-6.6
	31	8.3	-8.5
Ni/DOE5	15	6.9	-6.6
	29	8.4	-8.1
Ni/DOE6	16	4.8	-5.1
	31	8.0	-8.3

The current envelope only retains the most intense events regarding charge transfer and current flow, which should be linked with the charge steps with largest ΔQ_{step} . To link these events, a new analysis of the charge over 120 periods was carried out with different parameters for the peak selection compared to the analysis in section 5.3.2, that aim to isolate only the largest ΔQ_{step} (above ~ 1 nC). The histograms considered in this case regard the distribution of the events over time t_{step} (at which the charge steps occur) normalized over one period. This analysis was performed for selected experiments: empty reactor and packed with Ni/DOE0. The time histograms are layered with the current envelopes over one period and an example of Q signal, just to point to the region where charge steps are usually observed. These plots are in Figure 5.15. It is clear that the large charge transfer events are more numerous in the case of empty reactor and more spread over the half-cycles (Figure 5.15a and b), this might agree with the higher current envelope intensity of empty DBD compared with the catalyst packing. Furthermore, in both cases the large ΔQ_{step} events increase with power increase, as was shown by the widening of the charge distributions in Figure 5.7 and 5.8. For the packed bed DBD reactor, the large ΔQ_{step} are isolated in the first region of the current envelope, which was previously analysed to find variations in the current peak distribution between different materials. These charge transfer events at the beginning of ignition could be related with the first surface polarisation discharge over the catalyst packing.

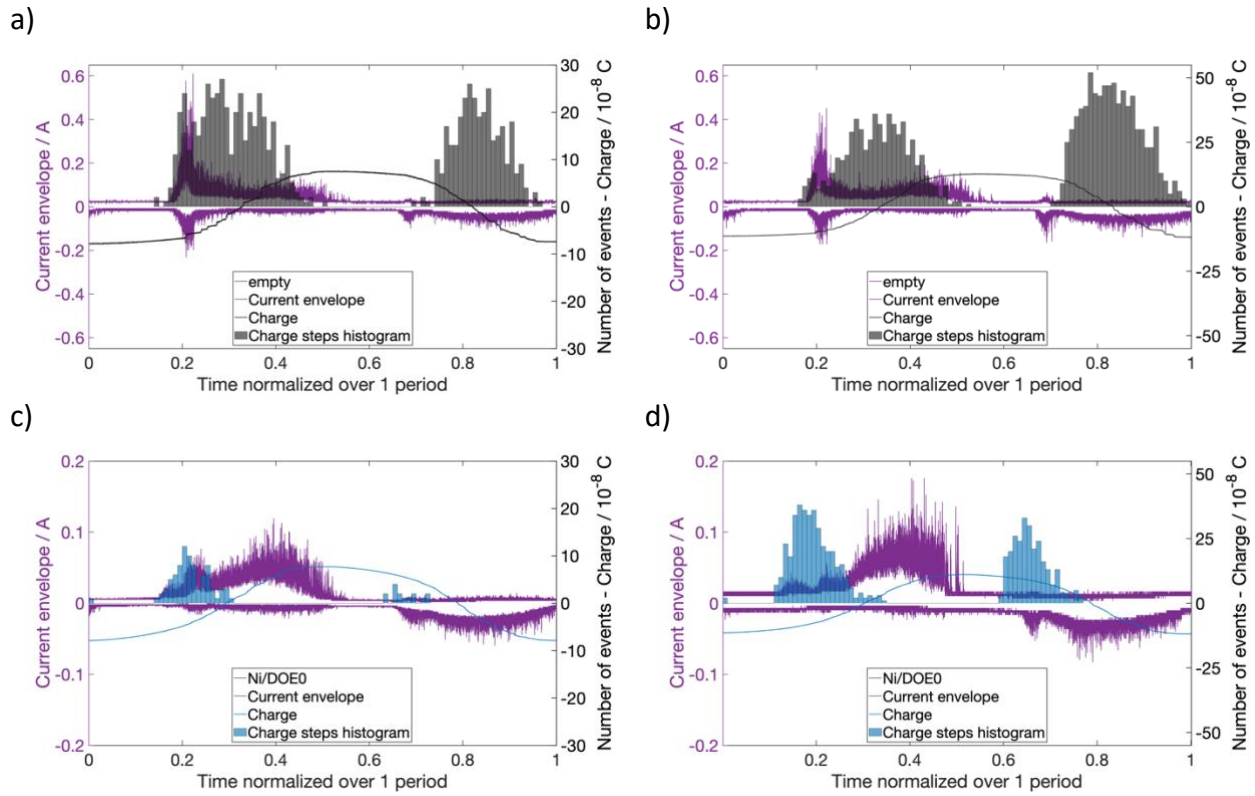


Figure 5.15: Current envelope layered with the charge transfer events time histogram and the charge signal over 1 period. The experiments were performed with a), b) empty DBD reactor and packed with c), d) Ni/DOE0 catalyst at a), c) 25.4 ± 0.2 kV_{p-p} and b), d) 27.7 ± 0.3 kV_{p-p}.

5.3.4. Effect of physicochemical features of the catalyst on the electrical behaviour of the packed bed DBD

The most relevant results coming from the analysis of V, Q and I signals as presented in the previous sections are reported in Table 5.4 with the values of C_{on} (from Lissajous figure analysis), Q_{total} (from the charge steps analysis), and $V_{ignition}$ (from the current envelope analysis). The catalytic activity in DBD plasma is assessed via CO₂ conversion (only the power condition at which high conversion is obtained is reported in this table), selectivity of CH₄ and energy efficiency, also in Table 5.4. The energy efficiency was also used as parameter in the discussion in the previous chapter and, as mentioned before in equation (2.12), it depends on power (in this case ranging 27-31 W), H₂ conversion, and CH₄ production.

C_{on} is found to be inversely proportional to efficiency, similarly to what was stated regarding $C_{reactor}$ in chapter 4. The dielectric permittivity of the catalysts is once again proven to be relevant for the CO₂ methanation reaction in plasma. In this case the catalysts rank as Ni/DOE0 < 5 < 3 < 6, which slightly differs from the previous results regarding $C_{reactor}$. However, the general trend of $\epsilon_{catalyst}$ versus efficiency, as shown in Figure 4.9, is confirmed by the experiments carried out in the modified DBD set-up. Furthermore, an easier ignition mechanism and lower charge deposition in the packed bed DBD, meaning lower $V_{ignition}$ and Q_{total} , seems to also favour the reaction. However, a clear relation

of such features with the plasma-assisted methanation yield could not be found, as the Ni/DOE6 catalyst, which is the worst catalyst of this series, presents low V_{ignition} and Q_{total} like the most active catalyst, Ni/DOE0. Nonetheless, Ni/DOE0 is characterized by the smallest values of V_{ignition} and Q_{total} of this series and has a charge step distribution that favours events below 10 nC.

The physicochemical properties of Ni/DOE0, 3, 5, and 6 catalysts and corresponding supports presented in chapter 3 have been screened to find a link between electrical and physicochemical features of these materials. The physicochemical properties that were found to be related with the dielectric and charge transfer behaviours are Ni crystallite size (from XRD, previously reported in Table 3.4), H_2 consumption at low temperature during TPR experiment (see Figure 3.25a and), Ce^{3+} defects concentration (from XPS analysis in Table 3.6), and total pore volume V_p (from N_2 physisorption, see Table 3.4), all in Table 5.4.

Table 5.4: Overview of CO_2 methanation catalytic results at 27.7 ± 0.3 kV_{p-p} applied voltage and with 29 ± 2 W injected power, electrical characterization, and selected physicochemical properties of the Ni/DOE0, 3, 5, and 6 catalysts.

Sample	X_{CO_2} , %	S_{CH_4} , %	Efficiency, %	C_{on} , pF	Q_{total} , nC	V_{ignition} , kV	Ni crystallite size, nm	Low T TPR, mmol/g	OV, Ce^{3+} %	V_p , cm^3/g
Ni/DOE0	80.9	100	23.5	12.88	160	7.8	17.8	30	19.3	0.21
Ni/DOE3	78.1	97.5	20.7	15.05	200	8.3	22.2	25	18.7	0.10
Ni/DOE5	79.8	100	22.4	14.49	180	8.4	29.2	18	16.9	0.21
Ni/DOE6	59.3	93.1	15.9	16.25	170	8.0	30.0	6	19.7	0.05

Increased metal phase dispersion can be related with lower dielectric permittivity, described by C_{on} . C_{on} is proportional to the low temperature H_2 consumption, previously linked with increased metal dispersion, and inversely proportional to Ni crystallite size. The enhanced metal dispersion, reducibility and MSI could decrease the surface polarizability and result in lower $\epsilon_{\text{catalyst}}$. Furthermore, with a material having lower dielectric permittivity it is expected to deposit less charge in the packed bed. Charges and electrons are thought to be deposited on the surface of the packing dielectric material by electrostatic interactions, which might be enhanced by increased polarizability (higher $\epsilon_{\text{catalyst}}$) [126]. Furthermore, surface defects such as oxygen vacancies on ceria are also important regarding conduction mechanism, and conductivity is reported to increase with larger amount of defects on the surface of ceria due to doping or non-stoichiometric CeO_2 [171,188]. The catalysts with largest amount of OV after Ni impregnation and reduction are found to have the lowest Q_{total} . This could be explained by the tendency of charges to tunnel the material instead of being deposited on the surface. However, the dielectric behaviour (C_{on}) could not be related directly

with surface defects. In addition, another physicochemical feature that could be linked with facilitated conduction mechanism in metal oxides is lower pore width due to the proximity of the particle boundaries [189].

According to the results gathered in Table 5.4, larger pore volume is linked with lower C_{on} . This difference in V_p can be ascribed to the different interparticle voids that are created due to the different morphology and size of the particles. The different interparticle voids configuration in the samples might affect the contribution of the gas discharge to C_{on} . The modal pore size (Table 3.4) is a way to quantify the pore size distribution shown in Figure 3.14b and at the range calculated for these catalysts (6.1-7 nm) it should not play a relevant role on the discharge [95]. In fact, it is unlikely that plasma will be created inside the pores of width $L = 6.1-7$ nm, as $L \gg \lambda_D$, which is de Debye length described in equation (1.9) and is typically several hundreds of nm [95]. The lowest size of mesopores in which DBD plasma could be ignited according to simulations is 50 nm, in which electrons barely penetrate at the beginning of the discharge [95]. For larger pores above 400 nm size the plasma propagation depends on the ϵ of the material, favoured with lower permittivity materials thanks to surface charges on the walls [187]. The N_2 isotherm graphs in Figure 3.14a show that Ni/DOE0 and 5 have the most relevant macroporosity feature and largest V_p among these four samples, meaning a rapid increase of slope at high partial pressure above 0.9. The presence of macroporous interparticle voids could favour ignition, as in the case of the needles supported catalyst, which has the lowest $V_{ignition}$ value.

All the aforementioned physicochemical properties are affected by the morphology and surface planes of the cerium oxide supports. The anisotropic structures along $\langle 011 \rangle$ axis such as nanoneedles and nanorods seem to possess the good OSC due to the less stable surface facet that is exposed which enhanced redox interactions and create wider interparticle pores between the elongated particles. The size of these structures might affect the interaction with Ni as the distribution of the metal phase is enhanced with the larger nanoneedles. It can be concluded that the morphology and physicochemical properties of the material affect the dielectric and conductive behaviours, changing its response once in contact with plasma and activity for plasma catalysis reactions.

5.4. Conclusions

Thanks to the electrical characterization reported in this chapter, more information on the plasma discharge were gathered and how this is affected by the presence of a catalysts in the discharge zone. The discharge is greatly affected by the packing material. In fact, a clear variation is observed between the empty and the packed bed DBD reactor. The current peaks are increase in intensity without a packing material, which translates to more charge deposited in the reactor in each half period. As expected, the effective capacitance of the DBD reactor decreases without a packing material and is affected by the choice of material used as catalyst. Further differences were shown regarding charge transfer behaviour and measured current peaks between packing materials such

as supports and catalysts. Different breakdown voltage, dielectric properties, and charge transfer events were recorded for four catalysts having different physicochemical properties and morphology. Some hypotheses on relations between physicochemical and electrical properties of the materials have been made, linked with possible electron and ion conduction mechanisms enhanced by surface defects, MSI, and interparticle interstitial configuration. Such features are optimised with nanoneedles ceria structures used as support for the Ni/DOE0 catalyst. Once again, the conventional physicochemical properties for methanation discussed in the previous chapter, such as basicity and surface area, are not the only features that are associated with the CH₄ production and efficiency. Plasma-assisted CO₂ methanation activity seems to be affected by the dielectric permittivity of the catalysts in the packed bed which also allows a facile plasma ignition. In general, the results point to a detrimental effect of high dielectric permittivity of the catalyst. Such feature can influence the surface polarizability of the catalyst, the local electric field enhancement, and the charge transfer events. It appears that large amount of charge transfer (shown by the charge step distribution and intense current peaks) linked with strong surface polarisation hence electric field is not favouring the CO₂ methanation reaction in the DBD plasma reactor.

Chapter 6: Proposed reaction mechanism of plasma-assisted and thermal CO₂ methanation with Ni/CeO₂ nanoneedles catalyst via operando studies

6.1.	<i>Introduction</i>	151
6.2.	<i>Methods</i>	152
6.2.1.	DBD plasma operando set-up	152
6.2.2.	Thermal operando set-up	153
6.3.	<i>Results and discussion</i>	154
6.3.1.	DBD plasma operando study.....	154
6.3.2.	Thermal operando study.....	160
6.4.	<i>Conclusions</i>	164

6.1. Introduction

The difference in activity in thermal and plasma-assisted CO₂ methanation with the Ni/CeO₂ catalysts of the DOE series was reported and assessed in chapter 4. This variation was linked with the different physicochemical and dielectric properties that the catalysts possess. Nonetheless, it is very important to understand how these features affect the surface chemistry during the catalytic reaction activated either by temperature or plasma. Further knowledge on the reaction mechanism in plasma catalysis will allow to identify the most relevant features of a catalyst to enhance the interactions required by the detected reactions occurring on its surface (such as basicity, hydrophobicity, affinity for a particular functional group). Such studies will further develop the rational design of catalysts made specifically for plasma catalysis.

FTIR spectroscopy has been reported as a reliable technique for operando analysis of the composition of IR active molecules on catalyst surface and in gas phase during thermochemical catalytic reaction [78,190]. The thermal CO₂ methanation reaction has been well characterised and previously studied in operando FTIR. It has been reported that it can follow either the CO [191] or the formate pathway [190]. The first one involves initially the formation of CO and then resembles the CO methanation reaction [191], while the latter involves formates and carbonates as intermediates without the presence of CO [190]. It has been reported in literature that CO₂ methanation reaction follows the CO pathway with Ni catalysts supported over irreducible metal oxides such as Ni/Al₂O₃ [192]. Regarding Ni/CeO₂, both CO and formate pathways have been reported [172,192,193]. The formate pathway seems to be linked with the presence of oxygen vacancies in the support such as for CeO₂ [192].

A deeper understanding of the nature of the groups formed on the catalyst surface exposed to the methanation reaction mixture and their evolution over time can give insights on the reaction

mechanism and highlight difference in the activation mechanism in thermal and plasma-assisted CO₂ methanation. The application of the FTIR operando technique to plasma catalysis has been recently developed [97,194–197], and it was shown how relevant it is to further have insights on the reactions occurring in plasma and on the plasma exposed surface of the catalyst, which might differ from the thermal case. Azzolina-Jury and Thibault-Starzyk reported the design of a low-pressure glow discharge cell used for time-resolved FTIR suitable for the investigation of the surface of the catalyst and the gas phase with plasma [194]. The implementation of such techniques remains a challenge when investigating atmospheric pressure DBD plasma [197]. Furthermore, due to the co-dependency of reactions occurring on the catalytic surface and in the plasma, there are only a few publications discussing the mechanisms for plasma-assisted CO₂ methanation [197,198]. Recently, Van Turnhout et al. and Aceto and al. [196,197] used a novel DBD FTIR cell to investigate surface species adsorbed on a Ru-catalyst during plasma-catalytic dry reforming of methane and CO₂ methanation, respectively.

6.2. Methods

The FTIR operando study was performed at LSC of ENSI-Caen under the supervision of Dr. Azzolina-Jury and with the precious help of Dr. Nguyen-Quang. The catalyst named Ni/DOE0 was used for the experiments reported in this chapter, as it showed an interesting variation in its activity in plasma-assisted and thermochemical CO₂ methanation. 20-30 mg of catalyst was pelletized into thin 16 mm diameter disks using a hydraulic press (Specac).

6.2.1. DBD plasma operando set-up

The custom-made operando DBD IR cell was previously described in recent publications [196,197], a scheme of the set-up can be found in Figure 6.1.

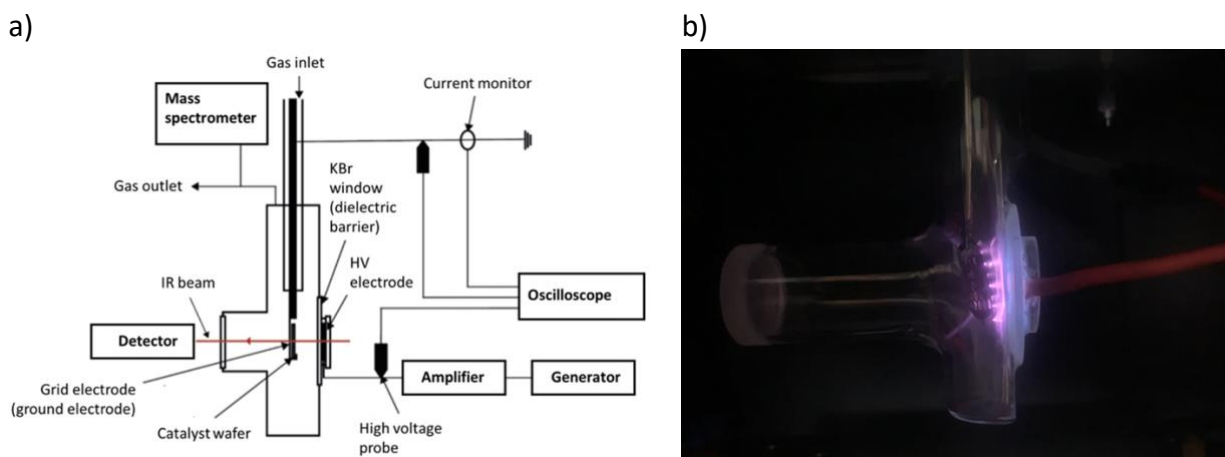


Figure 6.1: a) scheme of the operando DBD FTIR cell reproduced from [197]; b) a photograph of the operando DBD reactor while plasma is ignited.

The DBD IR cell was situated in the sample compartment of a Bruker Vertex 80v spectrometer with a liquid nitrogen cooled mercury-cadmium-telluride (MCT) detector (4000–400 cm⁻¹ range, 0.2 cm⁻¹ step, spectrum recorded every 9 s). The T-shaped DBD IR cell is made of glass with KBr windows placed to either side of the pellet to allow IR beam transmission. The sample pellet was inserted perpendicularly to the IR beam using a sample holder that consists of a metallic rod covered by glass, glass hooks that keep the pellet in place, and a metallic grid, which is placed behind the pellet and functions as ground electrode. The HV electrode is glued to one of the KBr windows, which acts as dielectric barrier (leaving a gap of ~3 mm). The design allows to ignite the plasma directly on the surface of the sample. The HV electrode was connected to a signal generator (Générateur de fonctions arbitraires 50 MHz, Française d'Instrumentation) through an amplifier (Trek 20/20C) and monitored by a voltage probe (Testec HVP-2739-1000:1). An external capacitor (3.3 pF) and a current monitor (Hioki CT6710) were placed on the ground connection. A voltage probe measures the voltage drop across the external capacitor. The voltage and current probes were connected to a Tektronix MDO3024 oscilloscope. CO₂, H₂ and Ar gas flows were controlled through Brooks Delta Smart II mass flowmeters. The gases were mixed through a six-ways valve and then let in the DBD cell directly above the catalyst pellet. The output gas was monitored by a MS (Pfeiffer OmnistarGSD 301). The cell was connected to a rotary pump (~0.3 Torr, Edwards nXDS6iC) and a turbopump (10⁻⁷ Torr, Pfeiffer vacuum HiCube 80) to allow for easy purging of the cell.

The catalyst was introduced in the cell and the system was purged under secondary vacuum (10⁻⁷ Torr). The sample was subjected to thermal activation at 300 °C 5 °C/min for 1 hour under vacuum. The reactor was then filled with Ar to reach atmospheric pressure and a reduction pre-treatment was performed in H₂/Ar plasma at 25 kV_{p-p} and 3 Hz with a 5%H₂/Ar 20 cc/min flow for 10 minutes. After purging again, Ar was used to return to atmospheric pressure. The reaction mixture was then let into the cell, with a total flow of 20 cc/min and in a 1/4/5 CO₂/H₂/Ar ratio. Once the cell is filled by the reaction mixture and the FTIR spectra are stabilised and MS signals reach a plateau, the plasma is ignited. Two power conditions were tested: the first one with 22 kV_{p-p} HV signal for 10 minutes and the second one at 25 kV_{p-p} for 15 minutes. The reaction time was sufficient to reach the steady state, i.e., when the spectra and MS signals do not show significant variation anymore. The plasma was then turned off and the cell was purged under secondary vacuum.

6.2.2. Thermal operando set-up

The pellet was inserted in the “sandwich” cell for operando thermal catalysts, which was mounted in a FTIR spectrometer (Thermo Scientific Nicolet 6700 spectrometer, equipped with a MCT detector, 4000–400 cm⁻¹ range, 4 cm⁻¹ step, 64 acquisitions per spectrum). This set-up was previously described by Wuttke et al. [199]. The “sandwich” cell consists of two KBr windows at the extremities, among which the sample pellet is placed in a cylindrical stainless-steel holder that is heated and its temperature is controlled by a K-type thermocouple. The KBr windows are cooled down to keep the temperature below 300 °C, the cell is sealed by O-rings and the experiment is

carried out at atmospheric pressure. The gas mixture is controlled by mass flow controllers and the exhaust gasses are analysed by a quadrupole MS (Pfeiffer Omnistar). The catalyst was activated in 5% H₂/Ar at 300 °C 3 °C/min for 2 hours. After this step, the reaction mixture of 2 cc/min CO₂, 8 cc/min H₂, and 10 cc/min Ar was introduced, and the temperature maintained at 300 °C during the methanation reaction.

6.3. Results and discussion

6.3.1. DBD plasma operando study

The overview of the FTIR spectra acquired during the plasma-assisted CO₂ methanation reaction is presented in Figure 6.2. The profiles in Figure 6.2 were obtained by subtraction of the spectrum just before the ignition of the plasma from each line in order to achieve a mostly linear baseline and assess the development during the plasma reaction [197]. The view of the full spectra presents immediately the critical points of working with pellets of such materials that are prone to breaking and due to the thickness and dark colour absorb light, resulting in a noisy signal above 3000 cm⁻¹ and below 800 cm⁻¹, which are regions of interest for carbonate species and potential methanation intermediates (C-H bonds) identification. In the full spectrum of the last point (25 mins) in the inset in Figure 6.2 the peaks relative to gas phase CO₂ (peak around 2350 cm⁻¹, which saturates) and CO are clearly shown (2200-2000 cm⁻¹ range) [194]. The CO contributions appear after a few minutes of plasma ignition and might be due to splitting occurring in the plasma or RWGS occurring. The main methane gas phase peaks around 3000 cm⁻¹ [194] were not detected in the spectra, probably due to the noisy signal in this region.

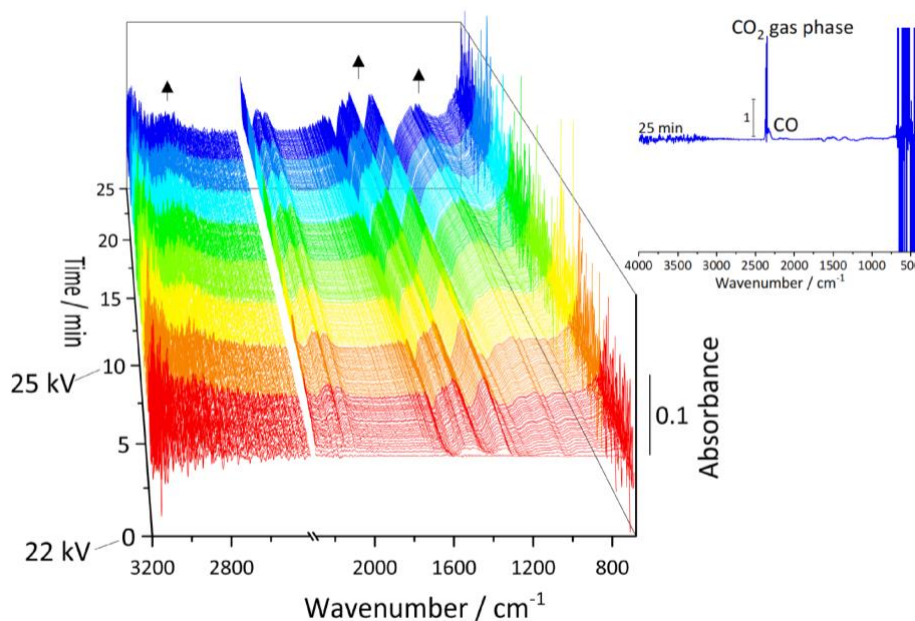
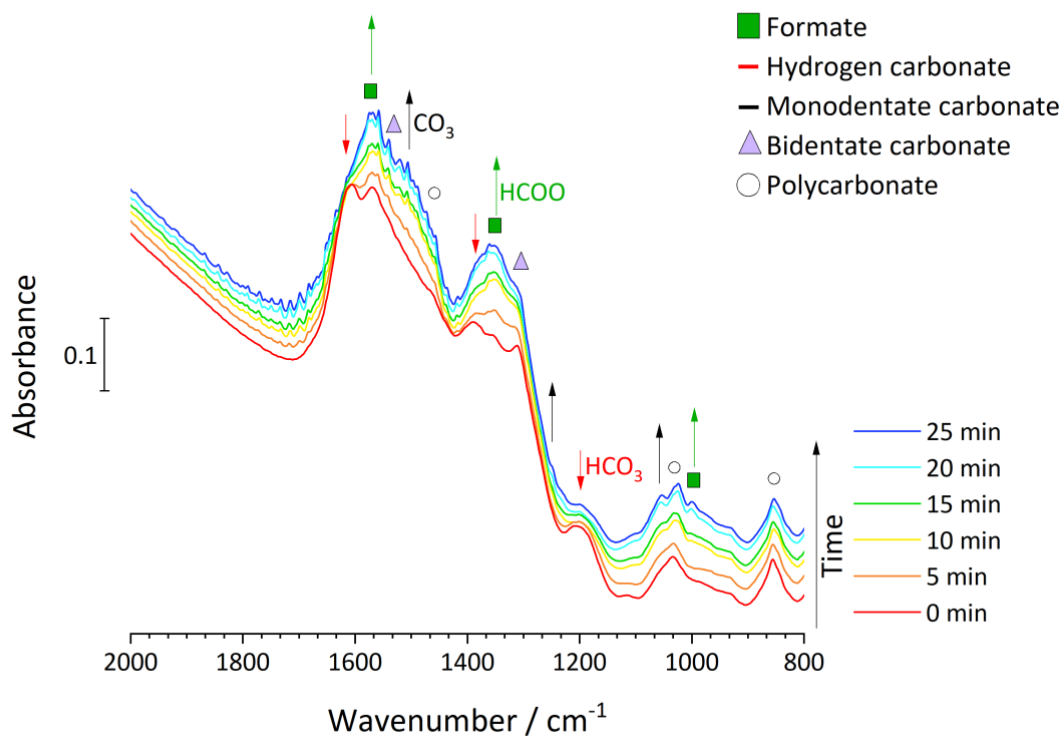


Figure 6.2: FTIR subtracted spectra in the 3200-680 cm⁻¹ range over 25 minutes time of plasma-assisted CO₂ methanation reaction with a break between 2400-2300 cm⁻¹. An example of the full spectrum is shown in the inset.

Mainly two regions of the full spectrum evolve over time and after around 15 minutes stabilize: 1600-800 cm⁻¹ and, despite the noisy signals, around 3000 cm⁻¹. The first is usually linked with presence of carbonate species, as seen in the ex-situ FTIR spectra in the previous chapter (Figure 4.19), while the latter is normally the region where C-H bands of different species are located. These two regions will be analysed in detail below. The spectra in the region of interest 1600-800 cm⁻¹ generally resemble the modality of the curve obtained from ex-situ FTIR analysis of the same catalyst after plasma reaction (Figure 4.19), except for the 1633 cm⁻¹ H-O-H bending peak. The intensity of the spectra in Figure 6.2 in the region above 1600 cm⁻¹ increases over time, however a clear peak is not detected at this position during the operando DBD plasma experiment probably due to an irregularity in the pellet which distorted the spectrum in this range or the fast desorption of water from the surface due to the energy deposited by the plasma [197]. In fact, the production of water due to the plasma ignition is shown by the noisy appearance of all spectra in 1850–1400 cm⁻¹ range, such equally spaced and sharp peaks are vapor phase H₂O vibrations [197,200]. The formation of H₂O is actually the symptom of CO₂ and H₂ reacting after plasma ignition and forming water, which is a co-product in both cases of CO₂ methanation and RWGS reactions, despite no clear CH₄ and CO evolution being observed in the MS at the initial stage (Figure 6.4). A negative effect might be the blocking of the catalytic sites due to water not desorbing from the surface of the material.

The evolution over 25 minutes of reaction (considering the two conditions combined) of the non-subtracted spectra in the regions just mentioned, 2000-800 cm⁻¹ and 3050-2500 cm⁻¹, are reported in Figure 6.3a and b, respectively. A qualitative band identification analysis was performed and is shown on the figure by the use of different symbols. It was considered that the peaks assigned to the same adsorbed specie vary accordingly and the vibrational frequencies obtained were compared with data from literature in order to assess the physical consistency of each peak. A summary of previously reported band position for carbonates and formate species on ceria surface can be found in Annex 3. In general, the assignation just presented is in agreement with previous work by Vayssilov et al., Lin et al., Pozdyakoka et al., and Pan et al. [159,179,201,202]. The several peaks of the same species are reported with the symbol in Figure 6.3. The most prominent peaks are situated at 1570 and 1350 cm⁻¹, they increase with time and are assigned to formates (together with the $\delta(OCH)$ vibration at 1000 cm⁻¹) [159]. The main peaks show several contributions and shoulders. The peaks at 1610 and 1200 cm⁻¹ decrease in prominence over time, together with the shoulder around 1390 cm⁻¹, which suggests that they are consumed during the reaction [159,179].

a)



b)

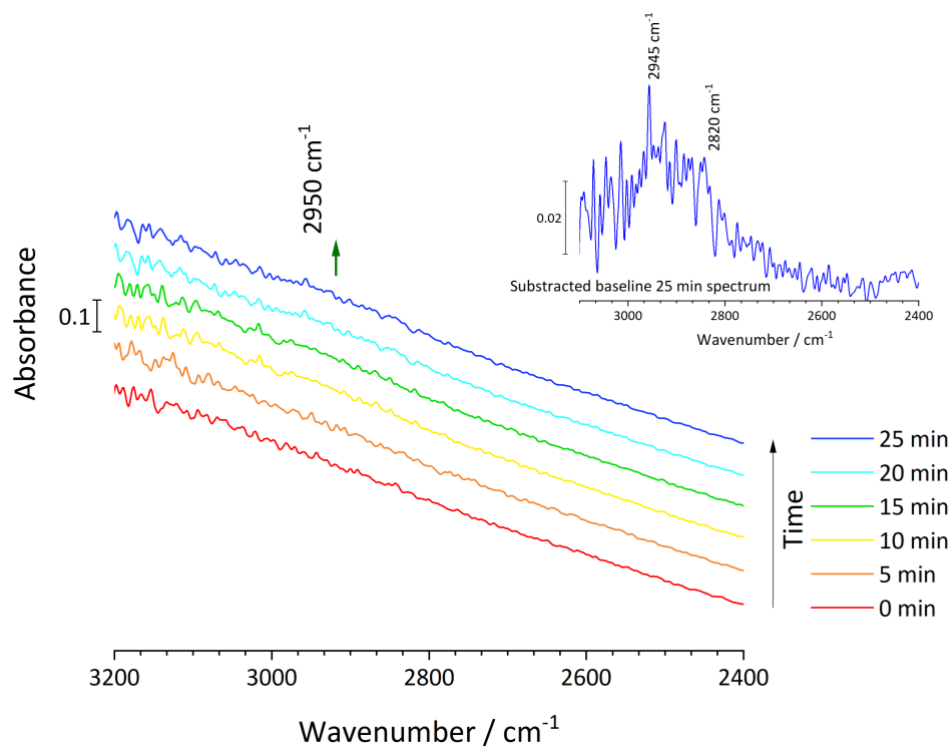


Figure 6.3: Time evolution of FTIR spectra in the a) 2000–800 and b) 3200–2400 cm⁻¹ regions during the plasma-assisted CO₂ methanation reaction. Peak assignment is shown by symbols, the arrows indicate the suggested growth trends. The inset in b) shows the baseline subtracted last spectrum.

The other peaks in the 1600-800 cm⁻¹ region are related to carbonate species with two or more bounds to the surface oxygens, which already adsorb at room temperature and continue being replenished once the plasma is ignited. The contributions at 850, 1030, and 1470 cm⁻¹ are probably of polycarbonates already present on the surface due to interaction with CO₂ at room temperature, which might do not participate in the reaction as no variation in absorbance in visible in Figure 6.3a [202]. Despite the very noisy spectra in 3200-2400 cm⁻¹ range in Figure 6.3b, it is possible to discern a growing wide peak around 2950 cm⁻¹ when a linear baseline is subtracted (in the inset). The wide peak is fitted by two components at 2945 and 2821 cm⁻¹, attributed to C-H vibration of formate and CH₂ absorbed species, respectively [159,194].

The spectrum at 0 min in Figure 6.3a corresponds to CO₂ adsorption on the catalyst surface at room temperature, the surface species at this condition are mostly carbonates (polydentate and hydrogen carbonates). In fact, CO₂ is expected to adsorbed on the basic sites of the ceria surface forming carbonates (CO₃) with the oxygen of one or more Ce-O pairs (mono-, bi- or tridentate) according to the configuration of the carbonate and the number of oxygens that link the C to the surface [203]. Switching on the plasma leads to an increase of formate peaks and decrease of hydrogen carbonates. The evolution of such species suggests that these molecules are related to the methanation reaction as the variation depends also on the applied voltage that is increased after 10 minutes. Nonetheless, all the adsorbed species detected are formed by the interaction of Ni/DOEO catalyst with the CO₂/H₂ gas phase and plasma, but they might be either intermediates or spectators of the methanation reaction. The surface of the catalyst was purged in-situ before the operando experiment and was left in contact with the reaction mixture until stabilization, therefore the evolution over 25 minutes reaction time can be attributed uniquely to the plasma interactions and surface reactions occurring. It should be mentioned that at the first condition with 22 kV_{p-p} applied voltage no methane production is observed via MS (see Figure 6.4), while the CH₄ signal starts to increase after the voltage is switched to 25 kV_{p-p}, which corresponds to a more rapid stabilization in growth of all peaks. With more power being injected into the plasma (second applied voltage condition), enough energy is available for the methanation reaction to occur. Yet, it should be pointed out that the CO₂ conversion observed during the operando experiments, both plasm-assisted and thermal, is negligible compared to the previous tests. This is probably due to the design of the reactors and of such experiments that require a very low amount of reactants and catalyst, which also results in very low surface area due to being pelletized. All contributions plateau after 20 minutes of plasma-assisted reaction as can be seen from the FTIR spectra in Figure 6.3a, which are almost unvaried between 20 and 25 minutes. The stabilization of such carbonates and formates species might be due to a reaction/desorption rate being in equilibrium with adsorption rate of these molecules, as at this condition CH₄ is produced it is possible to suggests that these species are involved in the reaction and consumed for CH₄ formation. As mentioned above, the only

contributions that do not vary over reaction time are the ones attributed to polycarbonates adsorbed at room temperature on probably strong basic sites of ceria. These are stable species that seem to not be consumed and do not participate in the reaction.

Instead, other carbonates already present on the surface are consumed and re-adsorb. The initial growth of carbonates might be attributed to interaction with CO₂ and CO in the gas phase as well as activated CO₂ from plasma with the basic adsorption sites on the ceria supports. H₂ is expected to adsorb on the metal sites (Ni particles) [81,96]. The interaction between adsorbed H₂ and CO₂ might allow the catalytic reactions to happen on the surface and produce water, which is the first molecule to be observed since the plasma ignition, CO (if not coming from CO₂ splitting entirely), and CH₄. Moreover, the FTIR spectra point to also more formates appearing on the surface. The reduction of hydrogen carbonates (pre-adsorbed on the catalyst) to formates seems to be the easier route as the HCO₃ is consumed first and water, that appears in the gas phase, is produced by this reaction. The adsorbed CO₃ could also be hydrogenated to form formates, that are probably the main intermediate of the plasma-assisted methanation reaction. The formate lines increase especially after 10 minutes (when the voltage is increased), peaking at 20 minutes and then stabilised, so their evolution is more tightly linked with the CH₄ production shown by the MS (Figure 6.4). It can be proposed formates are then stepwise hydrogenated to CH₂->CH₃->CH₄ with addition of hydrogen atoms, the latter then desorbed from the surface. Out of these hydrocarbon species, only CH₂ is detected in the FTIR spectra, and it was suggested by previous studies that such peak can be attributed to CH₂ adsorbed on Ni sites [96]. As only the peaks of formates and CH₂ species are identified in the spectra and grow in absorbance, it can be hypothesised that the slowest reaction rate is the ones involving the hydrogenation of formates to CH₂ and then the conversion of CH₂ to CH₃, while the final reduction to CH₄ is much faster and the product molecule desorbs quickly from the surface and therefore is not detectable by the FTIR spectra.

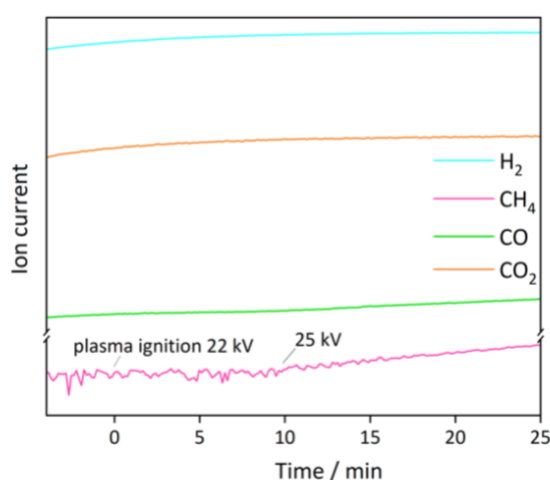


Figure 6.4: MS signals of H₂, CH₄, CO, and CO₂ over time during the operando plasma-assisted CO₂ methanation experiment.

It should be mentioned that due to large dead volume of the set-up the response of the MS is not very rapid, therefore the slow CH₄ observed after 10 minutes might probably be CH₄ formed right at the time of the condition switch to higher power but was detected afterwards. Both CH₄ and CO increase after the applied voltage is switched to 25 kV_{p-p}.

The electrical signals of Q, V, and I recorded during the experiment at both applied voltage conditions are reported in Figure 6.5. The Lissajous plots in Figure 6.5a appear very different compared to the ones obtained for the double dielectric set-up with cylindrical geometry used for the experiments reported in the previous chapters. The goal of the DBD used for the operando experiments is to form surface discharges on the pellet, which, at least from a visual analysis of Figure 6.1b, is obtained. Furthermore, the power injected in the system for ignition and measured via Lissajous cycle area calculation is one order of magnitude lower compared to the one previously reported, this difference could be due to the very different geometry and arrangement of the DBD set-up as well as thanks to the presence of Ar in the reaction mixture during the operando plasma-assisted methanation experiment, which is easier to ionize and allows to drop the breakdown voltage [204]. The first tested condition results in an almost negligible power, therefore it can be explained why no methane production is detected at this stage. With larger power (2.4 W) methane production seems to be triggered.

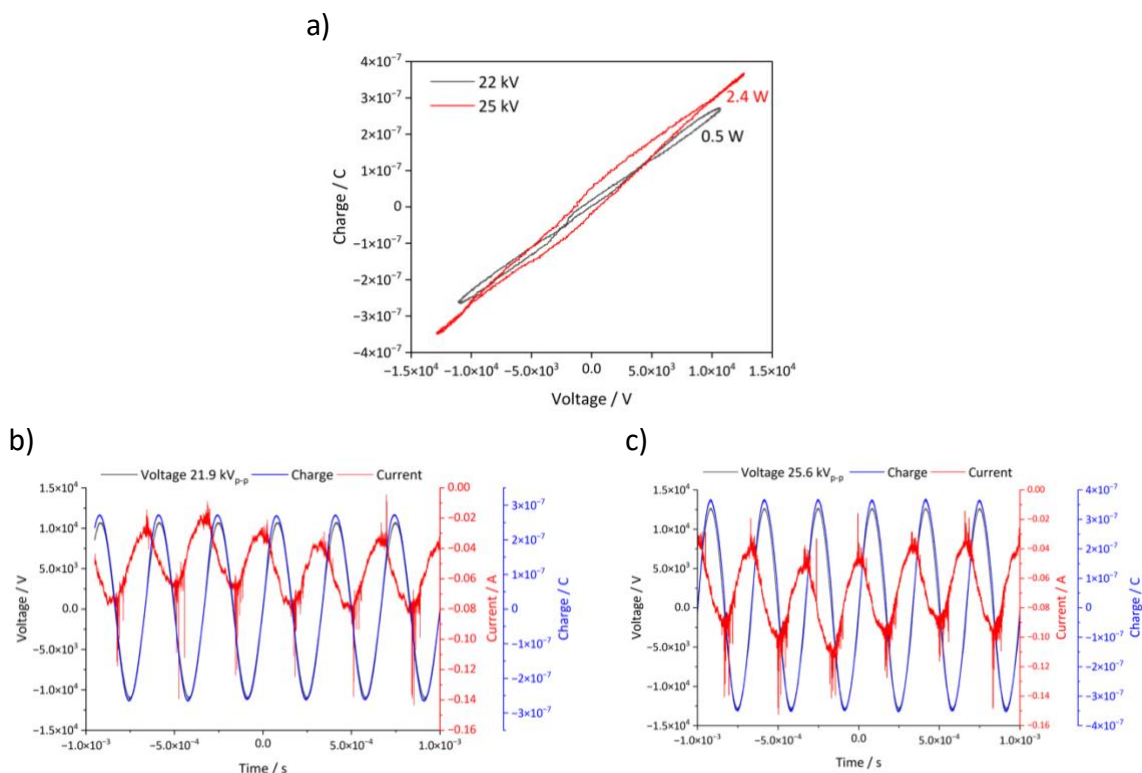


Figure 6.5: a) Q-V Lissajous figures obtained at the two tested conditions of the operando plasma-assisted CO₂ methanation experiment and V, Q, and I signals measured during the b) 22 kV_{p-p} and c) 25 kV_{p-p} conditions.

6.3.2. Thermal operando study

The FTIR spectra of surface and gas phase acquired during 15 minutes of thermal CO₂ methanation reaction with Ni/DOE0 catalyst pellet are reported in Figure 6.6a and b, respectively. Similar regions of interest compared with the previous operando experiment are identified for the thermal operando one, but also the same issues regarding noisy spectra are observed for the surface FTIR spectra in Figure 6.6a. The region where the peaks of carbonate species on ceria appear has to be limited between 1600 and 1000 cm⁻¹ due to the saturation below 1000 cm⁻¹ (inset of Figure 6.6a), but interesting bands are observed in this case between 2200-1700 cm⁻¹, therefore the extended area 2200-1000 cm⁻¹ is considered (Figure 6.7a). The second region studied in the previous section between 3000 and 2500 cm⁻¹ does not show an interesting evolution in Figure 6.6a except for the last spectrum at 15 minutes which exhibits a clear peak centred around 2850 cm⁻¹ (studied later in Figure 6.7b).

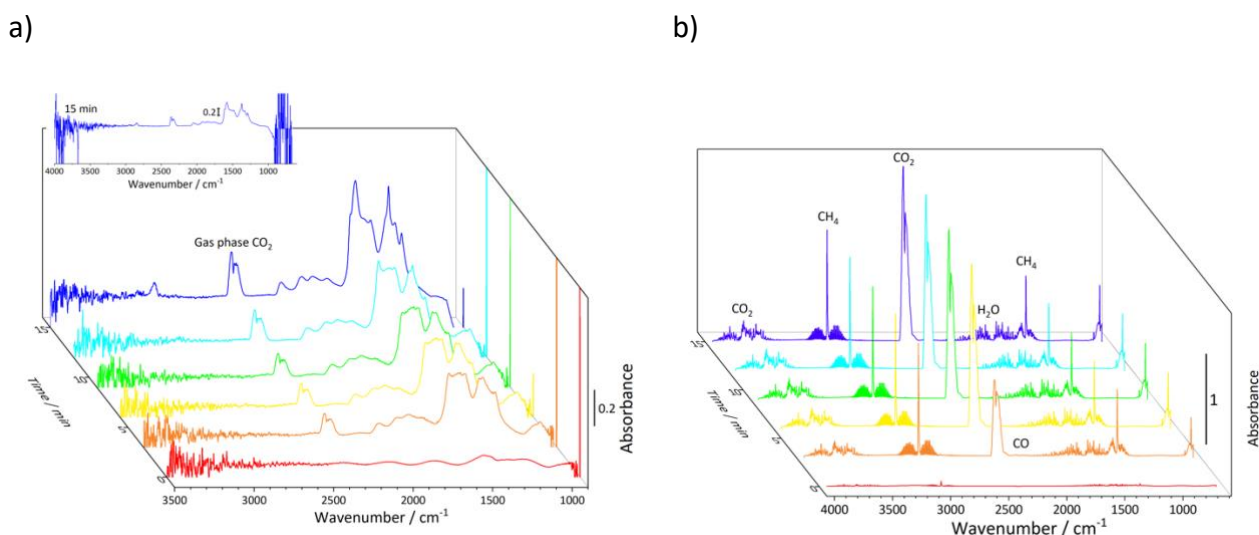


Figure 6.6: a) FTIR spectra of the surface of the catalyst in the 3500-900 cm⁻¹ range with the full final spectrum is shown in the inset and b) FTIR spectra of the gas phase in the 4000-600 cm⁻¹ range over 15 minutes time of thermal reaction.

The gas phase FTIR spectra over thermal reaction time in Figure 6.6b show the contributions of CO₂, CH₄, H₂O, and very low intensity peaks of CO, in agreement with the signals detected by the MS (Figure 6.8a). It is peculiar how the surface species do now stabilize quickly after the interaction with CO₂/H₂ reaction gas mixture but the gas phase peaks increase in intensity very rapidly and stabilize after just 5 minutes. The intensity of the main gas phase peaks have been plotted over time in Figure 6.8b. This slow evolution of surface adsorbed species compared to the plasma-assisted reaction (Figure 6.2) could be due to the different procedures adopted in both cases. It should be mentioned that the protocol of the thermal operando experiment fundamentally differs from the one carried

out in the DBD operando cell. In fact, in this case the pre-treated catalyst surface is maintained at 300 °C, temperature at which the methanation reaction is expected to occur with this catalyst (see chapter 4 and Figure 4.6), and then the reaction mixture is sent to the pellet and allowed to interact with the catalyst surface. It is expected that in this case we observe at the same time the catalytic reaction occur on the surface and the CO₂ adsorption to spectator species. On the other hand, the catalyst surface during the operando DBD plasma experiment was already saturated with carbonate species from the adsorption of CO₂ and the evolution occurring is purely caused by the plasma ignition triggering surface reactions and interaction of the adsorbed molecules with new species in the plasma and gas phase. It should be mentioned that the surface FTIR spectra were observed to stabilize after 15 minutes methanation reaction, meaning that the surface species stabilize and spectra acquired afterwards resemble the last spectrum of Figure 6.6 (data not shown).

Similar carbonate and formate contributions shown on the FTIR spectra acquired during the plasma-assisted reaction in the 1600-1000 cm⁻¹ region (Figure 6.3) are seen also in the spectra of the thermal operando experiment (Figure 6.7). The species proposed are mono- and bidentate carbonates, hydrogen carbonate, and formate. The peak positions of hydrogen carbonate are similar to the results shown previously. A shift of position is observed for formates and bidentate carbonates between the spectra of the two experiments. This can be explained by the different surface condition (regarding defects and OV) of the ceria surface exposed to plasma and heated at 300 °C, which greatly affects the carbonate adsorption and configuration on the surface, therefore the vibrational frequencies of such molecules [159]. Furthermore, the main peaks of adsorbed carbonates are proposed to be bidentate and monodentate due to the spacing between the $\nu(CO)$ frequencies [81,201,202]. The peaks identification is noted in Figure 6.7a and it is in line with frequencies reported in literature (see Annex 3) [159,179,201,202]. In addition to adsorbed carbonates and formates, four peaks in the 2200- 1700 cm⁻¹ regions appear after the first scan and grow in absorbance. The 1760 cm⁻¹ peak can be attributed to HCO [205], two components at 1840 and 1920 cm⁻¹ are known as vibrations of bridged carbonyls [197], and the 2040 cm⁻¹ is linked with linear carbonyls [206].

The FTIR spectrum region at higher wavenumber, where the peaks relative to C-H vibrations are usually observed, differs from the one acquired during the plasma operando test. In this case a peak centred around 2850 cm⁻¹ can be observed in Figure 6.7b, which is the contribution of two peaks at 2845 and 2871 cm⁻¹. Both are attributable to C-H stretching vibrations, the first of CH_x species and the latter of adsorbed HCOO [207]. It is interesting to notice that these two peaks appear only in the last spectrum of the thermal operando experiment, so when the equilibrium between surface and gas phase species is almost reached and the CO₂ methanation reaction has been established. The possible contribution of C-H vibration of formate which was observed in the previous experiment at 2945 cm⁻¹ is suggested (with a peak at 2952 cm⁻¹) but the actual presence of this band is masked by the noisy signal at this wavenumber range.

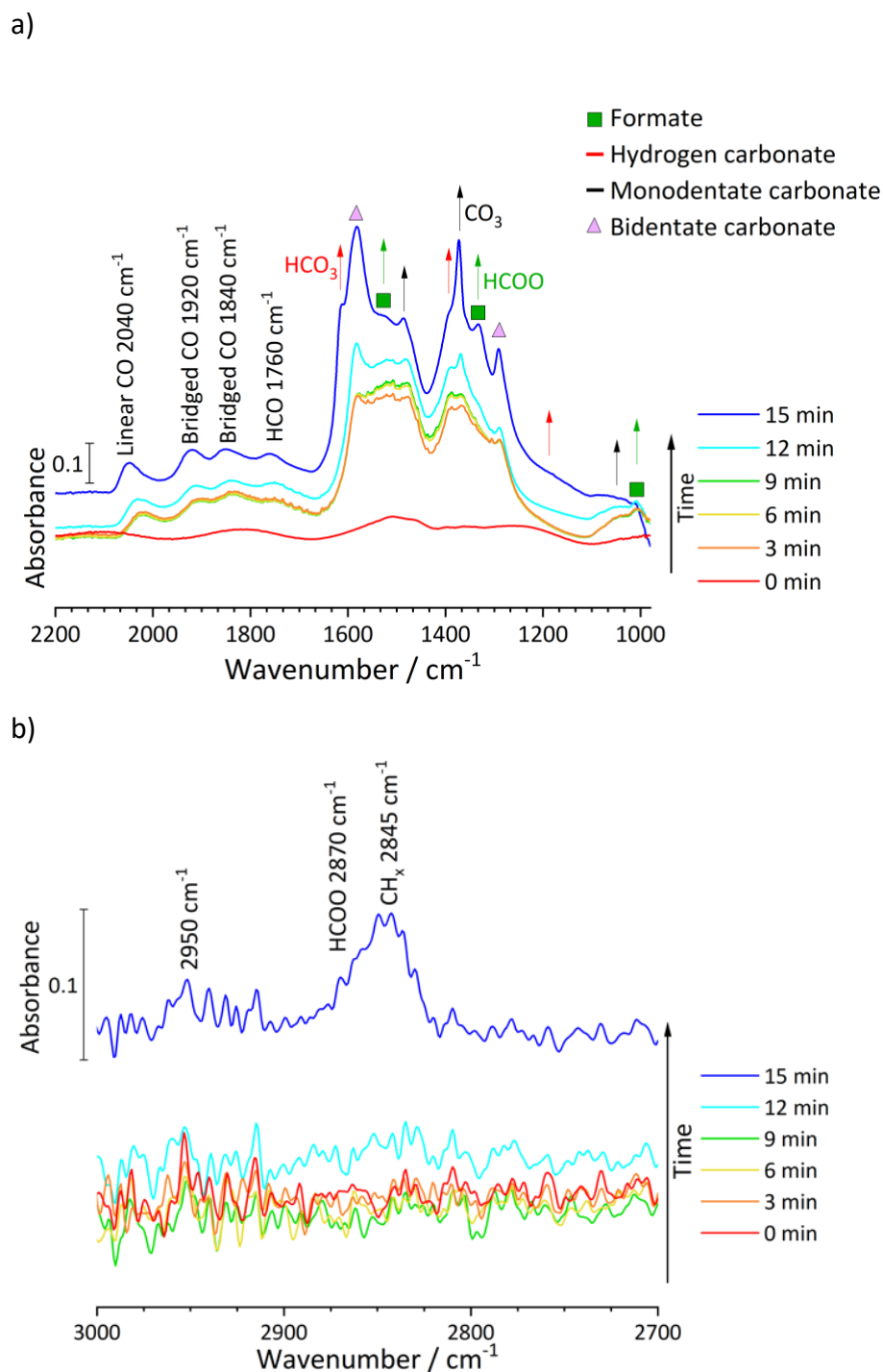


Figure 6.7: Time evolution of FTIR spectra in the a) 2200-950 and b) 3000-2700 cm⁻¹ regions during the thermal CO₂ methanation reaction. Line assignment is shown by vertical lines and symbols. An example of peaks deconvolution is given in the insets.

As observed in the FTIR spectra, all bands grow during the 15 minutes of thermal methanation reaction, with a slight stabilization between 3 and 9 minutes (Figure 6.7a). The peaks of carbonates

and formate increase, that might indicate that the adsorption from CO₂/H₂ gas phase is faster than the reaction rate until an equilibrium is reached. It suggests that there are several reactions competing on the surface once it is exposed with CO₂ and H₂ at 300 °C, meaning the CO₂ adsorption as carbonates and adsorbed CO₂ hydrogenation. The FTIR spectra evolution does not give a clear picture of possible intermediates. Moreover, the bands of C-H vibrations appear only after 15 minutes in the FTIR surface spectra, which can be misleading. However, the presence of CH_x and HCOO might be masked by the fast evolution of these intermediate species. A rapid consumption of carbonates to formate/HCOO to CH_x and finally methane, which is shown to be produced since the first 3 minutes by the gas phase FTIR spectra (Figure 6.8b), might be occurring at the beginning of the thermal reaction while an equilibrium is not reached yet, therefore the peak cannot be detected at this stage. Such reaction pathway is the formate route, which was suggested for the plasma-assisted reaction in the previous section. Nonetheless, the presence of carbonyl groups on the surface of the catalyst, not previously observed during the plasma-assisted methanation operando test, suggests the importance of CO₂ dissociative route in thermal CO₂ methanation. In conclusion, the combination of CO and formate pathway, previously suggested by Gonçalves et al. [193], is possible also with this Ni/CeO₂ nanoneedles catalyst.

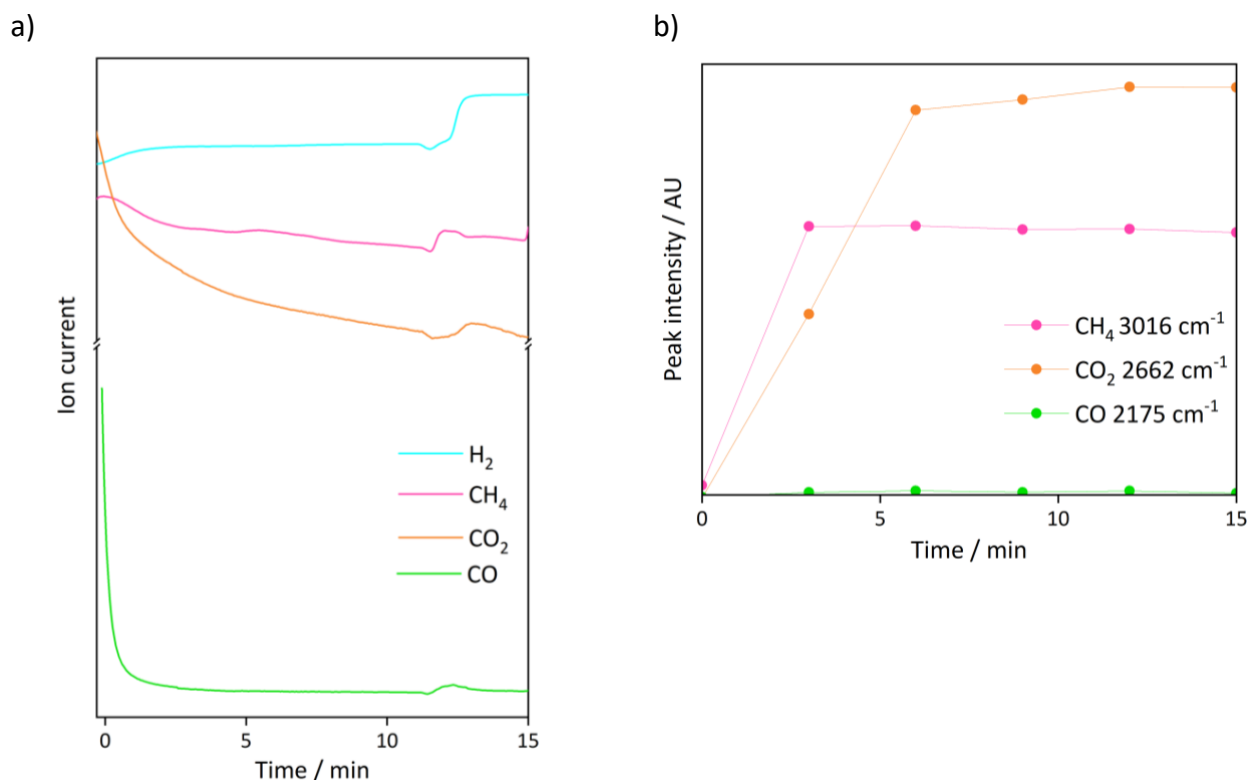


Figure 6.8: a) MS signals of H₂, CH₄, CO, and CO₂ and b) peak intensity of CH₄, CO, and CO₂ in the gas phase FTIR spectra over 15 minutes thermal CO₂ methanation reaction time.

6.4. Conclusions

Different reaction mechanisms are proposed for the plasma-assisted and thermal CO₂ methanation on the same Ni/CeO₂ DOE0 catalyst having nanoneedles morphology. CO₂ and possibly CO derived from the splitting in DBD plasma are adsorbed on the ceria surface into carbonates with one or several O in common with the metal oxide framework. It is suggested that the surface catalytic reactions go through carbonates, hydrogen carbonate and formate intermediates, which are progressively hydrogenated with H adsorbed on the Ni particles to methane, then desorbed from the surface. Also, during the plasma operando experiment it was shown how a minimal injected power is required for the methanation reaction to occur, and reaching the plasma breakdown is not sufficient for the gasses and surface activation. For the thermal catalytic reaction at 300 °C, similarly to previous publications [172,192,193], a combination of formate and CO pathways is suggested for the Ni/DOE0 catalyst. Such difference is remarkable and reinforces the different performance of this catalyst in plasma-assisted and thermal CO₂ methanation studied in chapter 4. The different mechanism might be affected by the new species formed in plasma (CO and excited CO₂ and H₂) which interact with the adsorption sites of the catalyst. Moreover, the CO₂ adsorption behaviour in DBD plasma and at 300 °C hints to a different configuration of defects and OV of ceria when exposed to plasma and electrons which seems to avoid the dissociative pathway.

The results shown in this chapter remain part of a preliminary study on surface reaction mechanism on nanostructured Ni/CeO₂ catalysts. A more in-depth analysis would be necessary in order to reach more solid conclusions on the reaction pathway. First of all, the same experimental protocol, both with and without CO₂/H₂ adsorption step, should be tested in the thermal and DBD reactors in order to better highlight the differences between the two processes, in addition testing a temperature ramp might be interesting in order to better assess the thermal stability of the surface species formed during methanation. Secondly, an in-situ CO₂ adsorption mechanism is required in order to discern the impact of the presence of hydrogen and the methanation reaction from the carbonates formation from CO₂ adsorption. Furthermore, studying the species desorption from the catalyst surface is also interesting in order to know which are more tightly bound. Finally, microkinetic models regarding the CO₂/H₂ plasma chemistry can provide information on the most relevant reaction steps and help complete picture of the complex interactions between the plasma and the catalyst in plasma-assisted CO₂ methanation.

Chapter 7: Conclusions and prospects

The main aim of this PhD thesis was to assess how the nanostructure of cerium oxide supports affects the performance of Ni catalysts in plasma-assisted CO₂ methanation and the dielectric properties of such materials.

Ceria nanomaterials with varying morphology and size were obtained by hydrothermal methods, whose parameters were selected by DOE factorial analysis. The varying morphology affects the physicochemical properties and defective nature of cerium oxide supports and Ni/CeO₂ catalysts. The temperature of the hydrothermal treatment and the NaOH concentration of the solution used for the synthesis have the most significant impact on the growth (quantified by XRD with the crystallite size) and surface reactivity of the ceria materials. Additionally, under increasing temperature, NaOH concentration, and time of synthesis reaction the morphology changes as nanorod > nanoneedle > nanocube > microrods+cubes. Each shape is linked with a preferential crystal plane exposed on the surface, which are <100> for cubes and <011> for the anisotropic needles and rods structures. The stability and configuration of the exposed surface influence the tendency to form oxygen vacancies (linked with enriched O_{surface} and Ce³⁺ on the surface shown by XPS), to interact with adsorbate molecules (surface basicity measured via CO₂-TPD), and to facilitate redox reactions on its surface (OSC). The size also affects the surface defects, which increase on small particles, and the same trend is considered for surface area (measured by S_{BET}). Moreover, the formation of interparticle pores between ceria structures of different shapes also affects the pore volume V_p. Once the Ni phase is introduced, the characteristics of the support condition the metal dispersion, therefore the size of the Ni crystallite size, their tendency to be reduced (via H₂-TPR), and the metal-support interaction.

The physicochemical properties and surface redox properties of the Ni/CeO₂ nanostructured catalysts affect the dielectric and conductivity behaviour, which are assessed via electrical characterization of the packed bed DBD reactor and are considered to be relevant when the material is subjected to the electric field and interaction with electrons and excited species. A larger dielectric permittivity of the packing material (represented by C_{reactor} and C_{on}) enhances surface polarisation and electric field, charge transfer, and affects the current peak distribution. Furthermore, having a material with interparticle macropores (large V_p) might facilitate the discharge ignition. The electrical characterization suggests that the plasma is indeed affected by the catalyst and its physicochemical features, such as reducibility, MSI, V_p, and surface defects, which might be involved in the conduction mechanisms.

These Ni/CeO₂ materials with different morphology were used for plasma-assisted CO₂ methanation. Both physicochemical, such as surface area and basicity, and dielectric features of the catalysts were linked to the performance in CO₂ methanation, quantified by CO₂ conversion, CH₄ selectivity, and energy efficiency. The conversion, selectivity, and stability obtained via plasma catalysis are comparable to the results in thermal catalysis above 300 °C but achieve an enhanced

efficiency due to the lower power requirement for DBD plasma ignition compared to the conventional process. Small ceria crystallite size, large surface area, intermediate strength surface basicity, Ni dispersion, and good reducibility are found to be crucial for the catalytic performance of the Ni/CeO₂ material, especially in the thermal process. It was established that a suitable catalyst for thermal methanation reaches a good conversion when used in the DBD reactor, but its efficiency depends also on the electrical behaviour of the catalyst in the plasma discharge. The most efficient catalysts of this study for plasma-assisted CO₂ methanation were found to possess the previously mentioned properties in addition to low dielectric permittivity, good OSC, and the presence of OV on the ceria support, which are affected by the morphology. These findings indicate that the catalysts supported on nanorods and nanoneedles share such advantageous properties for plasma-assisted CO₂ methanation. The reactivity of the surface of the catalysts, influenced by the morphology, affects the methanation reaction and the alterations that might occur to the catalyst due to plasma exposure, examined by the physicochemical characterization of the materials after use. It was shown for the nanoneedles catalyst that a certain degree of reorganization of the Ni/CeO₂ structures occurs, with a decrease in crystallite size, an increase of Ni dispersion, and variation in the oxidation state of the Ni and Ce surface species due to the interaction with possible reaction intermediates. Therefore, the catalysts are also altered and possibly enhanced by contact with plasma. The bidirectional interaction between plasma-catalyst suggests a mechanism of synergy, which is enhanced by the morphology, redox properties, and surface defects of the material in contact with the discharge.

Different reaction pathways are suggested for thermal and plasma-assisted CO₂ methanation by the FTIR operando studies. In the plasma case, formates are found to be the main reaction intermediate, suggesting the formate route. CO₂ and perhaps CO (from splitting) are adsorbed on the sites on the ceria surface, forming mono- and polydentate carbonates and hydrogen carbonates, which are progressively hydrogenated with H adsorbed on the Ni particles to formate, CH_x, and finally methane. For the thermal reaction at 300 °C, the FTIR spectra evidence a combination of formate and CO pathways, with carbonyl considered as intermediates.

Future steps in the development of materials for plasma catalysis, due to the relevance observed in this work of electrical behaviour of the catalyst to enhance efficiency, should include electrical and electrochemical characterization of the catalysts. Conductivity, dielectric permittivity, and polarisation and electric field at the surface, assessed by several techniques such as DC conductivity, cyclic voltammetry, impedance spectroscopy, and Mueller polarimetry, should be considered in the evaluation of the material together with the measurement of the thermal conductivity and the conventional physicochemical properties. It would be worth exploring new materials tailored for plasma catalysis with tuned conductivity and dielectric properties as well as cost-effective and possibly supported on macroporous structures as it might facilitate plasma ignition. Since optical spectroscopic plasma diagnostic techniques are difficult to applied coupled with catalysts, further implementation of such techniques to one-stage plasma catalysis reactors, together with the

electrical characterization methods used in this work, is required to better characterize the discharge, e.g., to measure the gas temperature and species densities. The combination of these measured parameters could be the starting point of a plasma chemistry model to describe the most relevant reactions occurring and be able to design the most suitable catalyst to help such pathway, which should be verified by in-depth plasma operando studies. Such advancements in plasma catalysis and energy efficiency of these processes, together with novel reactor design to enhance heat transfer, are promising for future applications of this technology for the decarbonization of the energy sector.

Conclusiones

El objetivo principal de esta tesis doctoral ha sido evaluar cómo afecta la nanoestructura de los soportes de óxido de cerio al rendimiento de los catalizadores de Ni en la metanación de CO₂ asistida por plasma y a las propiedades dieléctricas de dichos materiales.

Mediante síntesis hidrotermal se obtuvieron nanomateriales de cerio con morfología y tamaño variables, cuyos parámetros se seleccionaron mediante análisis factorial DOE. La distinta morfología afecta a las propiedades fisicoquímicas y al tipo de defectos presentes en los soportes de óxido de cerio y de los catalizadores Ni/CeO₂. La temperatura y la concentración de NaOH del tratamiento hidrotérmico tienen el impacto más significativo sobre el crecimiento (cuantificado con el tamaño de cristalito obtenido por XRD) y la reactividad superficial de los materiales de ceria. Además, al aumentar la temperatura, la concentración de NaOH y el tiempo de reacción de la síntesis, la morfología cambia como nanorod > nanoneedle > nanocube > microrod+cube. Cada nanoestructura está vinculada a un plano cristalino preferente expuesto en la superficie, que son <100> para los cubos y <011> para las estructuras anisótropas de agujas y varillas. La estabilidad y la configuración de la superficie expuesta influyen en la tendencia a formar vacantes de oxígeno (relacionadas con el enriquecimiento de O_{surface} y Ce³⁺ en la superficie, mostrado por XPS), a interactuar con moléculas adsorbidas (basicidad de la superficie medida mediante CO₂-TPD) y a facilitar reacciones redox en su superficie (OSC). El tamaño también afecta a los defectos superficiales, que aumentan en las partículas pequeñas, y la misma tendencia se considera para el área superficial (medida por S_{BET}). Además, la diferente formación de poros interpartículas en estructuras de ceria con diferente morfología, también afecta al volumen de poros V_p. Cuando se introduce la fase Ni, las características del soporte condicionan la dispersión del metal, por tanto el tamaño de los cristalitos de Ni, su tendencia a reducirse (vía H₂-TPR), y la interacción metal-soporte.

Las propiedades fisicoquímicas y las propiedades redox superficiales de los catalizadores nanoestructurados Ni/CeO₂ afectan al comportamiento dieléctrico y de conductividad, que se evalúan mediante la caracterización eléctrica del lecho de catalizador en el reactor DBD, y se consideran relevantes cuando el material se somete al campo eléctrico y a la interacción con electrones y especies excitadas. Una mayor permitividad dieléctrica del material de empaquetamiento (representada por C_{reactor} y C_{on}) mejora la polarización de la superficie y el campo eléctrico, la transferencia de carga y afecta a la distribución del pico de corriente. Además, disponer de un material con macroporos interpartículas (alto V_p) podría facilitar la ignición de la descarga. La caracterización eléctrica sugiere que el plasma se ve realmente afectado por el catalizador y sus características fisicoquímicas, como la reducibilidad, el MSI, el V_p y los defectos superficiales, que podrían estar implicados en los mecanismos de conducción.

Estos materiales de Ni/CeO₂ con diferente morfología se utilizaron para la metanación de CO₂ asistida por plasma. Las características fisicoquímicas, como el área superficial y la basicidad, y dieléctricas de los catalizadores se relacionaron con el rendimiento en la metanación de CO₂,

cuantificado por la conversión de CO_2 , la selectividad de CH_4 y la eficiencia energética. La conversión, selectividad y estabilidad obtenidas mediante catálisis asistida por plasma son comparables a los resultados en catálisis térmica por encima de $300\text{ }^\circ\text{C}$, pero logran una mayor eficiencia debido a la menor potencia requerida para el encendido del plasma DBD en comparación con el proceso convencional. El pequeño tamaño de los cristallitos de ceria, la gran área superficial, la basicidad superficial intermedia, la dispersión de Ni y la buena reducibilidad resultan cruciales para el rendimiento catalítico del material Ni/CeO_2 , especialmente en el proceso térmico. Se estableció que un catalizador adecuado para la metanación térmica alcanza una buena conversión cuando se utiliza en el reactor DBD, pero su eficacia depende también del comportamiento eléctrico del catalizador en la descarga de plasma. Se encontró que los catalizadores más eficientes de este estudio para la metanación de CO_2 asistida por plasma poseían las propiedades mencionadas anteriormente, además de una baja permitividad dieléctrica, un buen OSC y la presencia de OV en el soporte de ceria, que se ven afectados por la morfología. Estos resultados indican que los catalizadores soportados sobre nanorods y nanoneedles comparten dichas propiedades ventajosas para la metanación de CO_2 asistida por plasma. La reactividad de la superficie de los catalizadores, influida por la morfología, afecta a la reacción de metanación y a las alteraciones que pueden producirse en el catalizador debido a la exposición al plasma, examinadas mediante la caracterización fisicoquímica de los materiales tras su uso. Se demostró para el catalizador de nanoneedles que se produce un cierto grado de reorganización de las estructuras de Ni/CeO_2 , con una disminución del tamaño de los cristallitos, un aumento de la dispersión de Ni y una variación del estado de oxidación de las especies superficiales de Ni y Ce debido a la interacción con posibles intermedios de la reacción. Por lo tanto, los catalizadores también se ven alterados y posiblemente mejorados por el contacto con el plasma. La interacción bidireccional entre plasma-catalizador sugiere un mecanismo de sinergia, que se ve potenciado por la morfología, las propiedades redox y los defectos superficiales del material en contacto con la descarga.

Los estudios de operando FTIR sugieren diferentes vías de reacción para la metanación de CO_2 térmica y asistida por plasma. En el caso del plasma, los formiatos son el principal intermedio de reacción, lo que sugiere la ruta del formiato. El CO_2 y quizás el CO (procedente de la escisión) se adsorben en los sitios superficiales de la ceria, formando carbonatos mono- y polidentados y carbonatos de hidrógeno, que se hidrogenan progresivamente con el H adsorbido en las partículas de Ni a formiato, CH_x , y finalmente metano. Para la reacción térmica a $300\text{ }^\circ\text{C}$, los espectros FTIR evidencian una combinación de las vías de formiato y CO, con carbonilos considerados como intermedios de reacción.

Los futuros pasos en el desarrollo de materiales para la catálisis por plasma, debido a la relevancia observada en este trabajo del comportamiento eléctrico del catalizador para mejorar la eficiencia, deberían incluir la caracterización eléctrica y electroquímica de los catalizadores. La conductividad, la permitividad dieléctrica y la polarización y el campo eléctrico en la superficie, evaluados mediante varias técnicas como la conductividad CC, la voltamperometría cíclica, la espectroscopia de

impedancia y la polarimetría de Mueller, deberían tenerse en cuenta en la evaluación del material junto con la medición de la conductividad térmica y las propiedades fisicoquímicas convencionales. Sería de gran interés explorar nuevos materiales adaptados para la catálisis por plasma con propiedades de conductividad y dieléctricas optimizadas, así como bajo coste y posiblemente soportados en estructuras macroporosas ya que pueden facilitar la ignición del plasma. Dado que las técnicas espectroscópicas ópticas de diagnóstico de plasma son difíciles de aplicar con catalizadores acoplados, se requiere la implementación de estas técnicas en reactores de catálisis de plasma de una etapa para caracterizar mejor la descarga, por ejemplo, para medir la temperatura del gas y las densidades de las especies. La combinación de estos parámetros podría ser el punto de partida de un modelo de química de plasma más detallado que describa las reacciones más relevantes que se producen y poder diseñar el catalizador más adecuado para ayudar a dicha vía, lo que debería verificarse mediante estudios detallados de plasma operando. Estos avances en la catálisis asistida por plasma y la eficiencia energética de estos procesos, junto con el novedoso diseño de reactores para mejorar la transferencia de calor, son prometedores para futuras aplicaciones de esta tecnología para la descarbonización del sector energético.

Conclusion

L'objectif principal de cette thèse de doctorat était d'évaluer l'influence de la nanostructure de différents supports d'oxyde de cérium sur la performance des catalyseurs à base de Ni, utilisés dans la réaction de méthanation du CO₂ assistée par plasma.

Des nanomatériaux d'oxyde de cérium de morphologie et de taille variables ont été obtenus en suivant une route de synthèse hydrothermale, dont les paramètres ont été sélectionnés par une analyse factorielle DOE. La morphologie variable affecte les propriétés physicochimiques et la capacité d'échange d'oxygène de ces supports d'oxyde de cérium, ainsi que les propriétés et le comportement des catalyseurs Ni/CeO₂ préparés en utilisant ces supports nanostructurés.

La température du traitement hydrothermal et la concentration en NaOH de la solution utilisée pour ce synthèse ont l'impact le plus significatif sur la croissance des nanostructures (quantifiée par XRD avec la taille des cristallites), ainsi que sur la réactivité de la surface des matériaux à base de cérium. De plus, en augmentant la température, la concentration de NaOH et le temps de réaction de la synthèse, la morphologie change : nanorod > nanoneedle > nanocube > microrods+cubes. Chaque forme est liée à un plan cristallin préférentiel exposé à la surface, qui est <100> pour les cubes et <011> pour les structures anisotropes en aiguilles et en bâtonnets. La stabilité et la configuration de la surface exposée influencent la capacité d'échange d'oxygène (formation des trous d'oxygène, liée à l'enrichissement de l'O_{surface} et du Ce³⁺ en surface démontrés par XPS), à interagir avec des molécules adsorbées (basicité de surface mesurée par CO₂-TPD), et à faciliter les réactions d'oxydoréduction à sa surface (OSC). La taille détermine également la présence de défauts sur la surface de ces matériaux, qui augmentent sur les petites structures. La formation de pores entre les nanostructures de CeO₂ de différentes formes affecte la surface active, ainsi que le volume total de pore (adsorption N₂). Une fois la phase Ni introduite, les caractéristiques du support conditionnent la dispersion du métal, donc la taille des cristallites de Ni, leur réductibilité (H₂-TPR), et l'interaction métal-support.

Les propriétés physicochimiques et les propriétés redox de la surface des catalyseurs nanostructurés Ni/CeO₂ affectent le comportement diélectrique de ces matériaux, qui a été évalué via la caractérisation électrique du réacteur DBD à lit fixe. Le comportement diélectrique des matériaux utilisés en plasma-catalyse est de grande importance lorsque ces solides sont soumis au champ électrique et à l'interaction avec les électrons et les espèces excitées contenus dans la phase plasma. Une plus grande permittivité diélectrique du matériau de garnissage (représentée par C_{reactor} et Con) améliore la polarisation de surface et le champ électrique, le transfert de charge et affecte la distribution des pics de courant. En outre, un matériau présentant des macropores interparticulaires (grand V_p) pourrait faciliter l'allumage de la décharge. La caractérisation électrique suggère que le plasma est effectivement affecté par le type de catalyseur et ses caractéristiques physicochimiques, telles que la réductibilité, l'interaction phase active-support, le volume de pore, ainsi que par la présence des défauts de surface, qui pourraient être impliqués dans les mécanismes de conduction.

Ces matériaux Ni/CeO₂ de morphologie différente ont été utilisés pour la méthanation du CO₂ assistée par plasma. Les caractéristiques physicochimiques, telles que la surface et la basicité, et diélectriques des catalyseurs ont été liées au comportement catalytique observé sous telles conditions, et quantifiées par la conversion du CO₂, la sélectivité du CH₄ et l'efficacité énergétique. La conversion, la sélectivité et la stabilité obtenues via la catalyse plasma sont comparables aux résultats de la catalyse thermique au-dessus de 300 °C, mais à températures nettement plus faibles (environ 200°C) et sans autre apport énergétique que le plasma en lui-même. Des tailles de cristallite petites pour le CeO₂, une porosité plus développée, une basicité de surface adéquate, une bonne dispersion de la phase active Ni ainsi qu'une bonne réductibilité se sont avérées cruciales pour la performance catalytique du matériau Ni/CeO₂, en particulier dans le procédé activé par voie classique, i.e. thermique. Il a été établi qu'un catalyseur approprié pour la méthanation thermique atteint une bonne conversion lorsqu'il est utilisé dans le réacteur DBD, mais son efficacité dépend également du comportement électrique du catalyseur dans la décharge de plasma. Les catalyseurs les plus efficaces de cette étude pour la méthanisation du CO₂ assistée par plasma possédaient les propriétés mentionnées précédemment, en plus d'une faible permittivité diélectrique et d'une bonne capacité d'échange d'oxygène, propriétés qui dépend en grande mesure de la morphologie des nanostructures de CeO₂ synthétisés. Ces résultats indiquent que les catalyseurs supportés sur les support contenant des nanorods et des nanoneedles partagent ces propriétés avantageuses pour la méthanisation du CO₂ assistée par plasma. La réactivité de la surface des catalyseurs, influencée par la morphologie, affecte la réaction de méthanisation et les altérations qui peuvent se produire sur le catalyseur en raison de l'exposition au plasma, examinées par la caractérisation physicochimique des matériaux après utilisation. Il a été démontré pour le catalyseur à nanoneedles qu'un certain degré de réorganisation des structures Ni/CeO₂ se produit, avec une diminution de la taille des cristallites, une augmentation de la dispersion du Ni et une variation de l'état d'oxydation des espèces de surface Ni et Ce en raison de l'interaction avec d'éventuels intermédiaires de réaction. L'interaction bidirectionnelle entre le plasma et le catalyseur suggère un mécanisme de synergie, qui est renforcé par la morphologie, les propriétés redox et les défauts de surface du matériau en contact avec la décharge.

Les études FTIR operando suggèrent différentes voies de réaction pour la méthanisation du CO₂ assistée par la chaleur et le plasma. Dans le cas du plasma, les formates se révèlent être le principal intermédiaire réactionnel. Le CO₂ et peut-être le CO (provenant du fractionnement) sont adsorbés sur les sites de la surface de la céria, formant des carbonates et des hydrogénocarbonates mono- et polydentés, qui sont progressivement hydrogénés avec le H adsorbé sur les particules de Ni pour former du formiate, du CH_x, et finalement du méthane. Pour la réaction thermique à 300 °C, les spectres FTIR montrent une combinaison des voies du formiate et du CO, avec et le carbonyle considéré comme possible intermédiaire réactionnel.

Les étapes futures du développement de matériaux pour la catalyse par plasma, en raison de la pertinence observée dans ce travail du comportement électrique du catalyseur pour améliorer

l'efficacité, devraient inclure la caractérisation électrique et électrochimique des catalyseurs. La conductivité, la permittivité diélectrique, la polarisation et le champ électrique à la surface, évalués par plusieurs techniques telles que la conductivité DC, la voltampérométrie cyclique, la spectroscopie d'impédance et la polarimétrie de Mueller, devraient être pris en compte dans l'évaluation du matériau, de même que la mesure de la conductivité thermique et des propriétés physicochimiques conventionnelles. Il serait intéressant d'explorer de nouveaux matériaux adaptés à la catalyse par plasma, avec une conductivité et des propriétés diélectriques adaptées, ainsi qu'un bon rapport coût-efficacité, et éventuellement soutenus par des structures macroporeuses, car cela pourrait faciliter l'allumage du plasma. Étant donné que les techniques de diagnostic spectroscopique du plasma sont difficiles à appliquer en combinaison avec des catalyseurs, il est nécessaire de poursuivre la mise en œuvre de ces techniques dans les réacteurs de catalyse par plasma à une étape afin de mieux caractériser la décharge, par exemple pour mesurer la température du gaz et le type et concentration d'espèces activées. La combinaison de ces paramètres mesurés pourrait être le point de départ d'un modèle de chimie du plasma pour décrire les réactions les plus pertinentes qui se produisent et être en mesure de concevoir le catalyseur le plus approprié pour aider cette voie, ce qui devrait être vérifié par des études approfondies de plasma *operando*. De telles avancées dans la catalyse par plasma et l'efficacité énergétique de ces processus, ainsi qu'une nouvelle conception de réacteur pour améliorer le transfert de chaleur, sont prometteuses pour les applications futures de cette technologie pour la décarbonisation de notre secteur énergétique.

References

1. Lewis, S.L.; Maslin, M.A. Defining the Anthropocene. **2015**, doi:10.1038/nature14258.
2. Masson-Delmotte, V.; Zhai, P.; Pörtner, H.-O.; Roberts, D.; Skea, J.; Shukla, P.R.; Pirani, A.; Moufouma-Okia, W.; Péan, C.; Pidcock, R.; et al. *IPCC, 2018: Global warming of 1.5°C*; 2018;
3. Hausfather, Z.; Peters, G.P. Emissions – the ‘business as usual’ story is misleading. *Nature* **2020**, *577*, 618–630.
4. Marking the Kyoto Protocol’s 25th anniversary Available online: un.org/en/climatechange/marking-kyoto-protocol’s-25th-anniversary (accessed on Mar 6, 2023).
5. What is the Paris Agreement? | UNFCCC Available online: <https://unfccc.int/process-and-meetings/the-paris-agreement/what-is-the-paris-agreement> (accessed on Aug 20, 2020).
6. A European Green Deal Striving to be the first climate-neutral continent Available online: https://commission.europa.eu/strategy-and-policy/priorities-2019-2024/european-green-deal_en (accessed on Mar 6, 2023).
7. Van Vuuren, D.P.; Stehfest, E.; Gernaat, D.E.H.J.; Van Den Berg, M.; Bijl, D.L.; De Boer, H.S.; Daioglou, V.; Doelman, J.C.; Edelenbosch, O.Y.; Harmsen, M.; et al. Alternative pathways to the 1.5 °C target reduce the need for negative emission technologies. *Nat. Clim. Chang.* **2018**, *8*, 391–397, doi:10.1038/s41558-018-0119-8.
8. Poertner, H.-O.; Roberts, D.C.; Adams, H.; Adler, C.; Aldunce, P.; Ali, E.; Begum, R.A.; Betts, R.; Kerr, R.B.; Biesbroek, R. *Climate change 2022: Impacts, adaptation and vulnerability*; 2022;
9. Gabrielli, P.; Gazzani, M.; Mazzotti, M. The Role of Carbon Capture and Utilization, Carbon Capture and Storage, and Biomass to Enable a Net-Zero-CO₂ Emissions Chemical Industry. *Ind. Eng. Chem. Res.* **2020**, *59*, 7033–7045, doi:10.1021/acs.iecr.9b06579.
10. Vogt, C.; Monai, M.; Kramer, G.J.; Weckhuysen, B.M. The renaissance of the Sabatier reaction and its applications on Earth and in space. *Nat. Catal.* **2019**, *2*, 188–197, doi:10.1038/s41929-019-0244-4.
11. Jones, A.C.; J., L. *Carbon Capture and Sequestration (CCS) in the United States*; 2022;
12. Hong, W.Y. A techno-economic review on carbon capture, utilisation and storage systems for achieving a net-zero CO₂ emissions future. *Carbon Capture Sci. Technol.* **2022**, *3*, 100044, doi:10.1016/J.CCST.2022.100044.
13. Gür, T.M. Carbon Dioxide Emissions, Capture, Storage and Utilization: Review of Materials, Processes and Technologies. *Prog. Energy Combust. Sci.* **2022**, *89*, 100965, doi:10.1016/J.PECS.2021.100965.
14. Artz, J.; Müller, T.E.; Thenert, K.; Kleinekorte, J.; Meys, R.; Sternberg, A.; Bardow, A.; Leitner, W. Sustainable Conversion of Carbon Dioxide: An Integrated Review of Catalysis and Life Cycle Assessment. *Chem. Rev.* **2018**, *118*, 434–504.
15. Vogt, C.; Monai, M.; Kramer, G.J.; Weckhuysen, B.M. The renaissance of the Sabatier reaction and its applications on Earth and in space. *Nat. Catal.* **2019**, *2*, 188–197, doi:10.1038/s41929-019-0244-4.
16. IEA A new era for CCUS Available online: <https://www.iea.org/reports/ccus-in-clean-energy-transitions/a-new-era-for-ccus> (accessed on Mar 6, 2023).
17. Carbon Border Adjustment Mechanism: Questions and Answers Available online: https://ec.europa.eu/commission/presscorner/detail/en/qanda_21_3661 (accessed on Mar 6, 2023).
18. Velazquez Abad, A.; Dodds, P.E. Green hydrogen characterisation initiatives: Definitions, standards, guarantees of origin, and challenges. *Energy Policy* **2020**, *138*, 111300, doi:10.1016/J.ENPOL.2020.111300.

19. Meylan, F.D.; Piguet, F.P.; Erkman, S. Power-to-gas through CO₂ methanation: Assessment of the carbon balance regarding EU directives. *J. Energy Storage* **2017**, *11*, 16–24, doi:10.1016/j.est.2016.12.005.
20. Snoeckx, R.; Bogaerts, A. Plasma technology-a novel solution for CO₂ conversion? *Chem. Soc. Rev.* **2017**, *46*, 5805–5863, doi:10.1039/c6cs00066e.
21. Barbaresi, A.; Morini, M.; Gambarotta, A. Review on the Status of the Research on Power-to-Gas Experimental Activities. *Energies* **2022**, *Vol. 15, Page 5942* **2022**, *15*, 5942, doi:10.3390/EN15165942.
22. IEA International Energy Agency: The Future of Hydrogen Available online: <https://www.iea.org/reports/the-future-of-hydrogen> (accessed on Feb 26, 2023).
23. Kramer, G.J.; Haigh, M. No quick switch to low-carbon energy. *Nature* **2009**, *462*, 568–569.
24. IUPAC Catalyst: IUPAC definition Available online: <https://goldbook.iupac.org/terms/view/C00876#:~:text=A substance that increases the,> (accessed on Mar 6, 2023).
25. Inglezakis, V.J.; Pouloupoulos, S.G. Adsorption, ion exchange and catalysis: Design of operations and environmental applications. *Adsorpt. Ion Exch. Catal. Des. Oper. Environ. Appl.* **2006**, 1–602, doi:10.1016/B978-0-444-52783-7.X5000-9.
26. Gallagher, M.J.; Fridman, A. Plasma Reforming for H₂-Rich Synthesis Gas. *Fuel Cells Technol. Fuel Process.* **2011**, 223–259, doi:10.1016/B978-0-444-53563-4.10008-2.
27. Sabatier, P.; Senderens, J. Nouvelles synthèses du méthane. *Comptes Rendus Hebd. des Seances del Acad. des Scrences* **1902**, *82*, 514–516.
28. Rönsch, S.; Schneider, J.; Matthischke, S.; Schlüter, M.; Götz, M.; Lefebvre, J.; Prabhakaran, P.; Bajohr, S. Review on methanation – From fundamentals to current projects. *Fuel* **2016**, *166*, 276–296, doi:https://doi.org/10.1016/j.fuel.2015.10.111.
29. Younas, M.; Loong Kong, L.; Bashir, M.J.K.; Nadeem, H.; Shehzad, A.; Sethupathi, S. Recent Advancements, Fundamental Challenges, and Opportunities in Catalytic Methanation of CO₂. *Energy and Fuels* **2016**, *30*, 8815–8831, doi:10.1021/acs.energyfuels.6b01723.
30. Frontera, P.; Macario, A.; Ferraro, M.; Antonucci, P.L. Supported catalysts for CO₂ methanation: A review. *Catalysts* **2017**, *7*.
31. Kuznecova, I.; Gusca, J. Property based ranking of CO and CO₂ methanation catalysts. *Energy Procedia* **2017**, *128*, 255–260, doi:10.1016/j.egypro.2017.09.068.
32. Stangeland, K.; Kalai, D.; Li, H.; Yu, Z. CO₂ methanation: the effect of catalysts and reaction conditions. *Energy Procedia* **2017**, *105*, 2022–2027.
33. Wang, W.; Gong, J. Methanation of carbon dioxide: an overview. *Front. Chem. Sci. Eng.* **2011**, *5*, 2–10, doi:10.1007/s11705-010-0528-3.
34. Álvarez, A.; Borges, M.; Corral-Pérez, J.J.; Olcina, J.G.; Hu, L.; Cornu, D.; Huang, R.; Stoian, D.; Urakawa, A. CO₂ Activation over Catalytic Surfaces. *ChemPhysChem* **2017**, *18*, 3135–3141, doi:10.1002/cphc.201700782.
35. Le, M.C.; Van, K. Le; Nguyen, T.H.T.; Nguyen, N.H. The Impact of Ce-Zr Addition on Nickel Dispersion and Catalytic Behavior for CO₂ Methanation of Ni/AC Catalyst at Low Temperature. *J. Chem.* **2017**, *2017*, 1–12, doi:10.1155/2017/4361056.
36. Sreedhar, I.; Varun, Y.; Singh, S.A.; Venugopal, A.; Reddy, B.M. Developmental trends in CO₂ methanation using various catalysts. *Catal. Sci. Technol.* **2019**, *9*, 4478–4504, doi:10.1039/c9cy01234f.
37. Kuznecova, I.; Gusca, J. Property based ranking of CO and CO₂ methanation catalysts. In Proceedings

- of the Energy Procedia; Elsevier Ltd, 2017; Vol. 128, pp. 255–260.
38. Mills, A.; Le Hunte, S. An overview of semiconductor photocatalysis. *J. Photochem. Photobiol. A Chem.* **1997**, *108*, 1–35, doi:10.1016/S1010-6030(97)00118-4.
39. Bal, K.M.; Huygh, S.; Bogaerts, A.; Neyts, E.C. Effect of plasma-induced surface charging on catalytic processes: application to CO₂ activation. *Plasma Sources Sci. Technol.* **2018**, *27*, 024001, doi:10.1088/1361-6595/AAA868.
40. Whitehead, J.C. Plasma–catalysis: the known knowns, the known unknowns and the unknown unknowns. *J. Phys. D. Appl. Phys.* **2016**, *49*, 243001, doi:10.1088/0022-3727/49/24/243001.
41. Mei, D.; Zhu, X.; Wu, C.; Ashford, B.; Williams, P.T.; Tu, X. Plasma-photocatalytic conversion of CO₂ at low temperatures: Understanding the synergistic effect of plasma-catalysis. *Appl. Catal. B Environ.* **2016**, *182*, 525–532, doi:10.1016/J.APCATB.2015.09.052.
42. Albo, J.; Alvarez-Guerra, M.; Castaño, P.; Irabien, A. Towards the electrochemical conversion of carbon dioxide into methanol. *Green Chem.* **2015**, *17*, 2304–2324, doi:10.1039/C4GC02453B.
43. Chen, G.; Britun, N.; Godfroid, T.; Georgieva, V.; Snyders, R.; Delplancke-Ogletree, M.-P. An overview of CO₂ conversion in a microwave discharge: the role of plasma-catalysis. *J. Phys. D. Appl. Phys.* **2017**, *50*, 84001, doi:10.1088/1361-6463/aa5616.
44. Sun, C.; Li, H.; Chen, L. Nanostructured ceria-based materials: synthesis, properties, and applications. *Energy Environ. Sci. Pollut. Res.* **2012**, *5*, 8475–8505.
45. Montini, T.; Melchionna, M.; Monai, M.; Fornasiero, P. Fundamentals and catalytic applications of CeO₂-based materials. *Chem. Rev.* **2016**, *116*, 5987–6041.
46. Zhang, Y.; Zhao, S.; Feng, J.; Song, S.; Shi, W.; Wang, D.; Zhang, H. Unraveling the physical chemistry and materials science of CeO₂-based nanostructures. *Chem* **2021**, *7*, 2022–2059, doi:10.1016/J.CHEMPR.2021.02.015.
47. Gennard, S.; Cora, F.; Richard, C.; Catlow, A. Comparison of the Bulk and Surface Properties of Ceria and Zirconia by ab Initio Investigations. *J. Phys. Chem. B* **1999**, *103*, 10158–10170, doi:10.1021/JP9913923/ASSET/IMAGES/LARGE/JP9913923F00010.JPEG.
48. Vyas, S. Doctoral Thesis: SIMULATION OF CERIA: BULK AND SURFACE DEFECTS, 2005.
49. Zhang, D.; Du, X.; Shi, L.; Gao, R. Shape-controlled synthesis and catalytic application of ceria nanomaterials. *Dalt. Trans.* **2012**, *41*, 14455–14475, doi:10.1039/c2dt31759a.
50. Ma, Y.; Gao, W.; Zhang, Z.; Zhang, S.; Tian, Z.; Liu, Y.; Ho, J.C.; Qu, Y. Regulating the surface of nanoceria and its applications in heterogeneous catalysis. *Surf. Sci. Rep.* **2018**, *73*, 1–36, doi:https://doi.org/10.1016/j.surfrep.2018.02.001.
51. Cui, Z.; Gan, J.; Fan, J.; Xue, Y.; Zhang, R. Size-Dependent Surface Basicity of Nano-CeO₂ and Desorption Kinetics of CO₂ on Its Surface. *Ind. Eng. Chem. Res.* **2018**, *57*, 10977–10984, doi:10.1021/acs.iecr.8b01247.
52. Parastaev, A.; Muravev, V.; Huertas Osta, E.; van Hoof, A.J.F.; Kimpel, T.F.; Kosinov, N.; Hensen, E.J.M. Boosting CO₂ hydrogenation via size-dependent metal–support interactions in cobalt/ceria-based catalysts. *Nat. Catal.* **2020**, *3*, 526–533, doi:10.1038/s41929-020-0459-4.
53. Parastaev, A.; Muravev, V.; Huertas Osta, E.; van Hoof, A.J.F.; Kimpel, T.F.; Kosinov, N.; Hensen, E.J.M. Boosting CO₂ hydrogenation via size-dependent metal–support interactions in cobalt/ceria-based catalysts. *Nat. Catal.* **2020**, doi:10.1038/s41929-020-0459-4.
54. Ruiz Puigdollers, A.; Schlexer, P.; Tosoni, S.; Pacchioni, G. Increasing Oxide Reducibility: The Role of Metal/Oxide Interfaces in the Formation of Oxygen Vacancies. *ACS Catal.* **2017**, 6493–6513,

- doi:10.1021/acscatal.7b01913.
55. Melchionna, M.; Fornasiero, P. The role of ceria-based nanostructured materials in energy applications. *Mater. Today* **2014**, *17*, 349–357, doi:10.1016/j.mattod.2014.05.005.
 56. Boaro, M.; Colussi, S.; Trovarelli, A. Ceria-based materials in hydrogenation and reforming reactions for CO₂ valorization. *Front. Chem.* **2019**, *7*, doi:10.3389/fchem.2019.00028.
 57. Trovarelli, A.; De Leitenburg, C.; Dolcetti, G. CO and CO₂ hydrogenation under transient conditions over Rh-CeO₂: Novel positive effects of metal-support interaction on catalytic activity and selectivity. *J. Chem. Soc. Chem. Commun.* **1991**, 472–473, doi:10.1039/C39910000472.
 58. Web of Science Available online: webofscience.com (accessed on Feb 7, 2023).
 59. Zhou, G.; Liu, H.; Cui, K.; Xie, H.; Jiao, Z.; Zhang, G.; Xiong, K.; Zheng, X. Methanation of carbon dioxide over Ni/CeO₂ catalysts: Effects of support CeO₂ structure. *Int. J. Hydrogen Energy* **2017**, *42*, doi:10.1016/j.ijhydene.2017.05.154.
 60. Deng, X.; Chen, K.; Tüysüz, H. Protocol for the Nanocasting Method: Preparation of Ordered Mesoporous Metal Oxides. *Chem. Mater.* **2017**, *29*, 40–52, doi:10.1021/acs.chemmater.6b02645.
 61. Wang, F.; Li, C.; Zhang, X.; Wei, M.; Evans, D.G.; Duan, X. Catalytic behavior of supported Ru nanoparticles on the {1 0 0}, {1 1 0}, and {1 1 1} facet of CeO₂. *J. Catal.* **2015**, *329*, 177–186.
 62. Bian, Z.; Chan, Y.M.; Yu, Y.; Kawi, S. Morphology dependence of catalytic properties of Ni/CeO₂ for CO₂ methanation: A kinetic and mechanism study. *Catal. Today* **2020**, *347*, 31–38, doi:10.1016/J.CATTOD.2018.04.067.
 63. Hashimoto, N.; Mori, K.; Asahara, K.; Shibata, S.; Jida, H.; Kuwahara, Y.; Yamashita, H. How the Morphology of NiO_x-Decorated CeO₂ Nanostructures Affects Catalytic Properties in CO₂ Methanation. *Langmuir* **2021**, *37*, 5376–5384, doi:10.1021/ACS.LANGMUIR.1C00546.
 64. Du, Y.; Qin, C.; Xu, Y.; Xu, D.; Bai, J.; Ma, G.; Ding, M. Ni nanoparticles dispersed on oxygen vacancies-rich CeO₂ nanoplates for enhanced low-temperature CO₂ methanation performance. *Chem. Eng. J.* **2021**, *418*, 129402, doi:10.1016/J.CEJ.2021.129402.
 65. Bian, Z.; Chan, Y.M.; Yu, Y.; Kawi, S. Morphology dependence of catalytic properties of Ni/CeO₂ for CO₂ methanation: A kinetic and mechanism study. *Catal. Today* **2018**, doi:https://doi.org/10.1016/j.cattod.2018.04.067.
 66. Du, X.; Zhang, D.; Shi, L.; Gao, R.; Zhang, J. Morphology dependence of catalytic properties of Ni/CeO₂ nanostructures for carbon dioxide reforming of methane. *J. Phys. Chem. C* **2012**, *116*, 10009–10016, doi:10.1021/jp300543r.
 67. Trovarelli, A.; Dolcetti, G.; De Leitenburg, C.; Kašpar, J.; Finetti, P.; Santoni, A. Rh-CeO₂ interaction induced by high-temperature reduction. Characterization and catalytic behaviour in transient and continuous conditions. *J. Chem. Soc. Faraday Trans.* **1992**, *88*, 1311–1319, doi:10.1039/FT9928801311.
 68. Trovarelli, A. *Catalytic properties of ceria and CeO₂-Containing materials*; Marcel Dekker Inc., 1996; Vol. 38;.
 69. Trovarelli, A.; De Leitenburg, C.; Dolcetti, G.; Lorca, J.L. CO₂ methanation under transient and steady-state conditions over Rh/CeO₂ and CeO₂-promoted Rh/SiO₂: The role of surface and bulk ceria. *J. Catal.* **1995**, *151*, 111–124.
 70. De Leitenburg, C.; Trovarelli, A.; Kašpar, J. A temperature-programmed and transient kinetic study of CO₂ activation and methanation over CeO₂ supported noble metals. *J. Catal.* **1997**, *166*, 98–107, doi:10.1006/jcat.1997.1498.

References

71. Li, S.; Xu, Y.; Chen, Y.; Li, W.; Lin, L.; Li, M.; Deng, Y.; Wang, X.; Ge, B.; Yang, C. Tuning the selectivity of catalytic carbon dioxide hydrogenation over iridium/cerium oxide catalysts with a strong metal–support interaction. *Angew. Chemie Int. Ed.* **2017**, *56*, 10761–10765.
72. Li, M.; Amari, H.; van Veen, A.C. Metal-oxide interaction enhanced CO₂ activation in methanation over ceria supported nickel nanocrystallites. *Appl. Catal. B Environ.* **2018**, *239*, 27–35, doi:10.1016/j.apcatb.2018.07.074.
73. Konishcheva, M. V.; Potemkin, D.I.; Badmaev, S.D.; Snytnikov, P. V.; Paukshtis, E.A.; Sobyenin, V.A.; Parmon, V.N. On the mechanism of CO and CO₂ methanation over Ni/CeO₂ catalysts. *Top. Catal.* **2016**, *59*, 1424–1430.
74. Zhou, G.; Liu, H.; Cui, K.; Jia, A.; Hu, G.; Jiao, Z.; Liu, Y.; Zhang, X. Role of surface Ni and Ce species of Ni/CeO₂ catalyst in CO₂ methanation. *Appl. Surf. Sci.* **2016**, *383*, 248–252, doi:10.1016/j.apsusc.2016.04.180.
75. Tada, S.; Shimizu, T.; Kameyama, H.; Haneda, T.; Kikuchi, R. Ni/CeO₂ catalysts with high CO₂ methanation activity and high CH₄ selectivity at low temperatures. *Int. J. Hydrogen Energy* **2012**, *37*, 5527–5531.
76. Hao, Z.; Shen, J.; Lin, S.; Han, X.; Chang, X.; Liu, J.; Li, M.; Ma, X. Decoupling the effect of Ni particle size and surface oxygen deficiencies in CO₂ methanation over ceria supported Ni. *Appl. Catal. B Environ.* **2021**, *286*, 119922, doi:10.1016/j.apcatb.2021.119922.
77. Wang, F.; He, S.; Chen, H.; Wang, B.; Zheng, L.; Wei, M.; Evans, D.G.; Duan, X. Active site dependent reaction mechanism over Ru/CeO₂ catalyst toward CO₂ methanation. *J. Am. Chem. Soc.* **2016**, *138*, 6298–6305.
78. Cárdenas-Arenas, A.; Quindimil, A.; Davó-Quiñonero, A.; Bailón-García, E.; Lozano-Castelló, D.; De-La-Torre, U.; Pereda-Ayo, B.; González-Marcos, J.A.; González-Velasco, J.R.; Bueno-López, A. Isotopic and in situ DRIFTS study of the CO₂ methanation mechanism using Ni/CeO₂ and Ni/Al₂O₃ catalysts. *Appl. Catal. B Environ.* **2020**, *265*, 118538, doi:10.1016/j.apcatb.2019.118538.
79. Dreyer, J.A.H.; Li, P.; Zhang, L.; Beh, G.K.; Zhang, R.; Sit, P.H.L.; Teoh, W.Y. Influence of the oxide support reducibility on the CO₂ methanation over Ru-based catalysts. *Appl. Catal. B Environ.* **2017**, *219*, 715–726, doi:10.1016/j.apcatb.2017.08.011.
80. Lin, S.; Hao, Z.; Shen, J.; Chang, X.; Huang, S.; Li, M.; Ma, X. Enhancing the CO₂ methanation activity of Ni/CeO₂ via activation treatment-determined metal-support interaction. *J. Energy Chem.* **2021**, *59*, 334–342, doi:10.1016/j.jechem.2020.11.011.
81. Cárdenas-Arenas, A.; Quindimil, A.; Davó-Quiñonero, A.; Bailón-García, E.; Lozano-Castelló, D.; De-La-Torre, U.; Pereda-Ayo, B.; González-Marcos, J.A.; González-Velasco, J.R.; Bueno-López, A. Isotopic and in situ DRIFTS study of the CO₂ methanation mechanism using Ni/CeO₂ and Ni/Al₂O₃ catalysts. *Appl. Catal. B Environ.* **2020**, *265*, 118538, doi:10.1016/j.apcatb.2019.118538.
82. Upham, D.C.; Derk, A.R.; Sharma, S.; Metiu, H.; McFarland, E.W. CO₂ methanation by Ru-doped ceria: The role of the oxidation state of the surface. *Catal. Sci. Technol.* **2015**, *5*, 1783–1791, doi:10.1039/c4cy01106f.
83. Bogaerts, A.; Tu, X.; Whitehead, J.C.; Centi, G.; Lefferts, L.; Guaitella, O.; Azzolina-Jury, F.; Kim, H.-H.; Murphy, A.B.; Schneider, W.F.; et al. The 2020 plasma catalysis roadmap. *J. Phys. D: Appl. Phys.* **2020**, *53*, 443001, doi:10.1088/1361-6463/ab9048.
84. Tonks, L.; Langmuir, I. A general theory of the plasma of an arc. *Phys. Rev.* **1929**, *34*, 876–922, doi:10.1103/PHYSREV.34.876.

85. Shohet, J.L. Plasma Science and Engineering. *Encycl. Phys. Sci. Technol.* **2003**, 401–423, doi:10.1016/B0-12-227410-5/00584-6.
86. Chen, G.; Snyders, R.; Britun, N. CO₂ conversion using catalyst-free and catalyst-assisted plasma-processes: Recent progress and understanding. *J. CO₂ Util.* **2021**, *49*, 101557, doi:https://doi.org/10.1016/j.jcou.2021.101557.
87. PIONEER Database Available online: <http://db.co2pioneer.eu> (accessed on Apr 1, 2023).
88. Kim, H.-H.; Teramoto, Y.; Negishi, N.; Ogata, A. A multidisciplinary approach to understand the interactions of nonthermal plasma and catalyst: A review. *Catal. Today* **2015**, *256*, 13–22.
89. Dębek, R.; Azzolina-Jury, F.; Travert, A.; Maugé, F. A review on plasma-catalytic methanation of carbon dioxide – Looking for an efficient catalyst. *Renew. Sustain. Energy Rev.* **2019**, *116*, 109427, doi:10.1016/j.rser.2019.109427.
90. Neyts, E.C.; Ostrikov, K.; Sunkara, M.K.; Bogaerts, A. Plasma Catalysis: Synergistic Effects at the Nanoscale. *Chem. Rev.* **2015**, *115*, 13408–13446, doi:10.1021/acs.chemrev.5b00362.
91. Nizio, M.; Albarazi, A.; Cavadias, S.; Amouroux, J.; Galvez, M.E.; Da Costa, P. Hybrid plasma-catalytic methanation of CO₂ at low temperature over ceria zirconia supported Ni catalysts. *Int. J. Hydrogen Energy* **2016**, *41*, 11584–11592.
92. Benrabbah, R.; Cavaniol, C.; Liu, H.; Ognier, S.; Cavadias, S.; Gálvez, M.E.; Da Costa, P. Plasma DBD activated ceria-zirconia-promoted Ni-catalysts for plasma catalytic CO₂ hydrogenation at low temperature. *Catal. Commun.* **2017**, *89*, 73–76, doi:10.1016/j.catcom.2016.10.028.
93. Van Durme, J.; Dewulf, J.; Leys, C.; Van Langenhove, H. Combining non-thermal plasma with heterogeneous catalysis in waste gas treatment: A review. *Appl. Catal. B Environ.* **2008**, *78*, 324–333.
94. Wang, W.; Kim, H.H.; Van Laer, K.; Bogaerts, A. Streamer propagation in a packed bed plasma reactor for plasma catalysis applications. *Chem. Eng. J.* **2018**, *334*, 2467–2479, doi:10.1016/j.cej.2017.11.139.
95. Zhang, Q.Z.; Bogaerts, A. Propagation of a plasma streamer in catalyst pores. *Plasma Sources Sci. Technol.* **2018**, *27*, 035009, doi:10.1088/1361-6595/AAB47A.
96. Azzolina-Jury, F.; Thibault-Starzyk, F. Mechanism of Low Pressure Plasma-Assisted CO₂ Hydrogenation Over Ni-USY by Microsecond Time-resolved FTIR Spectroscopy. *Top. Catal.* **2017**, *60*, 1709–1721, doi:10.1007/s11244-017-0849-2.
97. Dębek, R.; Azzolina-Jury, F.; Travert, A.; Maugé, F.; Thibault-Starzyk, F. Low-pressure glow discharge plasma-assisted catalytic CO₂ hydrogenation—The effect of metal oxide support on the performance of the Ni-based catalyst. *Catal. Today* **2019**, *337*, 182–194, doi:10.1016/j.cattod.2019.03.039.
98. Parastaev, A.; Hoebe, W.F.L.M.; van Heesch, B.E.J.M.; Kosinov, N.; Hensen, E.J.M. Temperature-programmed plasma surface reaction: An approach to determine plasma-catalytic performance. *Appl. Catal. B Environ.* **2018**, *239*, 168–177.
99. Wang, L.; Yi, Y.; Guo, H.; Tu, X. Atmospheric Pressure and Room Temperature Synthesis of Methanol through Plasma-Catalytic Hydrogenation of CO₂. *ACS Catal.* **2018**, *8*, 90–100, doi:10.1021/acscatal.7b02733.
100. Biset-Peiró, M.; Guilera, J.; Andreu, T. Ignition of CO₂ methanation using DBD-plasma catalysis in an adiabatic reactor. *Chem. Eng. J.* **2022**, *433*, 133638, doi:10.1016/J.CEJ.2021.133638.
101. Mikhail, M.; Wang, B.; Jalain, R.; Cavadias, S.; Tatoulain, M.; Ognier, S.; Gálvez, M.E.; Da Costa, P. Plasma-catalytic hybrid process for CO₂ methanation: optimization of operation parameters. *React. Kinet. Mech. Catal.* **2019**, *126*, 629–643, doi:10.1007/s11144-018-1508-8.
102. Biset-Peiró, M.; Mey, R.; Guilera, J.; Andreu, T. Adiabatic plasma-catalytic reactor configuration:

- Energy efficiency enhancement by plasma and thermal synergies on CO₂ methanation. *Chem. Eng. J.* **2020**, *393*, doi:10.1016/j.cej.2020.124786.
103. Jwa, E.; Lee, S.B.; Lee, H.W.; Mok, Y.S. Plasma-assisted catalytic methanation of CO and CO₂ over Ni-zeolite catalysts. *Fuel Process. Technol.* **2013**, *108*, 89–93.
104. Wang, Y.; Fan, L.; Xu, H.; Du, X.; Xiao, H.; Qian, J.; Zhu, Y.; Tu, X.; Wang, L. Insight into the synthesis of alcohols and acids in plasma-driven conversion of CO₂ and CH₄ over copper-based catalysts. *Appl. Catal. B Environ.* **2022**, *315*, 121583, doi:10.1016/J.APCATB.2022.121583.
105. Wang, B.; Mikhail, M.; Cavadias, S.; Tatouliau, M.; Da Costa, P.; Ognier, S. Improvement of the activity of CO₂ methanation in a hybrid plasma-catalytic process in varying catalyst particle size or under pressure. *J. CO₂ Util.* **2021**, *46*, 101471, doi:10.1016/j.jcou.2021.101471.
106. Mei, D.; Tu, X. Atmospheric Pressure Non-Thermal Plasma Activation of CO₂ in a Packed-Bed Dielectric Barrier Discharge Reactor. *ChemPhysChem* **2017**, *18*, 3253–3259, doi:10.1002/CPHC.201700752.
107. Nizio, M.; Benrabbah, R.; Krzak, M.; Debek, R.; Motak, M.; Cavadias, S.; Gálvez, M.E.; Da Costa, P. Low temperature hybrid plasma-catalytic methanation over Ni-Ce-Zr hydrotalcite-derived catalysts. *Catal. Commun.* **2016**, *83*, 14–17, doi:https://doi.org/10.1016/j.catcom.2016.04.023.
108. Mikhail, M.; Costa, P. Da; Amouroux, J.; Cavadias, S.; Tatouliau, M.; Ognier, S.; Gálvez, M.E. Effect of Na and K impurities on the performance of Ni/CeZrO_x catalysts in DBD plasma-catalytic CO₂ methanation. *Fuel* **2021**, *306*, doi:10.1016/J.FUEL.2021.121639.
109. Mikhail, M.; Da Costa, P.; Amouroux, J.; Cavadias, S.; Tatouliau, M.; Gálvez, M.E.; Ognier, S. Tailoring physicochemical and electrical properties of Ni/CeZrO_x doped catalysts for high efficiency of plasma catalytic CO₂ methanation. *Appl. Catal. B Environ.* **2021**, *294*, 120233, doi:10.1016/J.APCATB.2021.120233.
110. Mikhail, M.; Da Costa, P.; Amouroux, J.; Cavadias, S.; Tatouliau, M.; Ognier, S.; Gálvez, M.E. Electrocatalytic behaviour of CeZrO_x-supported Ni catalysts in plasma assisted CO₂ methanation. *Catal. Sci. Technol.* **2020**, 13–17, doi:10.1039/d0cy00312c.
111. Mikhail, M.; Wang, B.; Jalain, R.; Cavadias, S.; Tatouliau, M.; Ognier, S.; Gálvez, M.E.; Da Costa, P. Plasma-catalytic hybrid process for CO₂ methanation: optimization of operation parameters. *React. Kinet. Mech. Catal.* **2019**, *126*, 629–643.
112. Biset-Peiró, M.; Guilera, J.; Zhang, T.; Arbiol, J.; Andreu, T. On the role of ceria in Ni-Al₂O₃ catalyst for CO₂ plasma methanation. *Appl. Catal. A Gen.* **2019**, *575*, 223–229, doi:10.1016/j.apcata.2019.02.028.
113. Mikhail, M.; Da Costa, P.; Amouroux, J.; Cavadias, S.; Tatouliau, M.; Ognier, S.; Gálvez, M.E. Electrocatalytic behaviour of CeZrO_x-supported Ni catalysts in plasma assisted CO₂ methanation. *Catal. Sci. Technol.* **2020**, doi:10.1039/D0CY00312C.
114. Guo, W.; Chen, H. Mechanochemical Synthesis of Ni-Y/CeO₂ Catalyst for Nonthermal Plasma Catalytic CO₂ Methanation. *Ind. Eng. Chem. Res.* **2022**, *61*, 1666–1674, doi:10.1021/ACS.IECR.1C04456/ASSET/IMAGES/LARGE/IE1C04456_0010.JPEG.
115. Hasrack, G.; Bacariza, M.C.; Henriques, C.; Da Costa, P. On the Effect of Cobalt Promotion over Ni/CeO₂ Catalyst for CO₂ Thermal and Plasma Assisted Methanation. *Catalysts* **2021**, *12*, 36, doi:10.3390/CATAL12010036.
116. Parastaev, A.; Kosinov, N.; M Hensen, E.J. Mechanistic study of catalytic CO₂ hydrogenation in a plasma by operando DRIFT spectroscopy. *J. Phys. D Appl. Phys.* **2021**, *54*, 9, doi:10.1088/1361-6463/abeb96.
117. Bacariza, M.C.; Biset-Peiró, M.; Graça, I.; Guilera, J.; Morante, J.; Lopes, J.M.; Andreu, T.; Henriques,

- C. DBD plasma-assisted CO₂ methanation using zeolite-based catalysts: Structure composition-reactivity approach and effect of Ce as promoter. *J. CO₂ Util.* **2018**, *26*, 202–211, doi:10.1016/j.jcou.2018.05.013.
118. Van Laer, K.; Bogaerts, A. How bead size and dielectric constant affect the plasma behaviour in a packed bed plasma reactor: A modelling study. *Plasma Sources Sci. Technol.* **2017**, *26*, doi:10.1088/1361-6595/aa7c59.
 119. James, B.W.; Falconer, I.S.; Kim, H.J.; Zhang, B.C.; Ibrahim, M.; Wouters, M.J.; Roupillard, G. LIF diagnostics for low temperature and fusion plasmas 2000.
 120. Du, Y.; Tamura, K.; Moore, S.; Peng, Z.; Nozak, T.; Bruggeman, J.P. CO (B 1 Σ + \rightarrow A 1 Π) Angstrom system for gas temperature measurements in CO₂ containing plasmas. *Plasma Chem. Plasma Process* **2017**, *37*, 29–41.
 121. Ashford, B.; Wang, Y.; Poh, C.K.; Chen, L.; Tu, X. Plasma-catalytic conversion of CO₂ to CO over binary metal oxide catalysts at low temperatures. *Appl. Catal. B Environ.* **2020**, *276*, doi:10.1016/j.apcatb.2020.119110.
 122. Li, D.; Rohani, V.; Fabry, F.; Ramaswamy, A.P.; Sennour, M.; Fulcheri, L. Direct conversion of CO₂ and CH₄ into liquid chemicals by plasma-catalysis. **2019**.
 123. Wang, B.; Mikhail, M.; Galvez, M.E.; Cavadias, S.; Tatouliau, M.; Da Costa, P.; Ognier, S. Coupling experiment and simulation analysis to investigate physical parameters of CO₂ methanation in a plasma-catalytic hybrid process. *Plasma Process. Polym.* **2020**, *17*, doi:10.1002/ppap.201900261.
 124. Harshkowitz, N. *How Langmuir Probes Work*, in *Plasma Diagnostics*; Auciello, O., Flamm, D.L., Eds.; Academic Press, Boston, 1989; Vol. 1;.
 125. Tu, X.; Gallon, H.J.; Whitehead, J.C. Electrical and spectroscopic diagnostics of a single-stage plasma-catalysis system: effect of packing with TiO₂. *J. Phys. D. Appl. Phys.* **2011**, *44*, 482003, doi:10.1088/0022-3727/44/48/482003.
 126. Guaitella, O.; Thevenet, F.; Guillard, C.; Rousseau, A. Dynamic of the plasma current amplitude in a barrier discharge: influence of photocatalytic material. *J. Phys. D. Appl. Phys.* **2006**, *39*, 2964, doi:10.1088/0022-3727/39/14/015.
 127. Benrabbah, R.; Nizio, M.; Cavadias, S.; Tatouliau, M.; Galvez, M.E.; Da Costa, P. Plasma-catalytic hybrid process for CO₂ methanation. In Proceedings of the 43rd EPS Conference on Plasma Physics; 2016.
 128. Chen, H.; Mu, Y.; Shao, Y.; Chansai, S.; Xu, S.; Stere, C.E.; Xiang, H.; Zhang, R.; Jiao, Y.; Hardacre, C.; et al. Coupling non-thermal plasma with Ni catalysts supported on BETA zeolite for catalytic CO₂ methanation. *Catal. Sci. Technol.* **2019**, *9*, 4135–4145, doi:10.1039/C9CY00590K.
 129. Mai, H.-X.; Sun, L.-D.; Zhang, Y.-W.; Si, R.; Feng, W.; Zhang, H.-P.; Liu, H.-C.; Yan, C.-H. Shape-selective synthesis and oxygen storage behavior of ceria nanopolyhedra, nanorods, and nanocubes. *J. Phys. Chem. B* **2005**, *109*, 24380–24385.
 130. Torrente-Murciano, L.; Gilbank, A.; Puertolas, B.; Garcia, T.; Solsona, B.; Chadwick, D. Shape-dependency activity of nanostructured CeO₂ in the total oxidation of polycyclic aromatic hydrocarbons. *Appl. Catal. B Environ.* **2013**, *132–133*, 116–122, doi:10.1016/j.apcatb.2012.10.030.
 131. Puértolas, B.; Navlani-García, M.; García, T.; Navarro, M. V; Lozano-Castelló, D.; Cazorla-Amorós, D. Optimizing the performance of catalytic traps for hydrocarbon abatement during the cold-start of a gasoline engine. *J. Hazard. Mater.* **2014**, *279*, 527–536, doi:https://doi.org/10.1016/j.jhazmat.2014.07.042.
 132. Hirano, M.; Kato, E. Hydrothermal synthesis of two types of cerium carbonate particles. *J. Mater. Sci.*

- Lett.* **1999**, *18*, 403–405, doi:10.1023/A:1006653305821.
133. Balzar, D.; Snyder, R.L.; Bunge, H.J.; Fiala, J. Voigt-function model in diffraction line-broadening analysis. *Int. Union Crystallogr. Monogr. Cryst.* **1999**, 94–124.
134. Thommes, M.; Kaneko, K.; Neimark, A. V.; Olivier, J.P.; Rodriguez-Reinoso, F.; Rouquerol, J.; Sing, K.S.W. Physisorption of gases, with special reference to the evaluation of surface area and pore size distribution (IUPAC Technical Report). *Pure Appl. Chem.* **2015**, *87*, 1051–1069, doi:10.1515/PAC-2014-1117/MACHINEREADABLECITATION/RIS.
135. Pierotti, R.; Chem, J.R.-P.A.; 1985, undefined Reporting physisorption data for gas/solid systems with special reference to the determination of surface area and porosity. *publications.iupac.org* **1985**.
136. Grosvenor, A.P.; Biesinger, M.C.; StC Smart, R.; Stewart McIntyre, N. New interpretations of XPS spectra of nickel metal and oxides. **2006**, doi:10.1016/j.susc.2006.01.041.
137. Pantaleo, G.; Parola, V. La; Deganello, F.; Singha, R.K.; Bal, R.; Venezia, A.M. Ni/CeO₂ catalysts for methane partial oxidation: Synthesis driven structural and catalytic effects. *Appl. Catal. B Environ.* **2016**, *189*, 233–241, doi:10.1016/j.apcatb.2016.02.064.
138. Jacquemin, M.; Genet, M.J.; Gaigneaux, E.M.; Debecker, D.P. Calibration of the X-ray photoelectron spectroscopy binding energy scale for the characterization of heterogeneous catalysts: Is everything really under control? *ChemPhysChem* **2013**, *14*, 3618–3626, doi:10.1002/cphc.201300411.
139. Peeters, F.; Butterworth, T. Electrical Diagnostics of Dielectric Barrier Discharges. In *Atmospheric Pressure Plasma - From Diagnostics to Applications*; 2018.
140. Manley, T.C. THE ELECTRIC CHARACTERISTICS OF THE OZONATOR DISCHARGE. **1943**, *16*, 450–460.
141. Pipa, A. V; Brandenburg, R. The Equivalent Circuit Approach for the Electrical Diagnostics of the Dielectric Barrier Discharges: The Classical Theory and Recent Developments. *atoms* **2019**, *7*.
142. Srinivasan, A.; Viraraghavan, T. Oil removal from water by fungal biomass: a factorial design analysis. *J. Hazard. Mater.* **2010**, *175*, 695–702.
143. Hirano, M.; Kato, E. Hydrothermal synthesis of nanocrystalline cerium (IV) oxide powders. *J. Am. Ceram. Soc.* **1999**, *82*, 786–788.
144. Hailstone, R.K.; DiFrancesco, A.G.; Leong, J.G.; Allston, T.D.; Reed, K.J. A study of lattice expansion in CeO₂ nanoparticles by transmission electron microscopy. *J. Phys. Chem. C* **2009**, *113*, 15155–15159.
145. Li, P.; Chen, X.; Li, Y.; Schwank, J.W. A review on oxygen storage capacity of CeO₂-based materials: Influence factors, measurement techniques, and applications in reactions related to catalytic automotive emissions control. *Catal. Today* **2019**, *327*, 90–115, doi:10.1016/j.cattod.2018.05.059.
146. Uzunoglu, A.; Zhang, H.; Andreescu, S.; Stanciu, L.A. CeO₂–MO_x (M: Zr, Ti, Cu) mixed metal oxides with enhanced oxygen storage capacity. *J. Mater. Sci.* **2015**, *50*, 3750–3762, doi:10.1007/s10853-015-8939-7.
147. Yang, M.; Shen, G.; Wang, Q.; Deng, K.; Liu, M.; Chen, Y.; Gong, Y.; Wang, Z. Roles of Oxygen Vacancies of CeO₂ and Mn-Doped CeO₂ with the Same Morphology in Benzene Catalytic Oxidation. *Molecules* **2021**, *26*, 6363, doi:10.3390/MOLECULES26216363.
148. López, J.M.; Gilbank, A.L.; García, T.; Solsona, B.; Agouram, S.; Torrente-Murciano, L. The prevalence of surface oxygen vacancies over the mobility of bulk oxygen in nanostructured ceria for the total toluene oxidation. *Appl. Catal. B Environ.* **2015**, *174–175*, 403–412, doi:10.1016/j.apcatb.2015.03.017.
149. Zhang, Y.; Zhang, K.; Yang, C.; Yang, M.; Peng, G.; Xie, Y.; Wen, J.; Xia, F.; Jia, L.; Zhang, Q. The promoting mechanism of SO₂– on CeO₂ for selective catalytic reduction of NO by NH₃: A DFT study.

- Theor. Chem. Acc.* **2022**, *141*, 1–15, doi:10.1007/S00214-022-02898-2/TABLES/2.
150. Agarwal, S.; Lefferts, L.; Mojet, B.L. Ceria Nanocatalysts: Shape Dependent Reactivity and Formation of OH. *ChemCatChem* **2013**, *5*, 479–489, doi:10.1002/cctc.201200491.
 151. Piumetti, M.; Bensaid, S.; Andana, T.; Dosa, M.; Novara, C.; Giorgis, F.; Russo, N.; Fino, D. Nanostructured ceria-based materials: effect of the hydrothermal synthesis conditions on the structural properties and catalytic activity. *J Catal.* **2017**, *7*, 174.
 152. Shan, W.; Luo, M.; Ying, P.; Shen, W.; Li, C. Reduction property and catalytic activity of Ce₁-XNiXO₂ mixed oxide catalysts for CH₄ oxidation. *Appl. Catal. A Gen.* **2003**, *246*, 1–9, doi:10.1016/S0926-860X(02)00659-2.
 153. Lykaki, M.; Pachatouridou, E.; Iliopoulou, E.; Carabineiro, A.C.; Konsolakis, M. Impact of the synthesis parameters on the solid state properties and the CO oxidation performance of ceria nanoparticles. **2017**, doi:10.1039/c6ra26712b.
 154. Zhou, R.; Mohamedali, M.; Ren, Y.; Lu, Q.; Mahinpey, N. Facile synthesis of multi-layered nanostructured Ni/CeO₂ catalyst plus in-situ pre-treatment for efficient dry reforming of methane. *Appl. Catal. B Environ.* **2022**, *316*, 121696, doi:10.1016/J.APCATB.2022.121696.
 155. Weidler, N.; Schuch, J.; Knaus, F.; Stenner, P.; Hoch, S.; Maljusch, A.; Schä, R.; Kaiser, B.; Jaegermann, W. X-ray Photoelectron Spectroscopic Investigation of Plasma-Enhanced Chemical Vapor Deposited NiO_x, NiO_x(OH)_y, and CoNiO_x(OH)_y: Influence of the Chemical Composition on the Catalytic Activity for the Oxygen Evolution Reaction. **2017**, doi:10.1021/acs.jpcc.6b12652.
 156. Cárdenas-Arenas, A.; Quindimil, A.; Davó-Quiñonero, A.; Bailón-García, E.; Lozano-Castelló, D.; De-La-Torre, U.; Pereda-Ayo, B.; González-Marcos, J.A.; González-Velasco, J.R.; Bueno-López, A. Design of active sites in Ni/CeO₂ catalysts for the methanation of CO₂: tailoring the Ni-CeO₂ contact. *Appl. Mater. Today* **2020**, *19*, doi:10.1016/j.apmt.2020.100591.
 157. Atzori, L.; Cutrufello, M.G.; Meloni, D.; Onida, B.; Gazzoli, D.; Ardu, A.; Monaci, R.; Sini, M.F.; Rombi, E. Characterization and catalytic activity of soft-templated NiO-CeO₂ mixed oxides for CO and CO₂ co-methanation. *Front. Chem. Sci. Eng.* **2020**, *15*, 251–268, doi:10.1007/S11705-020-1951-8.
 158. Mokkelbost, T.; Kaus, I.; Grande, T.; Einarsrud, M.-A. Combustion Synthesis and Characterization of Nanocrystalline CeO₂-Based Powders. **2004**, doi:10.1021/cm048583p.
 159. Vayssilov, G.N.; Mihaylov, M.; Petkov, P.S.; Hadjiivanov, K.I.; Neyman, K.M. Reassignment of the vibrational spectra of carbonates, formates, and related surface species on ceria: A combined density functional and infrared spectroscopy investigation. *J. Phys. Chem. C* **2011**, *115*, 23435–23454, doi:10.1021/jp208050a.
 160. Appel, L.G.; Eon, J.G.; Schmal, M. The CO₂-CeO₂ interaction and its role in the CeO₂ reactivity. *Catal. Letters* **1998**, *56*, 199–202.
 161. Eliasson, B.; Kogelschatz, U.; Xue, B.; Zhou, L.M. Hydrogenation of carbon dioxide to methanol with a discharge-activated catalyst. *Ind. Eng. Chem. Res.* **1998**, *37*, 3350–3357, doi:10.1021/IE9709401/ASSET/IMAGES/LARGE/IE9709401F00009.JPEG.
 162. Eliasson, B.; Hirth, M.; Kogelschatz, U. Ozone synthesis from oxygen in dielectric barrier discharges. *J. Phys. D. Appl. Phys.* **1987**, *20*, 1421, doi:10.1088/0022-3727/20/11/010.
 163. Suzuki, K.; Kato, M.; Sunaoshi, T.; Uno, H.; Carvajal Nunez, U.; Nelson, A.T.; McClellan, K.J. Thermal and mechanical properties of CeO₂. *J. Am. Ceram. Soc.* **2018**.
 164. Marco, D. Di; Drissi, K.; Delhote, N.; Tantot, O.; Geffroy, P.M.; Verdeyme, S.; Chartier, T. Dielectric properties of pure alumina from 8 GHz to 73 GHz. *J. Eur. Ceram. Soc.* **2016**, *36*, 3355–3361,

- doi:10.1016/J.JEURCERAMSOC.2016.05.047.
165. Steiner, C.; Walter, S.; Malashchuk, V.; Hagen, G.; Kogut, I.; Fritze, H.; Moos, R. Determination of the dielectric properties of storage materials for exhaust gas aftertreatment using the microwave cavity perturbation method. *Sensors (Switzerland)* **2020**, *20*, 1–18, doi:10.3390/S20216024.
166. Cárdenas-Arenas, A.; Cortés, H.S.; Bailón-García, E.; Davó-Quiñonero, A.; Lozano-Castelló, D.; Bueno-López, A. Active, selective and stable NiO-CeO₂ nanoparticles for CO₂ methanation. *Fuel Process. Technol.* **2021**, *212*, 106637, doi:10.1016/J.FUPROC.2020.106637.
167. Pan, Q.; Peng, J.; Sun, T.; Gao, D.; Wang, S.; Wang, S. CO₂ methanation on Ni/Ce_{0.5}Zr_{0.5}O₂ catalysts for the production of synthetic natural gas. *Fuel Process. Technol.* **2014**, *123*, 166–171.
168. Mikhail, M.; Da Costa, P.; Amouroux, J.; Cavadias, S.; Tatouliau, M.; Ognier, S.; Gálvez, M.E. Electrocatalytic behaviour of CeZrO_x-supported Ni catalysts in plasma assisted CO₂ methanation. *Catal. Sci. Technol.* **2020**, 1–4, doi:10.1039/d0cy00312c.
169. Bacariza, M.C.; Spataru, D.; Karam, L.; Lopes, J.M.; Henriques, C. Promising catalytic systems for CO₂ hydrogenation into CH₄: A review of recent studies. *Processes* **2020**, *8*, 1–45.
170. Siakavelas, G.I.; Charisiou, N.D.; AlKhoori, S.; AlKhoori, A.A.; Sebastian, V.; Hinder, S.J.; Baker, M.A.; Yentekakis, I. V.; Polychronopoulou, K.; Goula, M.A. Highly selective and stable nickel catalysts supported on ceria promoted with Sm₂O₃, Pr₂O₃ and MgO for the CO₂ methanation reaction. *Appl. Catal. B Environ.* **2021**, *282*, 119562, doi:10.1016/J.APCATB.2020.119562.
171. Wang, B.; Zhu, B.; Yun, S.; Zhang, W.; Xia, C.; Afzal, M.; Cai, Y.; Liu, Y.; Wang, Y.; Wang, H. Fast ionic conduction in semiconductor CeO₂-δ electrolyte fuel cells. *NPG Asia Mater.* **2019**, *11*, 1–12, doi:10.1038/s41427-019-0152-8.
172. Rui, N.; Zhang, X.; Zhang, F.; Liu, Z.; Cao, X.; Xie, Z.; Zou, R.; Senanayake, S.D.; Yang, Y.; Rodriguez, J.A.; et al. Highly active Ni/CeO₂ catalyst for CO₂ methanation: Preparation and characterization. *Appl. Catal. B Environ.* **2021**, *282*, doi:10.1016/j.apcatb.2020.119581.
173. Jeon, O.S.; Lee, H.; Lee, K.S.; Paidi, V.K.; Ji, Y.; Kwon, O.C.; Kim, J.P.; Myung, J.H.; Park, S.Y.; Yoo, Y.J.; et al. Harnessing Strong Metal-Support Interaction to Proliferate the Dry Reforming of Methane Performance by in Situ Reduction. *ACS Appl. Mater. Interfaces* **2022**, *14*, 12140–12148, doi:10.1021/ACSAMI.1C20889/SUPPL_FILE/AM1C20889_SI_001.PDF.
174. Nesbitt, H.W.; Legrand, D.; Bancroft, G.M. Interpretation of Ni2p XPS spectra of Ni conductors and Ni insulators. *Phys. Chem. Miner.* **2000**, *27*, 357–366, doi:10.1007/S002690050265/METRICS.
175. Liu, Z.; Duchoň, T.; Wang, H.; Grinter, D.C.; Waluyo, I.; Zhou, J.; Liu, Q.; Jeong, B.; Crumlin, E.J.; Matolín, V.; et al. Ambient pressure XPS and IRRAS investigation of ethanol steam reforming on Ni-CeO₂(111) catalysts: an in situ study of C-C and O-H bond scission. *Phys. Chem. Chem. Phys.* **2016**.
176. Carrasco, J.; López-Duran, D.; Liu, Z.; Duchoň, T.; Aime Evans, J.; Senanayake, S.D.; Crumlin, E.J.; Matolín, V.; Rodríguez, J.A.; Verónica Ganduglia-Pirovano, M.; et al. Metal-Support Interactions In Situ and Theoretical Studies for the Dissociation of Water on an Active Ni/CeO₂ Catalyst: Importance of Strong Metal-Support Interactions for the Cleavage of O-H Bonds**. **2015**, *54*, 917–3921, doi:10.1002/ange.201410697.
177. Jain, S.; Shah, J.; Negi, N.S.; Sharma, C.; Kotnala, R.K. Significance of interface barrier at electrode of hematite hydroelectric cell for generating ecopower by water splitting. *Int. J. Energy Res.* **2019**, *43*, 4743–4755, doi:10.1002/ER.4613.
178. Vantomme, A.; Yuan, Z.Y.; Du, G.; Su, B.L. Surfactant-assisted large-scale preparation of crystalline CeO₂ nanorods. *Langmuir* **2005**, *21*, 1132–1135, doi:10.1021/la047751p.

179. Wang, S.; Pan, Q.; Peng, J.; Wang, S. In situ FTIR spectroscopic study of the CO₂ methanation mechanism on Ni/Ce_{0.5}Zr_{0.5}O₂. *Catal. Sci. Technol.* **2014**, *4*, 502–509, doi:10.1039/c3cy00868a.
180. Valdivia-Barrientos, R.; Pacheco-Sotelo, J.; Pacheco-Pacheco, M.; Benítez-Read, J.S.; López-Callejas, R. Analysis and electrical modelling of a cylindrical DBD configuration at different operating frequencies. *Plasma Sources Sci. Technol.* **2006**, *15*, 237, doi:10.1088/0963-0252/15/2/008.
181. Wang, W.; Butterworth, T.; Bogaerts, A. Plasma propagation in a single bead DBD reactor at different dielectric constants: insights from fluid modelling. *J. Phys. D. Appl. Phys.* **2021**, *54*, 214004, doi:10.1088/1361-6463/ABE8FF.
182. Van Laer, K.; Bogaerts, A. Influence of Gap Size and Dielectric Constant of the Packing Material on the Plasma Behaviour in a Packed Bed DBD Reactor: A Fluid Modelling Study. *Plasma Process. Polym.* **2017**, *14*, 1600129, doi:10.1002/PPAP.201600129.
183. Van Laer, K.; Bogaerts, A. Fluid modelling of a packed bed dielectric barrier discharge plasma reactor. *Plasma Sources Sci. Technol.* **2015**, *25*, 015002, doi:10.1088/0963-0252/25/1/015002.
184. Gadkari, S.; Gu, S. Influence of catalyst packing configuration on the discharge characteristics of dielectric barrier discharge reactors: A numerical investigation. *Phys. Plasmas* **2018**, *25*, 063513, doi:10.1063/1.5030508.
185. Vanraes, P.; Nikiforov, A.; Bogaerts, A.; Leys, C. Study of an AC dielectric barrier single micro-discharge filament over a water film. *Sci. Reports* **2018**, *8*, 1–11, doi:10.1038/s41598-018-29189-w.
186. Falkenstein, Z.; Coogan, J.J. Microdischarge behaviour in the silent discharge of nitrogen - oxygen and water - air mixtures. *J. Phys. D Appl. Phys.* **1997**, *30*, 817–825.
187. Zhang, Q.Z.; Wang, W.Z.; Bogaerts, A. Importance of surface charging during plasma streamer propagation in catalyst pores. *Plasma Sources Sci. Technol.* **2018**, *27*, 065009, doi:10.1088/1361-6595/AACA6D.
188. Anirban, S.; Dutta, A. Structural and ionic transport mechanism of rare earth doped cerium oxide nanomaterials: Effect of ionic radius of dopant cations. *Solid State Ionics* **2017**, *309*, 137–145, doi:10.1016/J.SSI.2017.07.020.
189. Vakil, P.N.; Muhammed, F.; Hardy, D.; Dickens, T.J.; Ramakrishnan, S.; Strouse, G.F. Dielectric Properties for Nanocomposites Comparing Commercial and Synthetic Ni- and Fe₃O₄-Loaded Polystyrene. *ACS Omega* **2018**, *3*, 12813–12823, doi:10.1021/ACSOMEGA.8B01477/ASSET/IMAGES/LARGE/AO-2018-014779_0008.JPEG.
190. Ussa Aldana, P.A.; Ocampo, F.; Kobl, K.; Louis, B.; Thibault-Starzyk, F.; Daturi, M.; Bazin, P.; Thomas, S.; Roger, A.C. Catalytic CO₂ valorization into CH₄ on Ni-based ceria-zirconia. Reaction mechanism by operando IR spectroscopy. *Catal. Today* **2013**, *215*, 201–207, doi:10.1016/j.cattod.2013.02.019.
191. Beuls, A.; Swalus, C.; Jacquemin, M.; Heyen, G.; Karelovic, A.; Ruiz, P. Methanation of CO₂: Further insight into the mechanism over Rh/γ-Al₂O₃ catalyst. *Appl. Catal. B Environ.* **2012**, *113–114*, 2–10, doi:10.1016/J.APCATB.2011.02.033.
192. Lee, Y.H.; Ahn, J.Y.; Nguyen, D.D.; Chang, S.W.; Kim, S.S.; Lee, S.M. Role of oxide support in Ni based catalysts for CO₂ methanation. *RSC Adv.* **2021**, *11*, 17648–17657, doi:10.1039/D1RA02327F.
193. Gonçalves, L.P.L.; Mielby, J.; Soares, O.S.G.P.; Sousa, J.P.S.; Petrovykh, D.Y.; Lebedev, O.I.; Pereira, M.F.R.; Kegnæs, S.; Kolen'ko, Y. V. In situ investigation of the CO₂ methanation on carbon/ceria-supported Ni catalysts using modulation-excitation DRIFTS. *Appl. Catal. B Environ.* **2022**, *312*, 121376, doi:10.1016/J.APCATB.2022.121376.
194. Azzolina-Jury, F.; Thibault-Starzyk, F. Mechanism of Low Pressure Plasma-Assisted CO₂ Hydrogenation

- Over Ni-USY by Microsecond Time-resolved FTIR Spectroscopy. *Top. Catal.* **2017**, *60*, 1709–1721, doi:10.1007/s11244-017-0849-2.
195. DĘBEK, R.; WIERZBICKI, D.; MOTAK, M.; GALVEZ, M.E.; COSTA, P. DA; AZZOLINA-JURY, F. Operando FT-IR study on basicity improvement of Ni(Mg, Al)O hydrotalcite- derived catalysts promoted by glow plasma discharge. *Plasma Sci. Technol.* **2019**, *21*, 045503, doi:10.1088/2058-6272/aaf759.
196. Van Turnhout, J.; Aceto, D.; Travert, A.; Bazin, P.; Thibault-Starzyk, F.; Bogaerts, A.; Azzolina-Jury, F. Observation of surface species in plasma-catalytic dry reforming of methane in a novel atmospheric pressure dielectric barrier discharge in situ IR cell. *Catal. Sci. Technol.* **2022**, *12*, 6676–6686, doi:10.1039/D2CY00311B.
197. Aceto, D.; Bacariza, M.C.; Travert, A.; Henriques, C.; Azzolina-Jury, F. Thermal and Plasma-Assisted CO₂ Methanation over Ru/Zelite: A Mechanistic Study Using In-Situ Operando FTIR. *Catalysts* **2023**, *13*, 481, doi:10.3390/CATAL13030481.
198. Neyts, E.C. Plasma-Surface Interactions in Plasma Catalysis. *Plasma Chem. Plasma Process.* **2015**, *36*, 185–212, doi:10.1007/S11090-015-9662-5.
199. Wuttke, S.; Bazin, P.; Vimont, A.; Serre, C.; Seo, Y.K.; Hwang, Y.K.; Chang, J.S.; Férey, G.; Daturi, M. Discovering the Active Sites for C₃ Separation in MIL-100(Fe) by Using Operando IR Spectroscopy. *Chem. – A Eur. J.* **2012**, *18*, 11959–11967, doi:10.1002/CHEM.201201006.
200. Chon, B.; Xu, S.; Lee, Y.J. Compensation of Strong Water Absorption in Infrared Spectroscopy Reveals the Secondary Structure of Proteins in Dilute Solutions. *Anal. Chem.* **2021**, *93*, 2215–2225, doi:10.1021/ACS.ANALCHEM.0C04091/ASSET/IMAGES/MEDIUM/AC0C04091_M015.GIF.
201. Lin, L.; Yao, S.; Liu, Z.; Zhang, F.; Li, N.; Vovchok, D.; Martínez-Arias, A.; Castaneda, R.; Lin, J.; Senanayake, S.D.; et al. In Situ Characterization of Cu/CeO₂ Nanocatalysts for CO₂ Hydrogenation: Morphological Effects of Nanostructured Ceria on the Catalytic Activity. *J. Phys. Chem. C* **2018**, *122*, 12934–12943, doi:10.1021/ACS.JPCC.8B03596/ASSET/IMAGES/LARGE/JP-2018-03596T_0009.JPEG.
202. Pozdnyakova, O.; Teschner, D.; Wootsch, A.; Kröhnert, J.; Steinhauer, B.; Sauer, H.; Toth, L.; Jentoft, F.C.; Knop-Gericke, A.; Paál, Z.; et al. Preferential CO oxidation in hydrogen (PROX) on ceria-supported catalysts, part II: Oxidation states and surface species on Pd/CeO₂ under reaction conditions, suggested reaction mechanism. *J. Catal.* **2006**, *237*, 17–28, doi:10.1016/J.JCAT.2005.10.015.
203. Di Cosimo, J.I.; Díez, V.K.; Xu, M.; Iglesia, E.; Apesteguía, C.R. Structure and Surface and Catalytic Properties of Mg-Al Basic Oxides. *J. Catal.* **1998**, *178*, 499–510, doi:10.1006/JCAT.1998.2161.
204. Ramakers, M.; Michielsen, I.; Aerts, R.; Meynen, V.; Bogaerts, A. Effect of Argon or Helium on the CO₂ Conversion in a Dielectric Barrier Discharge. *Plasma Process. Polym.* **2015**, *12*, 755–763, doi:10.1002/PPAP.201400213.
205. Miao, B.; Ma, S.S.K.; Wang, X.; Su, H.; Chan, S.H. Catalysis mechanisms of CO₂ and CO methanation. *Catal. Sci. Technol.* **2016**, *6*, 4048–4058.
206. Azzolina-Jury, F. Novel boehmite transformation into γ -alumina and preparation of efficient nickel base alumina porous extrudates for plasma-assisted CO₂ methanation. *J. Ind. Eng. Chem.* **2019**, *71*, 410–424, doi:https://doi.org/10.1016/j.jiec.2018.11.053.
207. Raskó, J.; Kecskés, T.; Kiss, J. Formaldehyde formation in the interaction of HCOOH with Pt supported on TiO₂. *J. Catal.* **2004**, *224*, 261–268, doi:10.1016/J.JCAT.2004.03.025.
208. Binet, C.; Daturi, M.; Lavalley, J.C. IR study of polycrystalline ceria properties in oxidised and reduced states. *Catal. Today* **1999**, *50*, 207–225, doi:10.1016/S0920-5861(98)00504-5.
209. Li, C.; Sakata, Y.; Arai, T.; Domen, K.; Maruya, K.I.; Onishi, T. Carbon monoxide and carbon dioxide

- adsorption on cerium oxide studied by Fourier-transform infrared spectroscopy. Part 1.—Formation of carbonate species on dehydroxylated CeO₂, at room temperature. *J. Chem. Soc. Faraday Trans. 1 Phys. Chem. Condens. Phases* **1989**, *85*, 929–943, doi:10.1039/F19898500929.
210. Li, C.; Sakata, Y.; Arai, T.; Domen, K.; Maruya, K.I.; Onishi, T. Adsorption of carbon monoxide and carbon dioxide on cerium oxide studied by Fourier-transform infrared spectroscopy. Part 2.—Formation of formate species on partially reduced CeO₂ at room temperature. *J. Chem. Soc. Faraday Trans. 1 Phys. Chem. Condens. Phases* **1989**, *85*, 1451–1461, doi:10.1039/F19898501451.

List of contributions

- B. Musig, R. Arenal, A. Roy, T. García, M.E. Gálvez, M.V. Navarro “Nano-structured CeO₂ as support of Ni-catalysts for plasma-catalytic CO₂methanation: Influence of support’s morphology and physicochemical properties” (to be submitted)
- A. Salden, M. Budde, C.A. Garcia-Soto, O. Biondo, J. Barauna, M. Faedda, B. Musig et al. “Meta-analysis of CO₂ conversion, energy efficiency and other performance data of plasma-catalysis reactors with the open access PIONEER database” review paper, Journal of Energy Chemistry, 2023 (under review)
- Oral communication: B. Musig, M.E. Gálvez, M.V. Navarro “Effect of morphology of nanostructured CeO₂ supports on plasma-assisted CO₂ methanation” at the Plasma Tech conference, April 2022, Barcelona (Spain)
- Oral communication: B. Musig, M.E. Gálvez, M.V. Navarro “Thermal and plasma-catalytic CO₂ methanation over nanostructured Ni/CeO₂” at the ISGC, May 2022, La Rochelle (France)
- Oral communication: B. Musig, O. Guaitella, M.E. Gálvez, M.V. Navarro “Characterization of a Plasma Dielectric Barrier Discharge Reactor Packed with Ni/CeO₂ Nanostructured Catalysts for CO₂ Methanation” at the ISPCEM conference, July 2022, Liverpool (UK)
- Oral communication: B. Musig, O. Guaitella, M.E. Gálvez, M.V. Navarro “Nanostructured Catalyst for Plasma Assisted CO₂ Methanation” at the International Symposium Plasma Catalysis for CO₂ Recycling, September 2022, Krakow (Poland)
- Poster presentation: C. Fromentin, B. Musig, M. Nguyen-Quang “The PIONEERS of CO₂ recycling” at the MCAA Annual Conference, March 2022, Lisbon (Portugal)
- Poster presentation: B. Musig, O. Guaitella, M.E. Gálvez, M.V. Navarro “Physicochemical and electrical characterization of CeO₂-based nanostructured catalysts for plasma-assisted CO₂ Methanation in a DBD reactor” at the WE-Heraeus-Seminar Non-Thermal Plasmas for Sustainable Chemistry, April 2023, Bad Honnef (Germany)

Annex 1: Comparison of syntheses ceria with commercial metal oxides as supports for Ni catalysts

Ni supported on commercial CeO_2 , $\text{Ce}_{0.58}\text{Zr}_{0.42}\text{O}_2$ (CZ) and Al_2O_3 metal oxides were prepared via wet impregnation, briefly characterised via SEM and XRD, and used in plasma-assisted and thermochemical catalytic test as benchmark catalysts for CO_2 methanation, as they have been used in previous publications for methanation in a DBD reactor [109,112,115].

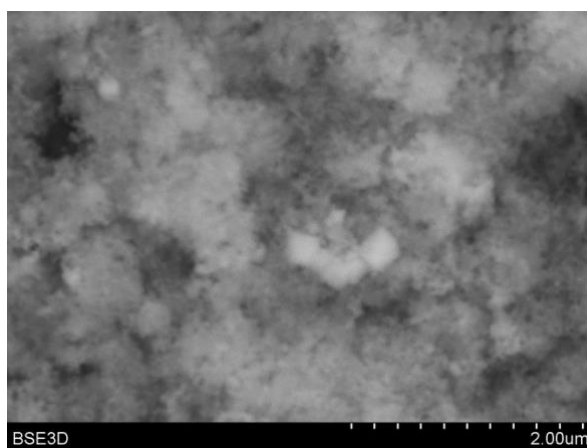


Figure A1.1: SEM image of commercial CeO_2 support from Sigma-Aldrich

Table A1.1: Results of Rietveld analysis of XRD characterization of commercial supports and the corresponding 15 %wt. Ni catalysts.

Sample	Support phase	Support crystallite size, nm	Support lattice parameter, Å	Ni crystallite size, nm
Ni/Al_2O_3	γ and δ Al_2O_3	NA	NA	NA
CeO_2	cerianite	19.3	a 5.411	
Ni/CeO_2	cerianite	26.3	a 5.411	25.9
Ni/CZ	cerianite	5.9	a 5.279	20.5

The SEM image of commercial CeO_2 support from Sigma-Aldrich shows small particles without any specific morphology, that tend to agglomerate. The cerianite phase of this commercial material is stoichiometric (lattice parameter 5.411 Å) with crystallite size of 26.3 nm. The Ni phase seems to be more dispersed on the CZ commercial support, which also has smaller support crystallite size, compared to the ceria support. Furthermore, the inclusion of Zr in the ceria lattice causes a distortion of the lattice parameter (5.279 Å), as expected. The XRD diffractogram of the Ni/ Al_2O_3

sample does not allow to perform the Rietveld analysis due to the low crystallinity of the material, it was only possible to identify the γ and δ alumina phases.

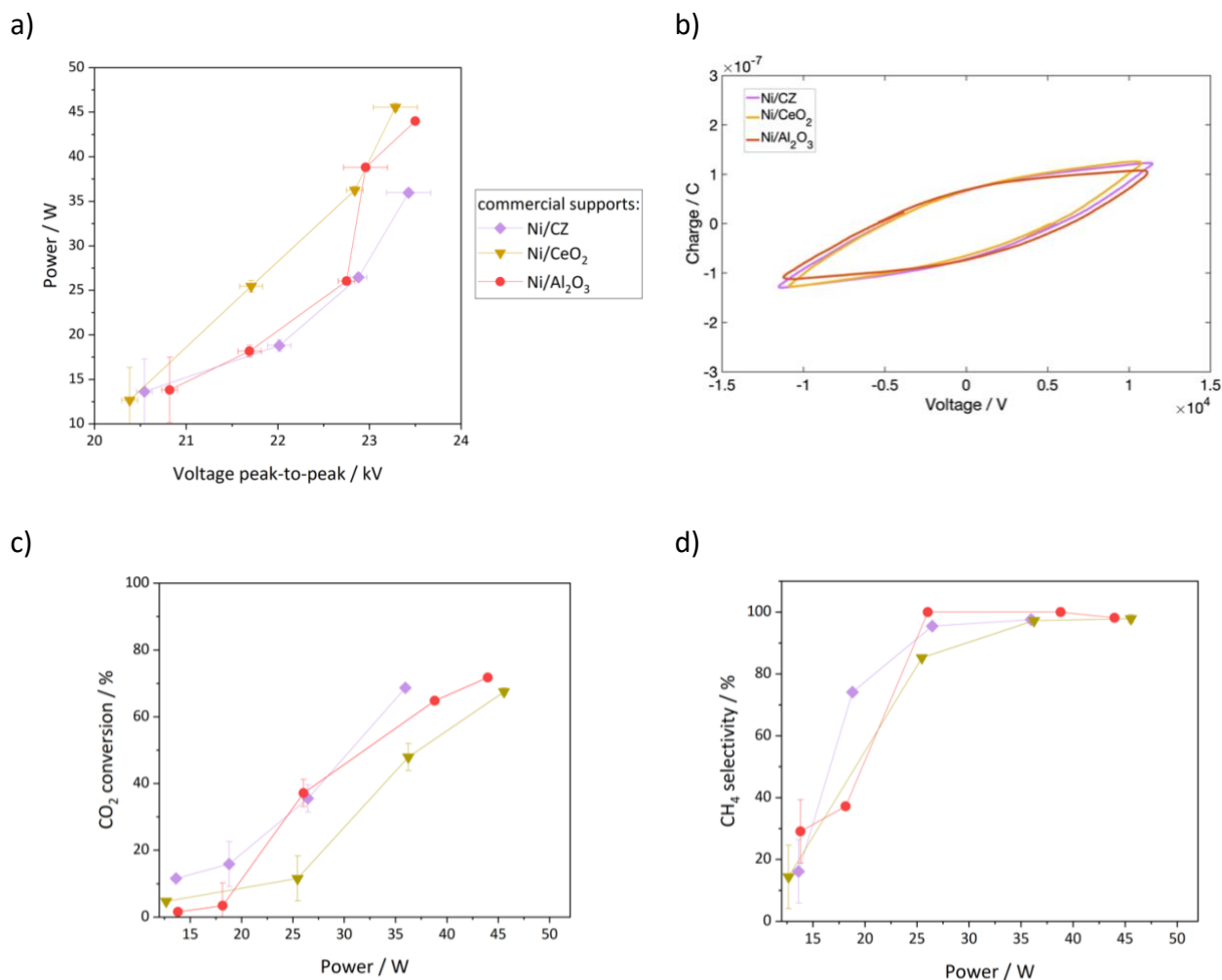


Figure A1.2: a) power as a function of the applied voltage b) Lissajous figures of a Ni catalysts on commercial supports at 25 W, c) CO₂ conversion and d) CH₄ selectivity results of plasma-assisted CO₂ methanation tests with the Ni catalysts supported on commercial CZ, CeO₂ and Al₂O₃ as a function of injected power. H₂/CO₂ = 4, WHSV 30000 mL/hg_{cat}.

Among this series of three catalysts supported on commercial metal oxides (with particle size 200-25 μ m), Ni/CZ is the one that shows the best activity with most efficient conversion at lower power. The commercial ceria-zirconia supported catalysts is considered as benchmark, its good activity for plasma-assisted methanation was previously reported as 73.5 % conversion at low power 14.4 W [109]. The result obtained with this DBD set-up is 68.6 % conversion at 36 W. The power is not comparable as the set-ups are different, under DBD plasma, both power input and temperature depend strongly on the frequency used, 12.3 kHz in this study and 70.3 kHz in [109], which explains the discrepancy of the results obtained compared to the published ones [109]. Generally, increasing the operating frequency improves the energy efficiency [109,111,180]. The results with the catalyst

supported on commercial materials are similar to the Ni/DOE3 and 4 catalysts, with high conversion achieved only above 35 W. Increasing power is required to reach 70 % conversion with the three catalysts supported on commercial materials Ni/CZ<Ni/Al₂O₃< Ni/CeO₂, showing again how the packing material affects the plasma behaviour and the reaction. Nonetheless, it should be commented that at these conditions the reducible (CeO₂ and CZ) or non-reducible (Al₂O₃) nature of the supports does not seem to play a role on the activity or indicate a different reaction mechanism and effect of the supporting materials on the plasma behaviour.

Two catalysts (Ni/CZ and Ni/CeO₂) supported on commercial materials that were used in the DBD reactor were also tested in thermal methanation. The trend is very similar between them and to the best performing cases of the Ni/DOE series, meaning Ni/DOE1, 3, 4, and 5. Thermal CO₂ methanation over Ni/CZ was also reported with similar activity (73 % at 300 °C) in other publications, validating the results obtained in this study [167,168]. This similarity in activity with benchmark materials and previous published results proves the successful synthesis of the Ni/DOE materials and the positive effect of selected synthesis conditions on the physicochemical properties of the catalysts for methanation.

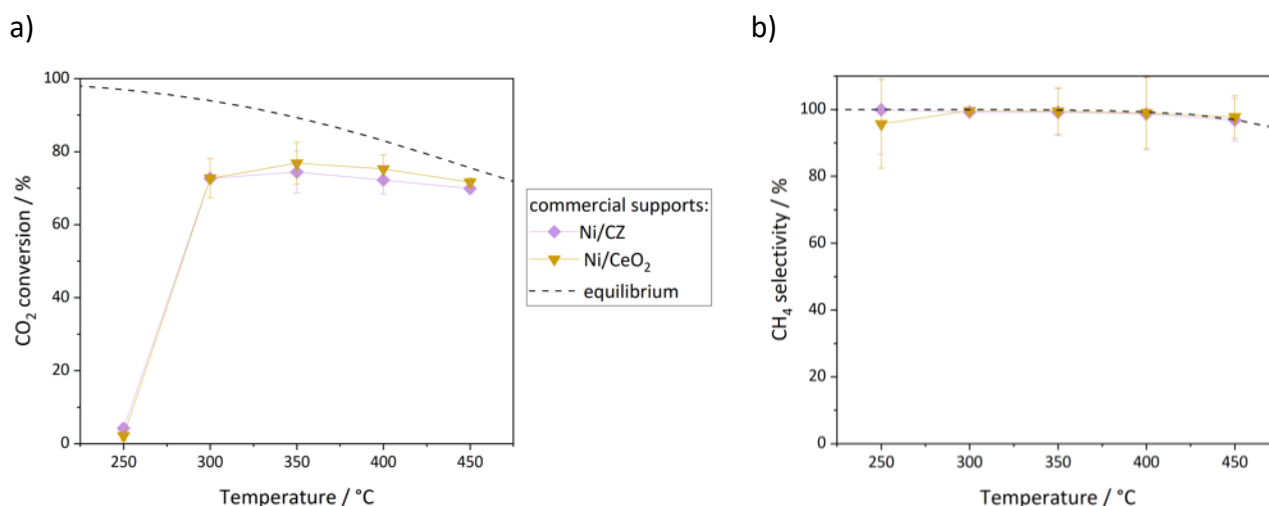


Figure A1.3: a) CO₂ conversion and b) CH₄ selectivity results of thermal CO₂ methanation tests with the Ni catalysts supported on commercial CZ and CeO₂ as a function of temperature.

H₂/CO₂ = 4, WHSV 30000 mL/hg_{cat}. The equilibrium curve is added in dashed line.

Annex 2: Effect of catalyst reduction and particle size on the plasma-assisted CO₂ methanation results in the DBD plasma reactor

The plasma reduction pre-treatment was tested as an alternative to ex-situ thermal reduction which required high temperature (600 °C) and long treatment (at least 2 hours and in addition the reactor cooling time). Plasma was ignited in the packed bed DBD reactor with a pure H₂ flow of 100 mL/min for 30 minutes with applied voltage 23 kV_{p-p} and 12.3 kHz frequency, reaching a reactor temperature of around 135 °C. After the in-situ catalyst pre-treatment the plasma-assisted CO₂ methanation experiment was carried out as usual. For comparison, the Ni/DOE0 catalyst was used fresh without any reduction pre-treatment (just after 550 °C calcination in air), reduced (at 600 °C in 5%H₂/Ar for 2 h, which is the condition used for all catalysts in this work), and reduced in H₂ plasma. The CO₂ conversion results obtained with the nanoneedles catalysts in these conditions are shown in Figure A2.1. It is clear that NiO is not performing well as catalyst in plasma-assisted CO₂ methanation and that a reduction step, either in plasma or at high temperature as they seem to be equivalent for such application of the Ni/CeO₂ catalyst, is required in order to have Ni particles that facilitate the CO₂ converting reaction.

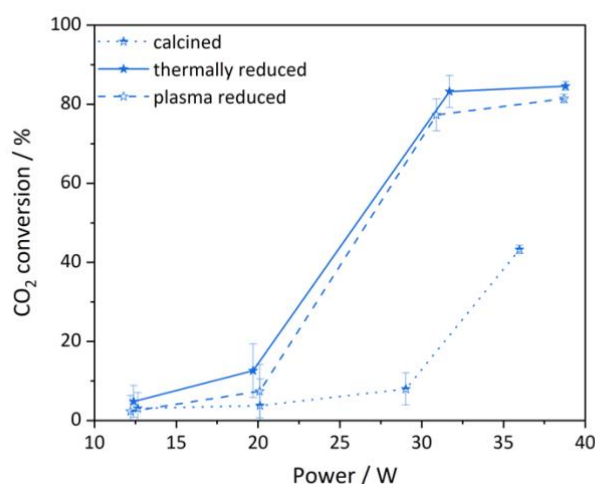


Figure A2.1: CO₂ conversion during plasma-assisted CO₂ methanation tests as a function of injected power of Ni/DOE0 calcined at 550 °C in air, reduced at 600 °C in 5%H₂/Ar, and pre-treated in H₂ plasma. H₂/CO₂ = 4, WHSV 30000 mL/hg_{cat}.

The importance of macroscopic shape and size of the catalyst is under debate for applications in plasma catalysis, especially in the case of in-plasma set-ups, as it is the case of the packed bed DBD reactor used in this study. The materials used were available as powders, but the grain size could be

selected by milling and sieving. Normally the 200-25 μm range was selected. In order to consider the effect of the powder grain size on the plasma and on the reaction, calcined NiO/DOE0 was sieved into three particle size sections 355-200 μm , 200-25 μm , and below 25 μm , reduced in plasma using the protocol describe above and tested for plasma-assisted CO₂ methanation. The results are shown in Figure A2.2, it can be concluded at this size range the powder grain size does not greatly affect the CO₂ conversion and CH₄ selectivity (which reaches >99 % with conversion above 70 %, not shown) results.

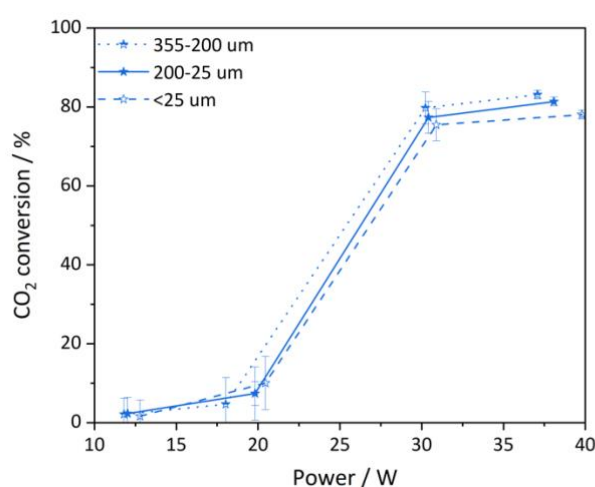


Figure A2.2: CO₂ conversion during plasma-assisted CO₂ methanation tests as a function of injected power of Ni/DOE0 with powder grain size 355-200, 200-25, <25 μm . H₂/CO₂ = 4, WHSV 30000 mL/hg_{cat}.

Finally, the H₂ plasma pre-treatment has great potential for further development of the CO₂ methanation process in DBD reactor, as it can make the catalyst preparation more efficient and faster [92].

Annex 3: Literature screening of FTIR bands of adsorbed C-species on ceria


The content of this annex aims to complement the analysis of operando FTIR spectra acquired during plasma-assisted and thermal CO₂ methanation with Ni/DOE0 catalyst shown in chapter 6. The schematics of the species that it was proposed adsorb on the catalyst surface due to interaction of the Ni/CeO₂ with H₂/CO₂ gas mixture and the vibrational frequencies collected in a literature survey regarding FTIR spectra analysis of oxo-carbonate species on ceria and Ni catalysts are reported in the following tables.

Table A3.1: Schematics of the adsorbed species on Ni/CeO₂ identified in chapter 6 [159].

Adsorbed specie	Structure
Monodentate carbonate	
Bidentate carbonate	
Bridged bidentate carbonate	
Hydrogen carbonate	
Formate	
Linear Carbonyl	
Bridged Carbonyl	
HCO	
CH2	

Table A3.2: Calculated and experimental vibrational frequencies (cm⁻¹) of various carbonate and formate species on cerium oxide surface considered in chapter 6 gathered from literature [81,159,160,179,201,202,208–210].

Species	[159] DFT calaculated	[159] experimental	[201]	[200, 201]	[202]	[81]	[179]	This study DBD	This study Therm.
Monodentate carbonate									
$\delta(OCO)$				854					
$\nu(CO)$	762			1066	1085	1040-1080			1050
$\nu(CO)$	1213			1348	1358	1300-1370			1372
$\nu(CO)$	1755			1454	1464				1490
Bidentate carbonate									
$\delta(CO)$	869-813		851		1014	1020-1030			
$\nu(CO)$	1194-1130	1147-1136	1292		1298	1250-1290		1310	1291
$\nu(CO)$	1718-1698	1732	1580		1565	1530-1620		1550	1580
Polycarbonate									
$\delta(OCO)$	830-797							850	
$\nu(CO)$	1020-1007				1050			1030	
$\nu(CO)$	1367-1331				1353			1367	
$\nu(CO)$	1568-1540				1463			1470	
Tridentate carbonate									
$\delta(OCO)$	823-806		856						
$\nu(CO)$	1038-990	1065-990	1037					1058	
$\nu(CO)$	1297-1258	1380-1280	1367					1310	
$\nu(CO)$	1536-1492	1618-1451	1474					1500	
Hydrogen carbonate									
$\nu(CO)$	1017-999	1030							
$\delta(OCH)$	1192-1174	1218				1200-1240	1200	1200	1200
$\nu(CO)$	1408-1332	1397				1400-1450	1400	1390	1393
$\nu(CO)$	1632-1588	1602				1640-1700	1600	1610	1615
$\nu(OH)$	3700	3616							
Formate									
$\delta(OCH)$	1022-1005		771					1000	1005
$\nu(CO)$	1349-1293		1372						
$\delta(OCH)$	1354-1330	1332				1330-1380		1350	1332
$\nu(CO)$	1562-1530	1561-1539	1565			1550-1590		1570	1530
$\nu(CH)$	2897-2945	2850-2845	2845			2900-3000		2945	2950



Instituto de Carboquímica ICB-CSIC
Calle Luesma Castan 4
50018 Zaragoza Spain